



**HAL**  
open science

# Design and fabrication of a MEMS scanner for OCT imaging endo-microscopic probe

Quentin Tanguy

► **To cite this version:**

Quentin Tanguy. Design and fabrication of a MEMS scanner for OCT imaging endo-microscopic probe. Micro and nanotechnologies/Microelectronics. Université Bourgogne Franche-Comté, 2018. English. NNT : 2018UBFCD035 . tel-02639175

**HAL Id: tel-02639175**

**<https://theses.hal.science/tel-02639175>**

Submitted on 28 May 2020

**HAL** is a multi-disciplinary open access archive for the deposit and dissemination of scientific research documents, whether they are published or not. The documents may come from teaching and research institutions in France or abroad, or from public or private research centers.

L'archive ouverte pluridisciplinaire **HAL**, est destinée au dépôt et à la diffusion de documents scientifiques de niveau recherche, publiés ou non, émanant des établissements d'enseignement et de recherche français ou étrangers, des laboratoires publics ou privés.



SPIM

Thèse de Doctorat



UFC

école doctorale **sciences pour l'ingénieur et microtechniques**  
UNIVERSITÉ DE FRANCHE-COMTÉ

Design and fabrication of a MEMS  
scanner for OCT imaging  
endo-microscopic probe

■ QUENTIN TANGUY





NNT:2018UBFCD035

THÈSE DE DOCTORAT DE L'UNIVERSITÉ BOURGOGNE FRANCHE-COMTÉ  
PRÉPARÉE À L'UNIVERSITÉ DE FRANCHE-COMTÉ

ÉCOLE DOCTORALE n° 37

SPIM

Doctorat de *Sciences pour l'Ingénieur*

Par

QUENTIN TANGUY

Design and fabrication of a MEMS scanner for OCT  
imaging endo-microscopic probe

Design, modélisation, fabrication et contrôle d'un scanner MOEMS et  
intégration à un microsystème endomicroscopique pour le diagnostic des  
cancers dans leur phase initiale

Soutenue publiquement le 9 février 2018, à Besançon, devant le Jury composé de :

VÉRONIQUE BARDINAL-DELAGNES	Directeur de Recherche CNRS, LAAS-CNRS, France	Président
FRÉDÉRIC ZAMKOTSIAN	Chargé de Recherche CNRS, LAM - Université Aix & Marseille, France	Rapporteur
HANS ZAPPE	Professeur, IMTEK - Université de Freiburg, Allemagne	Rapporteur
PAUL MONTGOMÉRY	Directeur de Recherche, ICube - Université de Strasbourg, France	Examineur
CHRISTOPHE GORECKI	Directeur de Recherche CNRS, FEMTO-ST, France	Directeur de thèse
PHILIPPE LUTZ	Directeur de Recherche, FEMTO-ST, France	Co-directeur de thèse
SYLWESTER BARGIEL	Ingénieur de Recherche UFC, FEMTO-ST, France	Encadrant
HUIKAI XIE	Professeur, Université de Floride, USA	Co-encadrant



*Ad Majorem Dei Gloriam !*

*La science moderne, procédant d'une limitation arbitraire de la connaissance à un certain ordre particulier, et qui est le plus inférieur de tous, celui de la réalité matérielle ou sensible, a perdu, du fait de cette limitation et des conséquences qu'elle entraîne immédiatement, toute valeur intellectuelle, du moins si l'on donne à l'intellectualité la plénitude de son vrai sens, si l'on se refuse à partager l'erreur "rationnaliste", c'est-à-dire à assimiler l'intelligence pure à la raison, ou, ce qui revient au même, à nier l'intuition intellectuelle. Ce qui est au fond de cette erreur, comme d'une grande partie des autres erreurs modernes, ce qui est à la racine même de toute la déviation de la science telle que nous venons de l'expliquer, c'est ce qu'on peut appeler l'"individualisme", qui ne fait qu'un avec l'esprit antitraditionnel lui-même, et dont les manifestations multiples, dans tous les domaines, constituent un des facteurs les plus importants du désordre de notre époque. Enfermée irrémédiablement dans le domaine relatif et borné où elle a voulu se proclamer indépendante, ayant ainsi coupé elle-même toute communication avec la vérité transcendante et avec la connaissance suprême, ce n'est plus qu'une science vaine et illusoire, qui, à vrai dire, ne vient de rien et ne conduit à rien.*

---

عبد الواحد يحيى —

# Acknowledgments

**T**HIS Ph.D. thesis was read in the Institute FEMTO-ST of the University of Bourgogne Franche-Comté in Besançon, France, and in the University of Florida located in Gainesville in the [United States of America \(USA\)](#). It was realized thanks to the french LabEx Action funding source and the [USA](#) National Science Foundation which I both express my gratitude.

Then, I would like to address a special word of thanks to my thesis advisor Dr. Christophe Gorecki and co-advisor Dr. Philippe Lutz for offering me the opportunity of joining such an interesting team and a challenging project.

I warmly thank the members of my defense jury for doing me the honor of being present for me and showing so much interest in my modest thesis work. Special thanks to my reporters: Dr. Frédéric Zamkotsian, CNRS researcher at the LAM Institute and the University of Aix & Marseille, France and Pr. Hans Zappe from the IMTEK Institute and the University of Freiburg, Germany. I am also very thankful to Dr. Véronique Bardinal-Delagnes, Professor at the LAAS-CNRS and Dr. Paul Montgomery, Professor at ICube, University of Strasbourg who accepted to be my examiners. Also in my thesis jury, I would like to give special thanks to my american advisor and my supervisor: Dr. Xie Huikai who believed in me from the day we met, for his patience and wise advices all along my stay in the University of Florida, for his involvement, time sharing and leadership; and Dr. Sylwester Bargiel especially for his tutoring, and for sharing his knowledge in microfabrication and being so involved in tedious tasks of our project.

Next, I will not wait more to address my warmest thanks to the most wonderful colleague God ever gave me to meet, Dr. Nicolas Passilly who gave me the motivation to fight during ups and downs. He has been working along with me tirelessly, knowing that he would gain nothing but helping freely. And I certainly owe him an unquestionable chunk of the outcome of this thesis work and of associated publications. Nicolas also taught me the meaning of having a scientific mind and of how to properly solve problems rationally. I really appreciated his amazing patience, his authenticity, sincerity, his efforts in keeping a sane integrity between people in complicated situations. I consider him as a mentor, as much as for his precious knowledge, his scientific approach and the fact of always being honest in it, his consideration and confidence in me. He really is the person I loved working with the most. Merci !

Another colleague that I couldn't ever forget, just for knowing him because he is so awesome, is Dr. Olivier Gaiffe, with whom I spent "human" times and relations during the last years of my thesis. He is both a passionate and "down-to-earth" person, who helped me with the most



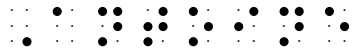

annoying problems ever, thanks to his valuable and broad knowledge which he never hesitated to share kindly.

I would like to thank my colleagues from the [Automatique et Systèmes Micro-Mécatroniques \(AS2M\)](#) department of FEMTO-ST: Dr. Yassine Haddab, the person who put the first stone of this Ph.D., Sotirios, Dr. Sergio Lescano, Dr. Micky Rakotondrabe, Dr. Cédric Clévy, Dr. Kanty Rabenorosoa and Dr. Nicolas Andreff. I would like to thank my wonderful colleagues from the [Micro Nano Sciences & Systems \(MN2S\)](#) department of FEMTO-ST for smiling all the time and bringing so much joy in this so rainy region: Dr. Cyril Millon, so easy going; my beloved system control teacher from the engineering school, who was my last resort in the most extreme situations, Dr. Gonzalo Cabodevila; Dr. Franck Chollet for telling me one time “when you have no brain, you need a pair of legs...”; Dr. Thérèse Leblois for being my floor mate till 10pm almost every weekday and for her amazing patience and kindness; Dr. Jean-François Manceau, Charles-Louis Azzopardi for always being positive, Claude Humbert, my last-year mate and friend, Dr. Rabah Zeggari for pushing me going to cleanroom, and the staff of the MIMENTO cleanroom: Jean-Claude Jeannot Djaffar Belharet, Laurent Robert, Florent Bernard, Franck Lardet-Vieudrin, Marina Raschetti, David Raddenzati Tristan Faure, Roland Salut, Juba Moussaoui and Alain Bresson; Dr. Fabien Rémy-Martin, Dr. Sameh Obeid, Dr. Sarah Benchabane, Dr. Wilfrid Boireau, Dr. Jean-Marc Cote for his precious help in electronics and programming, Dr. Laurent Hirsinger for reviewing my mechanical model; Sandrine Chatrenet, Claudia Laou-Huen, Sandrine Pyon, Joëlle Berthelot, Jocelyne Renaud who helped me so much with the administrative chores. And from the outside: Xu Xin from Accelonix; Fabian and Tobias Hickmann from TPT in Munich for their precious help on the packaging; Didier Bouvet from the EPFL for his precious help on the aluminum deposition; colleagues from FEMTO-ST belfort who lended me instruments of measure: Dr. Sylvie Bégot and Philippe Nardin,

From the MOEMS group of [MN2S](#), I address my thanks to: Dr. Vincent Maurice for his precious help building the setup and introducing me to Python and  $\text{\LaTeX}$ , Dr. Jarosław Rutkowski for showing me the ropes in electronics, with LT-Spice, Eagle and helping me building PCBs, Dr. Przemysław Struk for his presentation of the institute and his help in OCT, Dr. José V. Carrion Perez for his advices and kindness, Dr. Justine Lullin, Dr. Stéphane Perrin, Dr. Jorge Albero, Dr. Ravinder Chutani, Dr. 包程和日, Keshia Adèle Mekemeza Ona, my trainee, Thomas Bertin, Dr. Magali Barthès for reviewing my thermal model, and for the chocolate, Alpha D. Diallo for supporting me in the office without getting mad, Fernando E. Garcia Ramirez, to whom I both wish good luck for their thesis, and very special thanks to Sophie Marguier and Dr. Luc Froehly for the interesting conversations and relations we had.

As I spent half of my Ph.D. time in the University of Florida, I would like to thank sincerely IMG’s faculty: Dr. David Arnold, Dr. Jack Judy, Dr. Alexandra Garraud, Dr. Toshikazu Nishida, Dr. Roozbeh Tabrizian, Dr. Y. K. Yoon and Dr. Sheplak, my colleagues: Dr. 王伟, Dr. 段灿, Dr. Victor Farm-Guoo Tseng, 王禹正, Mayur Ghatge, Dr. Nicolas Garraud, Paul Chojecki, Dr. Camilo Vélez Cuervo, Paritosh Rustogi, Dr. 程翔, Dr. 文骁, Kartik Sondhi, Dr. Fang Shengpo, Dr. Chen Kangfu, Dr. Jose Varillas, Dr. Shashank Sawant, 周亮, Sam, Dr. 韩丰田, Dr. Dai Xianjin, Dr. 张笑阳, Ray; the staff from the NRF cleanroom: Dr. Brent Gila, Dr. David

Hays, Dr. Bill Lewis, Dr. Al Ogden, Andres Trucco and Tom Sanders, the most wonderful people ever. All the trainees who worked with me: Ryan Henry, Zachary Taylor alias “Zak”, Aleksandar S. Zivkovic alias “Sasha”; and my dear friends from Gainesville: the awesome Dr. B. J. Fregly, Gordon Green and his family, Emma, Kevin Kelsey, and all the members of IF; Aurélien Lancien alias “Patate”, Geoffrey Hutinet, Anthony alias “Ant”, Lexi, Rachael and Ville for his photograph skills, Tristan, 吕光, 蒋黎; Salman, Varun Maheshwari, and Akshat Sharma my roomates and Marie Pashkevich.

Thanks so much to my french friends who shared the joys and pains of this PhD adventure along with me: Manon Blaise, Emmanuel Grenot alias “Manu”, , , Pauline Aubanton, Maryne Joly alias “la vierge effarouchée”, Rosalie Douyon, and people from the parish who prayed for me so much: Fr. Eric poinsot, Fr. Norbert Petot, Br. Nicolas Morin, Fr. Axel Isabey, Sébastien Moine and the seminarists, Fr. Sébastien Girard, Fr. Pascal Perroux-Hummel, Fr. Pierre Imbert, Fr. Jean-Baptiste Moreau, Fr. Augustin Cayla, Fr. Bertrand Lacroix, Fr. Arnaud, Sr. Christiane Chavanis, Sr. Laura Amico, Sr. Claude-Marie, Sr. Pascale, Joël and Brigitte Vieille, Antoine and Agnès Bartzen Sprauer, Maxime Meister, Aline Pernin, la Source, l’Escale; Ashley Riddley for correcting my english and Guillaume Thévenon from Théophane; Cor Unum, Aude Dufay, Isabelle, Louis Ferrand, Maria, and Fernande.

Last before last, the most special thanks to my dearest friends Timothée Dupas and Olivier Rougé, 周礼, Nicolas Alexis Rivero Consuela de la virgen Santa Mariá Velazquez Hernandez and 刘亚东 who supported me until the end and will stay forever in my heart!

Very last but not least: my mom and dad, Catherine and Michel Tanguy, my brothers, Rémi and Léonard, my grand mother Ginette and grand father Roger Touron, my aunt, uncle and cousins, those who are not here anymore, but who will remain forever in my heart, and the rest of my family who believed in me until the very end, and whom I love so much!



# Contents

<b>Acknowledgments</b>	<b>vii</b>
<b>Nomenclature</b>	<b>xxxi</b>
<b>Introduction</b>	<b>1</b>
<b>1 Stomach and esophagus cancer detection techniques</b>	<b>5</b>
1.1 Stomach and esophagus cancers . . . . .	7
1.1.1 Definition . . . . .	7
1.1.2 Figures & early detection . . . . .	10
1.2 Intravital imaging approaches in cancer research . . . . .	11
1.2.1 Non-optical imaging methods . . . . .	12
1.2.1.1 Magnetic resonance imaging . . . . .	12
1.2.1.2 Computed tomography . . . . .	13
1.2.1.3 Ultrasounds . . . . .	14
1.2.2 Optical imaging methods . . . . .	14
1.2.2.1 Confocal microscopy . . . . .	15
1.2.2.2 Photoacoustic microscopy . . . . .	15
1.2.2.3 Fluorescence . . . . .	15
1.2.2.4 Non-linear optical microscopy . . . . .	16
1.2.2.5 Optical coherence tomography . . . . .	16
1.2.3 Synthesis . . . . .	16
1.3 Optical coherence tomography . . . . .	18
1.3.1 Low Coherence Interferometry . . . . .	18
1.3.2 TD-OCT . . . . .	20
1.3.3 FD-OCT . . . . .	21
1.3.4 SS-OCT . . . . .	21
1.3.5 Endoscopic OCT . . . . .	22
1.4 Conclusion . . . . .	23
<b>2 Miniaturization of OCT systems</b>	<b>25</b>
2.1 Endoscopic probe classification criteria . . . . .	26
2.1.1 Scan direction . . . . .	26
2.1.1.1 Forward-imaging . . . . .	26
2.1.1.2 Side-imaging . . . . .	26
2.1.2 Actuation location . . . . .	27

2.1.2.1	Proximal scanning . . . . .	27
2.1.2.2	Distal scanning . . . . .	28
2.1.3	Scan type . . . . .	28
2.1.3.1	1D rotational . . . . .	28
2.1.3.2	1D rotational with pullback . . . . .	28
2.1.3.3	2D rotational . . . . .	28
2.1.4	Scan pattern . . . . .	30
2.1.4.1	Raster scan . . . . .	30
2.1.4.2	Lissajous scan . . . . .	30
2.1.4.3	Spiral scan . . . . .	31
2.1.5	Scanning mechanism . . . . .	31
2.1.5.1	Galvanometers and micromotors . . . . .	31
2.1.5.2	MEMS scanners . . . . .	31
2.1.5.3	Others . . . . .	32
2.1.6	Encapsulation type . . . . .	32
2.2	Comparison and selection of the main features . . . . .	33
2.2.1	Forward and side view . . . . .	33
2.2.2	Proximal and distal scanning . . . . .	33
2.2.3	Scan type . . . . .	35
2.2.4	Scan patterns . . . . .	36
2.2.5	Encapsulation . . . . .	36
2.3	State of the art of distal side-imaging endoscopic OCT probes . . . . .	37
2.4	Component embedding level of MEMS-based endoscopic OCT systems . . . . .	39
2.4.1	Review of component embedding evolution . . . . .	39
2.4.2	Optical microbench assembly . . . . .	40
2.4.3	Wafer-level batch microfabrication . . . . .	41
2.5	Overview of DEMO4 endoscopic probe & optical specifications . . . . .	42
2.5.1	Continuum robotic arm . . . . .	43
2.5.2	Illumination block . . . . .	44
2.5.3	Mirau interferometer . . . . .	44
2.5.3.1	Integration of interferometers in the literature . . . . .	45
2.5.3.2	Comparison of interferometers . . . . .	46
2.5.3.3	A batch fabricated Mirau micro-interferometer . . . . .	47
2.5.4	Optical scanner . . . . .	49
2.6	Conclusion . . . . .	52
<b>3</b>	<b>Review of tilt 2D MOEMS scanners and actuation principles</b> . . . . .	<b>55</b>
3.1	Basic principle of the main actuation types . . . . .	55
3.1.1	Electrostatic actuation . . . . .	56
3.1.1.1	Basic principle . . . . .	56
3.1.1.2	Pros & cons of Electrostatic tilt MEMS scanners . . . . .	57
3.1.2	Electromagnetic actuation . . . . .	57
3.1.2.1	Basic principle . . . . .	57
3.1.2.2	Pros & cons of Electromagnetic tilt MEMS scanners . . . . .	57

3.1.3	Piezoelectric actuation . . . . .	58
3.1.3.1	Basic principle . . . . .	58
3.1.3.2	Pros & cons of Piezoelectric tilt MEMS scanners . . . . .	59
3.1.4	Electrothermal actuation . . . . .	59
3.1.4.1	Basic principle . . . . .	59
3.1.4.2	Pros & cons of Electrothermal tilt MEMS scanners . . . . .	60
3.2	State of the art of MEMS electrothermal tilt scanners . . . . .	61
3.3	Conclusion . . . . .	67
<b>4</b>	<b>Description and design of the micro-scanner</b>	<b>69</b>
4.1	Optical design . . . . .	69
4.2	Electrothermal actuation principle . . . . .	71
4.2.1	Electrothermal bimorph actuation principle . . . . .	71
4.2.1.1	Steady-state model . . . . .	72
4.2.1.2	Dynamic thermal considerations . . . . .	76
4.2.2	Thermomechanical model . . . . .	80
4.2.2.1	Curvature in bimorph cantilever . . . . .	80
4.2.2.2	Curvature in a multimorph cantilever . . . . .	83
4.2.2.3	Stiffness and natural frequency . . . . .	84
4.2.3	Material selection . . . . .	85
4.3	Micro scanner: Description and design . . . . .	87
4.3.1	Torsion beam . . . . .	88
4.3.2	Mirror coating and plate deformation . . . . .	93
4.3.3	Electrothermal actuators . . . . .	94
4.3.3.1	Bimorph array . . . . .	94
4.3.3.2	Meshed inverted-series-connected actuators . . . . .	96
4.3.4	Thermal model . . . . .	106
4.3.5	Improvements . . . . .	109
4.3.5.1	Gold pads . . . . .	109
4.3.5.2	Mechanical 45° stopper mechanism . . . . .	110
4.3.5.3	Increasing the degrees of freedom . . . . .	112
4.4	Conclusion . . . . .	113
<b>5</b>	<b>Fabrication</b>	<b>115</b>
5.1	Base device fabrication process . . . . .	116
5.1.1	Flow chart and layout . . . . .	116
5.1.2	Preliminary clean-up stage . . . . .	118
5.1.3	First layer of silicon dioxide - OXD1 . . . . .	118
5.1.4	Platinum heater - PT . . . . .	120
5.1.5	Second insulation layer opening - VIA . . . . .	120
5.1.6	Top side layer of aluminum - ALU1 . . . . .	121
5.1.7	Second layer of silicon dioxide - OXD2 . . . . .	123
5.1.8	Back side pit carving - BSD . . . . .	125
5.1.9	Release - REL . . . . .	126

5.2	Complementary fabrication tips . . . . .	126
5.2.1	Flow chart . . . . .	126
5.2.2	Gold pads - AUP . . . . .	128
5.2.3	Second mirror aluminum layer - ALU2 . . . . .	129
5.3	Packaging . . . . .	131
5.4	Conclusion . . . . .	132
<b>6</b>	<b>Characterization and integration</b>	<b>135</b>
6.1	Characterization of the micro-scanner . . . . .	135
6.1.1	Optical characteristics . . . . .	136
6.1.2	General features and static behavior . . . . .	136
6.1.3	Experimental setups . . . . .	139
6.1.4	Dynamic behavior and frequency response . . . . .	140
6.1.5	Lissajous scan for imaging . . . . .	145
6.1.5.1	Lissajous scan dynamic study . . . . .	145
6.1.5.2	Tracking and repeatability study . . . . .	147
6.2	Integration of the MOEMS probe head . . . . .	150
6.3	Conclusion . . . . .	152
	<b>Conclusion</b>	<b>155</b>
	<b>Appendix A Fabrication risks &amp; recommendations</b>	<b>161</b>
	<b>Appendix B Photolithography</b>	<b>165</b>
B.1	Basic principle . . . . .	165
B.2	Lift-off principle . . . . .	166
	<b>Bibliography</b>	<b>199</b>

# List of Figures

1.1	Comparison of stomach and esophagus cancer incidence and mortality worldwide in men population in 2012. Source: GLOBOCAN 2012, globocan.iarc.fr. Incidence of stomach <b>(a)</b> , and esophagus <b>(b)</b> cancers in men. Mortality rate of stomach <b>(c)</b> , and esophagus <b>(d)</b> cancers in men. . . . .	6
1.2	Sketch of the human stomach. <i>(left)</i> : Different parts of the human distal esophagus and stomach. “Stomach Pic for Food Poisoning Thingy” by Daniel X. O’Neil, license: CC BY 2.0. <i>(right)</i> : Detailed anatomy of the layers of the wall of the stomach. “Illustration from Anatomy & Physiology, Connexions Web Site” by OpenStax College, license: CC BY-SA 3.0. . . . .	8
1.3	<b>(A)</b> : Transmission electron micrograph of human stomach epithelial cells exposed to <i>H. pylori</i> for 1 hour. <b>(B)</b> : <i>H. pylori</i> located along one epithelial cell [14]. . . . .	9
1.4	Representation of invasive evolution of gastric tumors according to TNM classification. HGD=high-grade dysplasia. T4a lesions are resectable whereas T4b are not. [20] . . . . .	11
1.5	Micrograph of a surgical specimen showing gastric adenocarcinoma cells ( <i>arrows</i> ) infiltrating <i>muscularis propria</i> (stage T2) [25]. . . . .	12
1.6	Comparison of : <b>(a)</b> : Axial helical CT scan of the gastric body of a 44-year-old man with a T2 stage gastric carcinoma showing wall thickening with strong contrast enhancement. Cancer was incorrectly diagnosed at stage T1. <b>(b)</b> : T1-weighted MRI image of the same patient failed to show lesions. <b>(c)</b> : Helical CT scan showing concentric tumor with strong contrast enhancement in the gastric body of a 54-year-old man with T3 stage gastric cancer. Gastric tumor and infiltration in adjacent fat are well seen. <b>(d)</b> : Contrast-enhanced T1-weighted MRI image of the same patient. Demarcation of gastric tumor and lymph nodes is blurred with motion artifact. [25]	13
1.7	Lesion in the stomach of a 77-year-old man involving the <i>antrum</i> exhibiting a thickening of the gastric wall and infiltration into the <i>muscularis propria</i> . <b>(a)</b> : CT view showing the mucosal and submucosal thickening of the inner wall at the location of the arrow. <b>(b)</b> : EUS image showing the serosal layer and the location where the lesion penetrates the <i>muscularis propria</i> [36]. . . . .	14



1.8	Comparison of the resolution and penetration depth of bioimaging techniques; <i>ET</i> : epithelial thickness; <i>LP</i> : distance from epithelium surface to <i>lamina propria</i> ; <i>MP</i> : distance from epithelium surface to <i>muscularis propria</i> [22]; <i>HP</i> : maximum size of <i>H. pylori</i> ; <i>EGC</i> : Half-space limit of resolution required for the detection of early gastric cancers limited at stage II of the TNM classification; <i>AGC</i> : Half-space limit for detection of advanced gastric cancer as defined by Im <i>et al.</i> [15]. Note that the size of cells nuclei is compared with the resolution attainable [21]. . . . .	17
1.9	Schematic of the principle of a Michelson interferometer and low-coherence interferometry in time domain. Picture from [64]. . . . .	18
1.10	Light source spectrum $S(k)$ and its Fourier transform $\gamma(z)$ , the coherence function [56]. . . . .	19
1.11	A-scan of discrete reflectors recorded on a single detector by TD-OCT [56]. . . . .	21
1.12	(a):A-scan of discrete reflectors obtained by FD-OCT. (b):Profile of the intensity detected by a single reflector in FD-OCT. Pictures from [64]. . . . .	22
1.13	OCT images of neoplastic changes. (a): Normal colon; m: <i>mucosa</i> ; mm: <i>muscularis mucosa</i> ; sm: <i>submucosa</i> . (b): Specimen of colon with adenocarcinoma Fujimoto and Drexler [56]. . . . .	23
2.1	Endoscopy performed in hospital or clinical complexes. (a): Endoscopy service room set-up and patient positioning for endoscopy imaging. (b): Conventional double-channel therapeutic endoscope (gastroscope) used for detection and therapy operation. (c): Standard medical video endoscope for use <i>in vivo</i> with imaging tools; Pentax Precision Instrument, EB15 series J, Tokyo, Japan; minimum outer diameter 5.4 mm. Recent gastroscope's instrument ports have an average inner diameter of 2.8 mm [88]. . . . .	27
2.2	Simplified schematic view of forward and side-viewing configuration. From [90] . . .	27
2.3	Design of actuation system of Tearney <i>et al.</i> 's proximal endoscopic probe. (a): Catheter's tip. (b): Proximal actuation system. (c): Overview of the whole catheter. [73]. . . . .	28
2.4	Different OCT images obtained by means of various scan types, paths and mechanism. (a) 1D rotational full circumferential B-scan without pullback from [73]. (b) 1D rotational reduced circumferential FOV without pullback from [96]. (c) 1D rotational full circumferential B-scan in lumen from [97], and (d) its corresponding 3D OCT image by translational pullback from [97]. (e) Cross-sectional stack of a 2D rotational B-scans and C-scan by using a 2-axis MEMS micro-scanner raster scan of a hamster cheek pouch acquired <i>in vitro</i> by [98] and (f) its corresponding 3D rendering from the same hamster cheek pouch [98]. (g) 1D rotational reduced circumferential B-scan of a human esophagus performed by raster scan using proximal prism from [75]. (h) 1D rotational full circumferential B-scan with distal actuation, hindered by the shade of the electrical cable connecting the distal micromotor from [98]. (i) Full circumferential scan performed in a pig esophagus with a single-balloon imaging catheter from [82]. ep= <i>epithelium</i> ; lp= <i>lamina propria</i> ; mm= <i>muscularis mucosa</i> ; sm= <i>submucosa</i> ; mp= <i>muscularis propria</i> . . . . .	29

2.5	Raster scan with triangular waveform in the X-axis and smooth stair waveform in the Y-axis. . . . .	30
2.6	Lissajous scan of a 5 $\mu\text{m}$ image with sine waveforms of 1.39 Hz in the X-axis and 1.25 Hz in the Y-axis. . . . .	31
2.7	Spiral scan of 5 $\mu\text{m}$ with constant angular velocity. . . . .	31
2.8	Different sizes of 2-axis MEMS mirrors fabricated by Fraunhofer Institute for Photonic Microsystems. Image from Fraunhofer IPMS. . . . .	32
2.9	Simplified schematic view of a single-balloon catheter. From [90]. . . . .	33
2.10	Schematic view of a double-balloon endoscopic catheter. From [120]. . . . .	33
2.11	Endoscopic probe design by Weber <i>et al.</i> [54]. Sketch of the circumferential-scanning probe (left) and integrated micro-scanner-driven configuration (right). . . . .	36
2.12	Order of criteria of classifications of the endoscopic probes configurations. . . . .	38
2.13	Side-imaging MEMS-based probe design; FC: fiber collimator. From Aguirre <i>et al.</i> [98]. . . . .	38
2.14	SiOB assembled catheter design by Xu <i>et al.</i> [126]. . . . .	38
2.15	3D sketch of Samuelson <i>et al.</i> 's probe head. From [127]. . . . .	39
2.16	3D sketch of Duan <i>et al.</i> 's probe head. From [128]. . . . .	39
2.17	Comparison of the evolution of component integration level in micro-optical systems. (a): SEM picture of the front size of a 3D refractive microlens fabricated by Wu [145]. (b): Photograph of Weber <i>et al.</i> 's opto-fluidic silicon optical bench with all components integrated [149]. (c): SEM of a 300 x 400 $\mu\text{m}$ resonant scanning mirror electrostatically actuated with torsion bars, deflecting light in an out-of-plane direction Muller [147]. (d): Schematic of the final probe head of Aljaseem <i>et al.</i> [116], including the tunable lens and the scanning mirror. (e): SEM micrograph of two micro-optical component holders assembled onto a substrate rail and fabricated by Bargiel <i>et al.</i> [148]. (f): Schematic representation of a forward-imaging endOCT probe including a MEMS lens scanner, and details of the electrostatic MEMS lens scanner [151]. . . . .	42
2.18	Process of wafer-level batch microfabrication. Image from [154]. . . . .	43
2.19	Sketch of a batch fabricated vertical micro-scanner for phase modulation interferometry at the wafer level. Image from [153]. . . . .	43
2.20	Schematic of the probe designed by Tumlinson <i>et al.</i> [84]. BS: beam splitter; RM: reference mirror; GRIN: gradient index. . . . .	45
2.21	Comparison of Michelson, Linnik and Mirau interferometers. Pictures from [166]. . . . .	46
2.22	Schematic of the Mirau micro-interferometer. Pictures from [83] & Bargiel. . . . .	47
2.23	Sketch of the MOEMS optical probe with Mirau micro-interferometer from [83] in 1D forward-imaging. . . . .	47
2.24	Sketch of the MOEMS optical probe with Mirau micro-interferometer from [83] in 2D side-imaging with a micro-scanner and encapsulated. FM: Fixed mirror; MM: Moving mirror. . . . .	53
3.1	Schematic of (a) an electrostatic micro-scanner with integrated sensing mechanism (Picture from [180]) and (b) of a 2D scanning micromirror from [181]. . . . .	56

3.2	Principle of electromagnetically actuated micro scanners of type (1) <b>(a)</b> by Miyajima <i>et al.</i> [191] and type(2) <b>(b)</b> by Judy and Muller [195]. . . . .	58
3.3	Sketches of piezoelectric actuators. <b>(a)</b> : Multimorph configuration [202]. <b>(b)</b> : Unimorph configuration [203]. . . . .	58
3.4	Schematic of Buhler <i>et al.</i> 's electrothermal device. <b>(a)</b> : Cross section of the supporting cantilever beam actuators and the mirror plate. <b>(b)</b> : 3D view of the configuration of the different layers constituting the cantilever bimorph. . . . .	62
3.5	<b>Generation A1</b> of electrothermal micro-scanner fabricated by Pan <i>et al.</i> . <b>(a)</b> : Top-view schematic design of the first version with longitudinally positioned polysilicon resistor [231]. <b>(b)</b> : Second version with transversely oriented polysilicon resistor [231]. <b>(c)</b> : SEM picture of the whole structure in its initial bending. <b>(d)</b> : SEM close-up view of the electrothermal bimorph array generating the "draw bridge" motion. [99]. . . . .	63
3.6	<b>Generation A2</b> first reported by Xie <i>et al.</i> [237] in 2003. <b>(a)</b> : Top-view schematic of the improved scanner with polysilicon resistors attached in series. <b>(b)</b> : SEM overview of the 1D scanner. . . . .	63
3.7	<b>Generation A3</b> ; <b>(a)</b> : Top view showing areas of rotation. <b>(b)</b> : SEM picture of the micro-scanner fabricated. Pictures from Jain <i>et al.</i> [141] . . . . .	64
3.8	<b>Generation A4</b> ; <b>(a)</b> : Top view. <b>(b)</b> : SEM picture. Pictures from Jain <i>et al.</i> [232].	64
3.9	<b>Generation A5</b> ; <b>(a)</b> : Top view of the micromirror. The four actuators are highlighted. <b>(b)</b> : SEM picture. From Jain and Xie [225]. . . . .	64
3.10	<b>Generation ISC</b> ; <b>(a)</b> : Schematic top view. <b>(b)</b> : SEM picture. Pictures from [220].	65
3.11	<b>Generation DISC</b> ; <b>(a)</b> : Side-view sketch. <b>(b)</b> : SEM picture. Pictures from [252].	65
3.12	<b>Generation TISC</b> ; <b>(a)</b> : Side-view sketch. <b>(b)</b> : SEM picture. Pictures from Xie <i>et al.</i> [255], Wang <i>et al.</i> [256]. . . . .	65
3.13	<b>Generation LSF</b> . <b>(a)</b> : Layout top vie of LSF micromirror with actuators on each side. <b>(b)</b> : Corresponding SEM picture. <b>(c)</b> : Layout top view with actuators on opposite sides only. <b>(d)</b> : Corresponding SEM picture . <b>(e)</b> : Layout of curved LSF structures. <b>(f)</b> : Corresponding SEM view. Pictures from [214, 215, 267, 268, 272].	66
3.14	Schematic principles of actuation of the different generations of ETA. <b>(a)</b> : LVD with lateral shift; <b>generation A3</b> . <b>(b)</b> : Basic principle of single <b>ISC actuators</b> . <b>(c)</b> : <b>LSF LVD</b> actuation sketch. <b>(d)</b> : In-plane curved <b>LSF</b> actuators. Pictures from [215, 220, 222, 275]. . . . .	66
4.1	Schematic views of the optical design of the micro-scanner coupled within the MOEMS probe. <b>(a)</b> : Cross-sectional side view of the distal end from the BSP of the MOEMS probe with the mirror corresponding to the <b>(b)</b> : <i>En face</i> view from the top of the probe. . . . .	70
4.2	Schematic view of an electrothermal bimorph cantilever beam in a flat, undeformed shape. . . . .	72
4.3	Normalized temperature distribution along a bimorph transducer for a given applied power and $R_{TL} > R_{TR}$ and arbitrary value of resistance and power. Points of maximum temperature are depicted by triangles $\Delta$ whereas the average are located on their corresponding balancing factor curve and symbolized by circles $\circ$ . . . . .	75

4.4	LEM of the steady-state simplified electrothermal system without convection. Based on [231]. . . . .	76
4.5	LEM of the dynamic system for one ... . . . .	78
4.6	Frequency response of the electrothermal system of the average temperature change in the bimorph beam with respect to the square of the applied voltage. The numerical values used for the simulation are based on [216]. <b>(a)</b> : Bode diagram of $H_{et}(s)$ for the raw nonlinear system, the system linearized by limited development in $\hat{T}$ , and with or without the resistor simplification mentioned in Section 4.2.1.2. <b>(b)</b> : Error of each model with respect to the nonlinear electrothermal response. . . . .	79
4.7	Block diagram of the electrothermal system. $H_E$ : the electrical power system block ; $H_1$ : linear thermal system with the power in input ; $H_r$ : heater temperature conversion block. . . . .	80
4.8	Schematic view of the bimorph in an arbitrary deformed position and comparison with the stress-free state of the beam in uncolored. . . . .	82
4.9	Sketch of the MOTEMS of the first batch with torsion beam. . . . .	88
4.10	Schematic 3D view of the torsion beam as designed in the micro-scanner. . . . .	89
4.11	First four oscillation modes of the torsional micro-scanner. . . . .	89
4.12	SEM pictures of torsion beams composed of different materials and their state after identical actuation. <b>(a)</b> : Aluminum inlayed torsion beam. This structure is schematically described in Fig. 4.10(left). <b>(b)</b> : Aluminum-free torsion beam. . . . .	93
4.13	Mirror distortion due to dynamic torque. . . . .	94
4.14	Top-view schematic of the bimorph array electrical path. . . . .	95
4.15	Deflection of the ISC structure with overlapping section and parameters for calculation. . . . .	97
4.16	Schematic side view of the ISC actuator piling up order and configuration during fabrication and before release. . . . .	98
4.17	Schematic cross section of the <b>(a)</b> non-inverted bimorph, <b>(b)</b> inverted bimorph and <b>(c)</b> overlapping segment and <b>(d)</b> torsion beam for comparison. Courtesy from [176]. . . . .	98
4.18	Schematic view of the split up logic of the DSSISC actuator with the segments and the nodes. . . . .	99
4.19	MISC actuator proposed in this work (in light green), as an evolution of the basic pair of DSSISC structure (in dark red). . . . .	99
4.20	Side-view geometric schematic of mirror plate motion within the inner frame. The actuators are symbolized by springs. The springs in gray depict the actuators as they are initially during fabrication and after release of the micromirror. The mirror is represented in an out-of-plane position. . . . .	102
4.21	Variation of angular stiffness $k_m$ with respect to angle of mirror for three different width of torsion bar. The “rodless” labelled curve is the stiffness of the actuators without the torsion bar. . . . .	104
4.22	Resonance frequency versus amplitude of vibration of the mirror plate for four different average angles and three different widths of torsion bar denoted by their curve marks: $\diamond$ : width=22 $\mu\text{m}$ , $\triangle$ : width=28 $\mu\text{m}$ and $\square$ : width=38 $\mu\text{m}$ . . . . .	104
4.23	Resonance frequency variation with respect to thickness of the mirror plate for different angular amplitudes centered around an initial angular offset of 18°. . . . .	105

4.24	Evolution of the ISC-based actuators and their LEM equivalence in term of mechanical spring constant. . . . .	106
4.25	Schematic LEM of the thermal behavior of the micro-scanner in case 2 with symbols nomenclature. . . . .	108
4.26	Variation of the heat flow ratio $P_P/P_{ER}$ for different values of four thermal resistances of the structure. . . . .	109
4.27	Comparison of two types of stopper mechanisms used for MEMS technology. (a): Vertical stopper from [287]. (b): Bending down slanting stopper. Courtesy of Duan <i>et al.</i> . . . . .	110
4.28	Schematic view of mechanical stopper mechanism. Frame is represented in green (a) before and (b) after release. . . . .	111
4.29	Sketch of the geometry of the stopper mechanism and its dimensions for the calculation of the latch lock angle. (a): Layout top view of the latch and the actuators. (b): Side view of the stopper before release of the device. (c): Side view of the stopper slanting on the vertical wall of the handle layer after release. . . . .	111
4.30	SEM pictures of the two main devices (a) Tor2.x and (b) Quad2.0 of the second batch of fabrication. . . . .	113
5.1	Layout of the Tor1.x micro-scanner fabricated and presented in the current work. .	117
5.2	Schematic view of the fabrication step ⟨OXD1⟩ of the first batch. [a,k]: Substrate; [b]: Pads; [c]: Space between the pads and the bimorph array; [d]: Bimorph array; [e,i,l,p]: Inner frame; [f,h]: Torsion bar; [g,n]: Mirror plate; [j]: Gap between the substrate and the inner frame; [m]: ISC-based actuators; [o]: ISC-based actuators. . . . .	118
5.3	Image of step ⟨OXD1⟩ on the region of the thermal bridge after BOE wet etch and before PR strip. The region corresponds to the SEM picture shown in Fig. 5.15h. (a): Optical microscope. (b): Corresponding layout area. . . . .	119
5.4	Schematic view of the fabrication step ⟨PT⟩ of the first batch. [a,k]: Substrate; [b]: Pads; [c]: Space between the pads and the bimorph array; [d]: Bimorph array; [e,i,l,p]: Inner frame; [f,h]: Torsion bar; [g,n]: Mirror plate; [j]: Gap between the substrate and the inner frame; [m]: ISC-based actuators; [o]: ISC-based actuators. . . . .	120
5.5	SEM picture of the Pt heater continuous electrical path deposited on top of the first layer of SiO <sub>2</sub> . . . . .	121
5.6	Results of the Pt sputtering by microscope and SEM and comparison with the layout. . . . .	121
5.7	Schematic view of the fabrication step ⟨VIA⟩ of the first batch. [a,k]: Substrate; [b]: Pads; [c]: Space between the pads and the bimorph array; [d]: Bimorph array; [e,i,l,p]: Inner frame; [f,h]: Torsion bar; [g,n]: Mirror plate; [j]: Gap between the substrate and the inner frame; [m]: ISC-based actuators; [o]: ISC-based actuators. . . . .	122
5.8	Results of step ⟨VIA⟩ seen under optical microscope in different regions of the device and corresponding layout areas. . . . .	122
5.9	Schematic view of the fabrication step ⟨ALU1⟩ of the first batch. [a,k]: Substrate; [b]: Pads; [c]: Space between the pads and the bimorph array; [d]: Bimorph array; [e,i,l,p]: Inner frame; [f,h]: Torsion bar; [g,n]: Mirror plate; [j]: Gap between the substrate and the inner frame; [m]: ISC-based actuators; [o]: ISC-based actuators. . . . .	122

5.10	Fabrication results of step ⟨ALU1⟩. (a): Base of bimorph array layout. (b): Microscope image of parts burned by arcing on the same region. (c): SEM picture of the same region. (d): Overview layout of the device. (e): Microscope view of the corresponding region. (f): Black dots on aluminum. . . . .	123
5.11	Schematic view of the fabrication step ⟨OXD2⟩ of the first batch. [a,k]: Substrate; [b]: Pads; [c]: Space between the pads and the bimorph array; [d]: Bimorph array; [e,i,l,p]: Inner frame; [f,h]: Torsion bar; [g,n]: Mirror plate; [j]: Gap between the substrate and the inner frame; [m]: ISC-based actuators; [o]: ISC-based actuators. . . . .	124
5.12	Fabrication results of step ⟨OXD2⟩. (a): Black silicon around the MISC actuator area. (b): Corresponding layout. . . . .	125
5.13	Schematic view of the fabrication step ⟨BSD⟩ of the first batch. [a,k]: Substrate; [b]: Pads; [c]: Space between the pads and the bimorph array; [d]: Bimorph array; [e,i,l,p]: Inner frame; [f,h]: Torsion bar; [g,n]: Mirror plate; [j]: Gap between the substrate and the inner frame; [m]: ISC-based actuators; [o]: ISC-based actuators. . . . .	125
5.14	Fabrication results of step ⟨BSD⟩. (a): Profile of the back side of the SOI wafer. (b): State of the wafer after separation of some structures from the wafer. (c): Cluster of micromirrors ready for final release step. . . . .	126
5.15	Fabrication results of step ⟨REL⟩. (a): Three micro-scanners stucked on thermal tape after release and before being removed from the carrier wafer. (b): Bigger amount of devices after release. (c): Unreleased torsion bar. (d): Released torsion bar. (e): Front side SEM view of the Tor1.x. (f): Close-up view of the Tor1.x bimorph array. (g): Close-up of the MISC actuators. (h): Thermal insulation bridge between MISC actuators and mirror plate. . . . .	127
5.16	Layout of the (a) Tor2.x and (b) Quad2.0 micro-scanner fabricated and presented in the current work and their corresponding SEM pictures (c) and (d). . . . .	128
5.17	Schematic view of the fabrication step ⟨AUP⟩ of the second batch. [a,k]: Substrate; [b]: Pads; [c]: Space between the pads and the bimorph array; [d]: Bimorph array; [e,i,l,p]: Inner frame; [f,h]: Torsion bar; [g,n]: Mirror plate; [j]: Gap between the substrate and the inner frame; [m]: ISC-based actuators; [o]: ISC-based actuators. . . . .	129
5.18	Fabrication results of step ⟨AUP⟩. (a): SEM overview of an AuAl <sub>2</sub> pad subject to diffusion. (b): Close-up of the pad, roughness detail. . . . .	130
5.19	Schematic view of the fabrication step ⟨ALU2⟩ of the second batch. [a,k]: Substrate; [b]: Pads; [c]: Space between the pads and the bimorph array; [d]: Bimorph array; [e,i,l,p]: Inner frame; [f,h]: Torsion bar; [g,n]: Mirror plate; [j]: Gap between the substrate and the inner frame; [m]: ISC-based actuators; [o]: ISC-based actuators. . . . .	130
5.20	Fabrication results of step ⟨ALU2⟩ using dry PR. (a): Dry PR after lamination and photolithography on the back side of the SOI wafer. (b): Microscope image of the back side of the mirror plate aluminum reflective layer and measures. (c): SEM picture of the back side of the mirror plate before complete release of the torsion bars and inner MISC actuators. . . . .	131
5.21	Custom bonding PCBs fabricated for experiments and characterization. (a): Reduced-size narrow PCB holders in a gel pack for transportation. (b): Failed trials with 25 μm gold wire. (c): Successful trials with 17 μm gold wire. . . . .	132
5.22	Sketch of the micro-scanner holder PCB used for characterizations and testing. . . . .	132

6.1	Tor1.x (a) SEM picture, (b) topography front-side surface of the mirror plate and (c) topographic profile curve. . . . .	136
6.2	Comparison of resistance change upon actuation obtained experimentally and from the model. . . . .	137
6.3	Absolute static angular displacement of the inner frame and the mirror plate vs. DC voltage applied. . . . .	138
6.4	Power consumption of the actuators due to Joule heating vs. voltage applied. . . .	138
6.5	DC characterization of (a) optical angular pitch displacement of the inner frame compared with the model results and (b) corresponding calculated average temperature change $\Delta\bar{T}$ and maximum temperature change $\Delta\hat{T}$ across a bimorph actuator. . . . .	139
6.6	Sketch of the experimental optical setup used for characterization of the micro-scanner. . . . .	139
6.7	Sketch of the OA electrical circuit. . . . .	140
6.8	Elements constituting the driving setup. (a): Custom OA PCB. (b): DAQ with four connection cables for the Quad2.0. (c): micro-scanner PCB holder and routing wire connected. . . . .	141
6.9	Bode diagrams of three different types of Tor1.x, when (a) the pitch actuator is driven, (b) the roll actuators are driven and (c) the phase of the Tor1.28 for the pitch and roll axes. . . . .	142
6.10	Frequency response of the Tor1.22 for a voltage input on the roll actuator of amplitude $0.2 V_{pp}$ and varying offsets. (a): Frequency response over a bandwidth of 4 kHz and zoomed-in insets of the pure tilt mode response and third coupled mode given in (b) and (c), respectively. . . . .	144
6.11	Frequency response comparison of Tor1.22 with and without torsion bars. . . . .	145
6.12	Lissajous scan pattern for a duration of 200 ms. . . . .	146
6.13	Lissajous patterns obtained by sine excitations of frequencies 205 Hz and 1.445 kHz for the slow scan on the pitch axis and the fast scan on the roll axis, respectively, in elapsed times of (a) 4 ms, (b) 16 ms and (c) 45 ms. . . . .	146
6.14	Cover rate of the Lissajous scan pattern versus acquisition time. . . . .	147
6.15	Cover density of the laser spot in times of passing. . . . .	147
6.16	Schematic of the compensation model of the micro-scanner system for a given set of input signal frequencies. . . . .	148
6.17	2D rectified laser spot angular position (in blue, in background) and measured positions (in red, in foreground). . . . .	149
6.18	Histograms of distribution of the absolute angular error (a) in 1D (with respect to each axis), and (b) in 2D. . . . .	149
6.19	Schematic overview of the fully integrated MOEMS probe's head without the continuum robot arm. . . . .	150
6.20	(a) Micro-mirror handled by a vacuum pick-up tool. (b) Heated vacuum chuck. . . .	151
6.21	Fabrication of a thin and uniform layer of Epoxy glue. . . . .	151
6.22	Micro-scanner bonded to the interferometer-chip. . . . .	151
6.23	Preparation the step of bonding of the custom flexible PCB onto the micro-scanner's pads. (a): Epoxy glue drops are deposited on the pads. (b): The flexible PCB is folded at $90^\circ$ . . . . .	152

6.24 Views of the interferometer-scanner chip with the vacuum tool handling the flexible PCB. (a): <i>En face</i> view, with the capillary used to apply contact pressure. . . . .	152
B.1 Schematic diagram of a photolithography with positive and negative PR. . . . .	165
B.2 Schematic diagram of a lift-off process comparing the use of a positive and a negative PR. . . . .	166





# List of Tables

1.1	TNM classification of gastric cancers. [9]	11
1.2	Survival based on TN stages in the LST and SST groups; Data in bold font correspond to cases of EGCs [17, 20].	12
1.3	Comparison of performances of bioimaging techniques. NLOM: non-linear optical methods.	17
2.1	Comparison of features of different imaging endOCT probes.	34
2.2	Summary of the pros and cons of side-imaging and forward-imaging configuration from Gora <i>et al.</i> [88].	35
2.3	Comparison of principal scan patterns and their features.	37
2.4	Recap table of the dependency of the optical parameters of the system.	49
2.5	Summary of the parameters and specifications of the optical system.	49
2.6	Summary of the parameters and specifications required for the optical scan.	52
2.7	Summary of the specifications for the MOEMS scanner.	52
3.1	Comparison of four significant piezoelectric actuator-based 2D micro-scanners.	59
3.2	Comparative table of the features of the scanners with different types of actuation. Sources from [139, 165].	61
3.3	Color code of the different generations of electrothermal MEMS scanners developed in the BML group of the UF.	61
3.4	Exhaustive recap table of the publications concerning MOTEMS (excluding reviews) of the group BML of H. Xie from the University of Florida from 2004 to 2017. [a]: Intertwined ISC actuators; [b]: HFF hidden actuators. [c]: Al/W actuators; [d]: Planar degree of freedom; [e]: including sloping mechanical stopper; [f]: Cu/W actuators; [g]: Including vertical mechanical stopper; [h]: In-plane curved actuators; [i]: Hybrid aelectrothermal/electrostatic actuation; †.	68
4.1	Relations between lumped elements of different domains.	77
4.2	List of a few values of coefficient of convection calculated on electrothermal micro-scanners from different studies.	78
4.3	Comparison of the properties of a few materials. From [212, 213, 224, 323, 346, 347].	86
4.4	Resonant frequency, stiffness and other parameters of the vibrating modes of a rectangular cross-section torsion bar.	90
4.5	List of the main parameters of the mirror plate and torsion beam.	93
4.6	Parameters chosen for the first design of the bimorph array actuators.	96

4.7	Recap table of the main parameters of the MISC actuators. . . . .	107
5.1	Summary of the main parameters of the SOI wafer used for the batch of fabrication of the device Tor1.x. . . . .	116
5.2	Chronological list of steps of fabrication of the device Tor1.x with the corresponding color code of materials. . . . .	117
5.3	Comparison of two SiO <sub>2</sub> slow and fast etching SOPs. . . . .	124
5.4	Chronological list of steps of fabrication of the device Tor1.x with the corresponding color code of materials. . . . .	129
5.5	Summary of the parameters used for the 17 μm wire bonding SOP using the TPT <sup>®</sup> HB16 tool. . . . .	132
6.1	Summary of the measured resonance frequencies in Hz of the main modes constituting the frequency response of the three types of Tor1.x and of the model resonance of the pure tilt mode in red. . . . .	143
6.2	Summary and description of the different vibrating modes of the Tor1.22 without torsion rods. . . . .	144

# Acronyms

- AS2M** Automatique et Systèmes Micro-Mécatroniques. viii, 43, 155
- BHF** buffered hydrofluoric acid. 118, 119, 161
- BML** Biophotonics & Microsystems Laboratory. xxv, 61, 67, 68, 71, 86, 87, 106, 111, 115, 155
- BOE** buffered oxide etchant. xx, 119, 161
- BOX** buried oxide. 116, 125, 129
- BS** beam splitter. 19, 46, 150
- BSP** beam splitter plate. xviii, 48, 70, 151
- CM** confocal microscopy. 1, 15, 16, 31, 32, 57
- CMOS** complementary metal oxide semi-conductor. 39, 69, 201
- CT** computed tomography. xv, 1, 11–15, 17
- CTE** coefficient of thermal expansion. 60, 71, 81, 83, 85, 86, 93, 95
- DAQ** data acquisition. xxii, 140, 141
- DC** direct current. xxii, 135, 137–139
- DEMO4** Demonstrator n°4. 1, 2, 155, 157
- DIP** dual in-line package. 109
- DISC** double inverted-series-connected actuators of second generation. 105, 106, 121
- DOF** depth of field. 48, 49, 132
- dof** degrees of freedom. 65, 67, 87, 96, 97, 112, 140, 143, 156, 157
- DOT** diffuse optical tomography. 15
- DRIE** deep reactive-ion etch. 80, 112, 125, 126, 136, 162
- DSSISC** double S-shaped inverted-series-connected. xix, 96–101, 103, 105–107, 117
- EAP** electro-active polymers. 44

- EGC** early gastric cancer. xxv, 1, 2, 9, 10, 12, 14–16, 24, 25, 35, 37, 49, 153
- endOCT** endoscopic OCT. xvii, xxv, 22, 23, 26, 27, 31, 32, 34, 37, 39–42, 46, 49, 53, 55, 57, 62, 64
- ETA** electrothermal actuator. xviii, 66
- ETM** electro-thermo-mechanical. 61, 63, 64
- EUS** endoscopic ultrasound. xv, 14, 15
- exOCT** exoscopic OCT. 22, 40, 42
- FD-OCT** frequency-domain OCT. xvi, 18, 20–22, 44
- FEM** finite-element model. 72, 76, 77, 113
- FOV** field of view. xvi, 26, 29, 33, 37, 69, 147
- FWHM** full width at half maximum. 19
- GE** gastroesophageal. 7–9, 44, 49
- GI** gastrointestinal. 1, 2, 7–12, 14, 16, 22, 23, 25, 33, 53, 67, 155
- GRIN** gradient-index. 33, 40, 41, 43–45, 47, 71, 150, 152
- H. pylori** *Helicobacter pylori*. xv, xvi, 8, 9, 11, 15, 17
- HFF** high fill-factor. xxv, 68
- HFUS** high-frequency ultrasound. 14, 16
- ICP** inductive-coupled plasma. 121
- INC** National Institute of Cancers. 5
- IR** infrared. 16, 17, 49, 73, 86, 93
- ISC** inverted-series-connected. xviii–xxi, xxv, 60, 61, 63, 64, 66–68, 85, 87, 96–98, 103, 105–107, 112, 118, 120, 122, 124, 125, 129, 130, 156
- LEM** lumped-element model. xix, xx, 75–79, 106–108
- LFUS** low-frequency ultrasound. 14
- LSF** lateral-shift-free. xviii, 60, 61, 64, 66
- LST** large-sized tumor. xxv, 10, 12
- LVD** large-vertical-displacement. xviii, 60, 66
- MALT** mucosal associated lymphoid tissue. 9

- MEMS** micro electro-mechanical system. xvi, xvii, xx, xxv, 1, 2, 26, 28–32, 35–37, 39–43, 45, 50, 52, 53, 55–57, 59–61, 67, 69, 71, 88, 100, 110, 115, 136, 143, 149, 150, 156–158
- MIMENTO** Microfabrication for Mechanical Engineering, Nanoscience, Thermal science and Optics. 87, 115
- MISC** meshed inverted-series-connected. xix, xxi, xxvi, 98, 99, 105–109, 117, 124, 125, 127, 131
- MN2S** Micro Nano Sciences & Systems. viii, 155
- MOEMS** micro opto-electro-mechanical system. xvii, xviii, xxii, xxv, 2, 43, 47, 48, 52, 53, 55, 69, 70, 150, 153, 155–157
- MOMS** micro opto-mechanical system. 40, 45
- MOTEMS** micro-optical electro-thermo-mechanical scanner. xix, xxv, 61, 64, 65, 68, 78, 87, 88
- MPNST** malignant peripheral nerve sheath tumors. 9
- MRI** magnetic resonance imaging. xv, 1, 11–13, 15, 17
- MUMP** multi-user MEMS process. 57
- NA** numerical aperture. 20, 22, 25, 32, 34, 40, 46, 48–50, 147
- NET** Neuroendocrine tumors. 9
- NIH** National Institutes of Health. 9
- NLOM** nonlinear optical microscopy. xxv, 16, 17
- NMP** 1-methyl-2-pyrrolidinone. 120, 123, 125
- NRF** Nanoscale Research Facility. 86, 87, 111, 115, 120, 133, 155
- OA** operational amplifier. xxii, 140, 141
- OCT** optical coherence tomography. xvi, 1–3, 10, 15–18, 22, 23, 25–33, 35–37, 39, 44–46, 48, 49, 52, 53, 55, 57, 59, 60, 62–64, 67, 69–71, 91, 93, 100, 105, 108, 112, 132, 145–148, 153–157
- OPD** optical path difference. 18, 19
- PCB** printed circuit board. xxi–xxiii, 109, 131–133, 135, 140, 141, 150, 152
- PECVD** plasma-enhanced chemical vapor deposition. 118, 121, 123, 129
- PET** positron emission tomography. 11, 13, 14, 17
- PR** photoresist. xx, xxi, xxiii, 119–125, 129–131, 161–163, 165, 166
- PSD** position sensing detector. 136
- PZT** lead zirconate titanate. 32, 59

- RF** radio frequency. 12, 17, 120
- RIE** reactive-ion etch. 121, 123–125, 136, 162
- ROI** region of interest. 35, 50, 105, 146, 147
- SCS** single-crystal silicon. 116
- SD-OCT** spectral-domain OCT. 21, 22
- SEM** scanning electron microscope. xvii, xviii, xx–xxii, 42, 63–66, 112, 113, 119–121, 123, 126–131, 136
- SiOB** silicon optical bench. xvii, 26, 38, 39, 41, 65
- SMF** single-mode fiber. 22, 44, 47, 48, 71, 152
- SNR** signal-to-noise ratio. 15, 21, 48, 49
- SOI** silicon-on-insulator. xxi, xxvi, 70, 93, 110, 112, 116, 118, 125, 126, 130, 131, 161, 162
- SOP** standard operating procedures. xxvi, 123, 124, 132, 162
- SS-OCT** swept-source OCT. 2, 21–24, 91, 146, 155, 157
- SST** small-sized tumor. xxv, 10, 12
- TCR** temperature coefficient of electrical resistance. 73, 86, 137
- TD-OCT** time-domain OCT. xvi, 2, 18, 20–22, 35, 44
- TSV** through-silicon vias. 38
- TTP** tip-tilt-piston. 60, 63–65
- UF** university of Florida. xxv, 61, 67, 113, 115, 155, 158
- UFC** university of Franche-Comté. 113
- US** ultrasound. 1, 11, 12, 14–17, 44
- USA** United States of America. vii, 5, 115
- VCSEL** vertical cavity surface-emitting laser. 147
- WHO** World Health Organization. 5, 7, 8

# Nomenclature

## Electrical parameters

$\rho_D$	Detector's responsivity	-
$\rho_{E0}$	Electrical resistivity at the temperature of the substrate	$\Omega.m$
$\rho_E$	Electrical resistivity	$\Omega.m$
$\varepsilon_0$	Vacuum permittivity	$8.854 \cdot 10^{-12} \text{ F.m}^{-1}$
$q_e$	Power density of the electrical resistor of the beam	$\text{W.m}^{-3}$
$R_{E0}$	Initial total electrical resistance at temperature $T_0$	$\Omega$
$R_E$	Total electrical resistance of the bimorph transducer	$\Omega$
$P_E$	Electric power	W

## Geometric parameters

$\delta_{IN}$	Vertical displacement of the INverted bimorph	m
$\delta_{NI}$	Vertical displacement of the Non-Inverted bimorph	m
$\delta_{OL}$	Vertical displacement of the OverLap segment	m
$\theta_p$	Optical angle of mirror in pitch	rad
$\theta_r$	Optical angle of mirror in roll	rad
$d_M$	Distance between beam splitter outer surface and mirror center	m
$h_{caps}$	Thickness of probe capsule	m
$h_{mirau}$	Side of the squared base of the Mirau interferometer	m
$L_m$	Length of the mirror plate	m
$L_r$	Length of the torsion rod	m
$L_{IN}$	Length of the INverted bimorph	m
$L_{NI}$	Length of the Non-Inverted bimorph	m
$L_{OL}$	Length of the OverLap segment	m



$S$	Surface of the cross section of the transducer	$\text{m}^2$
$t_b$	Total thickness of layers constituting the bimorph/multimorph beam	$\text{m}$
$t_m$	Thickness of the mirror plate	$\text{m}$
$t_r$	Thickness of the torsion rod	$\text{m}$
$t_1$	Thickness of the top layer of a bimorph/multimorph beam	$\text{m}$
$t_i$	Thickness of the $i^{\text{th}}$ layer of a multimorph beam downward	$\text{m}$
$t_N$	Thickness of the bottommost layer of a multimorph of N layers	$\text{m}$
$w_b$	Width of the bimorph section	$\text{m}$
$w_m$	Width of the mirror plate	$\text{m}$
$w_r$	Width of the torsion rod	$\text{m}$
$Z_R$	Distance between the reference mirror and the beam splitter	$\text{m}$
$Z_r$	Rayleigh distance	$\text{m}$
$L_b$	Length of the bimorph	$\text{m}$
DOF	Depth of field of the optical system	$\text{m}$
WD	Working distance of the probe	$\text{m}$

### Mechanical parameters

$\chi$	Curvature coefficient of the cantilever bimorph beam	$\text{m}^{-1}$
$\delta$	Ordinate of the elevation of the beam on projection onto the vertical axis	$\text{m}$
$\ell$	Abscissa of the deflected tip of the bimorph in projection onto the horizontal axis	$\text{m}$
$\rho$	Total radius of curvature of the bimorph	$\text{m}$
$\rho_0$	Initial radius of curvature due to intrinsic stress	$\text{m}$
$\rho_b$	Radius of curvature due to extrinsic stress	$\text{m}$
$\tau$	Time constant	$s$
$\theta_b$	Tilt angle of the tip of the cantilever beam	$\text{rad}$
$f_b$	Bending mode natural frequency	$\text{Hz}$
$f_t$	Torsional mode natural frequency	$\text{Hz}$
$I_t$	Second moment of area of the torsion rod	$\text{m}^4$
$J_m$	Moment of inertia of the mirror plate	$\text{kg.m}^2$
$k_b$	Spring constant of a beam in flexion, bending stiffness	$\text{N.m}^{-1}$

$k_t$	Spring constant of a beam in torsion torsional stiffness	N.m
$m_b$	Curvature coefficient of the cantilever bimorph beam	Pa.m <sup>3</sup>
$M_m$	Mass of the mirror plate	kg
$M_{mol}$	Molar mass	kg.mol <sup>-1</sup>
$P$	Pressure	Pa
$s$	Laplace variable	rad.s <sup>-1</sup>

**Optical parameters**

$\Delta x$	Lateral resolution	m
$\Delta z$	Axial resolution	m
$\Delta \lambda$	Wavelength bandwidth	m
$\lambda_0$	Central wavelength	m
$\omega$	Angular frequency	rad.s <sup>-1</sup>
$d$	Diameter of focusing lens	m
$f$	Focal length	m
$k$	Wavenumber	m <sup>-1</sup>
$l_c$	Coherence length	m
$NA$	Numerical aperture	-

**Thermal parameters**

$\alpha$	CTE	K <sup>-1</sup>
$\alpha_p$	Thermal diffusivity	m <sup>2</sup> .s <sup>-1</sup>
$\bar{T}$	Average temperature	K
$\Delta \alpha$	Difference of CTEs	K <sup>-1</sup>
$\Delta T$	Temperature change across a beam	K
$\hat{x}$	Abscissa of maximum temperature	m
$\kappa$	Thermal conductivity	W.K <sup>-1</sup> .m <sup>-1</sup>
$\xi$	Thermal coefficient of electrical resistance	K <sup>-1</sup>
$C_h$	Thermal capacitance, also called heat capacity	J.K <sup>-1</sup>
$c_p$	Specific heat capacity	J.kg <sup>-1</sup> .K <sup>-1</sup>
$f$	Balancing factor	-

$h$	Coefficient of convection	$\text{W.K}^{-1}.\text{m}^{-2}$
$R_0$	Universal gas constant	$8.314, 4598 \text{ J.mol}^{-1}.\text{K}^{-1}$
$R_{TA}^{\rightarrow}$	Thermal resistance of the transducer due to conduction	$\text{K.W}^{-1}$
$T$	Temperature distribution along the x-axis of a beam	$\text{K}$
$T_0$	Temperature of the substrate	$\text{K}$

# Introduction

CANCERS are the second most common cause of death in the world today. If effective treatments are available against well-known cancers until advanced stages, late diagnoses of less commonly-known cancers, such as [gastrointestinal \(GI\)](#) malignancies, can be fatal. Early diagnoses of the [GI](#) tract are crucial to fight more efficiently against these killers. More than 80% of diagnosed stomach or esophagus carcinomas are in advanced stages and require heavy diagnostics and painful treatments such as biopsy and chemotherapy. One of today's challenges is to provide new methods tackling the drawbacks of biopsy's invasive, delayed and risky diagnosis to allow the patients to have access to safe, non-invasive, fast, and – the most important – preventive diagnoses. The earlier the diagnosis, the more efficient and “soft” the treatments.

Today's most common non-invasive detection modalities can be divided into two types: non-optical methods such as [magnetic resonance imaging \(MRI\)](#), [ultrasounds \(USs\)](#), [computed tomography \(CT\)](#) and optical techniques such as [confocal microscopy \(CM\)](#), [photoacoustic microscopy](#), [nonlinear microscopy](#) and [optical coherence tomography \(OCT\)](#). Non-optical techniques are often limited by their low spatial resolution inadequate to resolve abnormal changes in tissue whereas the main flaw of optical techniques is their shallow penetration depth.

Several techniques, offering similar properties, are in competition as of today. Furthermore, imaging systems are more and more demanded to do “multi-modal”, gathering several techniques to widen the quantity of information observable in one apparatus. The purpose of this work is to figure out a compromise in terms of performances, size and cost.

Miniaturization turned out being a promising tradeoff in the process of cost reduction and performance improvement, allowing to implement safe and non-invasive endoscopic imaging for sufficient penetration depths and high resolutions. Downscaling the endoscopic systems is not only a demonstration of how small we can fabricate systems today, but a true mean of reaching remote inner-body areas; reducing the costs of fabrication, assembly and components by batch micro-fabrication; increasing the flexibility of use and allowing disposability of the devices to replace the expensive sterilization procedures; and increasing the quality and speed of the imaging by embedding micro-optical and [micro electro-mechanical system \(MEMS\)](#) components.

In this purpose, the [Demonstrator n°4 \(DEMO4\)](#) project of FEMTO-ST Institute was proposed to research and develop an original demonstrator of endo-microscopic probe for [early gastric cancer \(EGC\)](#) detection. Based on three main subprojects comprising a continuum robot arm, a Mirau micro-interferometer and a [MEMS](#) scanner for vertical integration with the micro-interferometer.

This project was the occasion of combining microtechnologies and endoscopic imaging to build a micro-system meeting the specifications stemmed from the medical needs and adapted to the environment and the other components of the final demonstrator. I had the opportunity to work at the University of Florida and at the University of Franche-Comté for nineteen months and a half each, to adapt existing technologies and knowledge in the implementation of novel mechanisms of actuation and sensing.

Although a few constraints were imposed such as the mono-modality of the imaging and a few pre-conception dimensions linked to the size of the Mirau micro-interferometer and the robot arm, the rest of the parameters remained to be defined such as the specifications required, the type of imaging, the architecture of the endoscopic probe, the type of actuation and the layout of the micro-scanner.

This thesis is structured as follows:

- Chapter 1 gives a brief introduction on GI malignancies and EGC. It sets the specifications linked to the depth and size of GI cancers and the limit between early and advanced stages. Based on these figures, OCT imaging is selected among the main commonly-used and emerging types of optical and non-optical techniques. In many current OCT systems, swept-source OCT (SS-OCT) often stands out in terms of resolution and speed which makes it the more competitive OCT-based imaging method compared to other modalities. The basic principles of low coherence interferometry, time-domain OCT (TD-OCT) and finally SS-OCT are presented.
- Chapter 2 proposes a classification of the endoscopic OCT probes, a selection based on the pros and cons of each architecture and provides a state of the art of distal side-imaging endoscopic OCT probe architecture selected. In the objective of miniaturization of the probe intended to be developed in this work, a short review on the evolution of embedding micro opto-electro-mechanical system (MOEMS) components for endoscopic OCT probes is provided in order to evaluate the impact of the degree of integration of the MOEMS block. Then, the different components developed prior to this work in the DEMO4 project are briefly introduced as well as the parameters constraining the design of the core element: the micro-scanner. At last, an optical architectural model, recalling the features necessary to meet the biomedical imaging requirements is proposed. From this model, a list of fundamental specifications is established and will be used to complete the design of the MOEMS scanner.
- Chapter 3 covers the basic principles of the four most common types of actuation, and compares them, to finally summarize in a state of the art the selected electrothermal actuation-based MEMS tilt micro-scanners.
- In Chapter 4, the optical architecture is recalled and the principle of an electrothermal bimorph is presented. The electrothermal and thermomechanical models of a single bimorph are detailed. A novel structure is inspired from these models to build an electrothermal actuator. A set of materials are considered for the constitution of the different elements of the proposed structure. Three main designs are proposed, including an original architecture

with torsion bars, a dual-reflective mirror plate, a complex meshed-shape actuators and other (anticipated) improvements arising from the characterization of the first type of micro-scanner such as an embedded torsion-based strain gauge sensor.

- Chapter 5 describes the process of fabrication of the whole micro-scanner detailing each step of micro-fabrication of the base device as well of the complementary fabrication steps investigated for the development of the improvement stages. The design of the packaging support, intended to be employed for further characterizations, is also included in this chapter.
- Finally, Chapter 6 brings conclusions based on the characterization of the micro-scanner which could be tested within the remaining time. The experimental setup is described. The static and dynamic behavior as well as the frequency response of the micro-scanner are characterized, with and without torsion bar, for different widths of the torsion bar and other configurations. At last, the capability of carrying out OCT imaging is evaluated by performing Lissajous scans.



# Chapter 1

## Stomach and esophagus cancer detection techniques

CANCER is the second most common cause of death in the world today, exceeded only by heart diseases, with 8.2 million deaths (all forms of cancer combined) in 2012 and accounts for nearly 1 of every 4 deaths, according to the [World Health Organization \(WHO\)](#). In France, in 2015, 385,000 new cases of cancers (5.8% of the population) were diagnosed versus 5.2% in the [United States of America \(USA\)](#) [1, 2]. The incidence rate <sup>1</sup> trend is downhill or stagnant since 2005 in France with an age-adjusted rate <sup>2</sup> of 362.4 per 100,000 for men and 272.6 per 100,000 for women [3]. Mortality rate decreased of 1.5% per year between 1980 and 2012 for men and by 1% for women. Hence, given the French population demographic evolutions between 2011 and 2015, these figures denote an increase of the number of new cases for both sexes and a stabilization of the number of deaths per cancer. The direct medical cost for cancers in 2014 reaches 8.671 billion € in France according to the [National Institute of Cancers \(INC\)](#) and is estimated at \$87.8 billion in the [USA](#) by the Agency for Healthcare Research and Quality. Between 2007 and 2014, in the hexagon <sup>3</sup>, research on cancer detection and treatment represent up to 707 million €. There exist more than a hundred types of cancers, and the most “common” cancers are also the ones that are the best known and cured. However, if well-known cancers are subject to an efficient treatment process, for others, the bulk of the work is yet to come. For instance, the 5-year, 10-year, and 15-year relative survival rates for invasive breast cancers has improved in the past 3 decades and reached up 89%, 83% and 78% respectively [4] whereas, on the other hand, in 1998 “the overall contribution of a curative and adjuvant cytotoxic chemotherapy to 5-year survival in adults was estimated to be 2.1% in the [USA](#)” [5]. Gastric adenocarcinomas are the most common cancers occurring in the stomach in countries like Japan, China, South America and Eastern Europe (see Fig. 1.1). Ranking fourth and thirteen among all types of cancers in the world, the particularly high rate of mortality – with 39% and 93% of respective death rate <sup>4</sup> – of stomach and esophagus cancers and the considerable attention received because of the prevalence of esophageal and stomach carcinomas in gastrointes-

---

<sup>1</sup>The incidence rate is the number of new cancers of all types that occur in the world standard population, per 100,000 and per year.

<sup>2</sup>Weighted average of the age-specific rate, where the weights are the proportions of persons in the corresponding age groups of a standard population.

<sup>3</sup>The “Hexagon” depicts the mainland part of Metropolitan France, because of its approximate hexagonal shape.

<sup>4</sup>Estimation of 2017 based on the data of 2000-2014 US mortality rate, National Center for Health Statistics, Centers for Disease Control and Prevention [2].



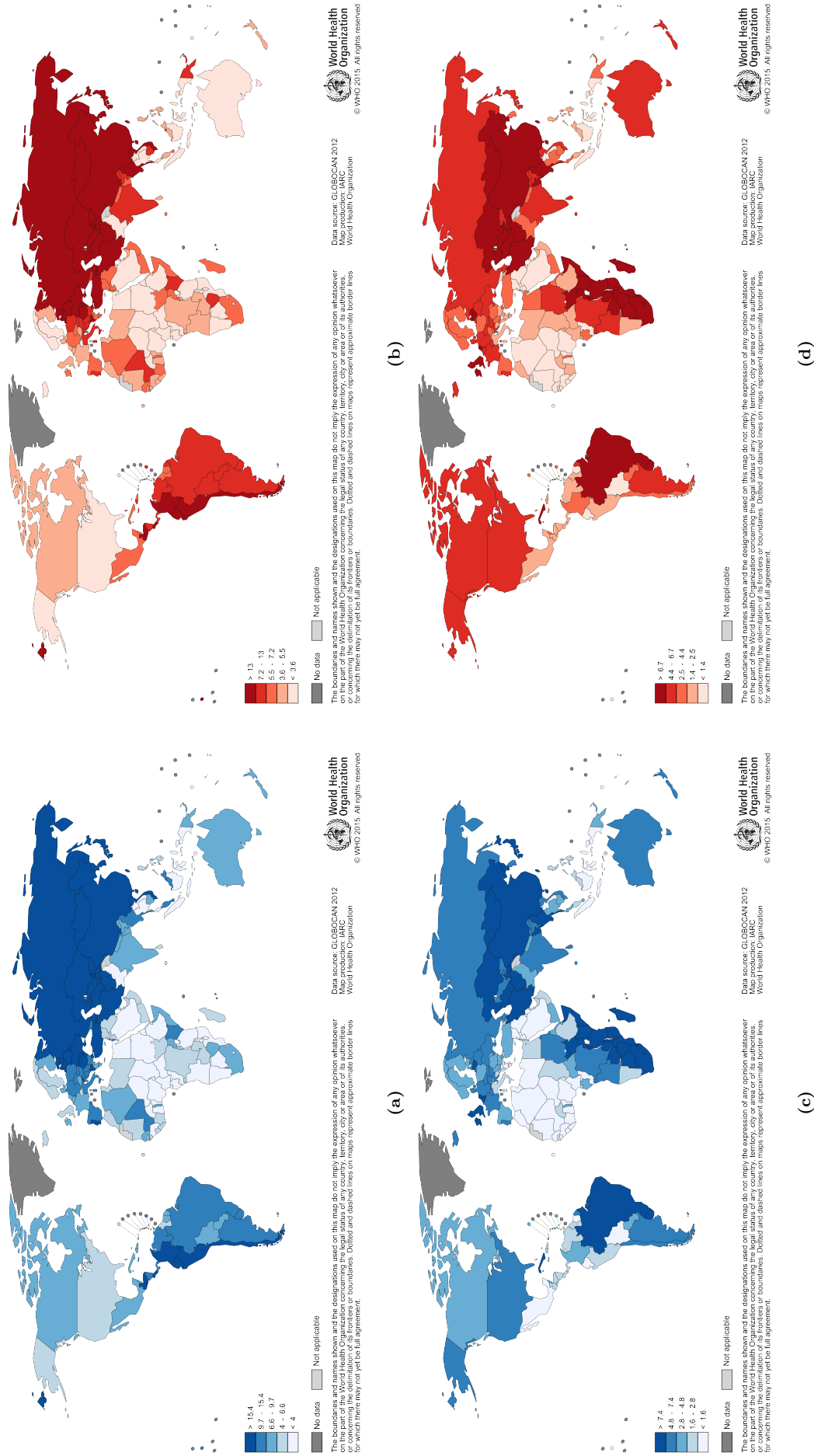


**Figure 1.1:** Comparison of stomach and esophagus cancer incidence and mortality worldwide in men population in 2012. Source: GLOBOCAN 2012, globocan.iarc.fr. Incidence of stomach (a), and esophagus (b) cancers in men. Mortality rate of stomach (c), and esophagus (d) cancers in men.

tinal endoscopy motivated our work, especially knowing that research does not need to reach a very advanced maturity in treatment techniques to start saving lives as long as this kind of cancers can be efficiently treated if diagnosed in their early stage.

## 1.1 Stomach and esophagus cancers

### 1.1.1 Definition

After food and fluid enter the mouth, the pharynx (throat) opens upon swallowing to allow entry into the esophagus. The esophagus is normally closed at either end by sphincters acting as valves. The upper sphincter is located below the pharynx, and the lower one is located at the entrance of the stomach called the **gastroesophageal (GE) junction**. The **GE** sphincter plays a crucial role in preventing the acidic content of the stomach from refluxing into the esophagus. The esophagus is a 23 to 37 cm long muscular tubular organ that connects the pharynx to the stomach. It has a diameter of 2 to 4 cm and is connected to the stomach through the **GE** junction whose diameter is about 5 mm [6]. The stomach is a pocket-like organ that receives and stocks the food swallowed after being carried through the esophagus and the **GE** junction. It is about 30.5 cm long and 15.2 cm wide and has a capacity of about 940 mL. It is composed of 5 parts represented in Fig. 1.2: the *cardia*, the closest to the esophagus; the *fundus*, the *upper part*, beside the *cardia*; the *corpus*, the main part; the *antrum*, the lower part, where the food is consolidated with gastric acid; and the *pylorus*, acting as a valve transferring the content of the stomach to the small intestine. The stomach is also characterized by 5 layers illustrated in Fig. 1.2: the *mucosa*, which is the innermost layer where acid and enzymes are fabricated; it's supported by the *submucosa*. Then, comes the *muscularis propria*, always in motion to mix the content of the stomach. Finally, the stomach is wrapped by two outer layers that are the *subserosa* and the *serosa*, the outermost one. The surface of the *mucosa* is honeycombed with over 35,000 gastric glands and is folded into multiple ridges that disappear when the stomach is distended with food. The esophagus, the stomach and the intestines belong to the **GI** tract whose role is to take the food, digests it to extract and absorb energy and nutrients, and expel the remaining waste. The **GI** tracts divides into two subgroups: the upper **GI** tract that consists of the mouth, the pharynx, the esophagus, the stomach and the duodenum and the lower **GI** tract including the small intestine and all of the large intestine. We limited our research to the upper **GI** tract and more specifically to the cancers that develop in the lower esophagus and the stomach for their “reachability”.

Cancer is defined by the American Cancer Society as “a disease characterized by the uncontrolled growth and spread of abnormal cells”. The definition of gastric cancers is given by the **WHO** as: “malignant epithelial tumors of the gastric mucosa with glandular differentiation”. The exact cause of **GI** cancers remains unknown today. However, most are believed to result from an exposure to carcinogen agents, and especially nitrates present in meats that are dried, smoked, salted or pickled <sup>5</sup>. They cause errors in the genetic code that controls growth and repair of cells. They can also spread to lymph vessels and nearby lymph nodes that help fight infections. They can be the hearth of metastases and play a significant role in cancer prognosing and staging. The risk of **GI** cancers can be increased depending on the individual’s medical condition (gastritis,

---

<sup>5</sup>As a matter of fact [7], it is recommended to intake frequently fruits and raw vegetables, as they contain antioxidants, to decrease significantly the risk of deaths related to gastric cancers.

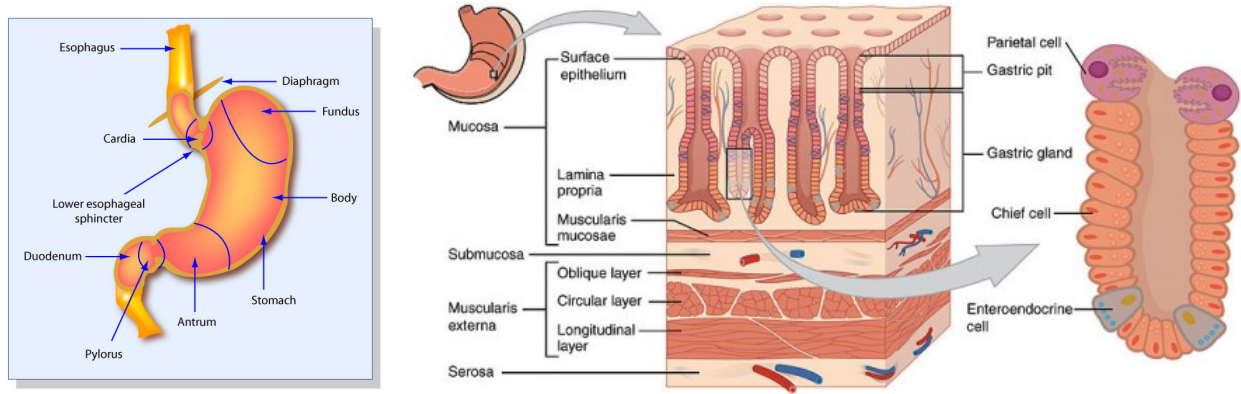


**Figure 1.2:** Sketch of the human stomach. (*left*): Different parts of the human distal esophagus and stomach. “Stomach Pic for Food Poisoning Thingy” by Daniel X. O’Neil, license: CC BY 2.0. (*right*): Detailed anatomy of the layers of the wall of the stomach. “Illustration from Anatomy & Physiology, Connexions Web Site” by OpenStax College, license: CC BY-SA 3.0.

deficiency of vitamin B12, chronic gastric ulcer, family history of gastric cancer, blood group A, genetic abnormalities, ...). People who use tobacco, alcohol, or who work in certain industries (coal mining, metal and rubber industries) are also subject to a higher risk. Stomach cancers can be classified according to different methods. However, the two most common classification methods are the Lauren and the WHO methods [8]. Gastric cancers divide into two pathological variants in the Lauren classification: the intestinal type and the diffuse type. The intestinal-type cancer is the consequence of an inflammation that progresses from atrophic gastritis to metaplasia and dysplasia. It is highly associated with the *Helicobacter pylori* (*H. pylori*) infection and is the most common type among elderly men; unlike the diffuse-type which is more prevalent among women and individuals under the age of 50. “The diffuse-type exhibits deep infiltration into the stomach wall with little gland formation” [8, 9]. There exist many different types of cancers occurring in the upper GI tract:

- Adenocarcinomas (from the Greek;  $\alpha\delta\eta\nu$ ,  $\alpha\delta\epsilon\nu\omicron\varsigma$ : “gland, glandular” and  $\kappa\alpha\rho\kappa\iota\nu\omicron\varsigma$ : “crab, cancer”) (intestinal and diffuse) are the most common malignancies of the stomach. Malignancies arising from the gastric epithelium represent between 90% to 95% of the GI tract and start in the glandular tissues lining the lower part of the esophagus, next to the GE junction and in the stomach. They are usually referred to as “gastric cancers” or just “stomach cancers”. Adenomas tend to occur in the *cardia* (31%), followed by the *antrum* (26%) and the *body* (14%) and often have prolonged precancerous stages and an expanding growth pattern [10]. 12.5% of tumors are located in the upper third of the stomach, 30.4% in the middle third and 57.1% in the lower third [11].
- Lymphomas account for 4% of GI cancers. They are due to a deficiency of the immune system tissue and can be found in the wall of the stomach. They develop from lymphocytes, a type of blood cell involved in the adaptive immune system.
- Gastrointestinal stromal tumors are uncommon tumors starting in special cells of the autonomic nervous system located in the wall of the GI tract. More than half of them start in the stomach in very early forms of cells called *interstitial cells of Cajal*. Some of these tumors appear to be benign.

- Neuroendocrine tumors (NET) start in the GI neuroendocrine cells. Carcinoid cancers are an example of NET as well as squamous cell carcinomas and small cell carcinomas. They represent less than 3% of stomach cancers.
- Soft tissue sarcomas (from the Greek;  $\sigma\alpha\rho\xi$ : “flesh”) such as leiomyosarcomas, angiosarcomas or malignant peripheral nerve sheath tumors (MPNST). They involve the connective tissues (muscles, fat, blood cells...) but remain very rare types of cancers.
- “Metastatic cancers from breast cancer, melanoma, and other primary sites of cancers can also be seen in the stomach” [12].

The highest risk factor identified in the development of gastric cancers is the infection of the *H. pylori* shown in Fig. 1.3. *H. pylori* are bacterias that measure about 2 to 4  $\mu\text{m}$  in length and 0.5 to 1  $\mu\text{m}$  in width. Studies have shown that *H. pylori* was at the root of gastritis development that progresses into gastric cancer [10] and Chronic atrophic gastritis associated with *H. pylori* infection is one of the most important risk factors for distal gastric cancers <sup>6</sup> [13]. Individuals infected with *H. pylori* have about 8% more chances to contract a gastric cancer over a 30-year period [10].

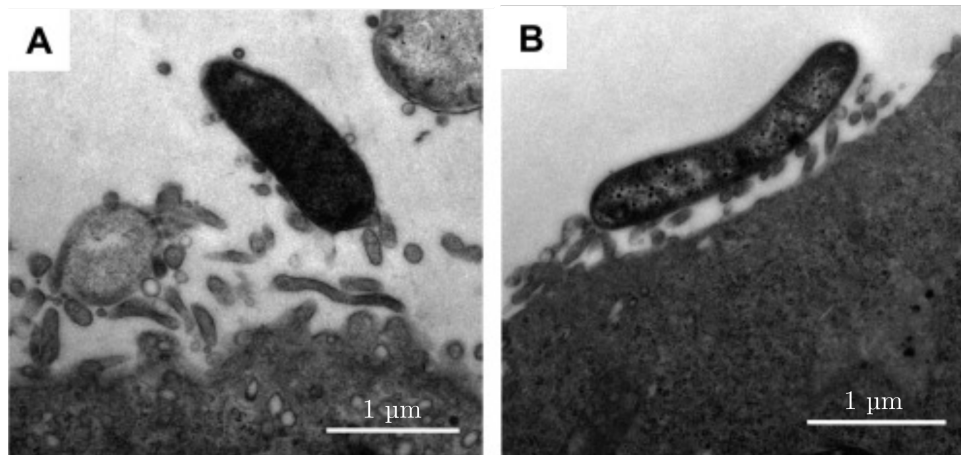


**Figure 1.3:** (A): Transmission electron micrograph of human stomach epithelial cells exposed to *H. pylori* for 1 hour. (B): *H. pylori* located along one epithelial cell [14].

As for most of other cancers, adenocarcinomas can spread to surrounding organs and blood vessels by direct invasion. Up to 80% may progress to invasion. Dysplastic proliferation creates a macroscopic protruding lesion described as tubular adenoma. They are diagnosed when the tumor penetrates the *muscularis propria* [9]. The maximum size of tumors of diagnosed patients with a survival rate greater than 5 years reaches an average of  $4.68 \text{ cm} \pm 2.33 \text{ cm}$  whereas small EGC

<sup>6</sup>“Despite this, the 1996 National Institutes of Health (NIH) consensus panel on *H. pylori* recommended that treatment not be initiated in asymptomatic infected individuals. Treatment of asymptomatic individuals remains a controversial issue, particularly because it takes more than 30 years before one-third of these individuals develop atrophic gastritis. The matter of treatment is even more confusing, because recent data suggest the eradication of *H. pylori* predisposes individuals to cancer of the proximal stomach (*cardia*) and esophagus. The overall incidence of gastric cancer is diminishing in western countries, but the incidence of proximal gastric cancers compared to distal is rising, and coincides with the widespread treatment of *H. pylori*. Some have proposed that *H. pylori* exerts a protective effect in the proximal stomach and esophagus by inducing achlorhydria and atrophic gastritis. Eradication of *H. pylori* restores gastric acid production and, individuals predisposed to GE reflux, could possibly contribute to cancers of the distal esophagus and cardia. Additional data is needed before treatment recommendations can be made in asymptomatic individuals. *H. pylori* leads to atrophic gastritis through direct and indirect mechanisms. *H. pylori* also appears to play a role in the pathogenesis of gastric mucosal associated lymphoid tissue (MALT) lymphomas, which arise as a reaction to infection of the stomach” [10].

tumor size does not exceed 2 cm [10, 15]. The symptoms often remain unspecific to GI symptoms such as heartburn in early stages, and anorexia, weight loss, abdominal pain, nausea or bleedings in advanced stages. Thus, the lack of decisive symptoms entails delayed diagnoses. Indeed, 80% to 90% of patients diagnosed with a GI adenocarcinoma already have a locally advanced disease. Most glandular tumors in a precancerous phase grow in expansion rather than in infiltration patterns. GI cancer prognostic variables are based on the stage, the category, degree of differentiation of tumor cells, size, location, invasion, age and gender. Figure 1.4 illustrates the evolution of GI cancers according to the “TNM” classifications given in Table 1.1 and described in Section 1.1.2.

### 1.1.2 Figures & early detection

Stomach cancers (also called gastric cancers) are more common in elder adults and twice as common in men as in women and esophagus cancers are 3 to 4 times more common in men as in women [2]. However, an early diagnosis increases significantly the chances of surviving. Cancers that are diagnosed before penetration of the full thickness of the wall or metastasised are referred to as EGCs. Unfortunately, they represent less than 5% of gastric carcinomas in the western world. This is mainly due to the absence of specific symptoms in early stages so that asymptomatic individuals with an EGC would not find a reason to undergo a prevention check. The most significant prognostic factor is the depth of the tumor invasion at the time of the diagnosis. The TNM classification, shown in Table 1.1 reflects the depth of the tumor infiltration (T), the node involvement (N) and the presence of distant metastases (M) to lymph nodes outside specified regional nodes or to other organs [10]. The primary tumor (T) is classified as T0 (no evidence of primary tumor), Tis (carcinoma *in situ*), T1 (invades lamina propria/submucosa), T2 (invades muscularis propria/subserosa), T3 (penetrates serosa) and T4 (invades adjacent structures). The lymph node status (N) ranges as N0 (no regional lymph nodes involved), N1 (metastasis in 1 to 6 lymph nodes), N2 (metastasis in 7 to 15 nodes) and N3 (metastasis in more than 15 nodes). The distant metastasis criterion (M) depends on whether the metastasis is distant (M1) or not (M0). Advanced TNM stages are associated with poor prognoses and low survival rates. The survival rate based on T and N criteria in the large-sized tumor (LST) and small-sized tumor (SST) was presented in a study on patients with gastric cancer in the lower third of the stomach by Wang *et al.* [16] in Table 1.2. Figure 1.5 shows a photomicrograph of a T2-staged adenocarcinoma detected on a 44-year-old patient. Most cases in the western world are diagnosed at late stages when the treatments are largely ineffective. Hence, the identification of EGC is crucial because of the high efficiency of early stage endoscopic therapy and leads to excellent prognoses. “The 5-year overall-survival rate in patients with EGCs is between 85% and 100%” [17, 18]. It is the goal of mass screening and surveillance (every 1 to 2 years) of the asymptotic population to expose EGCs and decrease the cost-effective ratio, especially in some parts of the eastern world where as many as 50% to 80% of detected malignancies are EGCs [19].

Most GI cancers occur on the epithelial layer of the concerned organs [21]. The thickness of each layer depends on each individual at the time of measurement and was estimated by OCT and histology by Bouma *et al.* [22] who showed that the maximum total thickness between the innermost layer (*squamous epithelial mucosa*) and the outer wall of the esophagus (*muscularis propria*) is about 1050  $\mu\text{m}$  [22] for normal specimens and between 2 and 4 mm for the stomach depending on the degree of distention [23] whereas the epithelial thickness is around 290  $\mu\text{m}$  [22].

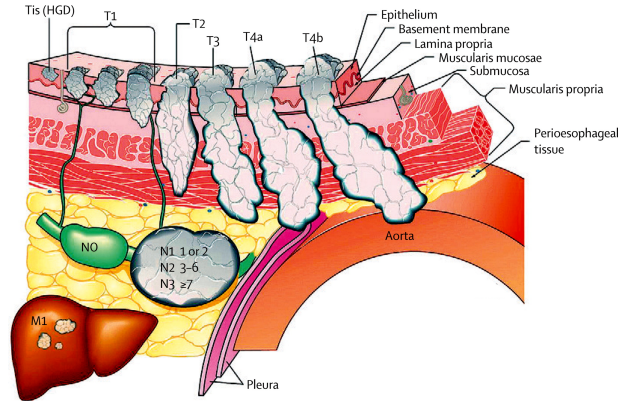


**Figure 1.4:** Representation of invasive evolution of gastric tumors according to TNM classification. HGD=high-grade dysplasia. T4a lesions are resectable whereas T4b are not. [20]

**Table 1.1:** TNM classification of gastric cancers. [9]

Stage	T	N	M
0	Tis	N0	M0
IA	T1	N0	M0
IB	T1	N1	M0
	T2	N0	M0
II	T1	N2	M0
	T2	N1	M0
	T3	N0	M0
IIIA	T2	N2	M0
	T3	N1	M0
	T4	N0	M0
IIIB	T3	N2	M0
IV	T4	N1,N2,N3	M0
	T1,T2,T3	N3	M0
	Any	Any	M1

Despite early lesions in preinvasive stages are almost undetectable [21], *H. pylori* are also often too small to be detected *in vivo* with optical imaging methods [14] whose resolution is limited by the wavelength used. Indeed, cancerous epithelial cell nuclei size (typically 5–10  $\mu\text{m}$  in diameter for non-dysplastic cells and can be as large as 20  $\mu\text{m}$  for dysplastic cells <sup>7</sup>) determines the resolution lower limit [21].

## 1.2 Intravital imaging approaches in cancer research

As ancient as our knowledge can reach, cancer was first described in ancient Egypt 3,600 years ago, as an incurable disease. Then, in ancient Greece, Hippocrates (460 BC - 370 BC) discovered different types of cancer and referred to them as *καρκινος* (“crab”) and drew representations of the outer body tumors. Prognostics for treatment were then given according to the patient’s *humor*. In the 18th century, the survival rate of breast cancers was lower than 4% due to the poor hygiene, the lack of detection equipment and the little knowledge modern medicine had about cancers. Today’s challenges of cancer detection are multiple: researchers must simplify the diagnostic processes and revolutionize the equipment that are complex, invasive, analysis-delayed, and very expensive. Indeed, for patients who potentially develop an upper GI tumor, at least 5 biopsies are required to emit a prognosis [17] that still lacks reliability due to the limited quantity and randomness of the samples collected. Furthermore, biopsy is always accompanied with *ex vivo* analyses and can lead to traumas for the patient [26] or increase the risk of exposition to diseases. Beside biopsy, alternative non-invasive bio-imaging techniques also exist such as MRI, CT, positron emission tomography (PET) and US, enabling faster or quasi real-time diagnosis for

<sup>7</sup>For most cells, the nuclear size is about 10 times smaller than the cell size and measure between 2 and 10  $\mu\text{m}$  according to Fawcett [24]

<sup>8</sup>Percentage are considered statistically significant when P-values (Cox regression model) are smaller than 0.05 [16].

**Table 1.2:** Survival based on TN stages in the LST and SST groups; Data in bold font correspond to cases of EGCs [17, 20].

T	N	5-year OS (%)		P value <sup>8</sup>
		LST	SST	
T2	N0	<b>88.9</b>	<b>96.7</b>	0.610
	N1	72.7	<b>91.1</b>	0.986
	N2	50.0	<b>87.1</b>	0.797
	N3	0.00	63.6	0.006
T3	N0	66.7	<b>100.0</b>	0.201
	N1	66.7	75.0	0.555
	N2	0.0	66.7	0.364
	N3	12.5	40.0	0.047
T4	N0	68.7	83.1	0.024
	N1	54.2	75.4	0.029
	N2	27.2	61.9	0.006
	N3	6.9	48.6	0.000

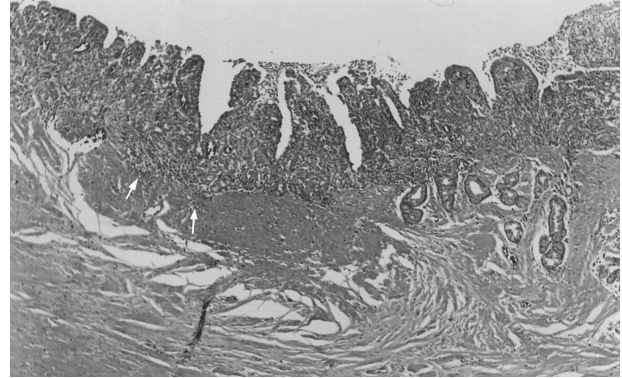


**Figure 1.5:** Micrograph of a surgical specimen showing gastric adenocarcinoma cells (*arrows*) infiltrating *muscularis propria* (stage T2) [25].

some of them; generally, imaging methods with low resolution are inadapted to detect preinvasive GI lesions [27] or microstructural abnormalities of neoplastic changes as shown in Fig. 1.6 as the typical nucleus size of malignancies of EGC is about 10  $\mu\text{m}$  or smaller.

Most imaging methods are combined with others to allow better staging concordance. For example, the evaluation of stages with both endoscopic US and dynamic CT showed a concordance of 73% compared to 45% for dynamic CT alone [23]. Expectations in biomedical imaging tend to evolve towards “all-in-one” (also called multi-modal) apparatus combining multiple imaging techniques with different and complementary features to increase the capabilities and accuracy of imaging and staging. Multidisciplinary imaging methods already exist and allow to collect more information [23, 28, 29]. A few intravital gastric cancer imaging approaches are presented and compared hereafter and summed up in Table 1.3.

### 1.2.1 Non-optical imaging methods

The most common techniques used today in hospitals and health facilities are mainly non-optical, due to their polyvalence. However, they tend to be caught up by optical imaging techniques. Hereafter will be presented the main non-optical modalities used for *in vivo* visualization.

#### 1.2.1.1 Magnetic resonance imaging

Magnetic resonance imaging is an imaging techniques based on nuclear magnetic resonance that was discovered in the 1930s in Harvard and adapted to medical diagnosis by R. Damadian in 1970. A more recent concept of high-frequency MRI was patented in 1988 by Roschmann [30]. MRIs exploit magnetic properties of hydrogen atom’s nuclei present in the water and fat molecules of the body. Atoms exposed to magnetic radio waves are excited and subsequently oscillate and re-emit a radio frequency (RF) signal (typically 40 to 340 MHz [31]) detected by coils. High-resolution MRIs can reach up to 10  $\mu\text{m}$  of resolution (however, MRIs resolution is typically in the range of

10 to 100  $\mu\text{m}$ ), are not limited in penetration depth [27] but require long acquisition time of about 6.5 min per scan [32].

MRI has a wide range of applications in medical diagnosis and can be combined to other imaging techniques such as PET/MRI that replaces PET/CT systems because of their limited contrast in soft tissue and high levels of radiation [28]. For gastric carcinoma TNM staging, MRI demonstrated accuracies of 73.3% and 55% for T and N staging respectively, but its unpopularity stems from a number of limitations such as motion artifacts, low contrast, low spatial resolution and high cost [25, 33].

### 1.2.1.2 Computed tomography

The term “CT” usually refers to X-ray CT, the most common imaging method. Other types of CT exist such as PET capable of detecting molecular biology details. Although CT and PET have been used in gastric cancer detecting and staging, they were rapidly replaced by other imaging techniques because of their low resolution and delayed-time diagnosis [25]. They exhibit comparable result as for MRI in staging accuracy. Gastric carcinoma images collected by CT are confronted to MRI pictures in Fig. 1.6.

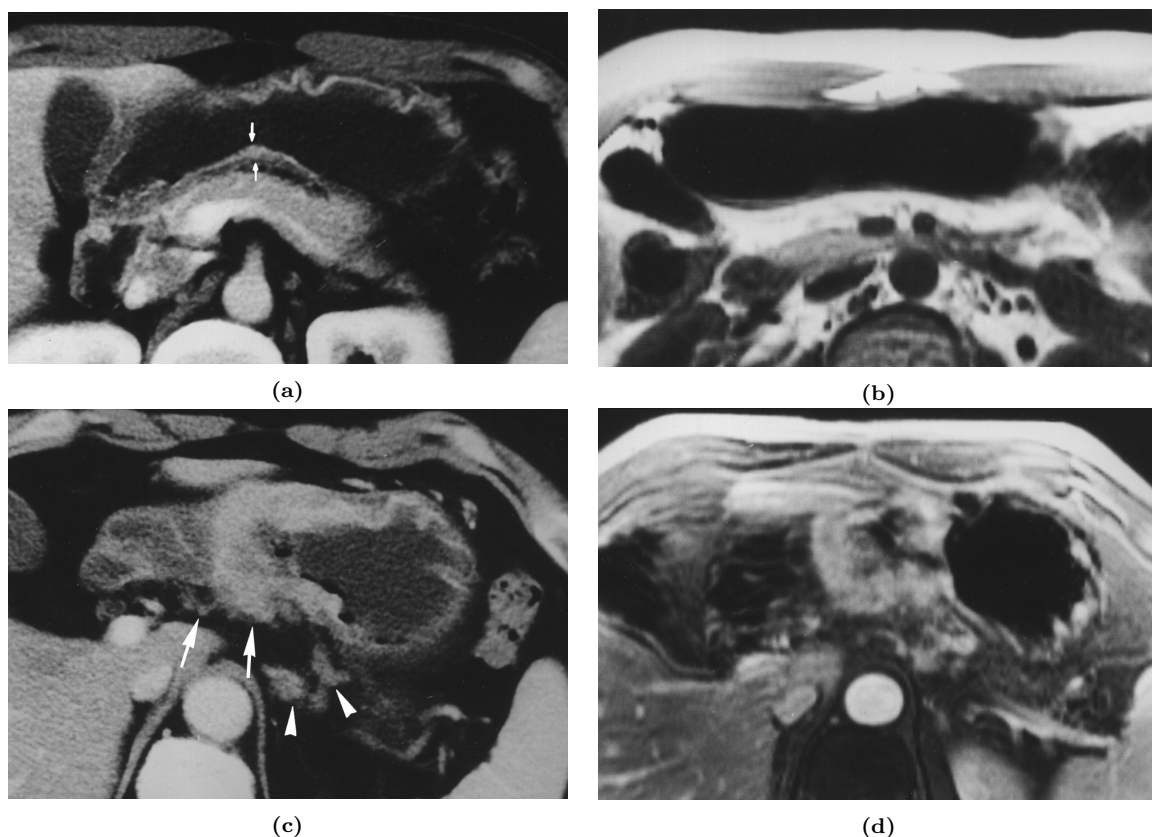


**Figure 1.6:** Comparison of : (a): Axial helical CT scan of the gastric body of a 44-year-old man with a T2 stage gastric carcinoma showing wall thickening with strong contrast enhancement. Cancer was incorrectly diagnosed at stage T1. (b): T1-weighted MRI image of the same patient failed to show lesions. (c): Helical CT scan showing concentric tumor with strong contrast enhancement in the gastric body of a 54-year-old man with T3 stage gastric cancer. Gastric tumor and infiltration in adjacent fat are well seen. (d): Contrast-enhanced T1-weighted MRI image of the same patient. Demarcation of gastric tumor and lymph nodes is blurred with motion artifact. [25]



### 1.2.1.3 Ultrasounds

US imaging is an exoscopic method that uses sound waves emitted from a transducer through gel directly applied on the skin over the area of interest of the inner body. The transducer collects the back-bounced sound waves that hit the boundaries in the body. The phase difference is then analysed by computer using the speed of sound in tissue ( $1540 \text{ m s}^{-1}$ ) and the intensity of the echoes are used to form an image. It is a real-time, radiation-free system. “US imaging” often refers to **low-frequency ultrasound (LFUS)** whose frequency is lower than 20 MHz. US’s spatial resolution depends on the emission frequency. Typical spatial resolutions are around 0.5 mm at 5 MHz, whereas axial and lateral resolutions can reach up to 80  $\mu\text{m}$  and 200  $\mu\text{m}$  at 20 MHz, respectively. Low-frequency US is particularly appreciated for its decent penetration depth that can reach up to a few cm although it remains inadequate for GI tract observation.

Beside low-frequency ultrasound, **high-frequency ultrasound (HFUS)**, whose excitation wave frequency ranges from 20 to 100 MHz reaches higher axial and lateral resolutions of 11  $\mu\text{m}$  and 30  $\mu\text{m}$  respectively [34] and achieves penetration depths of 10 mm. Although HFUS can image structures up to 8 mm thick, it is still quite limited by its resolution and thus somewhat not the most adapted imaging method for EGC detection.

**Endoscopic ultrasound (EUS)** is the endoscopic version of US as described above. A transducer is mounted on the distal end of an endoscopic probe and provides detailed views of layers invaded by a tumor. It is a very efficient tool in probing the depth and the location of a tumor and observe affected lymph nodes. Besides, it is often used as a complementary technique to CT/PET [35]. EUS has to be performed after filling up half of the gastric cavity with water to improve the US wave propagation. Resolution varies with depth so that elements imaged within 1 to 2 cm would be highly resolved (similar values to conventional US imaging) whereas tissue within 5 to 6 cm will have a poor resolution.

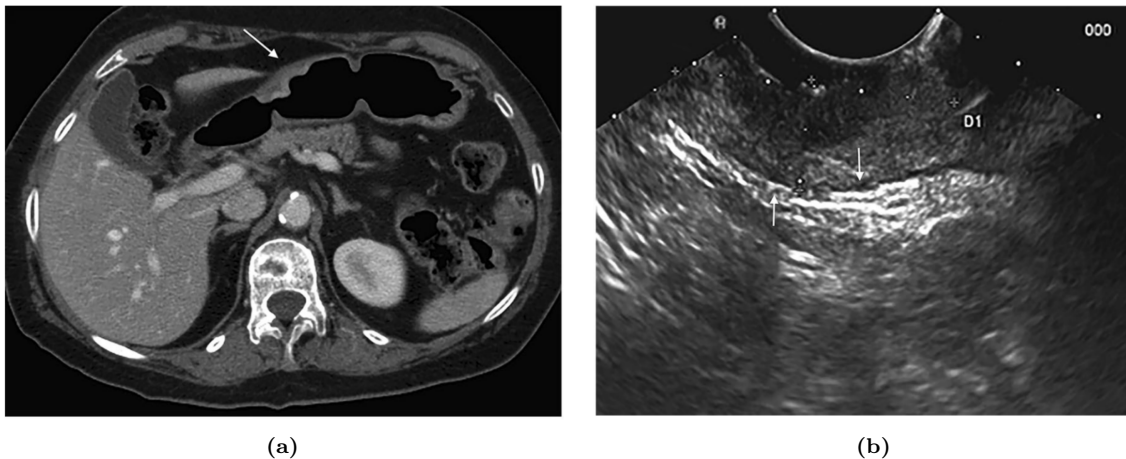


**Figure 1.7:** Lesion in the stomach of a 77-year-old man involving the *antrum* exhibiting a thickening of the gastric wall and infiltration into the *muscularis propria*. (a): CT view showing the mucosal and submucosal thickening of the inner wall at the location of the arrow. (b): EUS image showing the serosal layer and the location where the lesion penetrates the *muscularis propria* [36].

## 1.2.2 Optical imaging methods

As early detection leads to “lighter” therapy and higher chances of surviving, prognosis needs to be based on preinvasive “symptoms”, invisible for most non-optical imaging modalities as they occur

at the molecular/cellular level such as *H. pylori* for instance. As a “second eye”, optical imaging methods have been developed to overcome non-optical imaging shortcomings: low resolution, high cost, delayed diagnosis and potentially harmful radiations. Optical imaging methods exploit the properties of light absorption, transmission, reflection, scattering, or fluorescence in human tissue (*mucosa* is concerned in cases of early detection) to penetrate in depth and re-emit a light signal from continuous consecutive spatial variations constituting the tissue. As the penetration depth is limited by the absorption of light in human tissue, optical imaging methods are not as competitive as MRI, CT or US on the depth of penetration. However, they are highly appreciated for their high resolutions which is more appropriate to observe malignancies in early stages. Indeed, optical imaging makes possible biological observation at the molecular/cellular level *in vivo* but also *ex vivo* for instance in dermatology [34]. As light and sound behaviors inside human tissue differ one from another depending on boundary and diopter type, optical and non-optical modalities can be used to collect different information. Finally, rather than being in competition, optical imaging modalities such as OCT and CM and non-optical modalities such as EUS are complementary [35]. The most widely used optical intravital imaging techniques are CM, photoacoustic, fluorescence, non-linear optic microscopy, diffuse optical tomography (DOT) and OCT.

#### 1.2.2.1 Confocal microscopy

CM consists of blocking the out-of-focus light from reaching the photodetector using a pinhole as a spatial filter to combine enhanced contrast, ultra-high lateral and axial resolution up to 400 nm and 3  $\mu\text{m}$  respectively [37–39] and depth selectivity. 2D images can be obtained by confocal laser scanning microscopy [40], scanning laterally along 2 axes in the focal plane and 3D images can be reconstructed by an axial scan of the objective lens. Either the laser beam, either the stage holding the sample can be scanned depending on the environment (*in vivo* or *ex vivo*) and precision required. Unfortunately, the penetration depth, typically around 200  $\mu\text{m}$  [34] is limited by the signal-to-noise ratio (SNR) due to the optical scattering rate degrading with depth. However, this depth is sufficient to detect preinvasive lesions and EGC that take roots in the surface of the mucosal layer.

#### 1.2.2.2 Photoacoustic microscopy

This method is based on the photoacoustic effect which consists in the production of acoustic waves from light absorption of the sample. In this technique, the sample is irradiated with short laser pulses and produces a thermoelastic expansion detected by the acoustic waves propagating until an ultrasonic transducer. This acoustic wave contains information of the properties of the sample so that an image can be reconstituted from its analysis. Since acoustic waves are less scattered by tissue than light waves, this technique can achieve large penetration depths up to a few cm [41] with a spatial resolution ranging from micrometers to millimeters [42].

#### 1.2.2.3 Fluorescence

Fluorescence consists of illuminating a sample containing fluorophores with a light of a given wavelength and collecting the emitted light of higher wavelength after absorption of the incident light by the fluorophores. Using this method, it is possible to see only the molecules producing fluorescence [43]. The energy of the incident photons is absorbed by fluorophores and causes the electrons initially at the ground state to move to a higher energy state. Then, the excited electrons

lose energy and return to the ground state, emitting photons with less energy and therefore with a longer wavelength. Spatial resolution of fluorescence microscopy typically ranges about a few microns, however, its penetration depth is limited to 1 m m.

#### 1.2.2.4 Non-linear optical microscopy

The term of **nonlinear optical microscopy (NLOM)** refers to several imaging techniques which produce contrast from the interaction between molecules and ultrafast light pulses [44]. These techniques have several applications in tissue imaging and *in vivo* diagnostics [45]. Among these techniques are: multiphoton fluorescence, second harmonic generation, third harmonic generation, coherent anti-Stokes Raman scattering, stimulated Raman scattering and photothermal microscopy [46]. One of the advantages of the non-linear optical microscopy techniques is that commonly they use infrared light lowering significantly the scattering and absorption. Although **NLOM** achieves high spatial selectivities up to several  $\mu\text{m}$ , the imaging depth is limited to 1 m m [44].

#### 1.2.2.5 Optical coherence tomography

**OCT** was first demonstrated in 1991 by Huang *et al.* [47] and grew rapidly as a bioimaging modality. It was first used for ophthalmology [48–50] and then extended to dermatology [51], cardiology [52], dentistry [53, 54] and **GI** wall observation [47, 55]. **OCT** provides real-time, *in vivo*, 3D and cross-section imaging maps of optical backscattering from the tissue as a function of depth. **OCT** differs from **US** in that it uses light instead of sound and hence the time delays cannot be measured directly as for **US**. Unlike **CM**, **OCT** uses interferences between the backscattered light (from the sample) and the reference path light to “measure the magnitude and echo time delay with a very high sensitivity” [56]. Using near-infrared (**IR**) light decreases significantly the scattering effect in tissue, and enables to achieve penetration depths ranging from 1 to 3 m m. Current **OCT** systems achieve axial resolutions up to a hundred times higher than standard **US** imaging: 1 to 15  $\mu\text{m}$ . With a better resolution than **HFUS**, a higher penetration depth and a lower cost than **CM**, **OCT** is a competitive tradeoff and a great candidate for bioimaging.

### 1.2.3 Synthesis

Among the classical imaging techniques listed above, it is of a certain importance to keep in mind that each modality possesses its own specific features and can only be compared to others on a criterion which is the area of application. In the case of this present work, and based on Table 1.3, it appears that one modality’s resolution is roughly proportional to the inverse of its penetration depth as outlined in Fig. 1.8. Besides comparing the two most significant criteria of the formerly listed optical techniques, Fig. 1.8 compares each of them with the depth of penetration required and the size of the lesion/malignancy corresponding to different stages of gastric cancers within the same figure. From that comparison, **OCT** appears to match better than others the need for stomach and esophagus **EGC** detection to consequently provide the most efficient alternative treatment for healing.

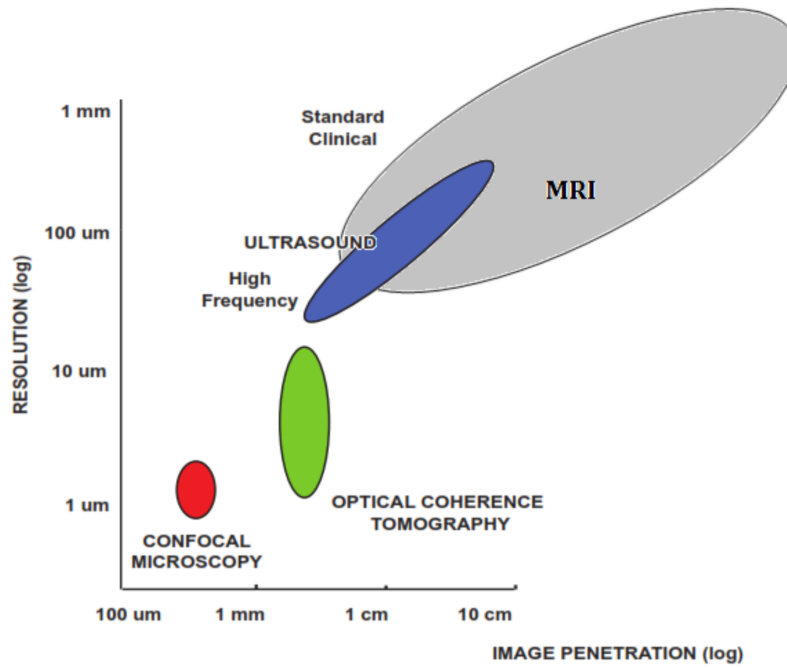


**Figure 1.8:** Comparison of the resolution and penetration depth of bioimaging techniques; *ET*: epithelial thickness; *LP*: distance from epithelium surface to *lamina propria*; *MP*: distance from epithelium surface to *muscularis propria* [22]; *HP*: maximum size of *H. pylori*; *EGC*: Half-space limit of resolution required for the detection of early gastric cancers limited at stage II of the TNM classification; *AGC*: Half-space limit for detection of advanced gastric cancer as defined by Im *et al.* [15]. Note that the size of cells nuclei is compared with the resolution attainable [21].

**Table 1.3:** Comparison of performances of bioimaging techniques. *NLOM*: non-linear optical methods.

Imaging technique	Wave type	Resolution		Tissue penetration depth	Label-free?
		Axial	Lateral		
MRI	RF	4 - 100 $\mu\text{m}$	-	Unlimited	Yes
CT	X-ray	12 - 50 $\mu\text{m}$	-	Unlimited	Yes
PET	$\gamma$ -ray	1 - 2 m m	-	-	
US	ultrasonic 7 MHz [57] - 20 MHz	50 $\mu\text{m}$	100 $\mu\text{m}$ at 21 MHz [58]	a few cm [59]	Yes
Endoscopic ultrasound	ultrasonic 5 - 12 MHz [23, 60]	-	0.5 - 1 m m [23]	4 - 7 cm [23, 61]	Yes
Confocal microscopy	optical	3 - 5 $\mu\text{m}$ [34]	0.4 - 1 $\mu\text{m}$ [34, 38]	$\leq$ 200 $\mu\text{m}$ [34]	Yes
Fluorescence microscopy	optical	1 - 5 $\mu\text{m}$	-	300 - 800 $\mu\text{m}$	No
Photoacoustic microscopy	visible or near-IR light and sound	15 $\mu\text{m}$ - 1 m m [42, 59]	220 nm - 560 $\mu\text{m}$ [41]	100 $\mu\text{m}$ - 4 cm [41, 42]	Yes
NLOM	-	$\sim$ 1 $\mu\text{m}$ [59]	-	$\sim$ 1 m m [59]	Limited
OCT	near-IR light	1 - 15 $\mu\text{m}$ [56, 62]	3 - 5 $\mu\text{m}$ [56]	1 - 3 m m [56, 62]	Yes

### 1.3 Optical coherence tomography

**OCT** is an optical, non-invasive, biomedical, real-time imaging method that provides cross-sectional images of scattering media, offering high resolution and sensitivity. Based on low-coherence interferometry, **OCT** achieves high axial and lateral resolutions and can penetrate up to 3 mm into biological tissue [27, 56, 62] (refer to Table 1.3). It was first discovered in 1991 by Huang *et al.* who defined the **OCT** system as: “an extension of previous low-coherence reflectometry systems” [47]. The first system designed was a **TD-OCT** configuration. More recently, a faster and more sensitive configuration called **frequency-domain OCT (FD-OCT)** has emerged and was implemented for *in situ* tissue imaging [55]. Fercher *et al.* were the very first to apply low-coherence interferometry to biological measurement [63].

#### 1.3.1 Low Coherence Interferometry

The core of a low-coherence interferometry for bioimaging is a fiber-optic Michelson interferometer illuminated by a low-coherence light source of low absorption in biological tissue (wavelength usually centered around 830 nm or 1310 nm), as shown in Fig. 1.9. A beam splitter divides the light beam into the two arms of the interferometer. The light in the reference path,  $E_R$  (reflected from the reference mirror) and the light in the sample path,  $E_S$  (backscattered from the sample) are redirected by the beam splitter and superimposed onto the detector where they interfere. When the **optical path difference (OPD)** between the reference and the sample path is zero, interferences are constructive and the detector reads a maximum of intensity whereas a non zero optical path will result in destructive interferences and dark fringes. The electric field of a low-coherence light

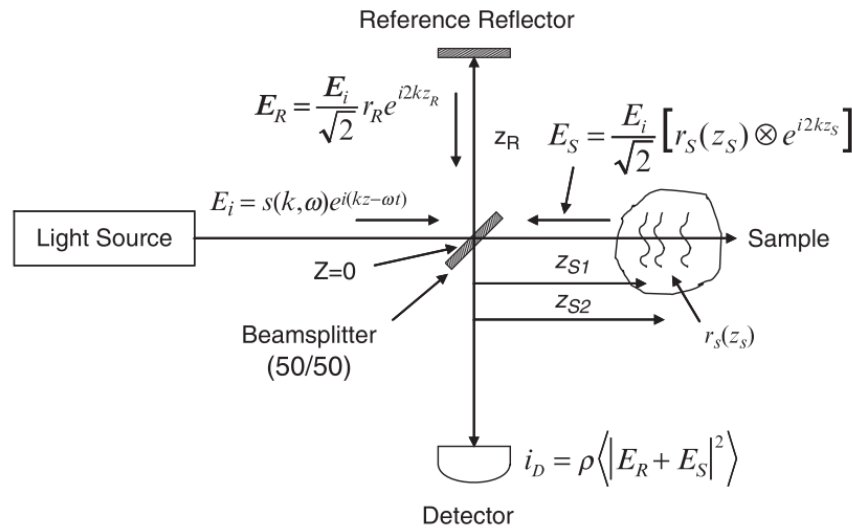


**Figure 1.9:** Schematic of the principle of a Michelson interferometer and low-coherence interferometry in time domain. Picture from [64].

source is expressed <sup>9</sup> as [56]:

$$E_i = s(k, \omega)e^{i(kz - \omega t)}, \quad (1.1)$$

where the amplitude of the low-coherent light emitted with a broadband spectrum,  $s(k, \omega)$  is a function of the wavenumber  $k = \frac{2\pi}{\lambda}$  and the angular frequency  $\omega = 2\pi\nu$  represented in Fig. 1.10.

<sup>9</sup>In the section, the same formalism as in [56] will be used to describe the principle of **OCT**

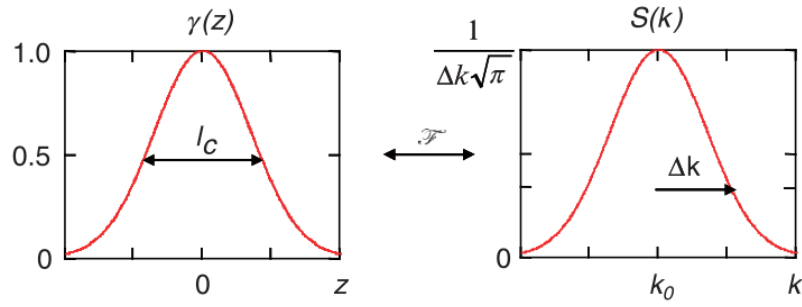


**Figure 1.10:** Light source spectrum  $S(k)$  and its Fourier transform  $\gamma(z)$ , the coherence function [56].

The wavelength  $\lambda$  and the frequency  $\nu$  are coupled by the index of refraction  $n(\lambda)$ . Interferences with low-coherence length light are only observed when the OPD remains within the coherence length, i.e.  $\text{OPD} < l_c$ , which is the **full width at half maximum (FWHM)** of the inverse Fourier transform  $\gamma(z)$  (the auto-correlation function) of the power spectrum  $s(k)$ :

$$l_c = \frac{2 \ln(2)}{\pi} \frac{\lambda_0^2}{\Delta \lambda} = \Delta z, \quad (1.2)$$

with  $\Delta \lambda$  the **FWHM** of the power spectral density,  $\lambda_0$  the central wavelength and  $\Delta z$  the axial resolution which is given by the **FWHM** of the autocorrelation function in low-coherence interferometry for a Gaussian spectrum.

It is assumed that the incident optical power is splitted evenly into the reference arm (that reflects on the surface of the reference mirror at  $z_R$ <sup>10</sup> of the beam splitter) and the sample arm (whose backscattered electric field depends on the depth-dependent profile of the tissue that is assumed to be a series of  $N$  discrete reflectors at distances  $z_n, n \in \{1, \dots, N\}$  from the beam splitter). The electric fields of the two paths are respectively:

$$\begin{aligned} E_R &= \frac{E_i}{\sqrt{2}} r_R e^{i2kz_R} \\ E_S &= \frac{E_i}{\sqrt{2}} \left[ r_s(z_S) \otimes e^{i2kz_S} \right] \\ &= \frac{E_i}{\sqrt{2}} \sum_{n=1}^N r_{S_n} e^{i2kz_{S_n}}, \end{aligned} \quad (1.3)$$

with  $r_s(z_S) = \sum_{n=1}^N r_{S_n} \delta(z_S - z_{S_n})$  and  $\delta$  the Dirac function.

The two back-reflected signals are mixed by the beam splitter and the optical powers are superimposed forming the total instantaneous electric field  $E$ :

$$E_D = E_R(k) + E_S(k) \quad (1.4)$$

<sup>10</sup>Caution:  $z_R$  refers to the distance of the reference mirror from the **beam splitter (BS)** and NOT to the Rayleigh distance that will be referred to as  $z_r$  in the following.

The intensity recorded on the detector is given by:

$$\begin{aligned} I_D(k, \omega) &= \frac{\rho_D}{2} \langle |E_k|^2 \rangle \\ &= \frac{\rho_D}{2} \left\langle \left| \frac{s(k, \omega)}{\sqrt{2}} r_R e^{i(2kz_R - \omega t)} + \frac{s(k, \omega)}{\sqrt{2}} \sum_{n=1}^N r_{S_n} e^{i(2kz_{S_n} - \omega t)} \right|^2 \right\rangle \end{aligned} \quad (1.5)$$

where  $\rho_D$  is the detector's responsivity. Then, assuming that the angular frequency is much higher than the response time of the detector and  $S(k) = \langle |s(k, \omega)|^2 \rangle$ , the real interferometric signal can be decomposed into 3 terms as shown in Eq. (1.6): a DC component, a cross-correlation term, usually prevailing by an order of  $10^4 \sim 10^5$  times the DC term, and an auto-correlation term which is an artifact, except in common-path OCT system designs. When the intensity is encoded as a function of time, we talk about **TD-OCT**, while encoding with wavenumber is called **FD-OCT** [56].

$$\begin{aligned} I_D(k) &= \frac{\rho_D}{4} \left[ S(k)(R_R + \sum_{n=1}^N R_{S_n}) \right] \\ &+ \frac{\rho_D}{2} \left[ S(k) \sum_{n=1}^N \sqrt{R_R R_{S_n}} \cos 2k(z_R - z_{S_n}) \right] \\ &+ \frac{\rho_D}{4} \left[ S(k) \sum_{n \neq m=1}^N \sqrt{R_{S_n} R_{S_m}} \cos 2k(z_{S_n} - z_{S_m}) \right]. \end{aligned} \quad (1.6)$$

### 1.3.2 TD-OCT

In **TD-OCT**, the position of the reference mirror  $z_R$  is scanned over time and the intensity received on the single-receiver is the integration over  $k$  of Eq. (1.6):

$$\begin{aligned} I_D^{TD}(z_R) &= \frac{\rho_D}{4} \left[ S(k)(R_R + \sum_{n=1}^N R_{S_n}) \right] \\ &+ \frac{\rho_D}{2} \left[ S_0 \sum_{n=1}^N \sqrt{R_R R_{S_n}} e^{-(z_R - z_{S_n})^2 \Delta k^2} \cos 2k_0 \underbrace{(z_R - z_{S_n})}_{\text{OPD}} \right], \end{aligned} \quad (1.7)$$

with  $S_0 = \int_0^\infty S(k) dk$ , the integrated spectral power of the light source. The interference pattern is a function of  $z_R$  and the discretized reflector's intensity profile is recorded in the "fringe bursts" term. A **TD-OCT** A-scan is represented in Fig. 1.11. The axial resolution is determined as equal to the coherence length and the carrier frequency of the A-scan reflectivity profile is a linear function of  $k_0$ , the center wavenumber of the source, and is limited by the scanning speed of the reference mirror. The lateral resolution (also called transverse resolution) depends on the diameter of the focal spot and is given by Rayleigh criterion for a unitary refractive index:

$$\Delta x \approx 1.27 \lambda \frac{f}{d} \approx 0.64 \frac{\lambda_0}{NA}, \quad (1.8)$$

with  $d$  the spot size of the beam on the objective lens and  $f$  the focal length [56]. Hence, the transverse resolution can be improved independently from the axial resolution by increasing the **numerical aperture (NA)**, focusing the beam to a smaller spot size.

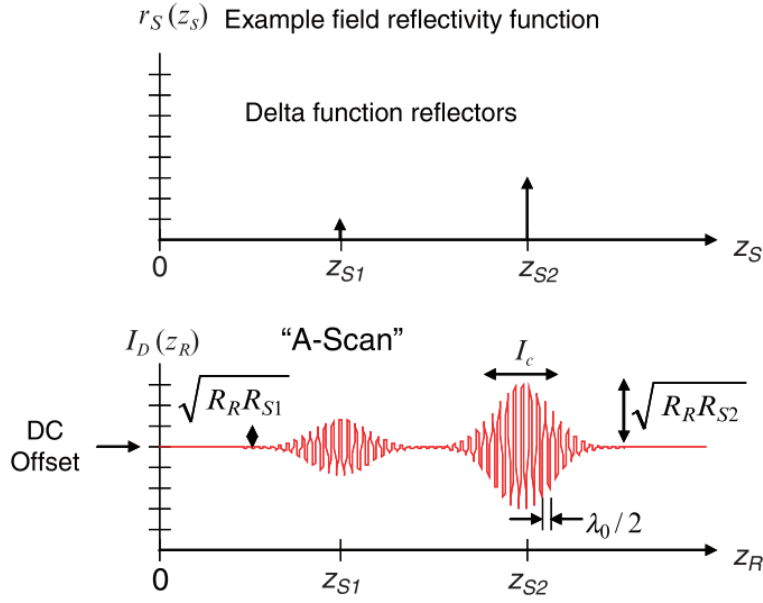


Figure 1.11: A-scan of discrete reflectors recorded on a single detector by TD-OCT [56].

### 1.3.3 FD-OCT

FD-OCT differs from TD-OCT of that the reference mirror formerly moving in TD-OCT is now fixed, therefore the reflectivity profile (see Fig. 1.12a) is recorded differently. The interference intensity can be captured either using a spectrometer (usually a diffraction grating and a line camera) to record either simultaneously on a detector (spectral-domain OCT (SD-OCT)), either sequentially on a single detector synchronized with the wavenumber of a swept linewidth of the laser source (SS-OCT). In both cases, the intensity detected is calculated by doing the Fourier transform of  $I_D(k)$  in Eq. (1.9). The resulting profile of the intensity is shown in Fig. 1.12b as a function of the wavenumber.

$$\begin{aligned}
 I_D^{FD}(z) = & \frac{\rho_D}{8} \left[ \gamma(z) \left( R_R + \sum_{n=1}^N R_{S_n} \right) \right] \\
 & + \frac{\rho_D}{4} \left[ \gamma(z) \otimes \sum_{n=1}^N \sqrt{R_R R_{S_n}} \delta(z \pm 2(z_R - z_{S_n})) \right] \\
 & + \frac{\rho_D}{8} \left[ \gamma(z) \otimes \sum_{n \neq m=1}^N \sqrt{R_{S_n} R_{S_m}} \delta(z \pm 2(z_{S_n} - z_{S_m})) \right] \quad (1.9)
 \end{aligned}$$

Finally, compared to TD-OCT, FD-OCT allows faster imaging and an improved SNR. Although SD-OCT is limited by the spectrometer range. A typical A-scan can reach up to 51.5 kHz [65].

### 1.3.4 SS-OCT

Unlike SD-OCT, in SS-OCT, the spectral intensity  $I_D(k)$  is captured synchronously with the narrowbands swept in wavenumber. The SS-OCT SNR is even higher than for SD-OCT and the speed of acquisition will depend on the speed of the swept-source since the detector is no longer a limiting factor. Typical A-scan are performed at a few hundred kHz. Novais *et al.* [66] and Jayaraman *et al.* [67] reported sweep rates at 400 kHz and 500 kHz respectively. SS-OCT is



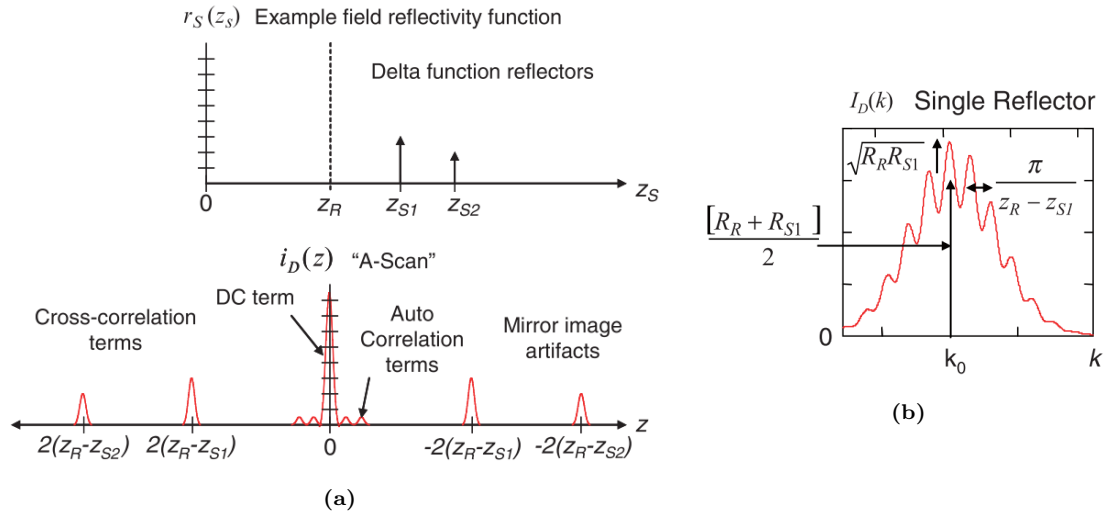


**Figure 1.12:** (a):A-scan of discrete reflectors obtained by FD-OCT. (b):Profile of the intensity detected by a single reflector in FD-OCT. Pictures from [64].

highly faster than TD-OCT or even FD-OCT and thus more adapted to provide densely sampled 3D visualizations upon short durations for biomedical visualizations. Another advantage is the sensitivity improved by 20 to 30 dB [64]. Although the phenomenon of sensitivity roll-off of the SS-OCT is not as pronounced as in SD-OCT, it remains a non-neglectable parameter. Because of the finite size of the instantaneous spectral linewidth of the source, the backscattered intensity is decreased with the imaging depth. Nevertheless, recent swept sources allow a considerable fall-off of the sensitivity roll-off. However, in practice, the signal losses due to absorption and scattering in tissue prevail on the sensitivity roll-off [68].

### 1.3.5 Endoscopic OCT

Endoscopy started to develop in the early 20th century. It greatly facilitates the detection process and increases the imaging accuracy, compared to biopsy. Along with biopsy, upper endoscopy represent 90% of the techniques used in gastric cancer detection today [27]. Before being an *in vivo* tool, OCT was first used in ophthalmology to map the retinal volume [48–50]. Early stage malignancies are both small in size, and are either located on the surface, either shallow under the internal organ epithelium. A non-invasive monitoring of such biological entities hence requires a high-resolution without the need for more than a few hundred  $\mu\text{m}$  of penetration depth capability. Although quite a few imaging techniques have been adapted for endoscopy imaging, endoscopic OCT (endOCT) combines the advantages of exoscopic OCT (exOCT) (high resolution and low cost) and of low NA which greatly simplifies the miniaturization and the integration into probes in order to reach internal parts of the body [27, 69]. On top of that, endOCT offers “portability” and has a real potential in *ex situ* diagnosis. EndOCT is not limited to GI tract screening, but expands to cardiovascular [70] and pulmonary [71] imaging as well. endOCT has already made its proofs in *in vivo* detection, in animals [26] and humans [55, 72] as shown in Fig. 1.13. In endOCT, light is brought by single-mode fiber (SMF) through a catheter, to the distal end of an endoscopic probe to illuminate the tissue under investigation. The light delivered is subject to back-reflection and backscattering and is collected on the same path, and then mixed up with the reference path (located either inside the probe or relocated outside of the catheter). Depending on

the configuration, the tissue can be illuminated *en face* or perpendicularly to the probe [69, 73–77]. In order to realize cross-sectional or 3D images, a rotating or scanning element is integrated at the distal end of the catheter.

The miniaturization, the integration capability, and consequently the cost of the apparatus, are as many challenges for *endOCT* probes today, to make them mass “plug’n’play” portable instruments. Today, the main limitations of *endOCT* probes are their size (probes with smaller diameters will enable more flexibility, penetrate deeper and even reach areas difficult of access as veins for instance), their cost, the complex packaging processes (delaying the arrival on the biomedical imaging market) and the speed of scan (that needs to be high in order to allow real-time diagnoses, and to prevent artifacts generated by non-idle objects [78–80]). A state of the art of existing endoscopic OCT systems will be provided in the next chapter.

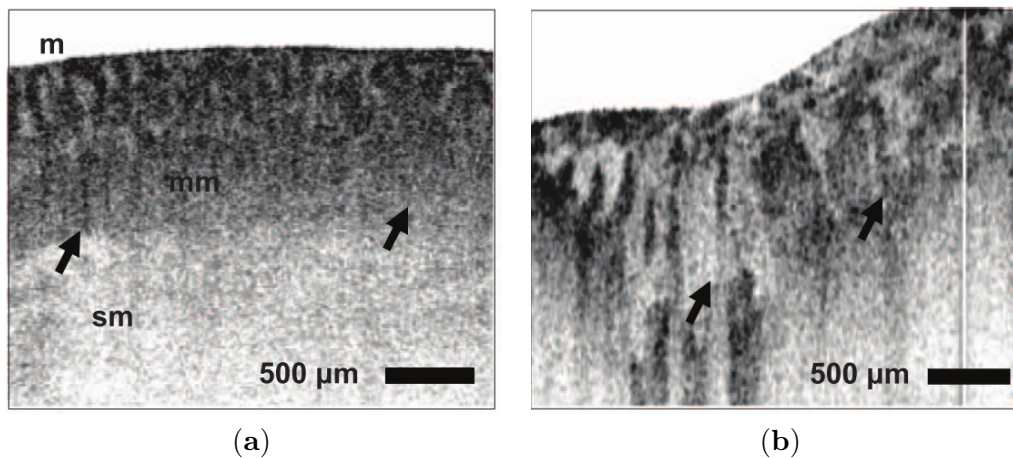


**Figure 1.13:** OCT images of neoplastic changes. (a): Normal colon; m: *mucosa*; mm: *muscularis mucosa*; sm: *submucosa*. (b): Specimen of colon with adenocarcinoma Fujimoto and Drexler [56].

## 1.4 Conclusion

Among all cancers, stomach and esophagus cancers are still among those who require to be better known and diagnosed earlier to provide softer and more efficient treatments before heavy operations such as painful series of biopsy and chemotherapy take over the last chances of survival of the patient. Because GI cancers grow very fast, they are too often diagnosed in advanced stages, when the chances of survivals are considerably low. The main causes which make stomach and esophagus carcinomas stealth until an abnormality triggers the concern of the patients, are the lack of attention and maturity in the detection techniques. More maturity, simplicity and safety would eventually encourage more patients to undergo more frequent and earlier surveillance prevention routines. From microstructural neoplastic changes and high-grade dysplasia to the dawn of invasion of the *serosa* and advanced stages, detection techniques need to be adapted to the size, the location and the nature of symptoms. Exoscopic imaging techniques have become unadapted to most detections of such a kind and were rapidly traded off for endoscopic techniques able to provide appropriate optical biopsies. Compared to non-optical and non-linear optical techniques, linear optical techniques match the best the depth and resolution requirements for adequate early stage GI malignancies observation *in vivo*. And in particular, *SS-OCT* has been widely adopted for this type of specific applications because of its high speed, high spatial resolution and sufficient

penetration depth. Endoscopic **SS-OCT** allows real-time, non-invasive, high resolution, inexpensive and radiation-free voluminous bioimaging. It has been developing fast during the past two decades and is still brimming with very promising possibilities awaiting to save more lives. Consequently, endoscopy **SS-OCT** is the starting point of this work which will intend to produce a **SS-OCT** endoscopic probe for **EGC** detection.

#### **Chapter summary**

After presenting the stomach and esophagus cancers' features, we came to the conclusion that endoscopic **SS-OCT** is the most suitable imaging technique for these cancers in early-stage diagnosis. In the following, we will focus on exploring the different types of existing endoscopic probes allowing the implementation of **SS-OCT**. Then, the selection criteria will be introduced in order to conceive an endoscope design and an optical model will be established to define the specifications of the microsystem constituting the core of this work.

## Chapter 2

# Miniaturization of OCT systems

THE former chapter reported the differences between the optical and non-optical imaging techniques, and their advantages and drawbacks. As a summary, optical imaging methods offer higher spatial resolution, higher sensitivity, and allow to focus onto targeted areas (such as esophagus sphincter, stomach *mucosa*, located epithelial lesions, etc.). Compared to non-optical modalities, optical techniques are mostly inexpensive (from both the instrumentation and operation point of view) and free from radioactivity. Among conventional optical bioimaging techniques, OCT appears to be particularly adapted to GI tract precancerous and EGC detection because of its high resolution and moderate imaging depth. In addition to most features shared by other optical imaging, OCT takes advantage of fiber-optic technologies for light delivery to catheters. Despite the lack of space and working distance reduction in integrated endoscopes, its low NA is rather an asset providing large working distances which makes OCT an imaging modality compatible with endoscopic integration. In this framework, a significant effort in order to downscale OCT systems has been provided for the last two decades. One of the first reasons was to comply with the endoscope size. Hence, most of the work was first concentrated on miniaturizing the scanning probe [81, 82]. Nevertheless, only the sample arm was consequently reduced whereas most of the OCT system (source, interferometer) was still located outside of the endoscope body. This asymmetry unfortunately leads to instability due to the discrepancy in the signal bearing the phase information. For this purpose, common path interferometers, for which both arms undergo the same environment are much more robust. However, long interferometer arms may still introduce uncompensated path length differences degrading the signal quality due to mechanical and thermal disturbances along the flexible fiber.

The miniaturization of OCT systems is also motivated by its multipurpose aspect that is to reach smaller and smaller zones of the body, thus making it a polyvalent technology. Miniaturizing every single component of the system is a challenge, but the smaller the size of the component is, the more tedious the assembly will be. Batch microfabrication allows to build monolithic systems at very low cost, and to simplify greatly the assembly of micro components since various alignments can be done at the wafer level. However, let us keep in mind that the degree of integration, defined by the simplicity of the assembly of the mechanical and optical parts is the central criterion that will determine the fabrication efficiency of the system and its competitiveness for industrial production [83, 84].

The illumination block will be selected depending on the type of OCT wanted. The light source, the interferometer and the lenses will determine the resolution, the penetration depth, the

focal length of the optical system and the scanning and sensing element will define the scan speed, precision and the quality of the image. This chapter reviews the miniaturization of OCT systems in general, the different existing types of probes, and the main components constituting these systems such as the interferometer, the lenses, the scanning elements, and the sensing systems.

## 2.1 Endoscopic probe classification criteria

Endoscopic optical imaging was first introduced in 1963 with fiber-based endoscopes [85]. Optical fibers enable to carry optical signals with flexible systems, allowing to deport some parts of the system while being able to reach specific parts of the inner body. Hence, the numerous components no longer necessarily have to be part of one unique monolithic block as in handheld OCT systems [86]. The illumination and detection blocks, the interferometer and the scanner can be independently integrated one from another.

For example, *endOCT* probes can be classified according to their scanning range, resolution, imaging speed, flexibility and *field of view* (FOV). These features can be achieved through various configurations such as: the scan direction (side or forward viewing), the scan actuator's location (distal or proximal), the scan type (1-axis rotation with or without pullback, 2-axis rotation), the scan path (circumferential, reduced circumferential FOV, raster, Lissajous, ...), the scanning mechanism (motor, micromotor, galvanometer, MEMS micro-scanner), the packaging type (standard, balloon, tethered, *silicon optical bench* (SiOB)), the component integration level (handcrafted, semi-integrated, full embedding), ...

Although the scan direction is the most significant criterion to pick up according to the organ and the type of cancer taken into account, the type of scan and the actuator's location will also play an influent role in the determination of the design of the probe and of the whole OCT system. The different types of scan mechanisms will be presented in this subsection while the component integration level will be developed in Section 2.4.

### 2.1.1 Scan direction

#### 2.1.1.1 Forward-imaging

One approach of *endOCT* imaging is the forward-viewing configuration where the light is emitted and recollected from the front of the distal end of the catheter. They are adapted to *en face* structure observation and catheter placement and guidance, so that they could be used without the complete endoscopic apparatus used when endoscopy is performed clinically. Representations of this clinical catheter are given in Fig. 2.1. Ourak *et al.* [87] demonstrated that it was possible to exploit an OCT image without conventional camera apparatus, to guide the catheter using the *en face* OCT probe image feedback only. This way, forward-imaging probes could be used alone as both a positioning and scanning system. A very simplified sketch of a forward-imaging probe is shown in Fig. 2.2a.

#### 2.1.1.2 Side-imaging

In side-imaging configuration, the beam is focused onto an axis perpendicular to the probe and recollected through the same path as shown in Fig. 2.2b. Side-imaging *endOCT* probes scan a sample at an angle of about 90° either over the whole circumference either over a reduced area.

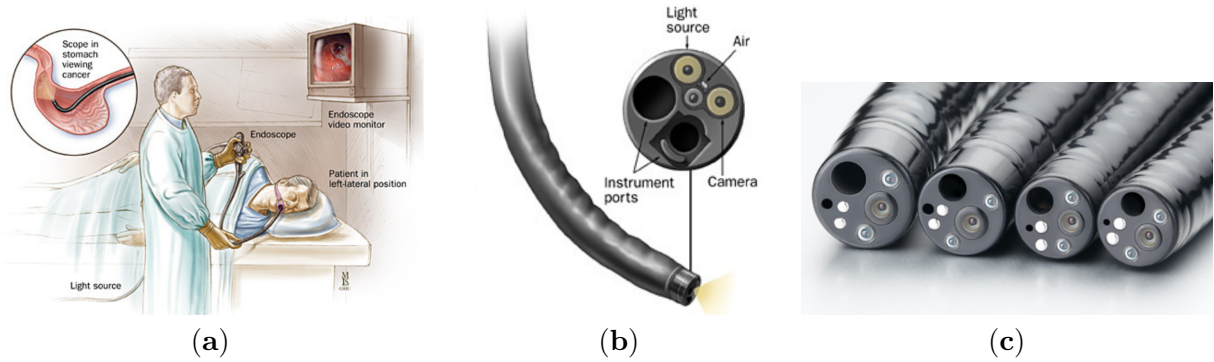


**Figure 2.1:** Endoscopy performed in hospital or clinical complexes. (a): Endoscopy service room set-up and patient positioning for endoscopy imaging. (b): Conventional double-channel therapeutic endoscope (gastroscope) used for detection and therapy operation. (c): Standard medical video endoscope for use *in vivo* with imaging tools; Pentax Precision Instrument, EB15 series J, Tokyo, Japan; minimum outer diameter 5.4 mm. Recent gastroscope's instrument ports have an average inner diameter of 2.8 mm [88].

They are the most common probe types found in the literature [89] and can provide structural views of tubular or hollow organs (called luminal organs) and are hence particularly adapted to esophagus imaging.

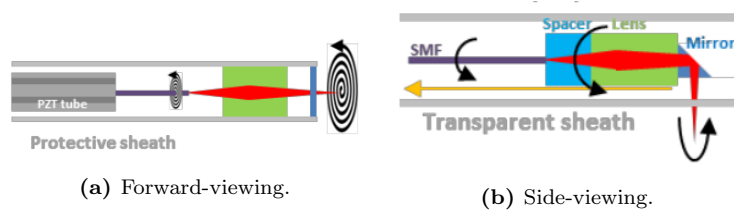


**Figure 2.2:** Simplified schematic view of forward and side-viewing configuration. From [90]

## 2.1.2 Actuation location

Side-imaging probes can be subdivided into two types: proximal and distal scanning. Their principle is presented hereafter.

### 2.1.2.1 Proximal scanning

Proximal scanning refers to a mechanism of actuation located outside of the body of the probe and transferred into the distal catheter. This method is the most common in *endOCT* imaging. It was first developed by Tearney *et al.* [73] in 1996 and is represented in Fig. 2.3. For proximal side-imaging, a prism used in total internal reflection with its face oriented at  $45^\circ$  is connected at the tip of the optical path deflecting the light beam perpendicularly to the length of the catheter. Then, a motor with or without a gear is used to rotate the optic fiber with the prism at the distal end. The rotation is conveyed via a torque coil located at the proximal end of the catheter. An optical rotary joint is used to continuously (or discontinuously in the case of reduced circumferential scan) rotate the catheter free end in one direction using motors or gears galvanometers. A translational slow scan (C-scan) is realized pulling back the whole probe or the catheter's shaft inside the transparent sheath. This operation can be realized using a galvanometer and provide an additional scan axis. Finally, a 3D *OCT* image can be obtained using this method.

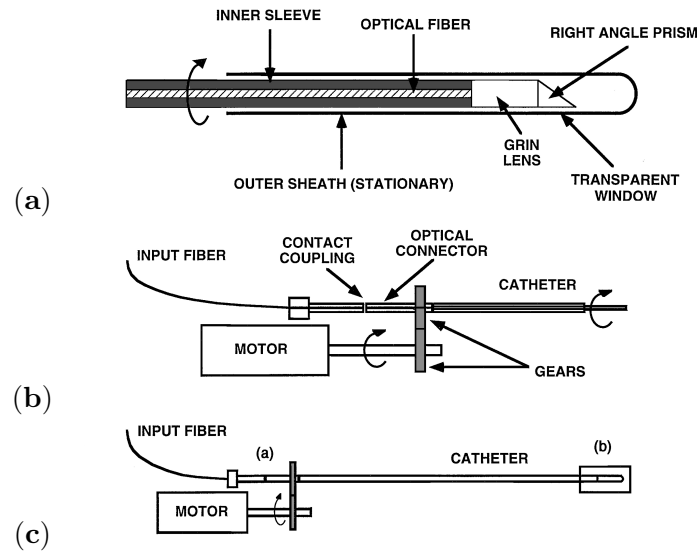


**Figure 2.3:** Design of actuation system of Tearney *et al.*'s proximal endoscopic probe. (a): Catheter's tip. (b): Proximal actuation system. (c): Overview of the whole catheter. [73].

### 2.1.2.2 Distal scanning

In distal scan, the actuation mechanism is located at the very tip of the probe, within the body. Unlike proximal actuation, the junction-driveshaft can be replaced by micromotor of a MEMS scanner [84, 91–95].

### 2.1.3 Scan type

Before introducing the different existing scans in details, it should be made clear that they can be classified according to three types of scan :

#### 2.1.3.1 1D rotational

In distal actuation side-viewing probes exclusively, 1D rotation scan is the basic and simplest type of scan possible. It is realized by a rotation component with or without interruption in its course. When the rotation is uninterrupted, the scan is also referred to as circumferential. This type of scan only allows a 2D OCT image performed by a rotational B-scan. An example of the result of a 1D rotational scan is shown in Figs. 2.4a to 2.4c.

#### 2.1.3.2 1D rotational with pullback

As an extension of 1D rotational scan, an additional “pullback” has been introduced in the scan motion of the catheters to provide a 3D image. A pullback is unidimensional translational displacement of the beam along the length of the catheter usually realized by pulling back the head of the catheter in the lumen. Hence, a pullback is a C-scan performed by retracting the probe and allowing to reconstitute 3D images (see Fig. 2.4d) from consecutive 2D cross sections (such as in Fig. 2.4c).

#### 2.1.3.3 2D rotational

Anyhow, as mentionned earlier, and regardless to the scanning mechanism, 1D rotational scan does require a pullback to provide a 3D OCT image. And a pullback goes along with proximal actuation,

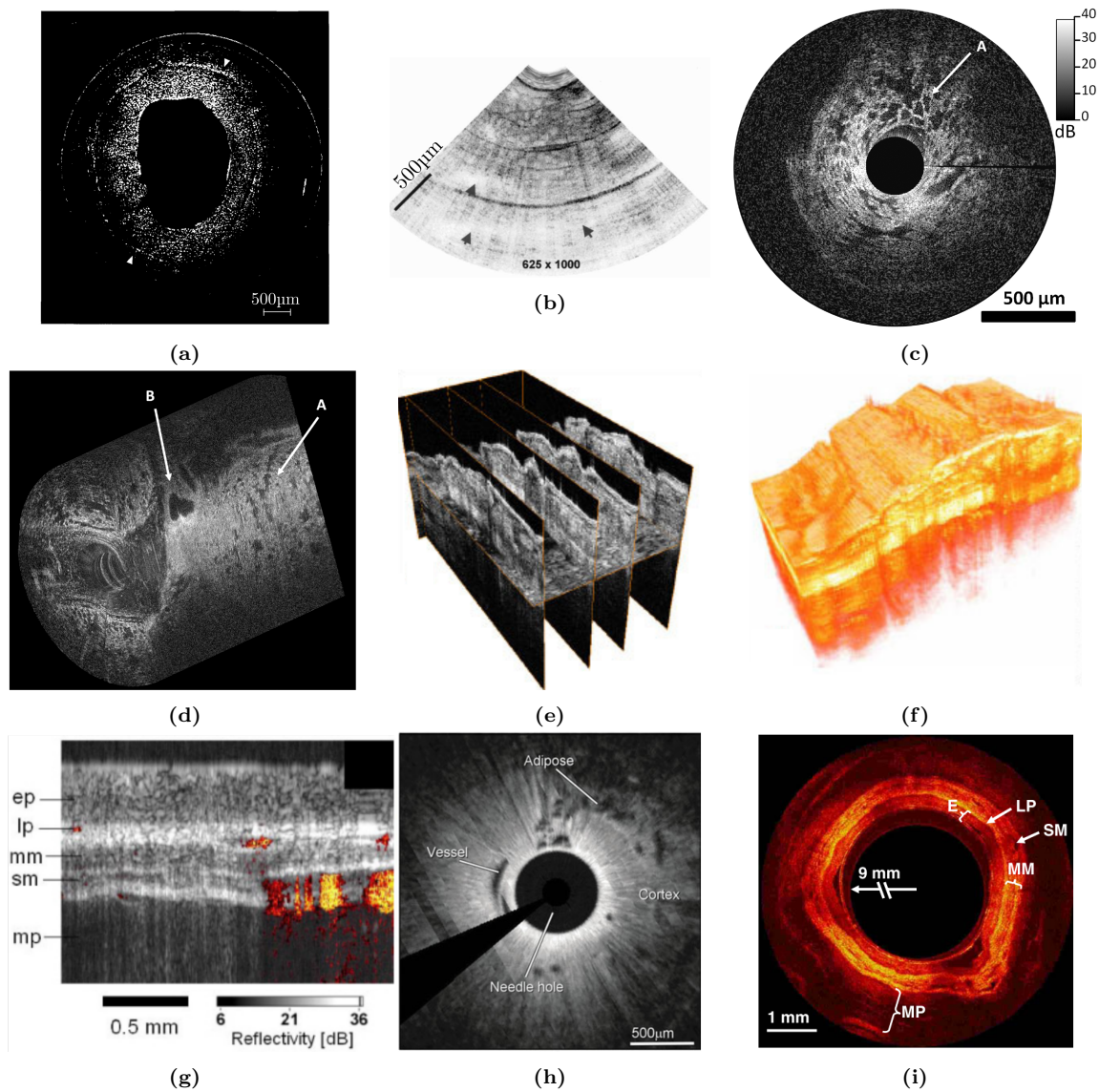


**Figure 2.4:** Different OCT images obtained by means of various scan types, paths and mechanism. (a) 1D rotational full circumferential B-scan without pullback from [73]. (b) 1D rotational reduced circumferential FOV without pullback from [96]. (c) 1D rotational full circumferential B-scan in lumen from [97], and (d) its corresponding 3D OCT image by translational pullback from [97]. (e) Cross-sectional stack of a 2D rotational B-scans and C-scan by using a 2-axis MEMS micro-scanner raster scan of a hamster cheek pouch acquired *in vitro* by [98] and (f) its corresponding 3D rendering from the same hamster cheek pouch [98]. (g) 1D rotational reduced circumferential B-scan of a human esophagus performed by raster scan using proximal prism from [75]. (h) 1D rotational full circumferential B-scan with distal actuation, hindered by the shade of the electrical cable connecting the distal micromotor from [98]. (i) Full circumferential scan performed in a pig esophagus with a single-balloon imaging catheter from [82]. ep=epithelium; lp=lamina propria; mm=muscularis mucosa; sm=submucosa; mp=muscularis propria.

and thus carry all the drawbacks of proximal scanning such as the distortion of the fiber that may affect the image, the non-uniform rotation, etc. As an alternative, 2D rotational scans replace the pullback motion by a second rotation. 2D rotational motions are exclusively carried out using distal MEMS micro-scanners and can easily provide 3D images using one unique device to perform and combine B-scans and C-scans. Although the scanning range of 2D rotational scans is reduced compared to 1D rotational circumferential scans, it has the ability to cover areas of several  $m^2$   $m$  [99], sufficient for applications such as preinvasive malignancy detection. Another asset of 2D rotational scans, is that they commonly achieve high speeds, up to a few tens of kHz [100, 101].



OCT images collected by 2D rotational scans are shown in Figs. 2.4e and 2.4f.

### 2.1.4 Scan pattern

Interpreting the data carried by the light backscattered by the tissue depends obviously on the scanning method and thus on the scan pattern. As long as the scan beam position can be dynamically tracked and can sufficiently cover an area of interest, any scan pattern could be utilized to retrieve an OCT image. However, chaotic scans usually denote uncontrolled motions or strong couplings of the scanning actuators. More common scan patterns are preferred such as raster, Lissajous, spiral or circumferential with pullback and will be briefly presented in the following subsection.

#### 2.1.4.1 Raster scan

One of the most common and easiest scan to implement is the raster scan. Raster scan allows to sweep a light beam using actuators of different types [74, 75, 102] to deflect light onto two orthogonal axes. Raster scan is a basic scanning method that was used in cathode ray tubes at first in 1880 and is inherent to Paul Nipkow’s disc scanning of 1884. The word “raster” comes from the latin *rastrum, radere*: “to rake”. Raster scan rakes along a fast-axis in a sawtooth pattern and along an orthogonal slow-axis in a stair function as shown in Fig. 2.5. Different setups can achieve such raster scans: on the one hand, in side-viewing probes using a distal micromotors (or 1D rotational micro-scanners) and a proximal translational motion (in pullback) to generate 3D images, the pullback actuator is usually used for the slow-axis scan and the prism or the 1D micro-scanner as the spinning fast-axis scan. On the other hand, MEMS scanner-based side-viewing probes and all types of even forward-viewing probes can easily achieve raster scans [76, 99, 103–105]. Figures 2.4e to 2.4g show OCT images obtained by raster scan in 2D, and 3D images reconstituted by pullback and after reconstitution respectively.

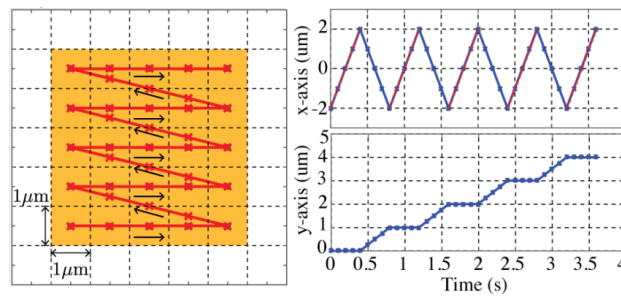


**Figure 2.5:** Raster scan with triangular waveform in the X-axis and smooth stair waveform in the Y-axis.

#### 2.1.4.2 Lissajous scan

Superimposing two single-tone harmonic waveforms over two orthogonal axes is called a Lissajous scan (see Fig. 2.6). Sampling a Lissajous scan is much more complicated than a raster scan as long as both axes are non-uniform and non-linear. Fortunately, as an *a priori* pattern is known, the result can be compared to the expected scanned path to reconstruct the 2D image. Furthermore, the advantage of the Lissajous scan over the Raster scan is that it can be performed within a much shorter time because it is working at resonance frequencies on both axes.

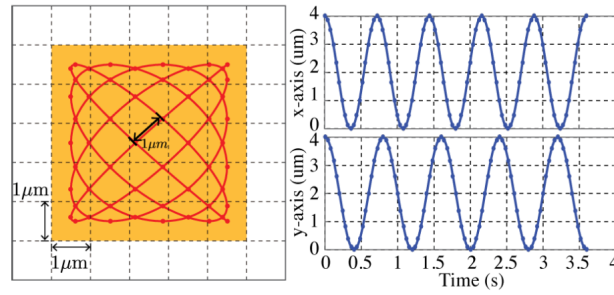


**Figure 2.6:** Lissajous scan of a 5  $\mu\text{m}$  image with sine waveforms of 1.39 Hz in the X-axis and 1.25 Hz in the Y-axis.

### 2.1.4.3 Spiral scan

Spiral scanning is a possible alternative to Raster or resonant Lissajous scan. Yet it is mostly used in forward-viewing configuration. It consists of applying two sine waves in quadrature of phases whose amplitudes are time-dependent as shown in Fig. 2.7; the tip of the fiber scanner is actuated in a precise spiral pattern actuated distally and “particularly adequate for high magnification, small field imaging, such as CM and multi-photon microscopy” [90].

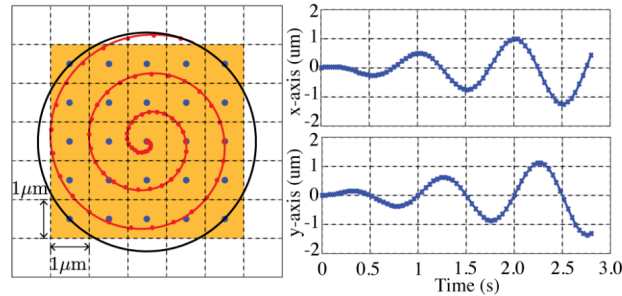


**Figure 2.7:** Spiral scan of 5  $\mu\text{m}$  with constant angular velocity.

## 2.1.5 Scanning mechanism

### 2.1.5.1 Galvanometers and micromotors

Commonly used opto-mechanical devices such as mirrors mounted onto galvanometers [106] were used for OCT [107]. Similarly, prisms at  $45^\circ$  with a reflective face mounted onto motors or micromotors are also used as proximal scanning systems [73, 96]. Galvanometers were also exploited to perform translational movements [74] (see Sections 2.1.1.1 and 2.1.1.2). Based on motors, rotating polygon mirrors allow resonance-free fast scanning but were seldom used in endOCT systems. The use of motors limitates the scan to a 2D image and provides circumferential images as shown in Fig. 2.4h. The main cons of micromotors used in the distal-scanning configuration for side-viewing is that the circumferential view is often hindered by the shade of the electrical cable connected to the distal opposite end of the probe to the generator block as shown in Fig. 2.4h.

### 2.1.5.2 MEMS scanners

Galvanometers were recently replaced by MEMS mirrors which are much faster and more compact [108] as shown in Fig. 2.8. They allow 2D scans, unlike galvanometers and micromotors rotating over 1 dimension only. MEMS scanners directly provide 2D rotational scans without the need for an additional translational motion.

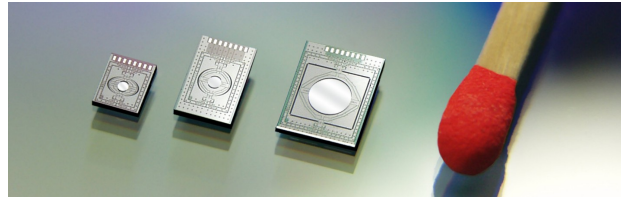


**Figure 2.8:** Different sizes of 2-axis MEMS mirrors fabricated by Fraunhofer Institute for Photonic Microsystems. Image from Fraunhofer IPMS.

### 2.1.5.3 Others

- Lead zirconate titanate (PZT) tubes are used as cantilever actuators to perform 2D beam scanings in spiral patterns. They are more adapted to forward-viewing and require high driving voltages (50 - 140 V) [109–111].
- Spinning disks (or Nipkow disks) initially used in CM also find their applications in OCT, but are relatively bulky and unadapted for miniaturization [112].
- Acousto-optic deflectors [38] are the only fully-rigid beam scanners. They are virtual gratings made from acoustic waves propagating in specific materials, to tune diffracting orders [106]. They enable ultra fast optical scans and can be combined to perform 3D images at up to 30 kHz [113]. Though, they still present a few shortcomings making them inadequate and were never implemented in endOCT [114].
- Other advanced systems include adaptive lenses on the optical path to generate displacements of the focal plane [115–117].

## 2.1.6 Encapsulation type

Among the other concerns that we can have about probes configurations, the encapsulation type is of secondary importance, because it is not directly related to the order of the criteria which have to be determined in the final design of our endoscope. Three types of encapsulation deserve to be presented here: the single-balloon, the double-balloon and the tethered catheters. Stability of the endoscopic probes in the vicinity of inner organs is highly likely to be affected by the disturbances that occur in the body such as the movement of tissue, heart beat, and breathing induced motion. Subsequently, all of these configurations consist of stabilizing the catheter and modify the area of observation. They are exclusively used in side-view configurations.

- Single balloon probes are called so because the optical needle is enclosed at the center of a spacious inflatable pill-shaped capsule of about 1 cm of radius which looks like a balloon. Single-balloons were first adopted in order to reduce this instability in luminal organs as the esophagus [118]. A sketch of a single-balloon probe is given in Fig. 2.9 and an OCT image collected from a scan performed in this configuration is shown in Fig. 2.4i. As the outermost wall of the catheter is formed by the surface of the inflated balloon after insertion in the gastroscope and the lumen, the working distance from the optics is increased. A typical working distance (from the optics) is around 9 to 12 mm. Consequently, the NA is reduced so that the focal length matches the radius of the balloon. Lateral resolution is thus a bit decreased to a typical values ranging between 20  $\mu\text{m}$  and 30  $\mu\text{m}$  [82, 119]. Unlike in thin

proximal probes using pullbacks where the catheter is brought very close to the tissue surface, which drastically narrows down the FOV, balloon-based catheters visualize a relatively large area of interest in the GI tract.

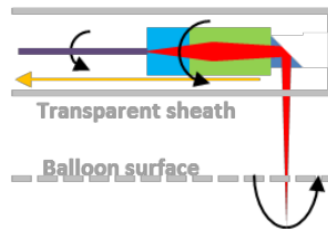


**Figure 2.9:** Simplified schematic view of a single-balloon catheter. From [90].

- Double balloons is an alternative to single-balloon probes in order to tackle the lack of stability of the catheter in lumen where the deformation of the tissue affects directly the quality of the OCT image [120]. As for single balloons, 3D OCT images are obtained by pullback of the inner needle inside the probe's sheath [88]. A schematic example of double-balloon endoscopic probe from Kang *et al.* [120] is shown in Fig. 2.10.

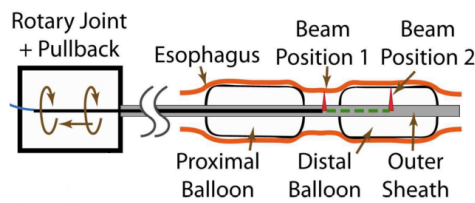


**Figure 2.10:** Schematic view of a double-balloon endoscopic catheter. From [120].

- Balloon-based systems require a sedation of the patient and specific settings to be used *in vivo*. Hence, tethered capsules were invented to tackle this issue. Tethered probes can be inserted into luminal organs by conscious patients without the need for a special predisposition [121, 122]. Tethered probes could be converted into *en face* imaging probes providing 3D images as reported by Liang *et al.* [121].

## 2.2 Comparison and selection of the main features

### 2.2.1 Forward and side view

From the definition of the scan direction criterion, we can as of now eliminate from the possibilities the forward-viewing configuration without investigating the pros and cons more in details. Indeed, even if forward-viewing could be a plausible method for stomach imaging, it is absolutely inappropriate for the luminal shape of the esophagus. Finally, the side-imaging modality will be taken on as the starting point to determine the outcome of the next criterion.

### 2.2.2 Proximal and distal scanning

The main advantages of proximal scanning are the simplicity of the optical design (some designs have gotten rid of *gradient-index* (GRIN) lenses which are hard to fabricate at small scale [123]),

the miniaturization capability, the reduction of spherical aberrations and the absence of distortions resulting from the beam scanning. Li *et al.* [96], Lorensen *et al.* [97] and Yang *et al.* [123] have reported proximal catheter diameters of 900  $\mu\text{m}$ , 310  $\mu\text{m}$  and 410  $\mu\text{m}$  for lateral resolutions around 30  $\mu\text{m}$ . Although, these sizes are revolutionnary, the corresponding working distances of these probes are significantly reduced (because of the subsequent increase of the NA), ranging from 80  $\mu\text{m}$  for the more shallow to  $\sim 350 \mu\text{m}$  for the deepest. On the downside, the bending of the flexible catheter can cause non-uniform rotations and the transmission of the torque through the coupling shaft can be a source of unstability caused by vibrations for optical distal components thus limiting the image quality [96]. Furthermore, the distortion of the fiber affecting the polarization is also a non-negligible factor that motivated the evolution of scanning types towards distal-end scanning. Although, the rotation speeds can reach up to 10,000 rpm (revolutions per minute), which corresponds to 167 B – scan/s of 150 fps depending on the light source [90] it is firstly limited to a few thousand rpm by the vibration of the torque driveshaft at high speed. The parameters of a few representative proximal probes are listed in Table 2.1.

**Table 2.1:** Comparison of features of different imaging endOCT probes.

Reference		Size (m m)	Lateral resolution ( $\mu\text{m}$ )	Working distance (m m)	Angular and lateral scan range	Speed
Proximal actuation						
Tearney <i>et al.</i>	[73]	1.1	38	$\sim 3.0$	$360^\circ$	1 rpm
Li <i>et al.</i>	[96]	0.41	17	0.08	$360^\circ$	-
Quirk <i>et al.</i> , McLaughlin <i>et al.</i>	[71, 124]	0.64	20	0.715 (at 836 nm) and 0.540 (at 1310 nm)	$360^\circ$	2 B – scan/s; $14 \mu\text{m s}^{-1}$ (translative)
Lorensen <i>et al.</i>	[97]	0.31	30	0.3	$360^\circ$	1 B – scan/s
Fu <i>et al.</i>	[82]	1.3	39	9	$360^\circ$	4 fps
Gora <i>et al.</i>	[122]	12.8	30	-	$360^\circ$	20 fps
Yang <i>et al.</i>	[123]	0.9	$\sim 26$	$\sim 0.35$	2.5 m m	-
Yang <i>et al.</i>	[75]	2	-	-	$4 \text{ mm}^2 \times 2 \text{ mm}$	4-16 fps
Distal actuation						
Tran <i>et al.</i>	[91]	2.4	$\sim 13$	2	$36^\circ$	1 Hz
Herz <i>et al.</i>	[92]	5	$\sim 8$	2	$36^\circ$	2 Hz
Su <i>et al.</i>	[93]	2.7	20	-	$360^\circ$	30 fps
Aguirre <i>et al.</i>	[98]	$< 5$	$\sim 12$	several hundred $\mu\text{m}$	$\pm 6^\circ_{\text{mech}}$	$< 2 \text{ min}$ (vol. $1.8 \text{ mm}^3 \times 1.0 \text{ mm}^3 \times 1.3 \text{ mm}^3$ )
Jung <i>et al.</i>	[125]	$< 4$	$\sim 20$	6.6	$\pm 5^\circ_{\text{mech}}$	3 fps (vol. $1.0 \text{ mm}^3 \times 1.0 \text{ mm}^3 \times 1.4 \text{ mm}^3$ )
Xu <i>et al.</i>	[126]	$< 4$	$\sim 20$	3.5	$17^\circ_{\text{mech}}$	21.5 fps (vol. $\sim$ $0.55 \text{ mm}^3 \times 0.55 \text{ mm}^3 \times 1 \text{ mm}^3$ )
Samuelson <i>et al.</i>	[127]	2.8	20	2	$23^\circ_{\text{mech}}$	$1.28 \times 10^6 \text{ voxel/s}$ (vol. $1.6 \text{ mm}^3 \times 1.6 \text{ mm}^3 \times 1.6 \text{ mm}^3$ )
Duan <i>et al.</i>	[128]	2.7	25	3	$20^\circ_{\text{mech}}$	1.25 Hz (fast scan)

A few distal probes are listed in the same table in order to compare the different features. In comparison, one of the assets of distal-scanning is the possibility to control parameters such as the size of the probe (outer diameter), the length of the rigid part of the catheter, the working distance and the lateral resolution. Another advantage is the possibility of deleting binding artefacts

stemming from the proximal translational and rotational actuations and replacing them either by micromotors either by embedded MEMS devices [96]. The scanning high speed of micromotors ( $\sim 240,000$  rpm [88]) and the general low stress induced by the bending of the probe makes it an OCT image distortion-free tradeoff. For instance, Wang *et al.* [129] recently reported a distal-scanning probe performing *in vivo* OCT images at a rate of 4,000 fps using a MHz swept source. Finally, distal-scanning is more prone to perform phase-sensitive and polarization-sensitive OCT because of its increased interference signal stability that can be improved even more making use of common-path endoscopes where the reference and the sample arms are subject to the same distortions (if they are in the fiber) [130] or no distortions if they are monolithically integrated into the catheter [84].

The pros and cons of proximal and distal imaging are summarized in Table 2.2. In conclusion, although proximal probes are smaller and allow more flexibility because of their shorter rigid length, similar area sizes with distal-imaging types can be obtained because the working distance of proximal probes is significantly reduced. Stomach and esophagus EGC detections does not require extremely thin catheters so that probes of a few mm in diameter are still suitable. At last, distal actuation allows to increase the speed of scan, is much more insensitive to stress and environment and can reach very low costs when MEMS micro-scanners are used instead of micromotors.

**Table 2.2:** Summary of the pros and cons of side-imaging and forward-imaging configuration from Gora *et al.* [88].

Scanning type	Proximal	Distal
Minimum probe diameter	$\sim 0.5$ m m	$\sim 1.5$ m m
Minimum rigid length	$\sim 1.0$ cm	$\sim 2.0$ cm
Maximum speed	$\sim 200$ rps	$\sim 4,000$ rps
Imaging area	large	large
Fiber stress-induced distorsion	moderate	smaller
Expense	low	high (with micromotor) low (with MEMS scanner)

### 2.2.3 Scan type

As mentioned earlier, a condition to adopt the distal configuration is the use of a MEMS micro-scanner located in the distal end of the catheter. Microscanners can be 1D or 2D in nature depending on their design. However, as 3D images are required in OCT modalities, a 1D micro-scanner would have to be coupled with a pullback system to achieve such an image. Recently, Sampson developed small side-viewing proximal catheters able to acquire 2D and 3D images using pullbacks [71, 97, 124, 131]. In these designs, a copper mirror mounted at the distal end of a needle rotating at 2 rpm, translates at a speed of  $14 \mu\text{m/s}$  using a stepper motor, rotating always in the same direction to avoid dragging the tissue and to reduce blurring artefacts. Weber *et al.* [54] fabricated and compared a linear and a rotational side-looking probe as shown in Fig. 2.11. In the first design, the scanning mechanism is a brushless DC micromotor with a prism at  $45^\circ$  glued on top of it and provides a  $360^\circ$  1D rotational image. The second design uses a 1D magnetic MEMS micro-scanner mounted at  $45^\circ$  to image a slice of the tissue linearly. Weber *et al.* concluded that the rotational speed (in the first design) limited the acquisition time to 25 rps (leading to a scan time of 1 to 5 min) in TD-OCT whereas in the second design, one image (with equivalent region of interest (ROI)) could be acquired in 500 ms, hence 120 times faster than in rotational at least.

Finally, the pullback mechanism is the limiting factor in terms of speed and thus acquisition time.

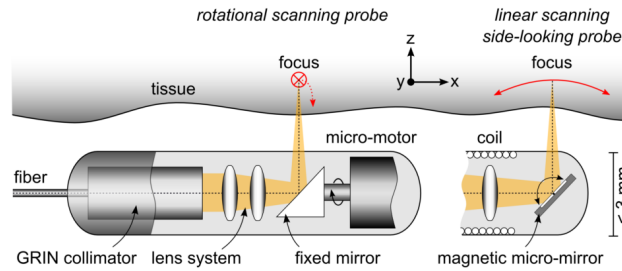


**Figure 2.11:** Endoscopic probe design by Weber *et al.* [54]. Sketch of the circumferential-scanning probe (left) and integrated micro-scanner-driven configuration (right).

One solution is the use of 2D rotational MEMS scanners.

### 2.2.4 Scan patterns

A recap array is given for comparison in Table 2.3. Raster scan is preferred for image reconstruction simplicity because it is based on constant speed and defines naturally a 2D cartesian grid. Nevertheless, a proper raster scan is not always the most appropriate especially because every mechanical system’s dynamics is not necessarily compatible with the sharp reset pattern of sawtooth signals. Unless a Nipkow disk is used to perform a raster scan, which limits drastically the applications as discussed earlier, alternatives are possible with resonant-mode scans such as Lissajous and spiral scans. Most Lissajous scans are performed upon resonance frequencies that optimizes the performance of the MEMS scanners. This method has been widely used as the actuation is very trivial in terms of driving signal. In addition, as the resonance frequencies are the natural frequencies of the system designed as such, most of the time, no feedback close-loop control is necessary, since movements highly repeatable [132]. However, the scanning density of the spiral and Lissajous patterns are also non-uniform. Another issue for these scanning methods is that the fiber tip is driven with frequencies close to the resonance. Any environmental perturbation or impact that contains the frequency components close to the resonance frequency of the fiber while imaging could couple into the motion of the fiber tip and disrupt the scanning pattern and pixel mapping. This is a common problem for raster, spiral, and Lissajous methods because they all drive the fiber at frequencies close to resonance. According to Tsai *et al.*, Lissajous and spiral scans “require very precise mapping of the pixels during the scan.” Initially, spiral methods were developed for forward-viewing probe and are not recommended for side-viewing because of the speed discrepancies between the center and the rim of the scan. Finally, although Lissajous scans are much more convenient methods than raster scans because they simplify the design and reduce the size of probes, they will be preferred for the operational OCT imaging scan.

### 2.2.5 Encapsulation

Balloon imaging is particularly adequate for circumferential imaging in long swaths of large luminal organs such as the human esophagus. However, balloon-based catheters have a few drawbacks: First, single balloons exert a pressure against the walls of the organs that may cause deformation or flattening of the tissue, misrepresenting the factual layer arrangement (*epithelium, mucosa, lamina propria, muscularis propria, ...*). Second, even if double-balloon configuration is an alternative,

**Table 2.3:** Comparison of principal scan patterns and their features.

Scanning mechanism	Advantages	Drawbacks
Circumferential	simple optical design small size no aberration	rotary non-uniformity pullback non-uniformity unstable slow scan
Raster	even speed moderate scanning range uniform	larger probe disturbance sensitive abberations low scanning speed
Spiral	small size simultaneous 2D scan	limited imaging range disturbance sensitive non-uniformity uneven speed
Lissajous	relatively even speed small size simultaneous 2D scan	limited imaging range disturbance sensitive non-uniformity

it still may not be adapted for narrow luminal junctions as the esophagus sphincter as long as the distal balloon could not be stabilized in the stomach. More generally, balloon-based **endOCT** probes may encounter difficulties to center the image inside the balloon and thus have a reduced imaging range even upon stabilization. Furthermore, the long working distance combined with the transparent plastic tube acting as a “negative cylindrical lens” [133] cause the beam to diverge with the curved interface and generates aberrations at the focal plane and astigmatism much more severe than for non-balloon-based designs. This can be overcome, but requires adding corrective optics in the design [119]. Finally, neither balloon, nor tethered probes can be used in the stomach. Our design will be non-balloon-based.

### 2.3 State of the art of distal side-imaging endoscopic OCT probes

After comparing the different configurations of each criteria, one design has finally stood out as the most appropriate to perform **OCT** with an endoscopic probe in the stomach and the esophagus in order to detect **EGC**. Figure 2.12 summarizes the choices made for each criterion of the classification proposed earlier.

This section will consist of a state of the art of the side-viewing probes using distal 2D rotational **MEMS** scanners in order to provide an overview of the framework of the **endOCT** probe intended to be fabricated in this work.

The first side-imaging **endOCT** probe utilizing a **MEMS** micro-scanner was reported in 2007 by Aguirre *et al.* [98] using an electrostatically actuated 2-axis **MEMS** fabricated by Piyawattanametha *et al.* [134] and shown in Fig. 2.13. It enables 3D imaging of sections of 1.8 m m x 1.0 m m x 1.3 m m of **FOV** reaching an axial resolution lower than 5  $\mu\text{m}$  ( $< 4 \mu\text{m}$  measured in tissue) and a lateral resolution of about 12  $\mu\text{m}$ . Its scanning area is a solid angle of  $\pm 6^\circ$  for both axes (mechanical angle) reached at more than 100 V. **OCT** images were acquired at a speed of 2000 A – scan/s allowing to provide 3D images of the volume mentioned in about 2 min.

Other electrostatically actuated **MEMS** scanner-based **endOCT** probes have been reported by



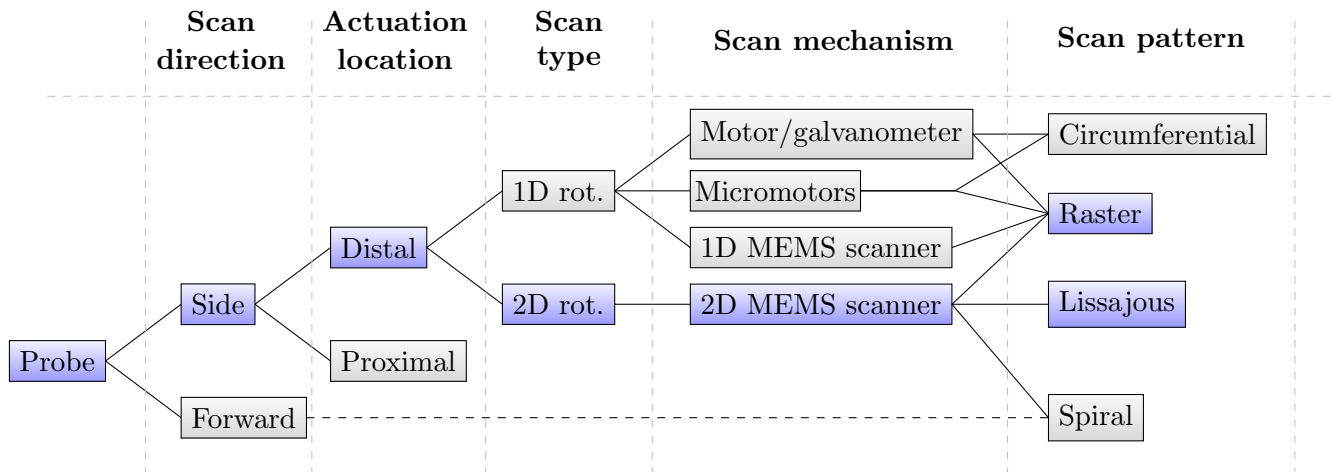


Figure 2.12: Order of criteria of classifications of the endoscopic probes configurations.

Jung *et al.* [125] with similar characteristics. However, the electrostatic actuation voltages are usually over the voltage standards authorized inside the body <sup>1</sup> [135, 136].

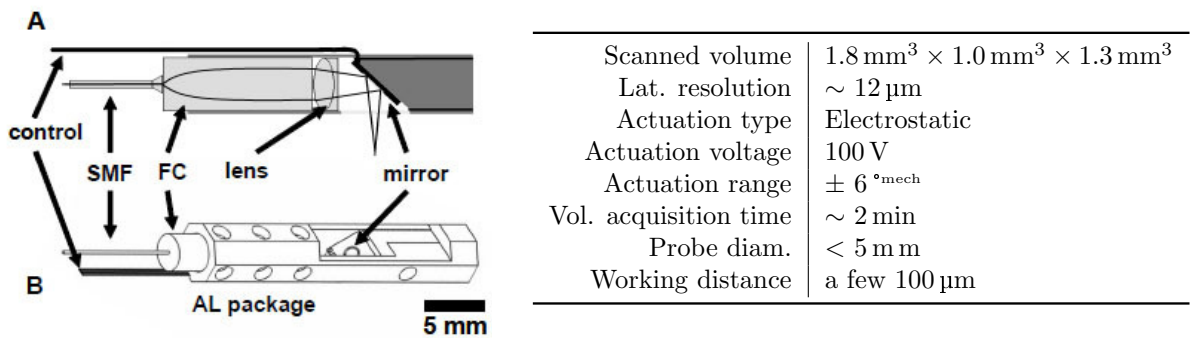


Figure 2.13: Side-imaging MEMS-based probe design; FC: fiber collimator. From Aguirre *et al.* [98].

In the last decade, probe designs have focused on the integration issues mainly due to alignment problems, assembly tediousness, wiring and packaging difficulties. Towards more integration, Xu *et al.* [126] developed a SiOB-based probe allowing large angles at very low voltages as shown in Fig. 2.14.

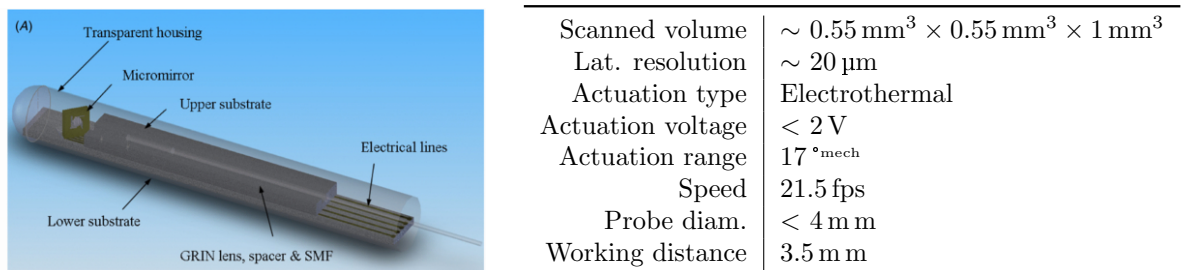


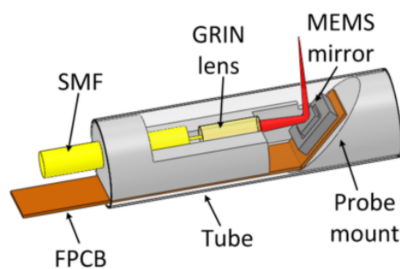
Figure 2.14: SiOB assembled catheter design by Xu *et al.* [126].

Samuelson *et al.* [127] proposed a through-silicon vias (TSV) solution for an even more com-

<sup>1</sup>The human body can be considered as a resistive medium of 70 k $\Omega$  and which can withstand no more than 15 mA for at most 5 s in extreme situations. However, the human body's electric charge flow is safe when it is lower than 1 mA which means that the voltage applied to an electrical apparatus inserted inside the human body should be limited to 70 V. The limit increases with the frequency of the electric signal.

compact packaging. In order to improve the performances of the **endOCT**, diverse **MEMS** micro-scanner actuation techniques have been implemented such as electromagnetic actuation [116, 137], piezoelectric [103, 138] and electrothermal [81, 128, 139–141]. The principle of actuation and a state-of-the-art of the different actuation types will be given in Chapter 3.

The latest novelties in terms of 2D **MEMS** micromirror-based side-viewing probes were reported last year by Duan, Tanguy, Pozzi, and Xie [128] from the University of Florida. We reported an upgrade of the **endOCT** probe developed by Samuelson *et al.* [127] in 2012: a compact micro **OCT** endoscope of 2.7 mm in diameter with a partially integrated **SiOB** providing mechanical support for optical components and oblique positioning at 45° for assembly-free side-imaging. 2 mm x 2 mm **OCT** images were acquired for low voltages (5.5 V on both axes) at a working distance of 3 mm with lateral and axial resolution of 23 μm and 10 μm, respectively. Samuelson *et al.*'s probe first design and Duan *et al.*'s evolution are shown in Figs. 2.15 and 2.16.



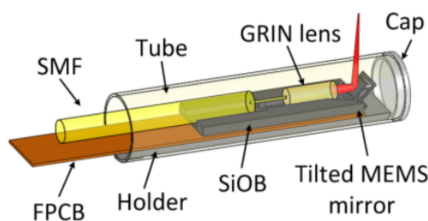
Scanned volume	$1.6 \text{ mm}^3 \times 1.6 \text{ mm}^3 \times 1.6 \text{ mm}^3$
Lat. resolution	20 μm
Actuation type	Electrothermal
Actuation voltage	4.8 V
Actuation range	23 ° <sup>mech</sup>
Speed	$1.28 \times 10^6$ voxel/s
Probe diam.	2.8 mm
Working distance	2 m

Figure 2.15: 3D sketch of Samuelson *et al.*'s probe head. From [127].

## 2.4 Component embedding level of MEMS-based endoscopic OCT systems

### 2.4.1 Review of component embedding evolution

With the emergence of **complementary metal oxide semi-conductor (CMOS)** micromachining and the capability of producing components at the micro scale in general, the potential of miniaturization of **endOCT** systems has significantly soared not only for micro-optical components but also for **MEMS** components. As soon as miniaturization is at stake in any field of area, **MEMS** have a part to play. The concept of **MEMS** was first introduced in the '60s and was called “Micromachines” in Japan before being actually named in 1986 by Jacobsen [142] under the acronym known as such today and officially adopted in 1989. **MEMS** truly started to develop when conventional semiconductor device fabrication techniques – used for electronics so far – began to be adapted to micro



Scanned area	$2.2 \text{ m} \times 2.2 \text{ m}$
Lat. resolution	25 μm
Actuation type	Electrothermal
Actuation voltage	5.5 V
Actuation range	20 ° <sup>mech</sup>
Speed	1.25 Hz (fast scan)
Probe diam.	2.7 mm
Working distance	3 m

Figure 2.16: 3D sketch of Duan *et al.*'s probe head. From [128].

systems, hence called “micromachining”. **MEMS** can be composed of a large range of materials such as semiconductors (silicon), metals, dielectrics, photoresists and polymers, by means of various processes, depositing, stacking up, etching them or modifying their structures in a compatible way. A few processes and materials will be introduced in Chapter 5.

Miniaturizing a system is not only making the endoscopes smaller by getting rid of most relocalizable components; but, the challenge relies in making each constituting parts smaller towards full integration [143]. The main motivations of considering **MEMS** components for integration into **endOCT** probes are stemmed from their micro scale and their competitiveness in terms of performance compared to macro scale opto-mechanical components that enable them to achieve real-time imaging. Galvanometers are more adapted to **exOCT** systems because they are bulky [144]; however, because of wafer-level mass production capability, the cost and size of **MEMS** components is significantly mitigated and they become more interesting than micromotors or galvanometers. Finally, **MEMS** power consumption is generally lower than macro devices. A few different actuation types have been developed according to the characteristics expected for the application sought and will be presented in Chapter 3.

Micro optical components can also be fabricated by surface micromachining technology. In typical fiber-based endoscopes, optical components are used to adjust parameters such as the magnification, the **NA**, the focal length, the aberrations, the lateral resolution, etc. For instance, because of their compact size and cylindrical shape, **GRIN** lenses, are usually used as the front-end imaging lenses and focusing elements. They are glued to the optical fiber at a given distance to define the magnification of the system [88, 89].

Consequently, **MEMS** micro-scanners have become the core of endoscopic probes along with **micro opto-mechanical systems (MOMSs)** and a new challenge emerged: assembly and packaging of these components. Assembly refers to the gathering, the alignment and the fixing of the components of the final system together in a relatively “manual” way whereas packaging assumes a more automated or integrated meaning. According to Wu: “Micromachining technology (...) offers unprecedented capabilities in extending the functionality of optical devices and the miniaturization of optical systems. Movable structures, microactuators, and micro-optical elements can be monolithically integrated on the same substrate using batch processing technologies”. In replacement of the “classic” method of assembly utilizing microtools to align the microcomponents on a microbench (see Section 2.4.2), batch fabrication at the wafer level – as described by Wu – has developed fast with new improving technologies available in surface micromachining. The purpose of the two following subsections is to compare the pros and cons of these two methods of packaging.

### 2.4.2 Optical microbench assembly

In 1995, the same author developed **MEMS** allowing an accurate positioning and “micro optical prealignment” of the optical components [145, 146], this technology of “free-space micro-optical bench” has allowed to build all kinds of micro optical systems such as Michelson interferometers, optical switches, modulators, micromechanical scanners, XYZ micropositioners... One of them is shown in Fig. 2.17a.

Later, his researchs inspired others as Muller [147] who developed micro-optical component able to fold out-of-plane to be utilized in micro optical benches enabling accurate auto alignment and assembly-free integration. Muller reported resonant scanners exhibited in Fig. 2.17c for ap-

plications such as bar-code reader, micro-raster scanning display and scanning diffraction grating spectrometer. Twelve years after Muller, this type of components kept on being developed by Bargiel *et al.* [148] who fabricated microgrippers in order to handle micro-optical components onto a microbench (see Fig. 2.17e) with the possibility of adjusting precisely the distances of the different components on the x- and y-axis.

The same year, Nakada *et al.* [79] reported the first all-optics fiber **endOCT** probe. It uses an electrostatic **MEMS** scanner as a spatial light modulator, a focusing lens and a **GRIN** lens onto an optical bench packaged into a probe of outer diameter of 6 mm.

This design was improved *a posteriori* by Weber *et al.* [149] [54] who proposed an accurate alignment based on auto aligning grooves allowing high modularity in the diversity of micro-optical components including axicons to generate bessel beams to achieve smaller focal spot sizes while maintaining a large depth of focus [150] and is presented in Fig. 2.17b.

Park *et al.* [151] also brought their contribution with a resonant electrostatic **MEMS**-based **SiOB** lens-scanning forward-imaging probe shown in Fig. 2.17d. The lenses are scanning orthogonally in a plane parallel to the *en face* cap of the catheter [152].

Towards more integration, Aljaseem *et al.* [116] proposed a very advanced system enabling dynamic variations of the focal point and a 2-axis scan of the laser beam. It demonstrated a lateral resolution of  $\sim 13 \mu\text{m}$  but still exhibits a few shortcomings that make it not mature enough for use in endoscopy and the assembly is still based on a conventional manual process.

### 2.4.3 Wafer-level batch microfabrication

Wafer-level batch fabrication is performed in a 3D vertical piling up integration as shown in Fig. 2.18. Although, this method has already been a revolution concerning micro-systems integration, it still remains a challenge for most novel processes. Wafer-level batch microfabrication consists of four main steps as sketched in Fig. 2.18. First, (1) wafer processing consists of a series of stages performed on one or several wafers<sup>2</sup> where various processes are used to create patterns and structures that will form the core of the device. Further details will be given in Chapter 5. Second, (2) wafer interconnection, or more commonly called wafer bonding, is the process of aligning together several wafers with different processes on them and connecting them permanently in a specific order and in a compatible way. Then, (3) wafer dicing, is the result of separating and extracting individual devices contained in the wafer stack and taking them apart (from the wafer level to the chip level). Finally, (4) wafer packaging is required to interface the micro systems with their environment. It consists of connecting electrically, confining into a vacuum cell, isolating from a hostile environment, sealing or encapsulating for protection and sterilization for instance. Most of the time, a fabrication step is interlaced with one or more other steps. Therefore, each step has to be designed and fabricated with full knowledge of the others. In the end, the yield of exploitable final devices will be higher or lower – depending on the quality of the design and fabrication of every single step – and a high degree of integration is always appreciated as – if the yield is high enough – it will reduce the cost and the labor. To illustrate the wafer-level batch fabrication, an example is provided in Fig. 2.19. Lullin *et al.* developed recently a micro-scanner for phase shifting interferometry fabricated by a complex batch fabrication process at the wafer level. It is composed

---

<sup>2</sup>A wafer is a substrate made of a semiconductor material and dedicated to the fabrication of microelectronic devices using various processes of surface micromachining.

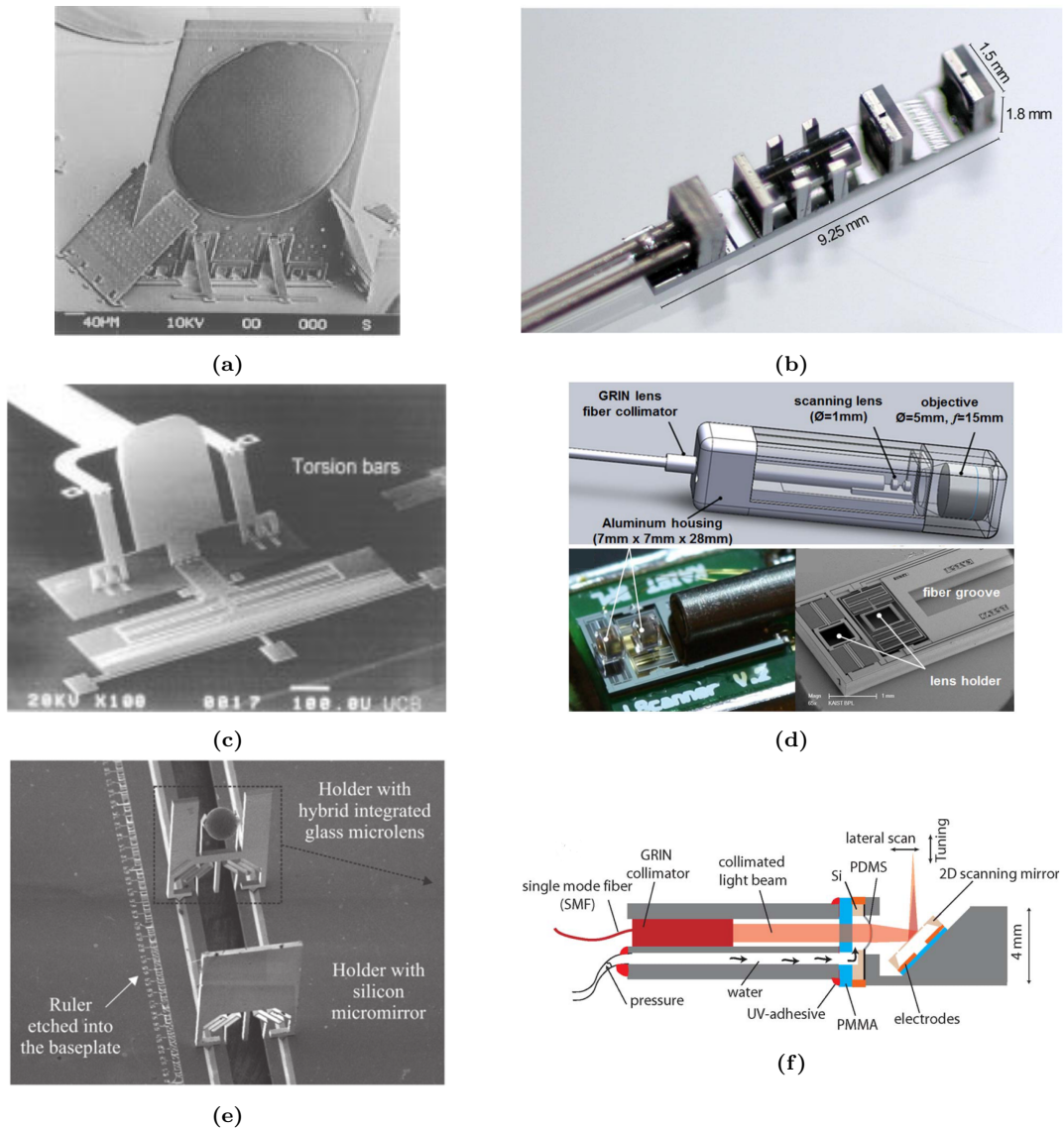


**Figure 2.17:** Comparison of the evolution of component integration level in micro-optical systems. (a): scanning electron microscope (SEM) picture of the front size of a 3D refractive microlens fabricated by Wu [145]. (b): Photograph of Weber *et al.*'s opto-fluidic silicon optical bench with all components integrated [149]. (c): SEM of a  $300 \times 400 \mu\text{m}$  resonant scanning mirror electrostatically actuated with torsion bars, deflecting light in an out-of-plane direction Muller [147]. (d): Schematic of the final probe head of Aljsem *et al.* [116], including the tunable lens and the scanning mirror. (e): SEM micrograph of two micro-optical component holders assembled onto a substrate rail and fabricated by Bargiel *et al.* [148]. (f): Schematic representation of a forward-imaging endOCT probe including a MEMS lens scanner, and details of the electrostatic MEMS lens scanner [151].

of a doublet of microlens matrices, a piston electrostatic microscanner, a beam splitter plate and several spacers piled up at the wafer level for use in exOCT detection [153].

## 2.5 Overview of DEMO4 endoscopic probe & optical specifications

In cooperation with other members of the French national LabEx-Action-financed “DEMO4” project, an endoscopic system is under development and will be the object of demonstration of the current work. The initial idea is based on the work accomplished in the field of endOCT probes bringing together all the aspects brought up earlier in order to improve it. This apparatus would be

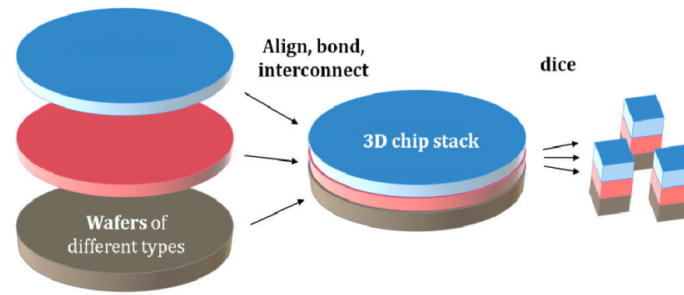


**Figure 2.18:** Process of wafer-level batch microfabrication. Image from [154].

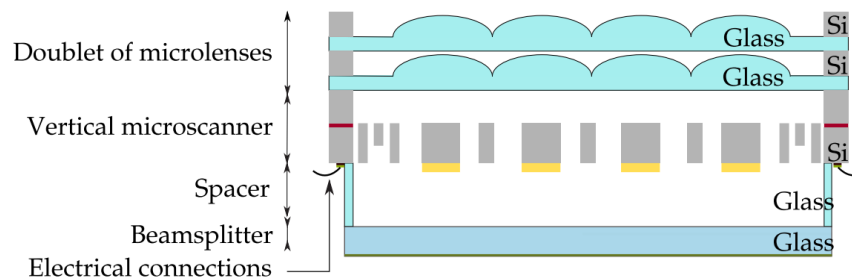


**Figure 2.19:** Sketch of a batch fabricated vertical micro-scanner for phase modulation interferometry at the wafer level. Image from [153].

configured in a side-view probe to cover both stomach and esophagus regions, with a 2-axis MEMS scanner including a monolithic compact interferometer in the tip and enabling a wafer-level batch fabrication suitable for further industrial production at low costs.

As described in [83], the system developed in this work “consists of a pigtailed illumination and detection blocks, connected via a GRIN lens collimator to a MOEMS measurement probe”. The measurement probe is composed of a GRIN lens, a Mirau micro-interferometer and a MEMS scanner. The Mirau micro-interferometer<sup>3</sup> is described in Section 2.5.3 and the MEMS scanner is selected among the main types of actuation in Chapter 3 according to the specifications established in the present section. The integrated probe is introduced into the esophagus via a robotic arm<sup>4</sup> used to reach the proper *in vivo* area under investigation in the stomach or the esophagus and is briefly described in Section 2.5.1.

### 2.5.1 Continuum robotic arm

To reach remote internal areas of the body such as the stomach, and bring probes and observation systems as close as possible to the region under investigation precisely, continuum robots have been widely employed in the medical field [155]. Continuum robots are the backbones of body guided systems in terms of positioning. They are used for laparoscopes, catheters, colonoscopes, and endoscopes in general for detection as well as for treatment.

Chikhaoui *et al.* developed a flexible continuum robotic arm for the endoscopic guidance and positioning of the MOEMS probe into the esophagus and the stomach. It is composed of three

<sup>3</sup>The Mirau micro-interferometer was developed in the dpt. MN2S, Femto-ST, 15B Avenue des Montboucons, 25030, Besançon Cedex, France.

<sup>4</sup>The robotic arm was fabricated in the dpt. Automatique et Systèmes Micro-Mécatroniques (AS2M) of the Institute Femto-ST, 24 rue Alain Savary, 25000 Besançon, France.

concentric flexible tubular telescopic sections whose curvatures are controlled based on **electro-active polymers (EAP)**. **EAP** exhibits quite a few assets making it the most adequate type of actuation for our application: it is light and allows large displacements at very low voltages ( $< 1\text{ V}$ ) without heat dissipation. Finally, **EAP** is biocompatible, provides accurate and fast curvature control and can be implemented on thin diameters ( $< 1\text{ mm}$ ) [156, 157].

The robotic arm is hollow and allows to pull out the electrical cables and optical fiber from the distal Mirau micro-interferometer and the micro-scanner to the external controller and the illumination and detection block so that the overall system is compatibly interconnected with the tip of the continuum robot and confined into the sheath of the arm. It is exclusively used for positioning and adjusting the distance between the probe (at the tip) and the sample to be scanned.

### 2.5.2 Illumination block

The illumination block includes the optical swept source. The wavelength of the source determines the axial resolution of the system and its penetration depth. The penetration depth is a measurement of how deep the light beam can penetrate into the tissue, providing sufficiently intense – typically over 70 dB [158] – backreflection/backscattering to be detected by the photodiode over a noise threshold. It basically depends on the properties of absorbance and scattering of the medium: the **GE** mucosa in our case. Optical properties of light in the stomach tissue were studied by Bashkatov *et al.* [159]. The highest penetration depth in the stomach tissue is obtained around a wavelength of 850 nm. Unlike **TD-OCT**, where the axial resolution is defined by the coherence length of the source, in **FD-OCT**, the axial resolution is inversely proportional to the bandwidth of the spectrum of the sweep and is recalled here:

$$\Delta z = \frac{2 \ln 2}{\pi} \frac{\lambda_0^2}{\Delta \lambda} \quad (2.1)$$

where  $\lambda_0$  is the central wavelength of the source and  $\delta \lambda$  the swept range. Although, swept sources in the range of MHz start to be used for a few applications [129], they still remain rare and out of the standards. Typically, commercialized swept sources reach A-scan rates around a few 100 kHz [48, 80, 144]. The light swept source employed in our project is an ESS-840 from Exalos<sup>©</sup> of central wavelength  $\lambda_0 = 840\text{ nm}$ , swept range  $\Delta \lambda = 60\text{ nm}$  and optical power  $P_s = 8\text{ mW}$  with a sweep rate  $f_0 \approx 110\text{ kHz}$ . The source has a coherence length  $l_c = 4\text{ m}$ . The estimated axial resolution equals  $5.2\text{ }\mu\text{m}$  according to [83]. The light of the swept source is injected into a **SMF** and collimated by a **GRIN** lens towards the Mirau micro-interferometer. An optical circulator working in the range of the central wavelength of the light source is employed to gather the reflected interferometer signals. The Mirau micro-interferometer is described Section 2.5.3.

### 2.5.3 Mirau interferometer

Unlike **USs**, **OCT** uses light to measure the echo time delay generated by successive boundaries or diopters between media with varying optical properties. Unfortunately, the capabilities of electronic detection are well under the requirements needed to detect light delay with a resolution of a few tens of  $\mu\text{m}$  (corresponding to tens of femtoseconds). Therefore, interferometry is used as the measurement method.

### 2.5.3.1 Integration of interferometers in the literature

So far, in Section 2.4, we have presented several systems integrating MEMS and/or MOMS components more or less in a flexible way in order to achieve modularity in diverse optical systems that could be dedicated for endoscopic optical imaging. One combination of optical components that we have not talked about yet is the interferometer. Starting from 1997, with the Mach-Zehnder compact interferometer of Gorecki *et al.* [160], interferometers were continuously miniaturized. The miniaturization of the interferometers and their integration will be discussed in Section 2.5.3.2.

In 2006, Tumlinson *et al.* [84] developed a side-imaging circumferential imaging catheter (which can potentially provide 3D images by retracting the catheter as described earlier) containing a Michelson interferometer integrated in the tip. A 1 mm, 1/3 pitch micro GRIN lens is integrated at the upstream of the interferometer as illustrated in Fig. 2.20. A 80/10 % beamsplitter receives the converging beam from the GRIN lens and the reference mirror has a radius of curvature matching the incident wavefront for a maximal efficiency in the backreflected coupled beam. The beamsplitter is oriented at an angle of 49° in order to avoid spurious backreflections from the exit diopter of the interferometer. The working distance reported is 300 μm with a lateral resolution of 10 μm and an axial resolution of 2.4 μm. Tumlinson *et al.* compared the integrated interferometer-based catheter with a common-path catheter: “An interferometer integrated into the distal tip of the endoscope overcomes some of the most troublesome aspects of ultrahigh axial resolution-OCT endoscopy. This geometry removes the need for a separate adjustable reference arm and therefore reduces system complexity and cost. Reference compensation is not required when a new endoscope is attached to the system, allowing “plug-and-play” utility that facilitates widespread clinical application, without the need for costly tolerances on the length of the endoscope fiber. The dynamically changing dispersion and polarization mismatch between sample and reference reflections introduced by fiber in the difference path of the interferometer is eliminated by design, allowing systems to achieve good, and potentially better and more stable, resolution and sensitivity without dispersion compensating prisms and polarization paddles. The beamsplitters demonstrated in both arrangements are spectrally flat over a much wider range than the fiber beamsplitters that are currently used in traditional Michelson interferometers. The spectral flatness of both configurations is currently limited by the chromatic error in the focusing lens and the extent to which the reference is reflected into the fiber’s spectrally dependant numerical aperture. The cost of placing the beamsplitter in the endoscope tip is [the] inaccessibility after manufacture [161]. Optimization of the reference reflection strength occurs as part of the design process rather than as part of an experimental procedure. This stability improves image quality and may enable phase measurement [162].”



**Figure 2.20:** Schematic of the probe designed by Tumlinson *et al.* [84]. BS: beam splitter; RM: reference mirror; GRIN: gradient index.

Such interferometers are based on a horizontal optical bench assembly and are not adapted for a vertical wafer-level batch integration : all the components would need to be assembled along



an optical bench parallel to the optical axis of the probe. In this configuration, the integration is limited and inherent to a tedious assembly of the components leading to misalignments and other cumbersome complications [84, 163]. In the author’s opinion, this configuration is somehow obsolete today as probes are required to be (1) cheaper, hence (2) monolithically or quasi fully integrated in order to reduce the tediousness of assembly that is often an obstacle to manufacturing, (3) nearly disposable, and finally, (4) more adapted to industrial production. In the following, we will present other configurations of interferometers among the most suitable for batch integration and OCT. From the comparison of the pros and cons of each configuration, we will present the one that was selected for our application in Section 2.5.3.

### 2.5.3.2 Comparison of interferometers

As we discussed in Section 2.4.1, the integration of the interferometer is part of the miniaturization process, and its configuration thereby matters. Three configurations of interferometers are adapted for OCT: Michelson, Linnik and Mirau. The configuration the most adapted to our application of endOCT system was selected based on the highest degree of “integrability” of the interferometers. Figure 2.21 shows a comparison of the three configurations of interferometers.

In the Michelson configuration, represented in Fig. 2.21a, the lens is placed at the beam splitter’s upstream and the reference mirror is located outside of the sample path and is thereby not very adapted for wafer-level optical axis piling up fabrication. Oliva *et al.* [164] reported a vertically-integrated diffraction grating-based Michelson micro-interferometer. Unfortunately, the high degree of complexity of fabrication and the low efficiency of these devices sidelines them *ex officio*. The magnification of Michelson interferometers typically ranges from 1 x to 5 x leading to low NA (because of the BS location) and a wide field of view.

In the Linnik configuration, two lenses are directly placed in the sample and reference arms to achieve an equal optical path and minimize the aberrations. Linnik interferometers provide very high magnifications (up to 200 x) [165], lateral resolutions and large working distances (depending on the objectives used). On the downside, Linniks are sensitive to mechanical and temperature influences and misalignments and even bulkier than the Michelson configuration.

Mirau interferometers consist of two parallel glass-planes at the downstream of the objective lens. It provides intermediate magnifications, between 10 x and 50 x and is the most adapted for potential miniaturizations [166].

Finally, for our application, the Mirau configuration appears to be the best trade-off between Linnik’s high NA and magnification and Michelson’s robustness, exhibiting in the meantime a high level of integrability [83, 167–169].

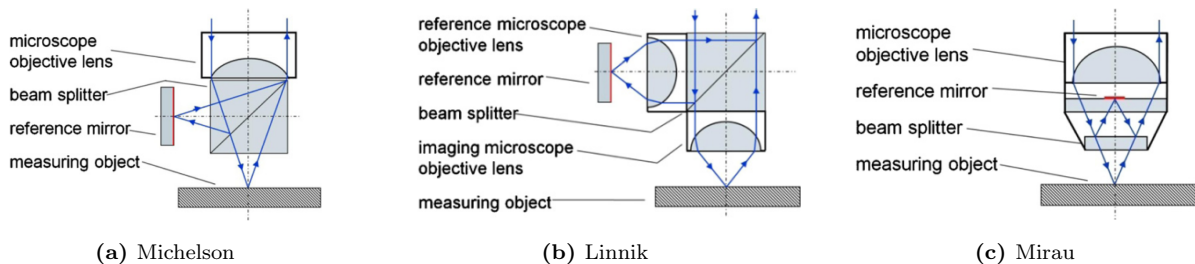


Figure 2.21: Comparison of Michelson, Linnik and Mirau interferometers. Pictures from [166].

### 2.5.3.3 A batch fabricated Mirau micro-interferometer

The interferometer which is intended to be integrated to the micro-scanner developed in this work is a Mirau micro-interferometer fabricated by Struk *et al.* [83] in 2015 in the MOEMS group of the MN2S department of Femto-ST under the project DEMO4, financed by the LabEx Action funding source. Struk *et al.*'s micro-interferometer is illustrated in Fig. 2.22a out of scale. A photograph of the diced Mirau micro-interferometer block is shown in Fig. 2.22b. It is a 5.3 m m-long squared-base parallelepiped of side  $h_{mirau} = 4$  m m. The SMF delivers light to the GRIN lens confined in a

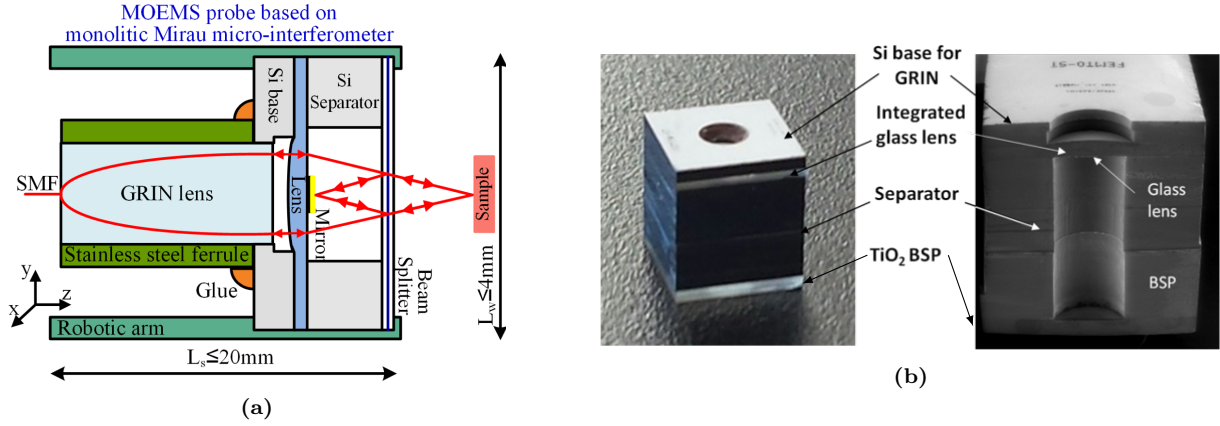


Figure 2.22: Schematic of the Mirau micro-interferometer. Pictures from [83] & Bargiel.

sheath of stainless steel ferrule auto-aligned to the base of the interferometer block and fixed using a Loctite<sup>®</sup> 5056 Silicone Sealant. The collimated outgoing light beam is thus focused by a glass lens of focal length  $f = 10$  m m. This focusing lens has a diameter of  $d_L = 1.9$  m m whereas the

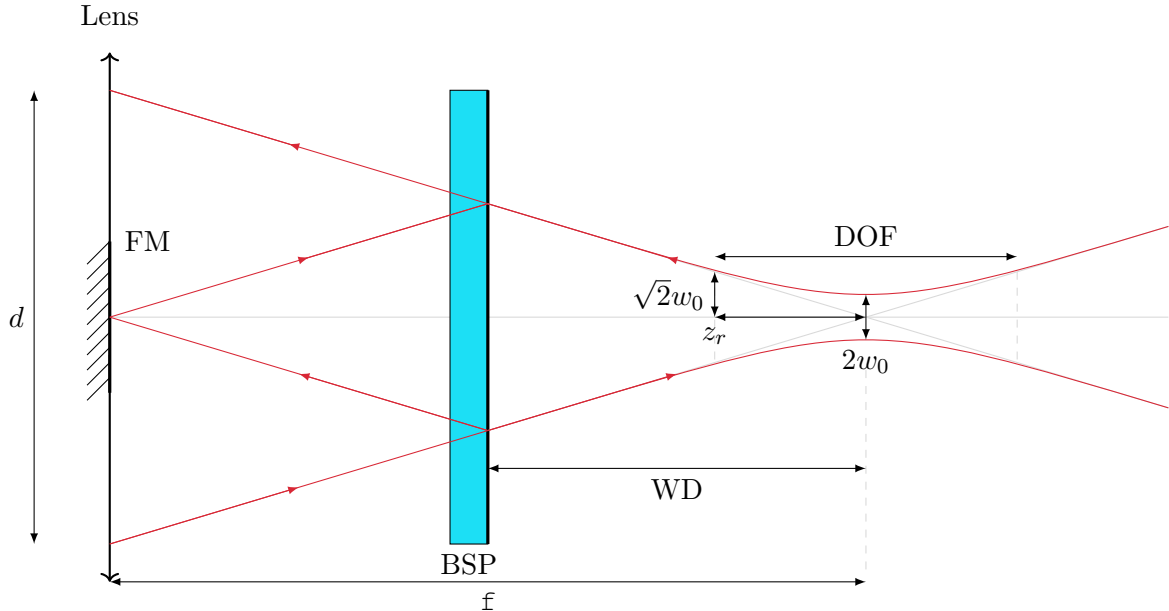


Figure 2.23: Sketch of the MOEMS optical probe with Mirau micro-interferometer from [83] in 1D forward-imaging.

diameter of the incident beam is  $d = 1$  m m. The numerical aperture is a unitless parameters and is approximated in Eq. (2.2).

$$NA = n \sin \theta_d \approx n \frac{d}{2f} = 0.05 \quad (2.2)$$

where  $\theta_d$  is the divergence angle of the gaussian beam and  $n$  the refractive index of the medium. The beam path is splitted by means of a **beam splitter plate (BSP)**, on the one hand, into the sample arm towards the sample, and into the reference arm on the second hand, towards a fixed reference mirror made of Cr/Au on the flat side of the surface of the plano-convex lens. Hence, the **BSP** is located at nearly half the focal length so that the reference mirror is in the focal plane. The backscattered light from the sample interferes with the light from the reference arm and is reinjected into the **SMF** and detected by a single point detector from Thorlabs<sup>©</sup> PDA series. Finally, an acquisition card takes charge of recording the data for further process.

The lateral resolution of the **MOEMS** probe optical system corresponds to the diameter of the spot size in the focal plane. It is given by [158, 170]:

$$\Delta x = 2w_0 = \frac{4\lambda_0 f}{n\pi d} = \frac{2\lambda_0}{\pi \text{NA}} = 10.7 \mu\text{m} \quad (2.3)$$

where  $w_0$ , represented in Fig. 2.23 is called the beam waist. For **OCT**, the waist should always be as small as possible in order to maximize the **SNR** [115]. Although a higher **SNR** yields a better image quality, shrinking the beam waist means diminishing the focal length and thereby the working distance of the probe. Unlike the axial resolution which only depends on the light source, the lateral resolution also depends on the numerical aperture and can be adjusted independently from the axial resolution. Ideally, axial and transverse resolutions are chosen close to each other so that the spatial resolution of the **OCT** image is isotropic.

The working distance is the clearance on the sample arm between the probe and the focal plane. It depends on the focal length and the packaging type. It is necessary to have a penetration depth greater than the working distance of the probe. In the configuration of Fig. 2.22, the working distance is half the focal distance because the **BSP** defines the distal end of the probe. Nevertheless, as seen in Section 2.1 endoscopic probes usually integrate a scanning system which needs an additional encapsulation by a bio compatible plastic material intended to be in direct contact with the tissue. In this case, the working distance is measured from the outermost surface of the capsule. An example of configuration is shown in Fig. 2.24 to facilitate the understanding of the dependency of the working distance with the thickness and position of the capsule.

Another specific issue to take into account is the gaussian property of the swept source inducing a depth-dependent transverse resolution. Indeed, the formula of Eq. (2.3) is only valid over the **depth of field (DOF)**. Otherwise, discrepancies in the lateral resolution may deteriorate the quality of the image and lesions outside of the **DOF** will appear blurer in the **OCT** B-scan. The **DOF** of the focused gaussian beam is the length over which the beam remains nearly collimated according to the Rayleigh criterion and equals twice the Rayleigh distance  $z_r = \frac{\pi w_0^2}{\lambda_0}$ . It is given by [171]:

$$\text{DOF} = \frac{\pi}{2\lambda_0} \Delta x^2 = \frac{2}{\pi} \frac{\lambda_0}{\text{NA}^2} = 213 \mu\text{m} \quad (2.4)$$

and varies with the inverse of the square of the **NA**. A high **DOF** is always appreciated in **OCT** so that the A-scan can cover a sufficiently deep zone without the need to readjust the position of the probe to scan a wider area as soon as the spectral linewidth  $\delta\lambda = l_c$ , of the source is thin (high) enough. However, as shown by Eq. (2.4), increasing the **DOF** also decreases the lateral resolution. Finally, finding the proper parameters for the system is a compromise between the resolution, the depth of field and the working distance. Table 2.4 recalls the dependency between the optical

parameters.

**Table 2.4:** Recap table of the dependency of the optical parameters of the system.

	$\Delta z$	$\Delta x$	DOF	WD
$\lambda_0$ ↗	↗	↗	↗	
$\Delta\lambda$ ↗	↘			
NA ↗		↘	↘	↘
$\Delta x$ ↗		↗	↗	
$f$ ↗		↗	↗	↗

As seen earlier in Chapter 1, preinvasive **GE** lesions that may characterize **EGC** are located between the epithelium and the outermost wall of the muscularis propria (which is located about 1 mm for the esophagus and 2 to 4 mm for stomach). The typical nuclei size of **GE** early stage malignancies is about 10  $\mu\text{m}$  and small **EGC** tumors do not exceed 2 cm in width. A resolution of about 10  $\mu\text{m}$  is usually sufficient to detect malignancies by means of **OCT** [55, 90, 172]. Finally, the lateral resolution is set at 10.7  $\mu\text{m}$  and is lower than the axial resolution by a factor of 2. The **NA** and the **DOF** are calculated at 0.05 and 202  $\mu\text{m}$  respectively although the **SNR** has not been reported in [83]. Let us notice that the **DOF** can be increased using **bessel beams**, by integration of **axicons** for examples as reported by Weber *et al.* [150]. Otherwise, another method consists of degrading slightly the resolution (for a focal length of 15  $\mu\text{m}$ , a **DOF** of  $\sim 480 \mu\text{m}$  can be achieved for a resolution of 16  $\mu\text{m}$ ). Table 2.5 summarizes the main parameters of the optical system which will be used as specifications to build the scanner.

**Table 2.5:** Summary of the parameters and specifications of the optical system.

$\lambda_0$	$\Delta\lambda$	$P_s$	$l_c$	$f_0$	PD <sup>5</sup>	$f$	$d$	$\Delta z$	$\Delta x$ <sup>6</sup>	NA	DOF <sup>7</sup>
840 nm	60 nm	8 m W	4 m m	110 kHz	1.9 m m	10 m m	1 m m	5.2 $\mu\text{m}$	10.7 $\mu\text{m}$	0.05	202 $\mu\text{m}$

## 2.5.4 Optical scanner

The system *statu quo* is a 1D **endOCT** system, which means that the information that can be collected is the interferometric signal generated by the backscattered light along one dimension: the A-scan that stands for “Axial scan” or sometimes “Amplitude scan” in the literature. **OCT** systems currently available on the market are demanded to enable at least 3D scans, *i.e.* to provide real time, 3D images [62]. To broaden the image to two more dimensions, an additional 2D scan is required in two directions orthogonal to the A-scan axis and orthogonal between each other. These two additional types of scan are mechanical in nature and realized by micromotors or micro-scanners as discussed in Section 2.1. The amplitude of the signal determines the brightness of

<sup>5</sup>PD stands for “penetration depth”. For a central wavelength  $\lambda_0$  of 850 nm, Bashkatov *et al.* [159] reported a light penetration depth of about 1.9 m m, a small absorption coefficient of about  $0.8 \text{ cm}^{-1}$  and a high transmittance of 0.48.

<sup>6</sup>Struk *et al.* estimated this value from the formula in the air, *i.e.* for a refractive index of 1. Although Bashkatov *et al.* reported higher refractive indices for scattering tissue and interstitial fluid of 1.45 and 1.36 respectively within the visible spectral range, no information were reported concerning the refractive index of the stomach mucosa for the range of near-**IR**. However, we can expect a refractive index higher than that of the air, thereby decreasing the value of the actual spatial resolution as shown by Eq. (2.3).

<sup>7</sup>DOF refers to the geometrical **DOF**. Struk *et al.* reported a **DOF** of 202  $\mu\text{m}$  unlike the value of 213  $\mu\text{m}$  found in our calculation.

the backreflected spot. Hence, the first out-of-optical-axis-plane scan inherited the suffix B as in “brightness”: B-scan. The term of C-scan is sometimes also used to refer to the third perpendicular scan completing the volumic image [34]. The combination of B-scan and C-scan allows to sweep different types of scan patterns such as raster or Lissajous. The type of scan will define the speed of acquisition of the frames, the size of the area of the sample observed (usually a few hundred of  $\mu\text{m}$  to a few  $\text{m m}$  [99, 173]), the percentage of the covered area, depending on the nature of the scan generated by the B-scan and C-scan waveform. For instance, a raster scan is slower (because run in non-resonant mode) but makes post-processing easier in terms of image reconstruction because the B-scan sawtooth pattern is constant and thus defines *ipso facto* a 2D cartesian grid.

3D real-time imaging is actually limited by the laser sweep rate. Although most swept-source lasers provide a repetition rate that roughly achieves a hundred kHz [132], electrothermal MEMS scanner’s sweep rate are limited to a few kHz [101]. The fastest mechanical scans are made possible under resonant Lissajous scanning mode, along the two complementary orthogonal axes swept at different frequencies. The size of the covered area and the cover rate depend on the scanning frequency of each axis. The resonance frequency can be chosen as the scanning frequency if the bandwidth allows it and if the cross-coupling is sufficiently negligible to form a Lissajous pattern. “Real time” is a concept that was never quite defined in science, however, the term “real time” is commonly used when the number of frames per second reaches the upper limit of differentiation of the human eye which is around 20 Hz. Nonetheless, real-time imaging was reported in the literature at rates close to a few frames per second [132].

The spatial resolution is given by the spot size stemmed from the NA given by the Mirau micro-interferometer (0.05) [83]. A Lissajous scan is intended to be used in the system with a real-time frame rate of  $\geq 5$  fps for a ROI covered at least at 95 % with a minimum of 3 averagings. The area aimed to be observed, ranges at  $\gtrsim 1 \text{ m}^2 \text{ m}$ . To meet these requirements, the scanning frequency of the x-axis is expected around the upper limit of the electrothermal actuation capability ( $\gtrsim 1 \text{ kHz}$ ) and the y-axis frequency will be determined using the system of equations Eq. (2.5) as described in [132] and based on the x-axis frequency. It does not need to be as high as the frequency of the x-axis because it is mainly responsible for the trajectory and the covering percentage rather than for the speed defining the real-time limiting frequency of the scan.

$$\begin{cases} x(t) = x_0 + \frac{A_x}{2} \sin(2\pi f_x t) \\ y(t) = y_0 + \frac{A_y}{2} \sin(2\pi f_y t) \end{cases} \quad (2.5)$$

for a time  $t \in [0, \mathcal{T}]$ , with  $\mathcal{T}$  the total duration for the trajectory to return to its initial position defined by the couple of coordinates  $(x_0, y_0)$ .  $A_x$  and  $A_y$  in  $\mu\text{m}$  determine the scan range, whereas  $f_x$  and  $f_y$ , the axis frequencies define the duration  $\mathcal{T}$ , the shape and hence the cover rate. However, the parameters  $A_x$  and  $A_y$  also depend on the amplitude of the response frequency of the system. The duration of one Lissajous cycle can be calculated by [132]:

$$\mathcal{T} = LCM(\mathcal{T}_x, \mathcal{T}_y) = \frac{LCM(f_x, f_y)}{f_x f_y} \in \mathbb{Q} \quad (2.6)$$

for integer frequencies, with  $LCM$  the least common multiple function and  $\mathcal{T}_x$  and  $\mathcal{T}_y$  the spatial period of the driving signals. Thus, for integer frequencies, we always have  $\mathcal{T} = 1/k$  with  $k \in \mathbb{N}^*$ . To

increase the cover rate, one can choose non-integer frequencies, that may lead to infinite durations, *i.e.*  $\tau \in \mathbb{R}$ . Another method for the calculation of frequencies and durations is given by Eqs. (2.7) and (2.8) [174]:

$$\frac{f_x}{f_y} = \frac{2N}{2N-1} \quad (2.7)$$

with  $N \in \mathbb{N}^*$  used for the ratio control. And then Cai *et al.* demonstrated that the pattern could be chosen by tuning the value of  $N$ . In addition, if  $N$  is chosen large enough, the Lissajous pattern can cover most of the scanned area. The duration  $\tau$  can also be calculated as:

$$\tau = \frac{1}{|f_x - f_y|} = \frac{2N}{f_x} \quad (2.8)$$

with  $f_x > f_y$ . Considering that the horizontal and vertical width of scans are equal ( $A_x = A_y = A$ ), the ratio  $N$  can be related to the target resolution of the Lissajous scan trajectory  $h$  defined by the distance between two nearest points around the origin [174, 175] as in Eq. (2.9):

$$N \approx \left( \frac{\pi A}{\sqrt{2}h} \right) \quad (2.9)$$

Assuming the A-scan rate is 100 kHz, mostly fixed by the swept source features, and that the length (for a line scan) of interest measures 500  $\mu\text{m}$ , considering a single B-scan, the spot size has to stay “idle” during the acquisition time of the A-scan (for 10  $\mu\text{s}$ , on the roundtrip). We define the term of “idle” by an “elementary” displacement of the focal spot  $\Delta\ell$  smaller than the limit of the spatial resolution ( $\sim 10 \mu\text{m}$ ) defined by the Rayleigh criterion to avoid the scan trajectory to be the limiting resolving factor. Hence, the B-scan is required to sweep the resolution length (elementary length) within a time equal or greater than the time needed by the A-scan for the roundtrip. In other terms, the following equation has to be satisfied:

$$\Delta\ell \cdot \underbrace{\frac{1}{2f_x}}_{\tau_x} / A_x > \frac{1}{f_0} \quad (2.10)$$

For the parameters mentioned earlier, the time elapsed between two simultaneous spots spaced of  $\Delta\ell = 10 \mu\text{m}$  equals the time of an A-scan. Thus, a frequency of more than 1 kHz would become the degrading factor of spatial resolution. In conclusion the frequency is a compromise between the speed of scan, the area scanned and the spatial resolution.

Similarly, for an area scanned by a B-scan and C-scan in a Lissajous pattern, Eq. (2.11) has to be satisfied.

$$\Delta\ell^2 \cdot \underbrace{\frac{2N}{f_x}}_{\tau} / A^2 > \frac{1}{f_0} \quad (2.11)$$

Using the same parameters again, Eq. (2.9) gives  $N = 111$  yielding a total duration of scan of  $\tau = 222 \text{ ms}$  for a scanned area  $A^2 = 0.25 \text{ m}^2$  and respective fast and slow-axis frequencies of  $f_x = 1 \text{ kHz}$  and  $f_y = 996 \text{ Hz}$ . In this example, the two frequencies are high and close to each other because  $N$  is an integer. Although it does not need to be an integer to provide a satisfactory cover rate enabling much lower C-scan frequencies. For instance, for an A-scan rate of 90 kHz and a Lissajous scan of frequencies  $f_x = 1.286 \text{ kHz}$  and  $f_y = 205 \text{ Hz}$ , the acquisition time of an area of  $500 \mu\text{m} \times 500 \mu\text{m}$  would take 1 s to be thoroughly completed. In this case, the cover rate is very

high. However, the acquisition time (1 s) is too long to be considered as real time. Fortunately, after a duration of only 45 ms in the same conditions, the scan has covered 99% of an area of  $770 \mu\text{m} \times 270 \mu\text{m}$  corresponding to an imaging frequency of 22 Hz without averaging and yields a elementary scan time of 22  $\mu\text{s}$  without degrading the resolution [176].

The main features and target specifications obtained from the type of scan are finally summarized in Table 2.6.

**Table 2.6:** Summary of the parameters and specifications required for the optical scan.

$\Delta\ell$	$A$	$f_x$	$f_y$	$\tau$	$f_{A\text{-scan}}$
$\sim 10 \mu\text{m}$	$0.2 - 0.25 \text{ m}^2$	$\sim 1 \text{ kHz}$	$\sim 200 \text{ Hz}$	$< 50 \text{ m s}$	$\sim 100 \text{ kHz}$

Figure 2.24 represents in 2D the change in the optical path due to the integration of the micro-scanner at the tip of the MOEMS probe on top of the Mirau micro-interferometer. The position of the mirror plate  $d_M$  and the capsule wall thickness play an important part in the value of the working distance and angle of scan. For her application, Duan [59] reported an encapsulation tube with a wall thickness  $h_{caps} = 150 \mu\text{m}$  that we also adopted for our calculation as a reference. The location of the micro-scanner depends on the size of the mirror  $w_m$ , itself depending on the angle to be scanned  $\theta_p^{opt}$ <sup>8</sup>. The scan angle is a function of the area of interest  $A$  as described earlier and of the working distance. Parameters are interdependent and some assertions have to be made to estimate parameters to start off with. Simulations were run using Matlab<sup>©</sup> to define roughly the size of the mirror, the working distance and the position of the mirror plate  $d_M$ . These parameters are summarized in Table 2.7.

**Table 2.7:** Summary of the specifications for the MOEMS scanner.

$w_m$	$d_M$	WD	$\theta_p^{opt}$
1 m m	1.8 – 2 m m	1.05 m m	$\pm 4.8^\circ$

## 2.6 Conclusion

The direction of observation required in the esophagus in parallel with the increased stability of the endoscopic probe are the main reasons in favor of the side-viewing method, among the two methods reviewed. Distal actuation, coupled with 2D rotation MEMS scanners reveals many notable advantages such as larger working distances, increased scanning speeds, a higher robustness and insensitivity to the environment as well as lower costs. Distal MEMS scanner-based actuation is thus the favorite candidate in terms of miniaturization and integration. The evolution of the level of embedding of components in endoscopic probes for OCT was reviewed and two modern method of integration were compared. From this comparison, the wafer level vertical batch fabrication was taken on for the integration of the MOEMS probe fabricated in the project DEMO4 in Femto-ST. All of the elements contributing to the project were presented briefly or more in details depending on their interaction with the core of this work. The micro-scanner is not an isolated element that can be built separately from the others and merely “plugged and played”. On the contrary, it is strongly dependent on the chain of the other components of the endoscopic system and has to

<sup>8</sup>The optical angle defines the scanned angle range of the light beam and is twice the mechanical of the mirror plate. To distinguish it, it is referred to as  $\theta_p^{opt}$ .

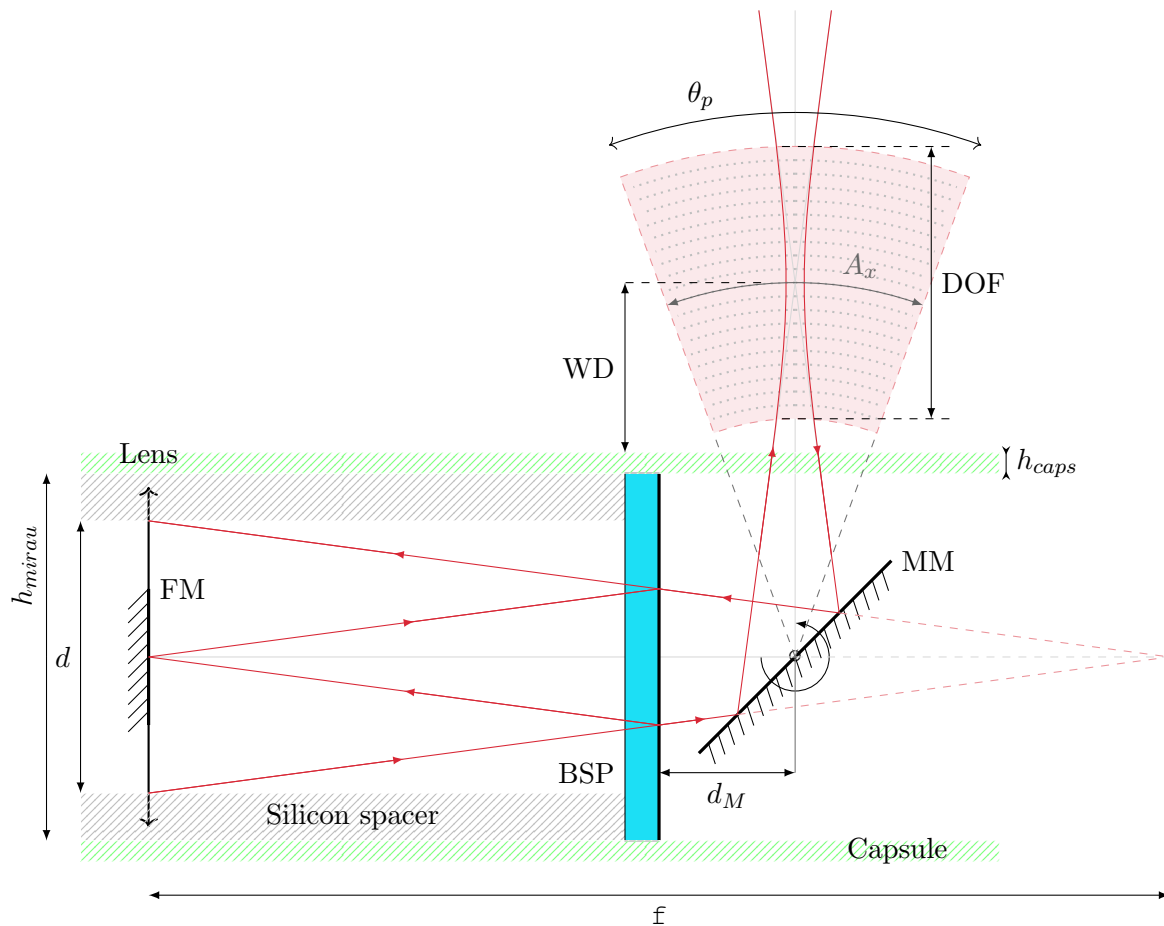


**Figure 2.24:** Sketch of the MOEMS optical probe with Mirau micro-interferometer from [83] in 2D side-imaging with a micro-scanner and encapsulated. FM: Fixed mirror; MM: Moving mirror.

take into account every single other “protagonist” to be properly designed at last. The continuum robotic arm, the Mirau micro-interferometer, and the work already accomplished by former authors of the project is an important milestone which was used to define the specifications that will help to pick up the type of actuation as well as the dimensions of the micro-scanner.

### Chapter summary

The state of the art of endOCT probes classified on the criterion of the scanning mechanism allowed to highlight the advantage of the side-viewing configuration for our application of *in vivo* endoscopic detection of the GI tract. After concluding that a MEMS micro-scanner in distal actuation was the most adapted option, the evolution of the level of embedding of components in endoscopic probes for OCT was reviewed and two “recent” methods of integration were compared. Finally, because of the objective of miniaturization, we opted for a vertical integration-compatible MOEMS micro-scanner as the scanning mechanism. Different technologies will be investigated for the actuators of the micro-scanner in the light of the specifications of the optical architecture established in the last section. This will be done in a brief review of the basic principles of the main existing actuation types in Chapter 3 in order to settle the architecture of the micro-scanner for good.





## Chapter 3

# Review of tilt 2D MOEMS scanners and actuation principles

WE saw in the former chapter that MEMS scanners are widely preferred for OCT endoscopic probe scanning actuation. In fact, MEMS scanners are generally appreciated for a much wider field of applications than bioimaging. As soon as miniaturization is at stake in any field of area, MEMS have a part to play. The MEMS scanner intended to be fabricated in this work belongs to a class of MEMS that merged with micro-optics. This type of micro-devices is called MOEMS. The term of MOEMS was introduced under that name in the '90s. Thus, optical switches, collimators, VCSEL, microbolometers, adjustable microlenses, bistable mirrors, dynamic micromirror displays, laser scanners are all gathered under the name of MOEMS. The aim of this chapter is to bind the real needs in terms of medical expectations for the specific application that is ours, to the technological novelties that need to be developed from the state of the art to meet these demands.

For endOCT of stomach and esophagus cancers, as a conclusion of Section 2.2, suitable MOEMS scanners should be 2D in nature, and more specifically consist of 2 rotations along 2 orthogonal axes to enable B-scan and C-scan. These types of micro-scanner are known in the literature as “tip-tilt”.

### 3.1 Basic principle of the main actuation types

Petersen [177] proposed, about 40 years ago a silicon torsional scanning micro-scale mirror actuated electrostatically and Toshiyoshi and Fujita [178] reported the first 1D MEMS switches 20 years ago, using electrostatic force to flip micromirrors in a binary way around a torsion bar axis. However, there are different ways and mechanisms to actuate micro-scanner. Literature is brimming with plenty of solutions exploited for MEMS scanners... We will present the most common types of actuations: electrostatic, electromagnetic, piezoelectric and electrothermal and will introduce a short review of the cornerstones of corresponding MEMS scanners and their features.

### 3.1.1 Electrostatic actuation

#### 3.1.1.1 Basic principle

Electrostatic actuation generates mechanical motions between two electrodes with opposite charges using the Coulomb force: “the intensity of the electrostatic force between two opposite charges is proportionnal to the product of the two charges and inversely proportionnal to the square of the distance between the two charges. The direction of the force is projected on the axis binding the two charges”. For electrostatic MEMS devices in rotation around a torsion axis, the moving part rotates until the electrostatic torque equals the restoring torque:

$$T_e = \frac{1}{2} \frac{\partial C}{\partial \theta} V^2 \text{ and } T_r = k\theta, \quad (3.1)$$

where  $V$  is the voltage applied between the two electrodes,  $\theta$  the angle of rotation,  $k$  the spring stiffness of the moving mirror and  $C = \frac{\epsilon_0 A}{g}$  the capacitance of the actuator, with  $\epsilon_0$  the permittivity of free space,  $A$  the surface of overlap of the electrodes and  $g$  the gap between them [179]. Two main types of geometries, parallel-plate and comb-drive actuation, are able to provide rotations and are both represented in Fig. 3.1. For parallel-plate actuation, the area of the overlap of the

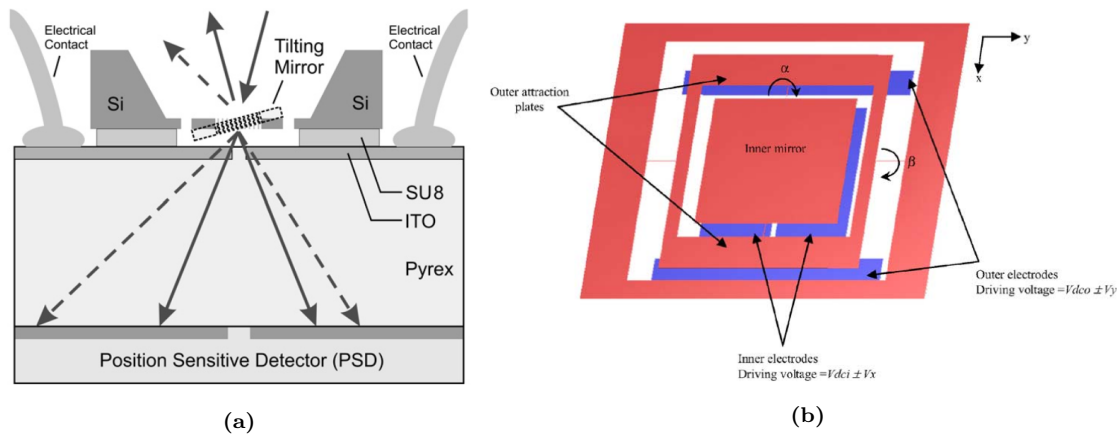


**Figure 3.1:** Schematic of (a) an electrostatic micro-scanner with integrated sensing mechanism (Picture from [180]) and (b) of a 2D scanning micromirror from [181].

electrodes  $A$  that has to be taken into account is the one of the fixed electrode, and the value of the gap  $g$  varies with the angle of rotation of the moving electrode. Hence, in order to generate an angle large enough, there is a tradeoff to figure between the length of the gap and the actuation voltage. Fabrication of parallel-plate actuators require a sacrificial layer that determines the gap value. The voltage is limited by the pull-in effect but is usually high and can be hazardous for endoscopic applications [182]. In comb-drive actuation, the gap between the fixed and the moving electrodes is constant, and smaller than for parallel-plate type (usually a few microns). The direction of the electrostatic force is perpendicular upward or downward to the array of the combs and thus more suitable for the generation of rotational scans. As a result, higher angles can be achieved for lower driving voltages. Comb-drive actuators are easier to fabricate because they are arranged in plane and require barely more than one step of dry etch.

### 3.1.1.2 Pros & cons of Electrostatic tilt MEMS scanners

Parallel-plate paradigm was the first ever to be implemented in MEMS scanners by Petersen [177]. Many more recent micromirrors were reported: electrostatically parallel-plate driven MEMS achieve angles between  $0.5^\circ$  [183] and  $11^\circ$  [184] (excluding IFA) for actuation voltages ranging from 2.7 V [183] to 300 V [180]. They reach high resonance frequencies from a few Hz up to a few tens of kHz [185]. A few surface electrodes micromirrors were employed for OCT applications. They can perform 2D scans and are fabricated by multi-user MEMS process (MUMP) technologies. [181, 186–188] Vertical comb-drive actuators are the most common configuration for rotational micro scanners. Many vertical comb-drive scanners were demonstrated with remarkable features. Typical angles range between a few degrees ( $1.5^\circ$  at 3.8 kHz for 35 V [189]) to a few tens of degrees with total optical angles of  $86^\circ$  at a resonance of 30.8 kHz at 70 V [190]). The highest natural frequencies achieved by comb-drive electrostatic scanners was reported by Hofmann *et al.* [190] at 38 kHz. However, most platforms or mirror plates are too small to be adapted to OCT applications. Bigger plates are also limited by their scanning frequency. Finally, electrostatic devices demonstrated low scanning ranges for reasonable driving voltages or reasonable scanning ranges for high voltages and are thus not the most adequate option for the requirements of our system. As a result, they were also rarely used in OCT.

## 3.1.2 Electromagnetic actuation

### 3.1.2.1 Basic principle

Electromagnetic actuation is based on the generation of a magnetic field generated by an electrical current. Thus, there are two different types of electromagnetic scanning devices represented in Figs. 3.2a and 3.2b respectively: (a) devices whose moving structure is not composed of a magnetic material and that usually have electromagnetic coils integrated onto the moving parts. Their actuation is directly based on the expression of the Lorentz force:

$$d\vec{F}_L = Id\vec{\ell} \wedge \vec{B}, \quad (3.2)$$

where  $\ell$  is the vector length of the conducting coil wire, tangent to the wire aligned with the direction of the conventional current  $I$  in a magnetic field  $\vec{B}$  as implemented in the rotational 1D scanner of Miyajima *et al.* [191]. These scanners are free from hysteresis effects. (b) Current-induced magnetic fields can exert a force onto the moving part of the scanner if it contains a magnetic material (usually nickel or permalloy). This method exhibits hysteresis and requires an additional step of integration of a permanent magnet or coil in the process [192–195].

### 3.1.2.2 Pros & cons of Electromagnetic tilt MEMS scanners

Rotative electromagnetic micro scanners were widely used for optical switching [196], CM [191] and OCT. Kim *et al.* [137] demonstrated an endOCT side-viewing probe based on a 1D electromagnetic scanner achieving optical angles of  $40^\circ$  at low voltages (3 V) and 350 Hz of resonance frequency in both axes. Other similar micro scanners were demonstrated [197–199]. Can-Jun *et al.* reported a bulky optical scanner achieving optical angles of  $\pm 6.8^\circ$  at a resonance frequency of 2.95 kHz. Electromagnetic micro devices are mainly limited by their size, especially devices that must accommodate bulky magnets; and devices that afford miniaturized magnets requires higher currents,

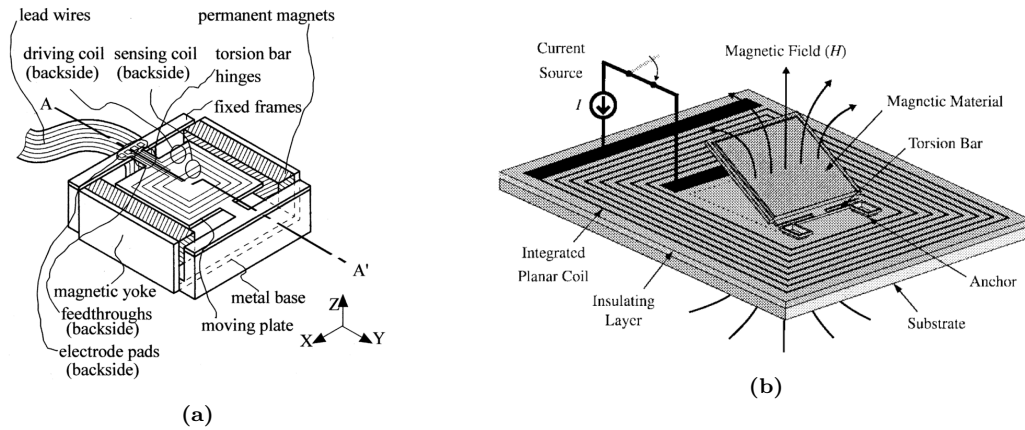


**Figure 3.2:** Principle of electromagnetically actuated micro scanners of type (1) (a) by Miyajima *et al.* [191] and type(2) (b) by Judy and Muller [195].

thus increasing the power consumption. Although commonly used electromagnetic micro-scanners demonstrate attractive features such as low power consumption, inexpensiveness, on the downside, they also suffer from low resonance frequencies, short bandwidths and relatively reduced scanning angle ranges compared to electrothermal micro scanners for instance.

### 3.1.3 Piezoelectric actuation

#### 3.1.3.1 Basic principle

Piezoelectric actuation is based on the deformation of a structure made of a piezoelectric material induced by an electric field across the structure. Piezoelectric material commonly used are the Quartz ( $\text{SiO}_2$ ), lead zirconate titanate (PZT) but also novel materials such as aluminum nitride (AlN) [200, 201]. Piezoelectric actuators can be of two types: multimorph (usually bimorph) or unimorph illustrated in Figs. 3.3a and 3.3b respectively. In the case of bimorph piezoelectric structures, the two elements extend or retract differently when crossed by an electric field and generate a bending of the final structure [202] whereas unimorphs employ passive elements [203, 204]. Reversely, applying a deformation onto the piezoelectric element would induce a stress generating an electric field. This bidirectional property is very appreciated when simultaneous sensing of the structure is required leading to built-in sensor/actuator piezoelectric designs [205, 206]. The behavior of a piezoelectric material is given by the coupled system of matrices described

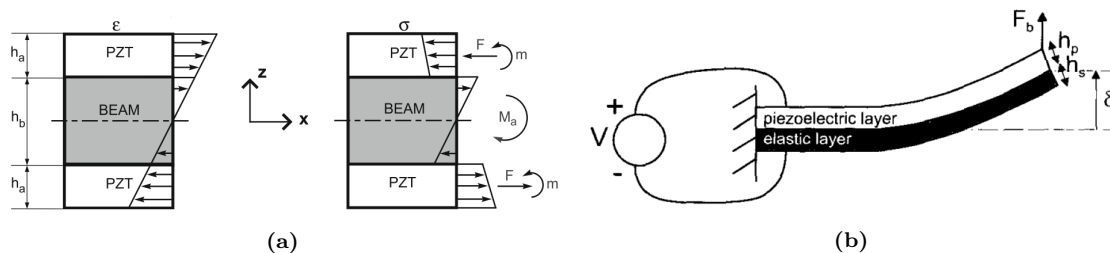


**Figure 3.3:** Sketches of piezoelectric actuators. (a): Multimorph configuration [202]. (b): Unimorph configuration [203].

by Eq. (3.3) in the IEEE Standard on Piezoelectricity [207].

$$\begin{cases} \varepsilon_{ij} = S_{ijkl}^E \sigma_{kl} + d_{kij} E_k \\ D_i = d_{ikl} \sigma_{kl} + \epsilon_{ik}^\sigma E_k \end{cases} \quad (3.3)$$

where  $\varepsilon_{ij}$  is the strain tensor,  $\sigma_{kl}$  the stress tensor,  $s_{ijkl}^E$  the compliance tensor,  $d_{kij}$  piezoelectric constants,  $E_k$  the electric field,  $D_i$  the electric displacement and  $\epsilon_{ik}^\sigma$  the permittivity, with  $(i, j, k, l) \in \{1, 2, 3\}^4$  (1,2,3 being the axes x,y,z).

Finally, the deflection of a piezoelectric unimorphic beam can be formulated as follows (in Eq. (3.4)) as the strain mismatch between two layers:

$$\delta = \frac{CL^2}{h_p(h_p + h_s)} d_{31} V, \quad (3.4)$$

with  $\delta$  the deflection of the beam,  $C$  a constant,  $V$  the voltage applied,  $L$ ,  $h_p$  and  $h_s$  the length of the beam, and the thickness of the piezoelectric layer and of the holding passive layer respectively.  $d_{31}$  is a constant of piezoelectric charge.

### 3.1.3.2 Pros & cons of Piezoelectric tilt MEMS scanners

Piezoelectric technology is very attractive as it provides large displacements and bandwidths within small footprints for low voltages and low power consumption. Also because of his high sensitivity, piezoelectric actuation was widely implemented for endoscopic microscopy. However, it also exhibits a strong hysteresis phenomenon [208] and the fabrication process for thin-film **PZT** requires alignment of the polarization by application of an electric field. Otherwise axis-oriented piezoelectric materials can also be grown onto the substrate but exhibits displacements of much smaller amplitudes. Finally, the solutions etching the patterns are very pollutant.

A few 1D piezoelectric micro-scanners were reported for **OCT** by Gilchrist *et al.* [103], Naono *et al.* [138] and other 2D mirrors were reported with competitive features. A short comparison of four 2D piezoelectric **MEMS** micromirrors is given in Table 3.1.

**Table 3.1:** Comparison of four significant piezoelectric actuator-based 2D micro-scanners.

Reference	Max. angle	Operating voltage	Resonance frequency
Tsaur <i>et al.</i> [209]	24°/26°	15 V	3.750 kHz
Zhu <i>et al.</i> [204]	5°	2 V	316 Hz
Pan <i>et al.</i> [210]	17.9°/2.6°	400 V	6.780 kHz
Liu <i>et al.</i> [211]	4°	5 V	2.4 kHz

## 3.1.4 Electrothermal actuation

### 3.1.4.1 Basic principle

Similarly to piezoelectric actuation, electrothermal actuation results from a strain mismatch between mainly two different materials exhibiting different thermal expansions. There exist three types of thermal actuators known as bent-beam, plane-flexural and bimorph actuators, however, only the latter type will be presented as far as the bent-beam and plane-flexural actuators are not

suitable for 2D MEMS scanners. Unlike piezoelectric materials, every material is subject to thermal expansion. Hence, there are no unimorphs in electrothermal actuation. Temperature change applied throughout the actuator induces a stress in each layer of a bimorph (or multimorph) and deforms the structure bending up or down as shown in Fig. 4.8 of Chapter 4 depending on the piling up order of the material coefficient of thermal expansions (CTEs)  $\alpha$  as figures in Eq. (3.5):

$$\theta = k(E_1, E_2, t_1, t_2)L_b\Delta\alpha\Delta T \propto V^2 \quad (3.5)$$

where  $\Delta\alpha$  the difference of CTE,  $\Delta T$  the temperature rise varying non-linearly with  $V^2$  and  $\theta$  is the tilt angle of the bimorph,  $k$  is a constant depending on the Young's modulus, the Poisson's ratio and the thicknesses of the layers  $t_1$  and  $t_2$  and  $L_A$  the length of the bimorph.

The materials used in electrothermal actuators are chosen in a way so that they are compatible one another and that one has a low CTE whereas the other one has a high CTE to increase the strain and thus the displacement for a given temperature. Materials reported in the fabrication process are reported as Al, SiO<sub>2</sub>, polysilicon, Pt, Ti, Ni, Cu [212]. The temperature is generated by Joule heating using an embedded resistor/heater across the whole bimorph structure to uniformize the temperature distribution [213].

#### 3.1.4.2 Pros & cons of Electrothermal tilt MEMS scanners

Many different designs were demonstrated proposing a variety of shapes configuration, piling, motions, materials [81, 127, 139, 141, 212–224]. Very large piston motions were achieved by the large-vertical-displacement (LVD) and later lateral-shift-free (LSF) configuration first reported by Wu and Xie [214], Jain *et al.* [222]. Later, Todd *et al.* (*rip*) developed tip-tilt-piston (TTP) inverted-series-connected (ISC) actuators to generate high angular displacements. ISC-based micro-scanners were widely adopted for OCT scanning [128, 139]. Electrothermal TTP devices show off up to 64° [141] in rotation and exhibit low driving voltages between 0.6 V and 12 V for 60° at operating frequencies of 104 Hz and 170 Hz respectively [218, 225]. Although, electrothermal actuation is the actuation technique that requires the most photomasks and steps of fabrication, these steps remain relatively realizable in most semi-advanced microfabrication facilities. They achieve very large angles for low voltages within frequency ranges able to provide real time imaging through adapted beam scannings. Apart from high power consumption, their high driving current is not a critical concern for us as far as the safety of the patient under diagnosis depends on the value of the voltage applied on the micro-scanner.

Table 3.2 summarizes the main features of the four actuation types presented in this chapter. A large angular actuation range is required to have the possibility to expand the scanned area. Resonance frequencies in the range of kHz are required and sufficient to perform real time 3D imaging. The maximum voltage is also a critical parameter and finally, as the device is supposed to be mounted onto a Mirau micro-interferometer within the same batch of fabrication (in a monolithic way), the easier the fabrication, the better to avoid any excessively time-consuming task during the bestowed period of the project of design, fabrication and integration. Based on all of these criteria, electrothermal actuation appears to be an opportune choice in our case. Additionally, a complete state of the art is available and electrothermal MEMS have been widely studied for a wide range of applications. Besides, a few of them will be presented in Section 3.2.

**Table 3.2:** Comparative table of the features of the scanners with different types of actuation. Sources from [139, 165].

Actuation principle	Scanning range	Speed	Driving voltage	Power consumption	Fabrication complexity	Linearity control	Comments
Electrostatic	$\pm 10^\circ$	+++	10–100 V	+	+	complex	small displacements
Electromagnetic	$\pm 20^\circ$	+	$\sim 1$ V	++	++	medium	hysteresis, complex assembly, bulky
Piezoelectric	$\pm 15^\circ$	+++	10–100 V	+	+++	simple	hysteresis compatibility issues
Electrothermal	$\pm 30^\circ$	++	1–20 V	+++	++	simple	slow response time

### 3.2 State of the art of MEMS electrothermal tilt scanners

This section will give a non-exhaustive review of the electrothermal MEMS scanners and their structural evolution until today. It will show off their design and features. However, the electro-thermo-mechanical (ETM) principle of actuation will be presented in Chapter 4. The quasi-monopoly of the electrothermal MEMS scanners is detained by Pr. Xie Huikai from the University of Florida that started to develop the first micro-scanner based on electrothermal actuators in 2001 [226]. In the following, we will refer to these devices by the acronym micro-optical electro-thermo-mechanical scanner (MOTEMS). All the publications relating the work of Pr. Xie’s students and collaborators concerning MOTEMS from the beginning until today, have been summarized in Section 3.3 and classified using a color coding according to the successive generations implemented and specified in Table 3.3. However, MOTEMS have been widely developed by other groups as a technology for various applications such as micro display, bioimaging or other medical applications. In 1992,

**Table 3.3:** Color code of the different generations of electrothermal MEMS scanners developed in the Biophotonics & Microsystems Laboratory (BML) group of the university of Florida (UF).

Generation	Type and color coding
First generations	A1 A2 A3 A4 A5 Curved
Second generations	simple ISC double ISC triple ISC
Third generations	LSF
Fourth generations	torsion bar

Buser *et al.* [227] were the first one to report a 2-axis microscanner based on a cantilever beam made of Al/SiO<sub>2</sub> in thin films. They achieved a mechanical angle of about 8° reached for a power of 180 mW. Although, a hysteresis phenomenon is observed over 100 mW. Later in 1995, Buhler *et al.* [228] integrated an embedded heater made of polysilicon into a cantilever beam actuator



composed of Al/SiO<sub>2</sub> as shown in Fig. 3.4. A maximum deflection of 14 μm was reported, which corresponds to a mechanical rotation angle of 4.6° for a very low power consumption of 4.6 mW. In addition, the response time of the device was measured at 2 ms and the driving frequency at 400 Hz. Jiang *et al.* [229] proposed SiC cantilever beams (*sic*) with both Pt and NiCr electrodes

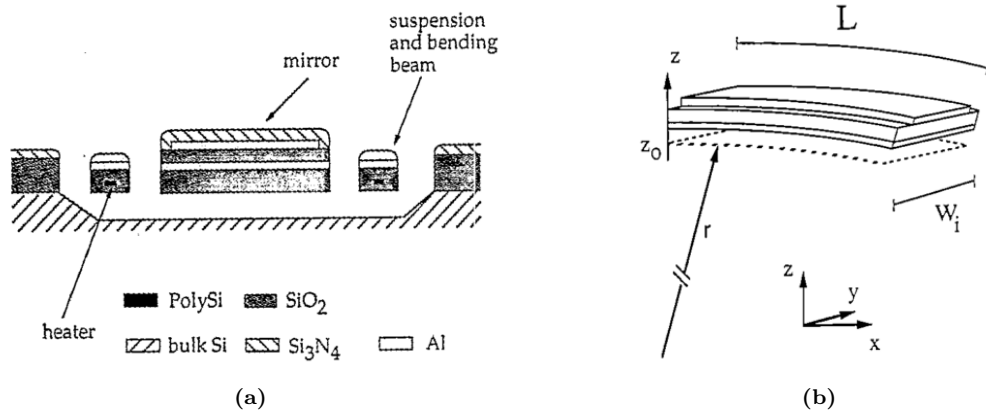


**Figure 3.4:** Schematic of Buhler *et al.*'s electrothermal device. (a): Cross section of the supporting cantilever beam actuators and the mirror plate. (b): 3D view of the configuration of the different layers constituting the cantilever bimorph.

to investigate the impact of these materials on the behavior and the performances of the beam. In 2002, Sinclair [230] proposed a structure actuated electrothermally, conceived to generate a high frequency resonant raster scan achieving a resonance frequency of 8 kHz. Pan *et al.* put in parallel electrothermal Al/SiO<sub>2</sub> bimorph cantilever beams to actuate in rotation a mirror plate used for OCT scanning [99]. Pan *et al.*'s work is the ancestor of the modern electrothermally actuated micro-scanner. They were used for implementation into an endOCT forward-viewing probe and allow  $\pm 15^\circ$  optical scan angle for 495 mW at 33 V and a resonance frequency of the “draw bridge” mode at 165 Hz. The device is represented in Fig. 3.5. The bimorph array is composed of polysilicon resistors and the silicon remaining underneath the actuators creates an overall stress generating buckling [231]. This first version, referred to as generation A has been replaced very early by the generation A2 devices in order to get rid of the buckling issue.

In this second generation, shown in Fig. 3.6, thermal isolation regions were considered between the bimorphs and the substrate and between the bimorph and the mirror plate to increase the temperature in the bimorph array (and hence the angular response) and the thermal response time of the device. When heating up the bimorphs, the mirror plate goes down in a rotational pitch motion. These actuators exhibit lateral shift and tip tilt as drawn in Fig. 3.14, *i.e.* their center of rotation is not fixed. Additionally, the angle of rotation is very large compared to the footprint and leads to complications concerning the packaging.

These designs inspired Jain *et al.* [141, 232] who implemented micro-scanners actuated by two bimorph arrays. Generation A3 exposes a mirror plate actuated by two independent electrothermal arrays *en face* culminating into either controlled 2D angle either a piston motion with lateral shift (see Figs. 3.7 and 3.14). Mechanical rotation angle deflects by 26.5° at 3 V when generated by the outer bimorph array and by -16.5° at 5.5 V when the smaller inner array is actuated alone. The simultaneous actuation of the two arrays enables a piston motion (vertical displacement) [232].

Generation A4 also employs a pair of independent arrays arranged perpendicularly so that a 2D tilt can be generated. The frame axis shows off 25° in rotation at 17 V (135 mW) and 40° at 15 V

(95 mW) for the mirror plate. Higher angles are possible but would increase the stress induced and diminish the life time significantly [141]. **Generation A5** is a fusion of the two former generations reported in 2006 by Jain and Xie [225] and demonstrates large deflections over two axes ( $\pm 30^\circ$ opt at  $12 V_{DC}$ ) and a high vertical displacements (up to  $500 \mu\text{m}$  at  $\sim 15 V_{DC}$ ). In this version, the leverages are even more pronounced than formerly so that this configuration cannot be utilized for a proper scanning for OCT as it also shows a strong thermal coupling between the frames. The consequent mass of the outermost frame limits the natural frequency of the overall device at 170 Hz. Single **ETM** bimorphs were also implemented in micro structures to generate 2-axis rotative movements. Schweizer *et al.* [233, 234] proposed **ETM** structures for microprojectors enabling large angles of  $10^\circ$ opt at 3 mW for one design and a torsional mode resonance frequency at 1.345 kHz and a thermal cut-off frequency at 30 Hz and  $30^\circ$ mech at 1.2 mW at a resonance frequency of 550 Hz. Pal and Xie [235] reported an elliptical micromirror (**generation C**) actuated by a curved **ETM** bimorph able to generate rotations at angles up to  $22^\circ$ opt at  $0.37 V_{DC}$  (9 mW) in three modes of actuations, along the first axis at 3.9 kHz and 8.6 kHz and along the perpendicular axis at 17 kHz. However, the center of the mirror is subject to strong fluctuations although Q-factors are not mentioned in these designs [236].

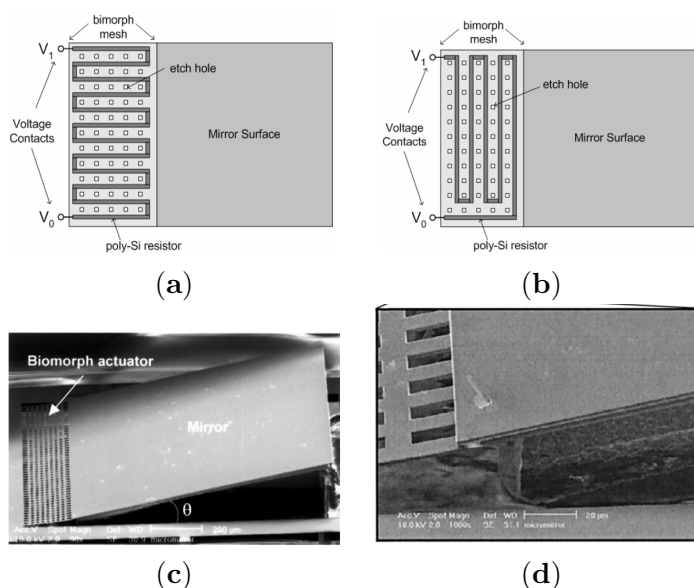


**Figure 3.5:** **Generation A1** of electrothermal micro-scanner fabricated by Pan *et al.*. (a): Top-view schematic design of the first version with longitudinally positioned polysilicon resistor [231]. (b): Second version with transversely oriented polysilicon resistor [231]. (c): SEM picture of the whole structure in its initial bending. (d): SEM close-up view of the electrothermal bimorph array generating the “draw bridge” motion. [99].

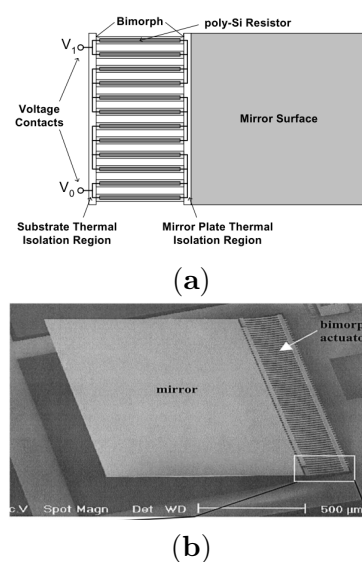


**Figure 3.6:** **Generation A2** first reported by Xie *et al.* [237] in 2003. (a): Top-view schematic of the improved scanner with polysilicon resistors attached in series. (b): SEM overview of the 1D scanner.

To overcome the issues stemmed from the floating center of rotation, Todd *et al.* [219] published an innovating structure composed of four **ISC** actuators in parallel regularly arranged around a mirror plate whose center is thus kept fixed around a rotation axis. The principle of actuation is presented in Fig. 3.14 and the first micromirror fabricated is shown in Fig. 3.10. The generations of **ISC** series were conceived to provide large-angle **TTP** micro-scanners and has undergone many evolutions to improve the performances to correspond to the numerous fields of applications covered by this type of actuation [105, 140, 219–221, 238–244]. The **generation ISC** evolved from

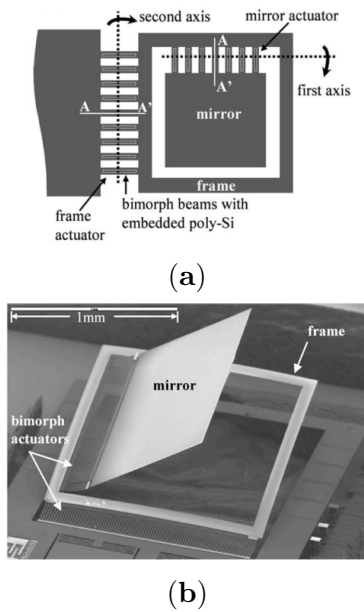


**Figure 3.7:** **Generation A3**; (a): Top view showing areas of rotation. (b): SEM picture of the micro-scanner fabricated. Pictures from Jain *et al.* [141]

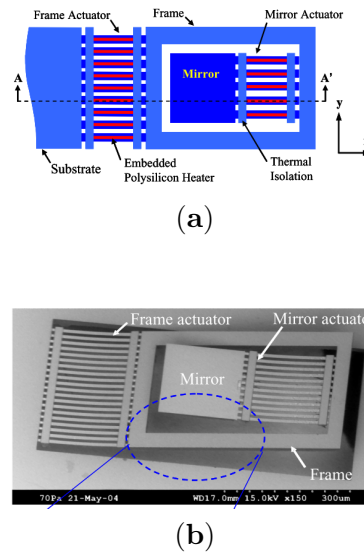


**Figure 3.8:** **Generation A4**; (a): Top view. (b): SEM picture. Pictures from Jain *et al.* [232].

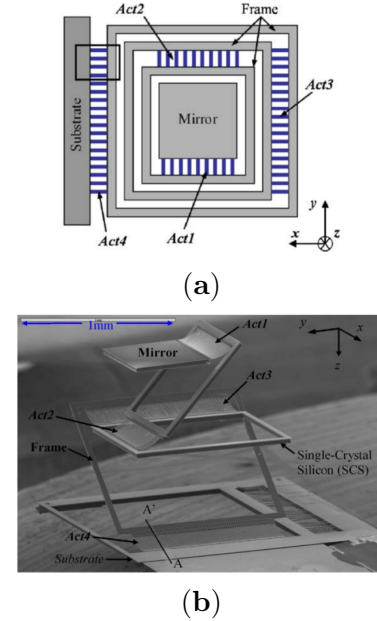


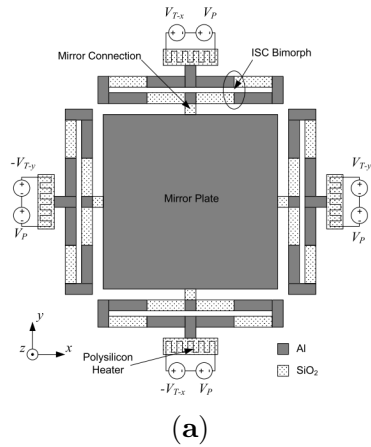
**Figure 3.9:** **Generation A5**; (a): Top view of the micromirror. The four actuators are highlighted. (b): SEM picture. From Jain and Xie [225].

simple ISC actuators to “hidden” ISC micro-scanners to increase the fill factor and eliminate the artefacts due to reflections onto the actuators [127, 163, 245–251]; to double ISC [252–254] and triple ISC [255, 256] in series to increase the vertical and angular displacement. Liu *et al.* reported a simple ISC MOTEMS reaching angles of  $\pm 26^{\circ\text{opt}}$  at 4.5 V and a resonance frequency of 460 Hz. Double and triple series/parallel-connected ISC actuators were implemented to provide higher displacements with an increased resonance frequency compared to single-ISC actuation at 1.1 kHz as reported by Samuelson and Xie [253] and higher than 560 Hz Wang *et al.*’s triple ISC structure [252–254, 256].

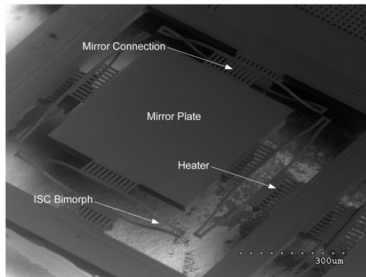
In parallel, a group of research from Singapore published similar 2D TTP MOTEMS using long cantilever beams and incorporated it into an endOCT system successfully [126, 257–261]. A mirror plate of 400  $\mu\text{m}$  in diameter is tilted along two axes by angles of  $17^{\circ\text{mech}}$  at 1.6 V<sub>DC</sub> (23 m W and 90 °C). Nevertheless, the radius of curvature of the mirror surface is significantly low (about 5 mm) and may affect the depth of focus.

Their design inspired Izhar *et al.* [262] in 2011 who developed an alternative ETM micromirror designed for an OCT system. The mirror plate achieves up to  $32^{\circ\text{mech}}$  at 12 m W of input power (70 °C) and demonstrates resonance frequencies over 1 kHz. A better roughness was reported around  $100\text{ nm} \pm 20\text{ nm}$ . And very recently, a similar design was adopted by Lara-Castro *et al.* [263] with reported very low power consumption, achieving tip vertical displacements of 10.3  $\mu\text{m}$  at 2.5 V, corresponding to 6.3 m W and 115 °C.

LSF actuators were created to generate very large displacements, mainly vertically and were thus used for mirrors that required a flat and stable vertical course minimizing the tilt of the mirror plate (see Fig. 3.13) [139, 214, 224, 264–292]. Other designs included curved LSF actuators [215] and electrothermal actuation coupled with electrostatic actuation for a forward-view fiber scanner [293, 294]. The formerly mentioned different types of actuation are all “planar” and require

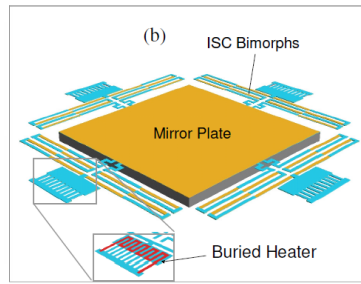


(a)

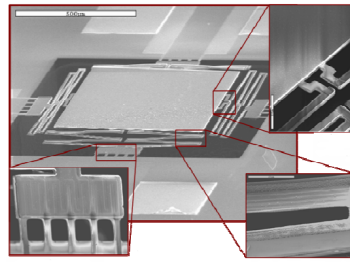


(b)

**Figure 3.10:** Generation ISC; (a): Schematic top view. (b): SEM picture. Pictures from [220].

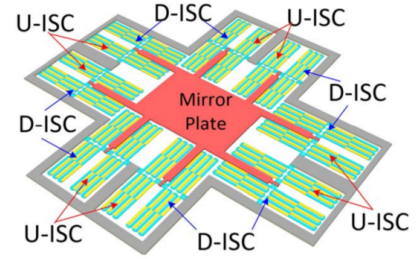


(a)

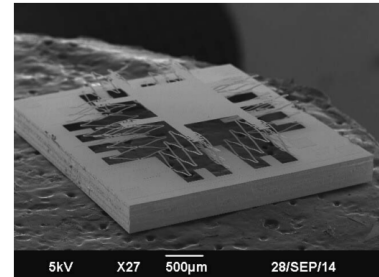


(b)

**Figure 3.11:** Generation DISC; (a): Side-view sketch. (b): SEM picture. Pictures from [252].



(a)



(b)

**Figure 3.12:** Generation TISC; (a): Side-view sketch. (b): SEM picture. Pictures from Xie *et al.* [255], Wang *et al.* [256].

an additional step of integration when used within endoscopic probes for optical imaging. This additional step is the positioning of the scanner at  $45^\circ$  to deflect the laser beam perpendicularly away from the micro-scanner surface as depicted in Figs. 2.15 and 2.17f [59, 141, 176, 238, 242, 250, 257, 289, 295–299]. To overcome this cumbersome aspect, Duan *et al.* broke off the planarity of the former generations and developed a pre-tilted MOTEMS integrating onto a SiOB for a simplified assembly [128, 296, 300].

Among all the generations of actuation presented above, none has a fixed rotation axis. Furthermore, rotating micromirrors also exhibit piston motions as TTP micro-scanners have 3 degrees of freedoms (dofs) for instance. Both tilt and piston motions are rarely needed in a system together, so that one dof is worthless and thus ignored. Unfortunately, the unexploited motion cannot be altogether left out as if it did not exist, because it can take different values or positions without impacting the two others and is an input parameter that must be controlled if one does not want to blindly control the actuation system. Unfortunately, from an observability point of view, and depending on the sensing system, the piston and the tilt motion for example cannot be sensed simultaneously which makes the system only partially observable<sup>1</sup>, unless in some very specific cases the target system also acts as a sensor [292]. A pure vertical piston motion without the least dofs for the tilt, in the author's opinion, is a pipe dream, yet the contrary would be worth considering.

<sup>1</sup>In the sense of state space system observability.

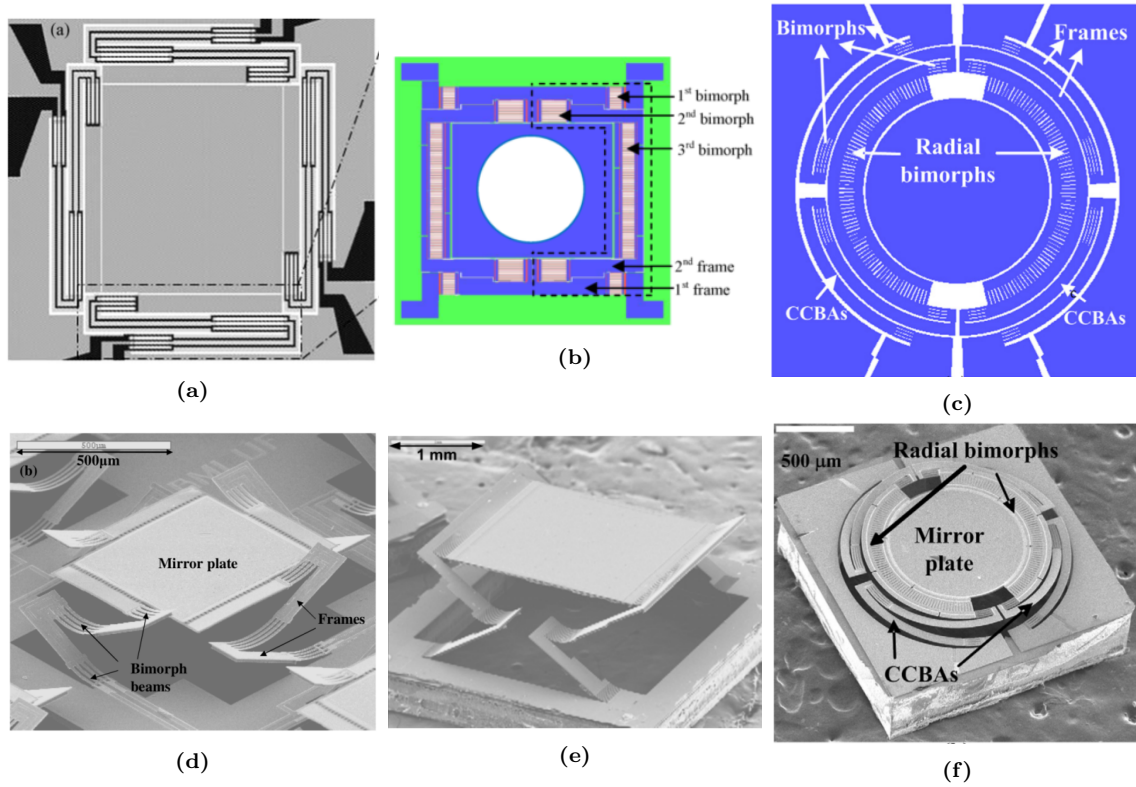


**Figure 3.13:** Generation LSF. (a): Layout top vie of LSF micromirror with actuators on each side. (b): Corresponding SEM picture. (c): Layout top view with actuators on opposite sides only. (d): Corresponding SEM picture. (e): Layout of curved LSF structures. (f): Corresponding SEM view. Pictures from [214, 215, 267, 268, 272].

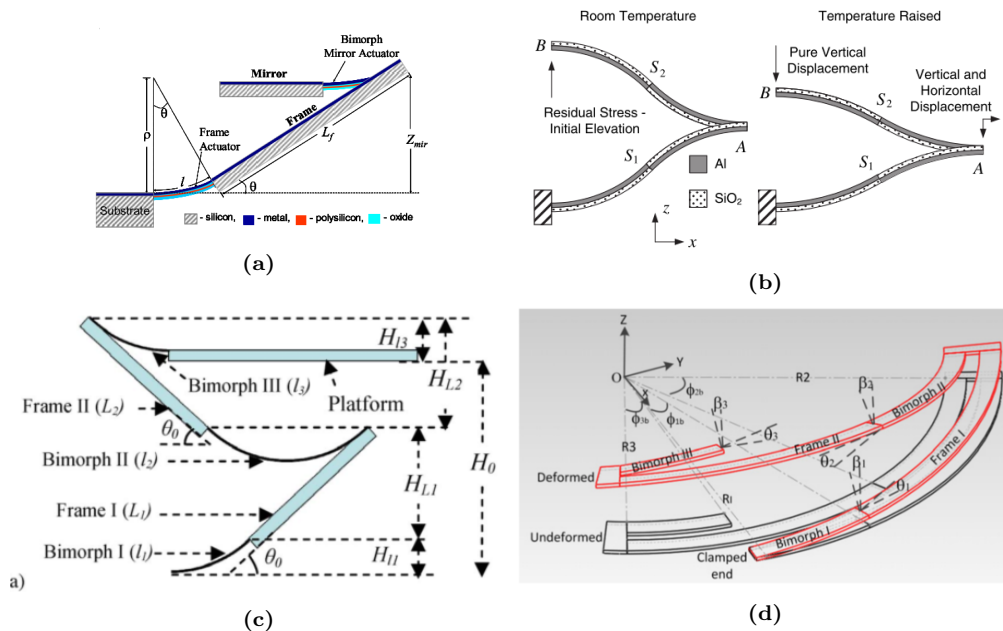


**Figure 3.14:** Schematic principles of actuation of the different generations of electrothermal actuator (ETA). (a): LVD with lateral shift; generation A3. (b): Basic principle of single ISC actuators. (c): LSF LVD actuation sketch. (d): In-plane curved LSF actuators. Pictures from [215, 220, 222, 275].

### 3.3 Conclusion

Among the four main actuation mechanisms presented in this chapter, electromagnetic and electrothermal actuation are in competition in terms of performance sought for an application such as ours. Features that motivated the selection of electrothermal actuation relies in the fact that electromagnetic actuation possessed a few undesired flaws. First, either hysteresis is present in the system response, either systems are bulky and become too cumbersome to be suitable for endoscopic integration whereas electrothermal micro-scanners do not exhibit hysteresis and can be greatly miniaturized. Although, electrothermal actuation is slower than electromagnetic actuation, it still reaches paces compatible with real time imaging [176]. Second, electrothermal actuation is much more linear and can even be used sometimes in open-loop to provide repeatable scans and sufficient quality images [134].

In a few research centers, and especially the BML group of the UF, electrothermal MEMS scanners have been developed for the two last decades to match the need of diverse applications by the design of various shapes of actuators. Four generations of actuators were distinguished denoting an evolution in the motion of actuation, the number of dofs and the general performances in speed and motion amplitude.

Because of the constraints linked to the type of scan required for the endoscopic GI OCT imaging, ISC-based actuators have revealed to be the most relevant shape. However, among all types of structures already existing in the former generations, none matches our needs in terms of dofs.

As a result, an “upgrade” in the design at the structure level needs to be taken into account to meet the new requirements.

#### Chapter summary

In this chapter, a comparison of the four main types of MEMS actuation was presented, and after selecting the electrothermal actuation for its advantages of size, dynamic performances and linearity, the basic principle of electrothermal actuators was introduced. An exhaustive list of the evolution of the electrothermal actuators developed in BML was provided in a state of the art to lay the foundations of a new type of actuators to be developed in the work which will be presented in the next chapter. Next chapter consists of presenting the model and the design of the whole structure of the micro-scanner conceived for integration with the Mirau micro-interferometer at the end.

**Table 3.4:** Exhaustive recap table of the publications concerning MOTEMS (excluding reviews) of the group BML of H. Xie from the University of Florida from 2004 to 2017. [a]: Intertwined ISC actuators; [b]: High fill-factor (HFF) hidden actuators. [c]: Al/W actuators; [d]: Planar degree of freedom; [e]: including sloping mechanical stopper; [f]: Cu/W actuators; [g]: Including vertical mechanical stopper; [h]: In-plane curved actuators; [i]: Hybrid aelectrothermal/electrostatic actuation; †.

Author	Publication years													
	2004	2005	2006	2007	2008	2009	2010	2011	2012	2013	2014	2015	2016	2017
Xie							[245] <sup>a</sup> <sub>b</sub>					[255]		
Pan		[301]												
Jain	[141] [232]	222 [302] 303 [304]	[225] [305]	[306]										
Todd	[307]	[219]	[216] [220]		[213]				†					
Wu			[308]	[309] [265] [266] [310]	[311] [267] [214]	[295] [268] [269] [312] [270] [271]	[272] [273]	[246] <sup>b</sup>						
Jia				[252]		[247] <sup>a</sup> <sub>b</sub> [238] [221]	[248] <sup>a</sup> <sub>b</sub>	[249] <sup>a</sup> <sub>b</sub>						
Pal				[313]	[314]	[315] [217] [316] [319]	[317] [235] <sup>c</sup> [318] [319]	[236] <sup>c</sup> [274] <sup>c</sup> [320] <sup>c</sup> [218] <sup>c</sup>	[321] <sup>d</sup> [322] [323]	[324] <sup>d</sup>				
Sun							[275] [139]		[276] [250] <sup>b</sup>					
Liu							[277]	[278] [325]	[279] [215] <sup>h</sup>	[239] [280]		[281]		
Samuelson									[127] <sup>b</sup>	[326] <sup>d</sup>	[253]			
Duan										[163] <sup>b</sup> [105]	[251] <sup>b</sup>	[296] <sup>e</sup>	[300] <sup>e</sup> [128] <sup>e</sup>	
Zhang										[293] <sup>i</sup>		[282] [240] <sup>f</sup> [283] [224] <sup>f</sup>	[294] <sup>i</sup> [284] [241]	
Wang												[254] <sup>e</sup> [285]	[286] <sup>g</sup> [287] <sup>g</sup> [288] <sup>g</sup>	[256]
Others						[289] [290]				[242] [243]		[244]	[140] [291] [292]	
This work													[327]	[176] [328] <sup>e</sup>

## Chapter 4

# Description and design of the micro-scanner

THE former chapters have contributed to determine the “unknowns” of the system intended to be built up in this work. Specifications were defined in order to design the core of the system and the central element of this work: the micro-scanner. An electrothermal MEMS scanner for full integration into an embedded OCT side-imaging Mirau micro-interferometer-based probe is proposed in this chapter. Although several designs have been realized in this work, only three of them, exhibiting the best performances are thoroughly presented. In a first time, the principle of electrothermal bimorph actuation is introduced. A second section describes the overall design and the model of the structure in its main features. The different types of actuators are studied as systems composed of two main subsystems that are the electro-thermal and the thermo-mechanical systems from static and dynamic approaches. A first batch of fabrication was carried out followed by a second one implementing subsequent modifications worth to be quoted as “improvements” in the design. Although these enhancements came up after the first series of characterization of the first batch of micro-scanner, they were still incorporated in the same section of the present chapter. Finally, all the choices in the design were made in a way so that the micro-scanner can meet the specifications defined in the former chapters. Additional aspects such as CMOS process compatibility as well as packaging and control simplification were also taken into account in the design.

### 4.1 Optical design

The optical design of the micro-scanner is briefly recalled here in its alignment with the Mirau micro-interferometer, although it was already overviewed in Chapter 2 to define the main specifications necessary to build the MEMS scanner. Ideally, the micro-scanner would be monolithically integrated onto the Mirau micro-interferometer block and electrically connected to an external signal generator. Figure 4.1 shows two cross-sectional views: parallel to the optical axis and from the distal end of the probe.

Although, the MOEMS probe is designed to provide OCT images whose sizes range within 1 mm at most, the need for imaging larger biological specimens at high resolution motivated the enlargement of the FOV by the implementation of mosaic techniques. “Mosaicing is the



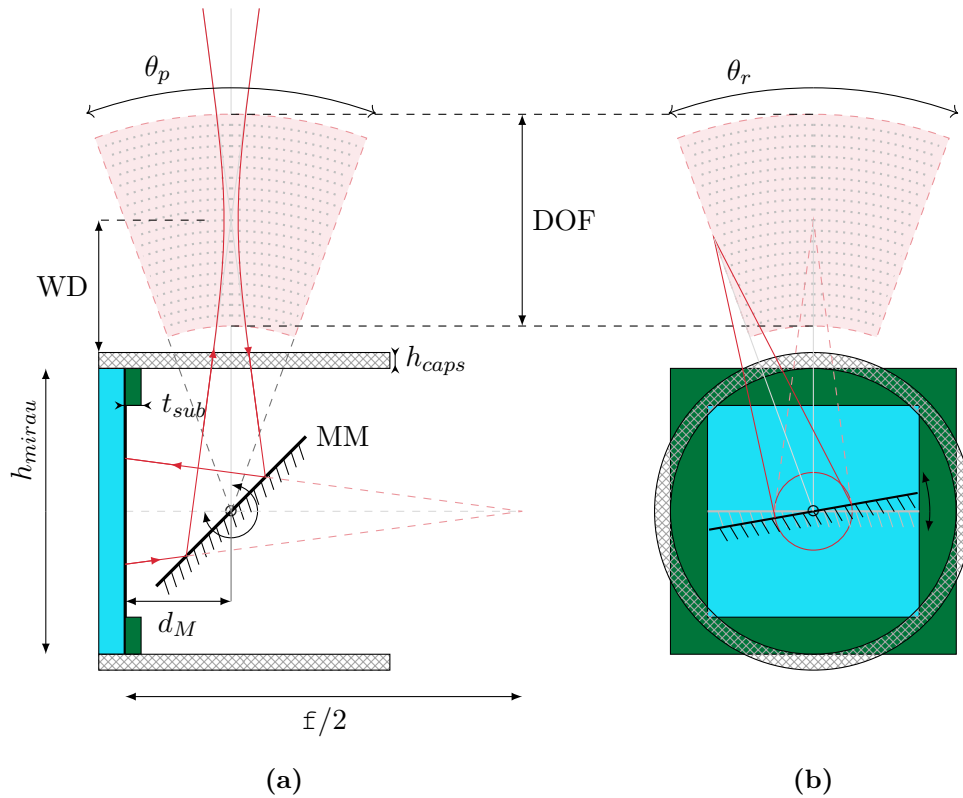


**Figure 4.1:** Schematic views of the optical design of the micro-scanner coupled within the MOEMS probe. (a): Cross-sectional side view of the distal end from the BSP of the MOEMS probe with the mirror corresponding to the (b): *En face* view from the top of the probe.

alignment of multiple images into larger compositions which represent portions of a 3D scene” [329]. Considering elementary images of 1 mm, a mosaic of a series of 16 adjacent images could thus reconstitute a total image area of about 4 mm with about 10% of overlap between each elementary image. The common value of 10 to 15% of overlap is generally used to avoid artefacts [330]. The stitching is more likely to be performed by the robotic continuum arm (part of the whole apparatus) precisely moving the distal MOEMS probe’s head along a tiled pattern. Larger angles provided by the micro-scanner itself can also allow mosaicing for different bias angular positions, but within more limited areas and may induce distortions and a significant intensity drop due to the large angle-related increased scattering of the tissue.

All the dimensions rely on the mirror plate size and location within the MOEMS probe. The center and the size of the mirror plate are defined so that the laser beam remains confined within the reflective area of the mirror plate upon actuation between the highest and the lowest angle of scan. The working distance is related to the distance between the mirror plate and the BSP. Therefore, the thickness of the substrate the micro-scanners were fabricated on, was chosen in the range of 300 to 500  $\mu\text{m}$  ( $t_{sub}$ ). This value refers to the sum of the thicknesses of the silicon-on-insulator (SOI) wafer handle and device layers and will be introduced more in details in Chapter 5. The substrate thickness is represented in green in Fig. 4.1a. This figure shows the micromirror in the theoretical initial position at 45° in a cross-section view around an axis that will be referred to as “pitch axis” in the following, whereas Fig. 4.1b depicts the rotation around the “roll axis”. The rotations of the micromirror around the “pitch” and “roll” axes drive the B and C-scans of the OCT image. In order to avoid anticipating the architecture of the micro-scanner, a realistic view

of the probe – including the **GRIN** lens, the Mirau micro-interferometer and the **MEMS** scanner – in its final version is shown in Fig. 6.19 of Chapter 6.

The thickness of the sheath encapsulating the endoscopic probe has only been taken into account for the estimation of the working distance, however, no design of capsule was brought up in this work. As both the Mirau micro-interferometer and the micromirror have an identical squared footprint of 4 mm side, the capsule may either possess a squared shaped, either be cylindrically circumscribed about the length of the whole probe. If a cylinder is used, then the diameter of the probe will be increased by a factor of  $\sqrt{2}$  from the circumscription of the square base of the Mirau micro-interferometer. In both cases, the capsule would be ending by a cylindrical or spherical cap with a curvature adapted to the shape of the scan.

Finally, a cylindrical shape would bring more astigmatism and aberrations than a cylindrical shape where the beam would always cross the diopters of the capsule perpendicularly. On the downside, remaining perpendicular with respect to the probe capsule may induce artefacts in the **OCT** image due to unwanted backreflections on the diopters. Indeed, in the literature, angles of approximately  $47^\circ$  or  $43^\circ$  are chosen in order to deviate the specular reflexion from the optical axis. When **SMF** and **GRIN** connexions are required, it is crucial to minimize the backreflexion, so that both components are polished with an angle of  $8^\circ$  and a few endoscopic systems adopt this design in the very tip of the optics constituting the catheters [123].

## 4.2 Electrothermal actuation principle

Electrothermal bimorph actuation has been widely studied and optimized during the past decade, in particular by Todd [231] who was the first student from **BML** in Florida to establish a static (steady-state) model of the electrothermal bimorph cantilever beam. Others from the same group brought enhancement to the model especially on a dynamic aspect [217, 317, 331]. We will study in this section the core element of the electrothermal bimorph-based actuators: the bimorph/multimorph cantilever beam in their principle as well as the materials that can be used to fabricate them. An thermal bimorph cantilever beam is a beam composed of two layers of materials with different **CTE** stacked one over another. When the beam is subject to a change in temperature, the two layers expand or shrink differently. As the layers are welded together on their common boundary surface, the strain of both layers on that surface is equal and the one-dimensional displacement of each layer taken separately is converted into a bending motion. A representation is given Fig. 4.2. The angle, lateral shift and tip tilt of the beam depend on the materials **CTE** and on the temperature as described by Eq. (3.5). It can be assumed that the Young's modulus, the thicknesses, the length of the beam and the **CTE** are parameters that do not depend on the temperature and remain constant along the beam at all time. However, the temperature change  $\Delta T$  has a non-uniform distribution along the bimorph beam that must be studied in the first place before deriving any other displacement variables.

### 4.2.1 Electrothermal bimorph actuation principle

Models of bimorph cantilever beams were established using the heat transport equation and lead to simple equations that can easily describe models able to relate the input, which is the electrical voltage applied across the system, and the output which is the temperature change throughout the

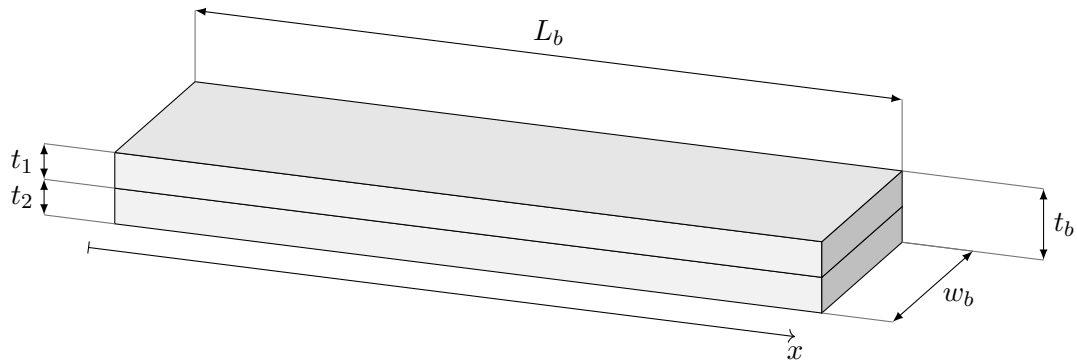


**Figure 4.2:** Schematic view of an electrothermal bimorph cantilever beam in a flat, undeformed shape.

beam. The temperature change is due to the heat dissipation of the resistance by Joule heating and thereby causes the beam to deflect. In former designs, this resistor used to be externally attached to the fixed end of the actuator (on the substrate) [220, 252]. However, recent configurations tended to embed the heater into the bimorph structure leading to a better control of the thermal gradient, and a more uniform distribution of temperature all along the actuator [221]. Other critical parameters will also be extracted from this very model and reinserted into the thermomechanical model. A dynamic model inspired from the work of Pal and Xie will be presented and used to deduce preliminary parameters to design our basic bimorph cantilever. In a second phase, these parameters will be considered at the structure level and rectified by [finite-element model \(FEM\)](#) simulation if necessary.

#### 4.2.1.1 Steady-state model

A complete analytical electrothermal model can be complicated if all the thermal non-linearities are taken into account. Steady-state models, in particular, are appreciated to keep an analytical form so that basic information can be simply deduced, and a range of adequate parameter values can be quickly established. Mathematical parameters that are going to be used for calculation from now on will also be listed in the mathematic nomenclature. As shown in Fig. 4.2,  $L_b$  is the length of the bimorph,  $w_b$  is the width of the section of the bimorph (when the two layers have the same width),  $t_1$  and  $t_2$  denote the thickness of each layer of the top and the bottom respectively. For multimorphs of  $N$  layers,  $t_i$  will represent the thickness of the layer  $i$  for  $i \in [1 : N]$  with  $t_N$  the thickness of the bottommost layer. As the length of the transducer is much larger than its width and thickness, an assertion of one-dimensional propagation is made for the conduction. The temperature distribution  $T(x)$  only varies along the length of the bimorph over the  $x$ -axis. The temperature change is denoted as:

$$\Delta T(x) = T(x) - T_0, \quad (4.1)$$

where  $T_0$  is the temperature at the fixed end of the bimorph (when the bimorph element is studied independently to other elements) or the ambient temperature if the actuator is fixed onto the substrate in ambient air. Assuming, the thermal conductivity of the transducer's material  $\kappa$  remains constant with temperature, it can be approximated by the weighted average<sup>1</sup> of all the thermal conductivities of the materials constituting the composite structure. We consider a heater

<sup>1</sup>Weighted average over the thickness of each layer.

embedded into the bimorph made of a material of electrical resistivity  $\rho_E$ .  $\rho_{E_X}$  will denote the electrical resistivity of the periodic element  $X$  of the table of Mendeleev. The electrical resistivity varies with temperature, and for an abscissa  $x$ , equals:

$$\rho_E(x) = \rho_{E0}(1 + \xi\Delta T(x)), \quad (4.2)$$

with  $\rho_{E0}$  the electrical resistivity at the temperature of the substrate  $T_0$ , and  $\xi$  the **temperature coefficient of electrical resistance (TCR)**.  $R_{TL}$  and  $R_{TR}$  refer to the thermal resistances at the left and right end of the bimorph beam at  $x = 0$  and  $x = L_b$  respectively. In many models established, the radiation has been a neglected parameter [307, 309, 318, 331, 332]. Although some authors claim that radiation is responsible for less than 1% of the total heat loss [333], this determination depends on the estimated value of the convection coefficients, which differ significantly from one author to another as shown in Table 4.2. Indeed, the contribution of the radiation could be higher, and therefore not negligible for high temperatures of the bimorph. Temperature distributions were sometimes measured using thermal cameras detecting radiative **IR** waves [141, 322]. In our case, the bimorph actuators reach temperatures up to  $\sim 400$  °C [240]. The steady-state heat transport equation in 1D is given by Eq. (4.3) [216, 262] including the conduction throughout the transducer and the convection on the surface.

$$\frac{d^2T(x)}{dx^2} - \frac{\overbrace{2(w_b + t_b)}^{\text{perimeter}}}{\underbrace{w_b t_b}_{\text{surface } S}} \frac{h}{\kappa} \Delta T(x) = -\frac{P_E(x)}{S\kappa L_b} = -\frac{q_e(x)}{\kappa} \quad (4.3)$$

$P_E$  is the applied electric power and  $q_e$  the power density generated by the electrical resistor and will be detailed lower. However, the radiation was neglected by the authors, we prefer to consider that the coefficient of radiation can be included in the coefficient of convection  $h$ . Indeed, although the term of radiation is proportional to  $(T^4 - T_0^4)$ , it can be consolidated with  $h$  around a working point.

Todd and Xie [216] suggested three models to describe the electrothermal behavior of a bimorph cantilever actuator with different arbitrary thermal resistances in its ends. Comparing the three models led to the conclusion that assuming a simple model where the electrical resistance generates a uniform power density in the transducer, ignoring the convection coefficient ( $h=0$ ) could be satisfactory enough to describe the steady-state electrothermal behavior of the bimorph and determine preliminary parameters for the transducer. Using these assertions, it was shown that “the average temperature change v.s. the applied power and v.s. the applied voltage relationships (...) always agree with the more accurate model within factors of  $12/\pi^2$  and  $2\sqrt{3}/\pi$  respectively”, and “the balancing factor (...) can be used to calculate the relative position of maximum temperature and matches the thermal imaging data within 3%” [216].

Solving Eq. (4.3), and applying the same boundary conditions as in [216] leads to the temperature distribution along the electrothermal transducer as shown in Eq. (4.4) [231]:

$$\Delta T(x) = P_E \left[ R_{TA}^{\rightarrow} \left( -\frac{x^2}{2L_b^2} + f \frac{x}{L_b} \right) + f R_{TL} \right], \quad (4.4)$$

where  $R_{TA}^{\rightleftharpoons}$ <sup>2</sup> is the thermal resistance of the beam due to conduction, and  $f$  is called the “balancing factor” and is a unitless variable such that  $f \in [0, 1]$ .

$$R_{TA}^{\rightleftharpoons} = \frac{L_b}{\kappa S} \text{ and } f = \frac{R_{TA}^{\rightleftharpoons}/2 + R_{TR}}{R_{TL} + R_{TA}^{\rightleftharpoons} + R_{TR}}, \quad (4.5)$$

The boundary resistors have been purposely chosen arbitrary in order to match any value of resistance due to conduction and/or convection depending on the location of the transducer in the final structure of the micro-scanner. In the first generation of micro-scanners, the mirror plate was connected to a substrate via an array of electrothermal bimorph cantilever beams arranged in parallel generating bending [99, 213, 216, 217, 295, 307–309, 311, 313–319, 323]. Hence, the resistance seen on the left is connected to a substrate at the stable ambient temperature  $T_0$  and the mirror plate on the other side in series with the thermal isolation bridge constitute the thermal resistor seen on the right of the transducer. The thermal insulation resistance between the bimorph transducer and the substrate ( $R_{TL}$ ) increases the bimorph temperature upon actuation by “holding in” the temperature on the upstream of the cold end of the system and leads to a larger static displacement. The isolation bridge between the mirror plate and the bimorph ( $R_{TR}$ ) limits the heat flow from the heating source to the suspended mirror plate and thus improves the transient response of the mirror to an applied power. In practice, we will arrange  $R_{TR} > R_{TL}$ .  $R_{TA}^{\rightleftharpoons}$  has a role on the position of maximum temperature along the bimorph transducer. When  $R_{TA}^{\rightleftharpoons}$  is large, the maximum temperature abscissa moves towards the center of the bimorph. The balancing factor defines the power flow towards each side of the transducer and subsequently the maximum temperature point [231]. Figure 4.3 shows the normalized temperature distribution along a bimorph beam for a given applied power versus the length of the transducer for different balancing factors.

The position of the maximum temperature readily leads to:

$$\hat{x} = fL_b \quad (4.6)$$

and the maximum temperature change is given by:

$$\Delta\hat{T} = \Delta T(\hat{x}) = P_E(f^2 R_{TA}^{\rightleftharpoons}/2 + fR_{TL}), \quad (4.7)$$

from where is deduced the average temperature across the transducer:

$$\Delta\bar{T} = \frac{1}{L_b} \int_0^L \Delta T(x) dx = P_E \underbrace{\left[ \left( f - \frac{1}{3} \right) \frac{R_{TA}^{\rightleftharpoons}}{2} + fR_{TL} \right]}_{\bar{R}_T} \quad (4.8)$$

As the total power is linear with the temperature change, we can define an equivalent average thermal resistance  $\bar{R}_T$  for the transducer’s system as defined above in Eq. (4.8) and derive the expression of the total power versus the current  $I$  across the transducer and the applied voltage  $V$  in Eqs. (4.11a) and (4.11b). It is also interesting to notice that the average temperature is a linear

<sup>2</sup>In the formalism chosen by the author for the sake of clarity, the thermal resistances topped by a double arrow  $\rightleftharpoons$  are due to conduction, the ones topped by a snaky single arrow  $\rightsquigarrow$  are due to convection, and the resistances untopped are likely to be due to both conduction and convection.

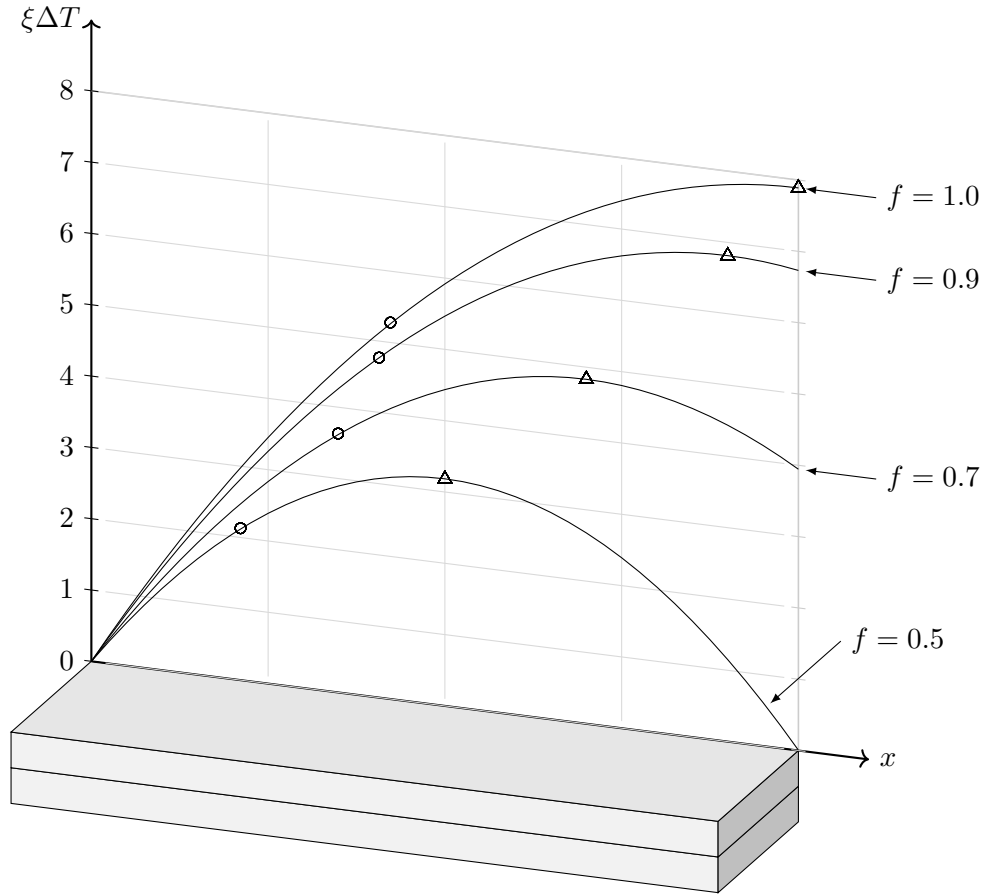


**Figure 4.3:** Normalized temperature distribution along a bimorph transducer for a given applied power and  $R_{TL} > R_{TR}$  and arbitrary value of resistance and power. Points of maximum temperature are depicted by triangles  $\Delta$  whereas the average are located on their corresponding balancing factor curve and symbolized by circles  $\circ$ .

function of the power applied. A **lumped-element model (LEM)** is a good way of representing the thermal behavior of the transducer and has been widely adopted for models in the literature [232, 307]. A **LEM** of the transducer with arbitrary thermal resistance on the left and right boundaries of the transducer with  $R_{TL} < R_{TR}$  is given in Fig. 4.4 and includes the maximum temperature and its location node, the average temperature and its node, and the virtual thermal resistances within the transducer.

The electrical domain is also represented and described simply in Eq. (4.9). The electrical resistance varies with the average temperature change in the transducer.

$$R_E = \frac{\rho_{E0}}{S} \int_0^{L_b} (1 + \xi \Delta T(x)) dx = R_{E0}(1 + \xi \Delta \bar{T}) \quad (4.9)$$

The total electrical power can be derived from Eq. (4.9) and also varies with the average temperature of the bimorphs and is given by Eq. (4.10).

$$P_E = \frac{V^2}{R_E} \quad (4.10)$$

The total power can be extracted from the inspection of the **LEM** and can be expressed with

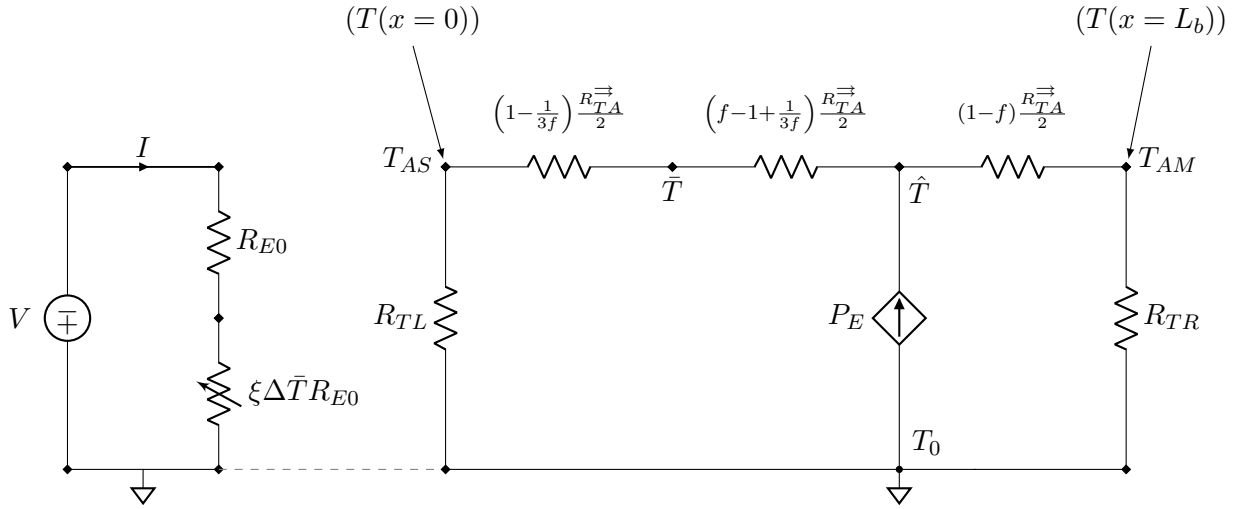


**Figure 4.4:** LEM of the steady-state simplified electrothermal system without convection. Based on [231].

respect to current or voltage as in Eqs. (4.11a) and (4.11b).

$$P_E(I) = \frac{I^2 R_{E0}}{1 - I^2 R_{E0} \xi \bar{R}_T} \quad (4.11a)$$

$$P_E(V) = \frac{1}{2\xi \bar{R}_T} \left( \sqrt{\frac{4\xi \bar{R}_T}{R_{E0}} V^2 + 1} - 1 \right) \quad (4.11b)$$

where  $R_{E0} = \rho_{E0} \frac{L_b}{S}$  is the initial total electrical resistance at temperature  $T_0$ . The LEM and the total electrical power clearly show off the positive feedback of the electrothermal system on the applied power. The relationship between the average temperature change in the transducer and the applied power was rewritten in Eq. (4.12) and describes the steady-state electro-thermal behavior of the transducer system.

$$\Delta \bar{T} = \frac{1}{2\xi} \left( \sqrt{\frac{4\xi \bar{R}_T}{R_{E0}} V^2 + 1} - 1 \right) \quad (4.12)$$

Finally, the LEM results were compared with FEM simulation and match within 10% for all actuation ranges according to Todd and Xie [216].

#### 4.2.1.2 Dynamic thermal considerations

To establish a dynamic model, one has to introduce time-dependent thermal component. Unlike the electrical domain that provides two common components that have a time-dependent behavior (coils and capacitors), only capacitances have a corresponding physical component in the thermal domain. The fluid Mechanics, the physical meaning of a thermal inertance is a phenomenon that induces a change in the kinetic energy of a fluid. However, in the thermal domain, thermal inertance has no physical meaning. The electrothermal principle of the bimorph beam can be clustered around thermal resistors and capacitances exclusively [334]. Table 4.1 summarizes the main equivalent between the different domain that can be merged in a LEM. A thermal heat capacity, also called capacitance is expressed in  $\text{JK}^{-1}$  and is equivalent to a capacitor in the

**Table 4.1:** Relations between lumped elements of different domains.

General	Electrical	Thermal	Mechanical
Effort	Voltage (V)	Temperature difference (K)	Force (N)
Flow	Current (A)	Heat flow (W)	Velocity ( $\text{m s}^{-1}$ )
Displacement	Charge (C)	Heat (J)	Displacement (m)
Resistance	Resistor ( $\Omega$ )	Thermal resistance ( $\text{K W}^{-1}$ )	Damper ( $\text{kg s}^{-1}$ )
Capacitance	Capacitor (F)	Heat capacity ( $\text{J K}^{-1}$ )	Spring ( $\text{N m}^{-1}$ )
Inertance	Inductor (H)	- ( $\text{K J}^{-1}$ )	Mass (kg)

electrical domain and is a function of the specific heat capacity  $c_p$ , the density  $\rho$  and the volume  $V$  of the body. For our single bimorph model, the bimorph beam is connected in its left end to a bulky substrate via an insulation bridge and in its right end to a thin mirror plate via another insulation bridge. Several combinations of thermal resistances due to conduction, convection and heat capacitances were studied for the model [217, 295, 317, 319, 331, 335].

Unlike the mirror plate, the substrate is a bulky component usually bonded onto a thermal and electrical ground. It has a very high thermal inertia and can be considered as a thermostat because its temperature will barely vary over short operation times. Consequently, it is assumed that the substrate maintains a thermal setpoint that can be assimilated to the ambient temperature. Hence, the thermal potential of the boundary between the substrate isolation bridge and the substrate itself is at the ambient air temperature  $T_0$  [331][318][317]. Another constant temperature different from  $T_0$  can also be set instead as in [217]. However, Pal and Xie [217] also considers the substrate as a thermal adiabatic well *stricto sensu*<sup>3</sup>.

The isolation bridges are considered for conduction exclusively. Indeed, the surfaces of exchange with the air have a negligible size compared to the bimorph and the mirror plate. Based on the calculation method of Todd and Xie, the thermal resistances for each isolation bridge due to convection were 2 orders of magnitude larger than their corresponding resistance due to conduction and were then ignored for the dynamic model [231]. The electrothermal LEMs were compared to FEM models several time with accuracy (less than 1.4% of error for short bimorphs [318]). It was always observed 2 cut-off frequencies due to the thermal behavior [217, 317, 319, 331]. Pal and Xie claim that the system can be accurately modeled by a linear transfer function consisting of 2 poles and 1 zero [217]. These two poles, which stand for energy storages are necessarily located on the mirror plate region for one of them, and on the bimorph for the second one [217, 317]. As a result, the thermal capacitances are neglected on the isolation bridges as in Wu [335].

The mirror plate is a thin (compared to the substrate thickness) suspended plate that accumulates heat and whose dissipation is constrained by the convection with the ambient surrounding air. Depending on the coating and the shape of the mirror plate, the thermal inertia of this component will be a more or less significant parameter on the dynamic behavior of the system. In addition, as the oscillation magnitude of the mirror is amplified compared to the one of the bimorph (by the leverage effect), the convection coefficient of a component can vary significantly from the other one. On the second hand, as radiation was ignored altogether, – although the bimorph can reach very

<sup>3</sup>Pal and Xie in their LEM model, represented thermal setpoints by the use of constant temperature generators connected to an undefined thermal ground which is the 0 K reference ground apparently. However, their model is inconsistent with the reality of the system because the heat flow generator as well as both thermal capacitances are also connected to this very 0 K ground. Therefore, in the heat flow (which is a non linear function of the temperature as seen in Eq. (4.9)), the temperature change is measured from 0 K and not from the ambient reference temperature.



high temperatures – the convection coefficients measured empirically will include the value of the neglected term of radiation and will be biased compared to real convection values. This will induce one more source of error in the convection coefficients. Convection coefficients are significantly larger than typical values used for macrosystems [336, 337]. A few values, listed in Table 4.2, were reported for MOTEMS in the literature and are strongly dependent on the configuration and the dimension of the devices [338].

**Table 4.2:** List of a few values of coefficient of convection calculated on electrothermal micro-scanners from different studies.

Author & Ref.	Convection coefficient in ( $\text{W K}^{-1} \text{m}^{-2}$ )		Actuator length ( $\mu\text{m}$ )	Mirror plate surface ( $\text{m}^2 \text{m}$ )
	bimorph	mirror plate		
Todd and Xie [216]	193	-	170	1.12
Todd <i>et al.</i> [220]	30	-	400	0.25
Feng <i>et al.</i> [332]	900	2600	200	0.22
Wu [295]	170	126	200	1
Pal and Xie [318]	188	47	173	1.32
Zhang <i>et al.</i> [283]	188	-	450	-
Zhou <i>et al.</i> [331]	1900 – 2282	-	287	1

The mirror plate is lumped by a thermal resistance due to convection and a capacitance. The bimorph transducer is substituted for 2 thermal resistors on each side of the point of maximum temperature generated by the applied power. The resistance of the bimorph due to convection and the capacitance of the bimorph are also considered. A comprehensive schematic of the LEM is given in Fig. 4.5 from which the analytical equation of the system is calculated. The thermal resistance  $R_A^{\leftrightarrow}$  depicts the convection of the bimorph with the ambient air. It was represented in parallel with the heat flow generator and the heat capacitance for a concern of clarity in the figure and is still consistent with the electrical domain circuit rules [217].

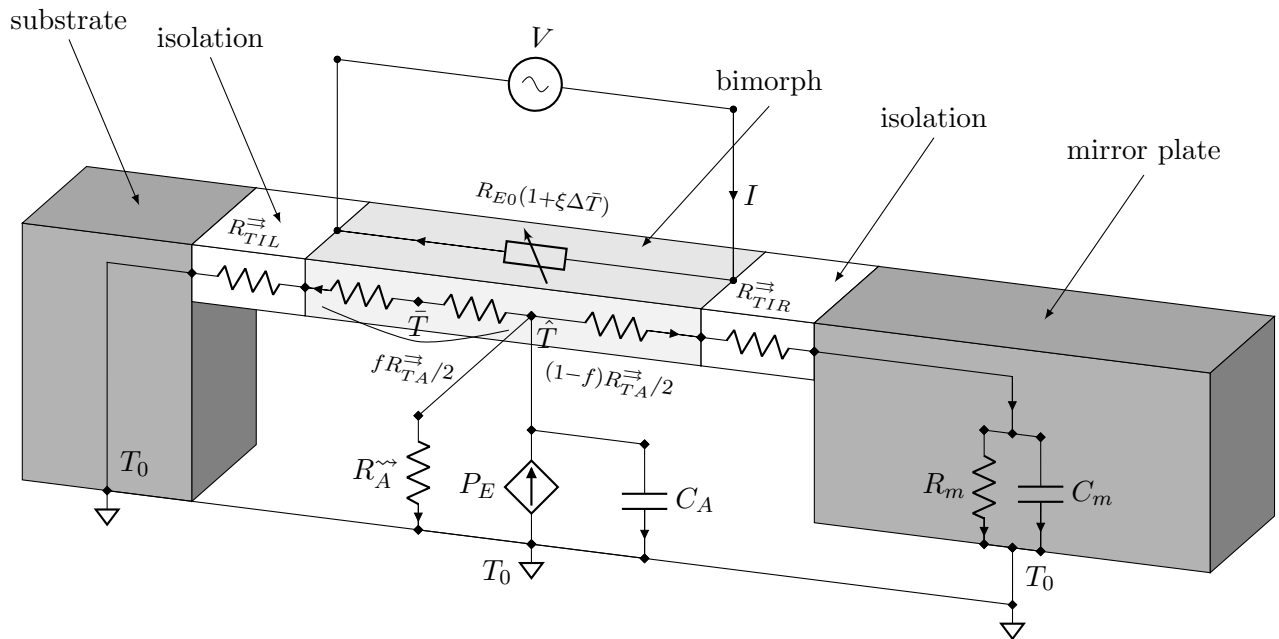


**Figure 4.5:** LEM of the dynamic system for one ...

The capacitances  $C_A$  and  $C_m$  refer to the heat capacity of the bimorph and the mirror plate

respectively. They were roughly calculated according to each material constituting the two elements by Eq. (4.13) and are in the order of magnitude of  $1 \times 10^{-9} \text{ J K}^{-1}$  and  $1 \times 10^{-7} \text{ J K}^{-1}$  respectively.

$$C_h = c_p \rho L_b S = c_p M \quad (4.13)$$

with  $C_h$  the heat capacity of a body,  $c_p$  its specific heat capacity (at constant pressure),  $L_b$  its length,  $L_b S$  its volume and  $M$  its mass. Hence, the mirror that is much bulkier than the bimorph is the first element responsible for the narrowing of the thermal bandwidth and hampers the system speed. We notice that  $R_{TIL}^{\leftrightarrow}$  and  $R_A^{\leftrightarrow}$  have a slight effect on the transfer function of the system as compared in the Bode diagram of the electrothermal system in Fig. 4.6, where the magnitude of the system is given by  $H_1 = 20 \log(\frac{\Delta \bar{T}}{P_E})$ . Subsequently we suggested to keep on simplifying the system and set  $R_{TIL}^{\leftrightarrow} = 0$  and  $R_A^{\leftrightarrow} = +\infty$ . The electrothermal system transfer function can

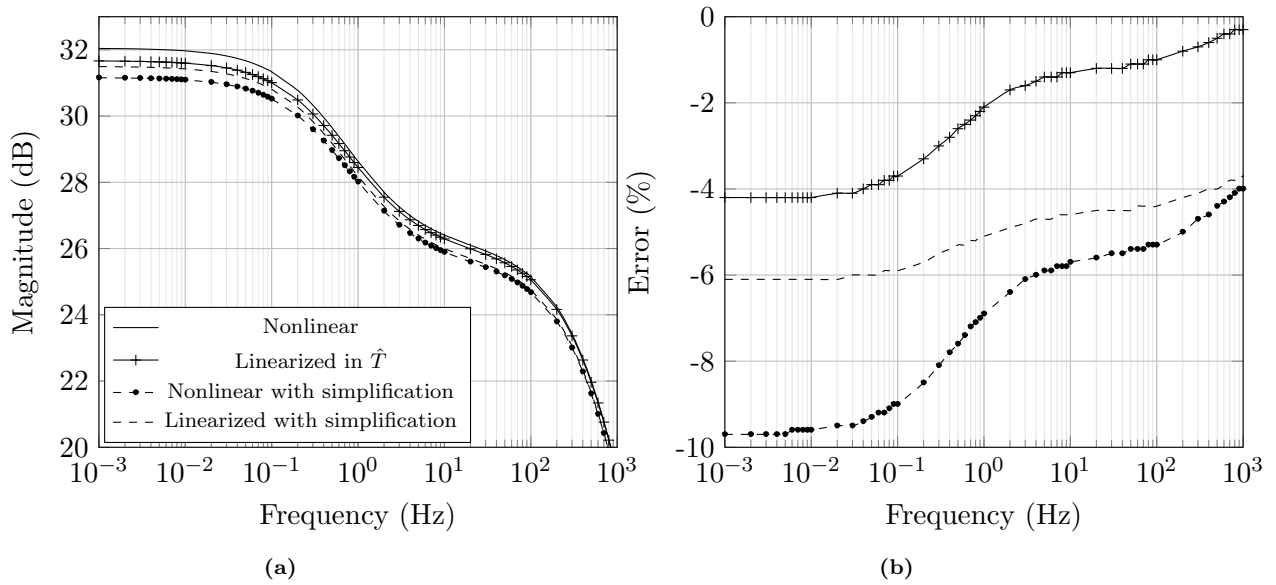


**Figure 4.6:** Frequency response of the electrothermal system of the average temperature change in the bimorph beam with respect to the square of the applied voltage. The numerical values used for the simulation are based on [216]. (a): Bode diagram of  $H_{et}(s)$  for the raw nonlinear system, the system linearized by limited development in  $\hat{T}$ , and with or without the resistor simplification mentioned in Section 4.2.1.2. (b): Error of each model with respect to the nonlinear electrothermal response.

be readily derived from the resolution of the LEM and has the form of Eq. (4.14) in the Laplace transform where  $s$  is the variable of Laplace.

$$H_1(s) = \frac{\Delta \bar{T}(s)}{P_E(s)} = K_1 \frac{(s + z_0)}{(s + p_1)(s + p_2)} \quad (4.14)$$

This form for the transfer function was first modeled by Han *et al.* [291], Pal and Xie [319]. The two poles  $p_1$  and  $p_2$  correspond to the thermal capacitances of the electrothermal system and  $z_0$  a zero. Time constants directly depend on the thermal properties and geometry of an element and can be roughly related to the diffusivity as shown in Eq. (4.15). For a simple element made of an homogeneous material subject to heat conduction exclusively [224]:

$$\tau = \frac{L_b}{\kappa S} \times c_p \rho L_b S = \frac{L_b^2 c_p \rho}{\kappa} = \frac{L_b^2}{\alpha_p} \quad (4.15)$$

The diffusivity is the measure of the heat transfer rate of the material. A higher diffusivity will yield faster thermal responses. In reality, the thermal response is very dependent from the fabrication process and may lead to significant variations from the simulations. One example of parameter that illustrates this possible variation is the undercut: the quantity of matter etched underneath the SiO<sub>2</sub> isolation bridges by **deep reactive-ion etch (DRIE)** during the last step of fabrication at the chip-level. It was shown that the undercut affects the thermal response gain and poles [315]. Another visualization of the electrothermal system is given in Fig. 4.7 from a block diagram approach, and was introduced by Pal and Xie [317]. It can be easily implemented in Matlab Simulink<sup>®</sup> and can be used for a dynamic extension of the model.

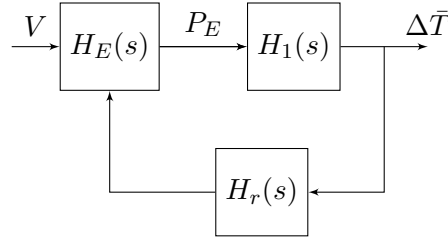


**Figure 4.7:** Block diagram of the electrothermal system.  $H_E$  : the electrical power system block ;  $H_1$  : linear thermal system with the power in input ;  $H_r$  : heater temperature conversion block.

$H_r(s)$  is a function converting the temperature of the bimorph into the temperature of the heater. However, we consider that the distribution of temperature into a cross section of the bimorph is uniform and that the heater crosses the whole bimorph which leads  $H_r(s) = 1$ .  $H_E(s)$  is a nonlinear system and is given by Eqs. (4.10) and (4.11b). Though, around a temperature working point,  $H_E$  can be linearized at the first order and becomes linear in  $V^2$ . Under dynamic operation,  $V$  is a sine voltage signal mainly used for Lissajous scan of frequency  $f_x$  and offset  $V_b$ :  $V = V_b + V_{pp} \cos 2\pi f_x t$  and  $V_{pp}$  the amplitude of the signal peak to peak.  $H_1(s)$  is given in Eq. (4.14). The whole electrothermal system referred to as  $H_{et}(s)$  and depicted in Fig. 4.7 is thus a linear system as long as the power generated or the square of the voltage applied is taken as the input. It was shown that the gain  $K_{et}$  of the system, can also be linearized around a working point and becomes a linear function of the biased voltage  $V_b$  applied on the heater resistor [291]. Finally, the electrothermal transfer function is given by Eq. (4.16) and is linear for a given bias voltage.

$$H_{et}(s) = K_{et}(V_b) \frac{(s + z_0)}{(s + p_1)(s + p_2)} \quad (4.16)$$

## 4.2.2 Thermomechanical model

It was demonstrated by Todd [231] that “the thermal parameter that affects the mechanical rotation angle is the average temperature change of the bimorph beams”. Hence, the thermomechanical model of an electrothermal bimorph/multimorph is a model of input  $\Delta\bar{T}$  and of output the deflection or the rotation angle of the cantilever beam.

### 4.2.2.1 Curvature in bimorph cantilever

There exist two types of stress present in the bimorph cantilever beams. In nature, the bimorph cantilever is subject to a type of stress called intrinsic stress because it is stemmed from the internal boundary constraints of the two-layer beam. It depends on the material properties, the process

of “growth” and the environment temperature and other external conditions. After fabrication, two layers (at least) are piled up by processes of deposition that differ from their characteristics (temperature for example) and a stress is induced leaving the bimorph into a deformed curved shape of maximum stress. Freeing the bimorph from its intrinsic stress would release the layers from their constraint and inverse the original curvature creating a deflection of the cantilever beam. Once the device is released from the fabrication support, the intrinsic stress is present in the layers for good; it can be compensated by an extrinsic stress only that can be created by a process of inversion of the conditions of deposition during the fabrication. In the electrothermal actuation principle, the extrinsic stress is based on the temperature change throughout the cantilever beam. The origin of the intrinsic stress has never been the subject of a detailed study in the past; it is just known that it results from a few factors inherent to the structure itself such as the stoichiometry, the impurity incorporation, the grains... The study about the stress and the curvature of the bimorph will be based on the extrinsic stress exclusively. When a temperature change arises in the bimorph cantilever beam, the layer of higher CTE will expand more than the one of lower CTE introducing a gradient of strain about the thickness in each layer. The difference in the strains develop a stress mismatch between the upper and the lower stacks bonded together. Let us assume a bimorph cantilever beam composed of an upper and a lower layer of thickness  $t_i$ , Young’s modulus  $E_i$ , Poisson’s ratio  $\nu_i$ , CTE  $\alpha_i$  and of width, length and total thickness  $w_b$ ,  $L_b$  and  $t_b$  respectively, with  $i \in \{1, 2\}$  an index to denote the first upper or the second lower layer. A comprehensive schematic view of the deflected bimorph cantilever beam is given in Fig. 4.8. A few assertions are made to study the behavior of the cantilever beam: (1) every material involved in the beam deforms within the elastic domain: the yield strength point is never reached. Hence, the stress is proportional to the strain in each layer and the relation of Piola-Kirchhoff can be linearized at the first order. (2) The properties of the materials are invariant with temperature. (3) The gradient of displacement through the beam remains small enough compared to its thickness. (4) The materials are homogeneous and isotropic. The homogeneity of the material yields the radius of curvature to be uniform throughout the beam: the deformed shape is an arc of circle of radius of curvature  $\rho$  given by Eq. (4.17).

$$\frac{1}{\rho} = \frac{1}{\rho_0} + \frac{1}{\rho_b} \quad (4.17)$$

where  $\rho_0$  is the initial radius of curvature due to intrinsic stress and  $\rho_b$  the radius of curvature due to extrinsic stress.

$$\boxed{\frac{1}{\rho_b} = \frac{\theta_b}{L_b} = \frac{\Delta\varepsilon}{\chi}} \quad (4.18)$$

with  $\chi$  the curvature coefficient of the bimorph beam and  $\theta_b$  the tilt angle of the tip of the beam as represented in Fig. 4.8 and the thermal extrinsic strain is given in Eq. (4.19)

$$\Delta\varepsilon = (\alpha_2 - \alpha_1)\Delta\bar{T} \quad (4.19)$$

with  $\alpha_i$  the CTE of layer  $i$ .

Letting:

$$m = \frac{t_1}{t_2} \text{ and } n = \frac{E'_1}{E'_2},$$

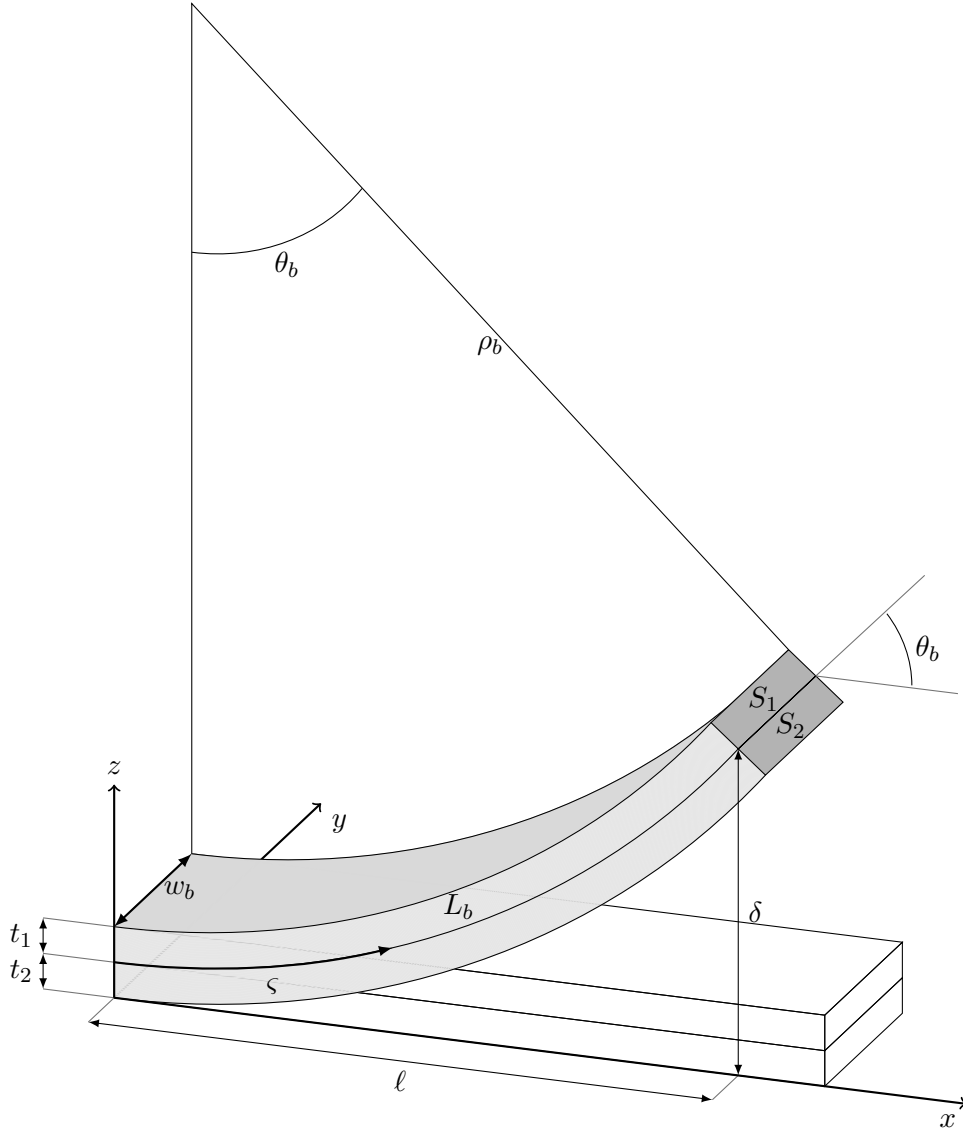


**Figure 4.8:** Schematic view of the bimorph in an arbitrary deformed position and comparison with the stress-free state of the beam in uncolored.

the curvature coefficient can be written as in [339] and is recalled in Eq. (4.20).

$$\chi = \frac{6(1+m)^2}{t_b \left[ 3(1+m)^2 + (1+mn) \left( m^2 + \frac{1}{mn} \right) \right]} \quad (4.20)$$

where  $E'_i$  is the reduced Young's modulus of layer  $i$  defined by the ratio  $\frac{E_i}{1-\nu_i}$ . In the case the thicknesses and the Young's moduli are the same, the radius of curvature can be simplified as follows in Eq. (4.21).

$$\frac{1}{\rho_b} = \frac{3}{2t_b} \Delta\varepsilon \quad (4.21)$$

Let us also notice that whenever a layer is much thicker than the other one, for example  $t_2 \gg t_1$ , *i.e.*  $m \rightarrow +\infty$ , then the formula of stoney is retrieved as expressed in Eq. (4.22) [340].

$$\frac{1}{\rho_b} = 6 \frac{E'_1 t_1}{E'_2 t_2} \Delta \varepsilon \quad (4.22)$$

At that point, it is important to see that the bimorph can be optimized to obtain the highest displacement that can be reached by its dimension. The sensitivity of the thermomechanical system is defined in Eq. (4.23) by the ratio of the output and the input of the system, which correspond to the displacement (angular displacement for instance) and the average temperature change respectively.

$$\Xi = \frac{\theta_b}{\Delta \bar{T}} = \frac{\Delta \alpha L_b}{\chi} \quad (4.23)$$

The sensitivity  $\Xi$  increases with the length, the CTE and the inverse of the thickness of the bimorph. For a given total thickness, Villarceau [341], Peng *et al.* [342] have shown that the ratio of the thicknesses of each layer  $m$  can be optimized depending on the ratio of the Young's moduli  $n$  to obtain the highest sensitivity in Eq. (4.24).

$$m\sqrt{n} = 1 \quad (4.24)$$

The curvature coefficient becomes constant regardless to the materials and has a value of 3/2. In addition, it yields that the selection of the materials will be based on the high CTE difference because the value of the Young's moduli and thus the coefficient of curvature do not affect the curvature of the bimorph beam when the condition of Eq. (4.24) is met.

#### 4.2.2.2 Curvature in a multimorph cantilever

In reality, the so called "bimorph" beam is not only composed of two layers. Indeed, the two main layers whose CTE play the main part in the bending must meet a few requirements such as the being compatible, be electrically conductive and sufficiently thermally resistive to generate enough heat to provide the expected temperature change in the beam. Unfortunately, some materials are not compatible and require intermediate layers to weld to each other. Besides, an additional material will have to be introduced as heater throughout the length of the beam to homogenize the temperature distribution. Thus, more than two layers can compose our cantilever. In fact, we'll talk of multimorph<sup>4</sup> rather bimorph, however the term of bimorph will be abusively used in the following even to denote a multimorph. Timoshenko's bi-metal thermostat model can be extended to  $N$  layers ( $N \in \mathbb{N}, N > 1$ ). The radius of curvature is given by Eq. (4.25) [226].

$$\frac{1}{\rho_m} = \frac{\sum_{i=1}^N D_i (z_e - z_i)}{\sum_{i=1}^N E_i I_i - C_i (z_e - z_i)} \quad (4.25)$$

---

<sup>4</sup>The term of multimorph is found in the literature as well as polymorph. There is no difference and depends mostly on the preference of the greek or the latin root of the word.

with:

$$D_i = E_i S_i \left( \varepsilon_1 - \varepsilon_i - \frac{\sum_{j=2}^N (\varepsilon_1 - \varepsilon_j) E_j S_j}{\sum_{j=1}^N E_j S_j} \right) \quad (4.26)$$

$$C_i = \frac{E_i S_i}{2} \left( t_1 + 2 \sum_{j=2}^{i-1} t_j + t_i - \frac{\sum_{j=2}^N \left[ E_j S_j \left( t_1 + 2 \sum_{k=2}^{j-1} t_k + t_j \right) \right]}{\sum_{j=1}^N E_j S_j} \right) \quad (4.27)$$

$$z_e = \frac{\sum_{i=1}^N z_i E_i S_i}{\sum_{i=1}^N E_i S_i} \quad (4.28)$$

$$z_i = \frac{t_i}{2} + \sum_{j=i+1}^N t_j \quad (4.29)$$

where  $z_e$  is the position of the neutral axis of the multimorph beam on the vertical axis, *i.e.* where the strain is null. This position will be taken as the ordinate on the vertical axis of the base of the curved abscissa commonly assimilated to the unidirectional abscissa of the heat flow for the 1D thermal analysis. Indeed, the length of the multimorph  $L_b$  is unchanged on the section of vertical ordinate  $z_e$ .  $S_i$  is the section area of the  $i$  as represented in Fig. 4.8. Equations (4.25) to (4.29) are true for any actuation principle, as they include the strain of each layer. In the thermal actuation, the strain is proportional to the average temperature change in the multimorph as in Eq. (4.30).

$$\Delta \varepsilon_i = \alpha_i \Delta \bar{T} \quad (4.30)$$

#### 4.2.2.3 Stiffness and natural frequency

Another factor that has to be taken into account for a dynamic aspect of the vibrating behavior of the bimorph beam is its stiffness directly linked to the natural frequency that will also be abusively called “resonance frequency” because of the lack of consideration of the damping ratio in the bimorph system. Equation (4.18) can also be seen in terms of moment where the moment caused by the temperature change is a linear function of the difference in the thermal strain in the layers and is defined by Eq. (4.31) as in [213].

$$M_T(\varsigma) = - \underbrace{\frac{S_N}{2} \left( \frac{1}{t_1 E'_1} + \frac{1}{t_2 E'_2} \right)}_{m_b}^{-1} \Delta \alpha \Delta T(\varsigma) \quad (4.31)$$

where  $S_N$  is the total area of the bimorph cross section,  $m_b$  is the moment coefficient of the bimorph and is a positive function of the moduli and cross section of the bimorph beam. The moment due to the increase in temperature exerts a counter moment with respect to the initial moment due to residual stresses in the beam. In the theory of small displacement, the relation

between the equivalent local force applied on the tip of the bimorph and the displacement can be derived from the well known equation of the beam of Bernoulli (Eq. (4.32)):

$$Fz' = k_b \delta z' \text{ with } k_b = \frac{3\widehat{EI}}{L_b^3} \quad (4.32)$$

with  $\widehat{EI}$  the composite stiffness of the bimorph which can be extended to a multimorph using Eqs. (4.25) and (4.31) [339, 343] (see Eq. (4.33)).

$$\widehat{EI} = \frac{m_b}{\chi} = \widehat{E}' I_b \text{ with } \widehat{E}' = \frac{E'_1 t_1 + E'_2 t_2}{t_1 + t_2}$$

$$m_m = \frac{S_N}{2} \left( \sum_{i=1}^N \frac{1}{t_i E'_i} \right)^{-1} \quad (4.33)$$

with  $I_b$  the second moment of area of the beam bending.

Finally, most parameters of the electrothermal and thermomechanical bimorph system can be evaluated in order to obtain the best trade-off between the displacement range and resonance frequency. Increasing the length of the bimorph beam would have for effect to raise the displacement range, reduce the stiffness and the resonance frequency. Whereas increasing the width and the thickness of the bimorph will also increase the mechanical frequency response but decrease the quality factor. Diminishing the mass of the mirror would extend the bandwidth of the thermal system but also raise the resonance frequency of the mechanical system.

### 4.2.3 Material selection

The sensitivity of the thermomechanical system given in Eq. (4.23) and defines the ratio of the output and the input of the system. We saw in Eq. (4.24) that an optimization of the thickness of the layers constituting the bimorph was given by the elastic moduli of the materials chosen. The moduli should not be too far apart in order to prevent disproportionned thicknesses of the layers. Furthermore, a high difference in the CTE will be preferred to maximize the sensitivity of the thermomechanical actuation. A broadly used materials list is given in Table 4.3 in order compare the electrical, thermal and mechanical properties of these materials.

Different pairs of materials have been investigated in the literature as the materials constituting the layers of the bimorph cantilever beam. Pal and Xie developed a micromirror based on a Al-W bimorph achieving a large difference of CTE of  $\Delta\alpha_{\text{Al-W}} = 19.1 \times 10^{-6} \text{ K}^{-1}$  and allowing a fast thermal response because of the high diffusivity of metal [236, 344].

Zhang *et al.* proposed an alternative Cu-W design including tungsten as both the low-CTE material and the embedded heater material so that the bimorph is perfectly symmetric and works out without the need for balancing the length of the inverted and non-inverted bimorph in the ISC structure [224, 240]. Although, the metals are insulated and protected by layers of  $\text{SiO}_2\text{SiN}$ , these designs still strongly suffer from oxidation and would require some time to gain maturity [240]. On the other hand, they require additional fabrication steps – such as additional aluminum deposition for the mirror reflective layer – that complexify the process and extend the phase of development of characteristic processes. Finally, during fabrication, all processes that may expose



the structures to O<sub>2</sub> are to be strictly proscribed in order to prevent oxidation at all steps.

Even if metal-polymer or metal-SiO<sub>2</sub>-based bimorphs are more prone to failure due to brittleness and have lower thermal responsivities due to low diffusivity in general; they are still the most broadly used couples of materials in electrothermal cantilever beams: out of 103 publications utilizing electrothermal bimorph beams for micro-scanner-based applications in BML group during 2004 and 2017, only 7 of them are based on a technology different from Al-SiO<sub>2</sub> (see Section 3.3). Indeed, the pair Al-SiO<sub>2</sub> offers a few assets making it competitive compared to bi-metal configuration. First, the difference in CTE is higher than Al-W and Cu-W,  $\Delta\alpha_{\text{Cu-W}} = 12.4$ , whereas  $\Delta\alpha_{\text{Al-SiO}_2} = 23.2$  yielding a higher steady-state sensitivity. Second, the processes went through much more technical development and optimization since they started to be developed in Nanoscale Research Facility (NRF). According to the author, the quality and the cost of fabrication of the microsystems is indubitably improved with the immutability of the environment of work. Finally, when Al is used in the process, it can be used as both the high-CTE layer material and the mirror plate reflective film due to its high reflectivity in the near-IR range.

In former designs including tungsten in the bimorph materials, no additional heater was required but the tungsten itself because of its sufficiently high electrical resistivity. Poly-Si has also been exploited as an outer and embedded heater [220, 222] because of its high electrical resistivity and decent thermal conductivity at  $13.2 \times 10^{-6} \Omega \text{ m}$  and  $29 \text{ W K}^{-1} \text{ m}^{-1}$  respectively [220]. The main shortcomings of Poly-Si are the hysteresis phenomenon and the self-annealing behavior limiting the scanning range [345]. As an alternative, platinum has been widely adopted because of its high electrical resistivity, thermal conductivity, mechanical resistance and TCR making it one of the most adapted choices of material as an embedded heater into an Al-SiO<sub>2</sub>-based bimorph beam. In this design, the couple Al-SiO<sub>2</sub> was selected for the bimorph, as well as the platinum as the resistive embedded heater. The piling order of the different components that are composed of these materials is represented in Fig. 4.17 of Section 4.3.3.2.

**Table 4.3:** Comparison of the properties of a few materials. From [212, 213, 224, 323, 346, 347].

Material	Symbol	Unit	SiO <sub>2</sub>	Si	Al	Au	Cu	Cr	Pt	Ti	Ni	W	Invar
Young's modulus	$E$	GPa	70	179	70	78	120	279	168	116	200	411	145
Poisson's ratio	$\nu$	-	0.17	0.27	0.35	0.44	0.34	0.21	0.38	0.32	0.31	0.28	0.29
Shear modulus	$\mu$	GPa	30	70.5	26	27	45	115	61	44	76	161	56
CTE	$\alpha$	$10^{-6} \text{ K}^{-1}$	0.4	3.0	23.6	14.5	16.9	5.0	8.9	8.6	12.8	4.5	0.36
Density	$\rho$	$\text{g/cm}^3$	2.66	2.33	2.69	19.4	8.95	7.19	21.5	4.51	9.04	19.3	8.15
Electrical resistivity	$\rho_E$	$10^{-9} \Omega \cdot \text{m}$	-	-	28.2	22.1	16.8	125	106	420	69.9	56.0	800
Thermal conductivity	$\kappa$	$\text{W/mK}$	1.4	150	237	318	401	93.9	71.6	21.9	90.9	174	13
Thermal diffusivity	$\alpha_p$	$10^{-6} \text{ m}^2/\text{s}$	0.87	93.4	97	127	115	29	25	8	22.7	68	3.1
Specific heat	$c_p$	$\text{J/kgK}$	700	691	900	129	387	440	133	611	444	132	515
TCR	$\xi$	$10^{-3} \text{ K}^{-1}$	-	-	4.3	3.7	4.0	-	3.7	-	-	4.4	-
Min. yield strength	$\sigma_Y$	MPa	-	-	124	200	-	-	-	650	-	-	-

### 4.3 Micro scanner: Description and design

Several devices were designed over two batches of fabrication. The first batch was completely developed and fabricated in the NRF at the University of Florida. Several improvements stemming from a first series of testing contributed to the development of a second batch in BML and partly fabricated in NRF and in Microfabrication for Mechanical Engineering, Nanoscience, Thermal science and Optics (MIMENTO) in France during the bestowed remaining time. In this section, the design of the micro-scanner of the first batch will be thoroughly described. The improvements and modifications that differ from the first design will be highlighted in this section as well.

As we saw in Section 3.2, most MOTEMS developed enable 3D scans in nature but also provide one or more dof left behind. Most MOTEMS used for angular scans also enable an unwanted piston motion that adds an uncontrollable parameter in the model's equation and gives the robotic system's input an infinity of solutions. The micro-scanner of the first batch is based on pure tilt motions mechanically uncoupled from each other, over two dependent and orthogonal axes. It consists of three main rigid bodies actuated one from another via electrothermal bimorph-based structures designed to provide each element with the performances needed to meet the requirements of the probe presented in Section 4.1. The effective surface of the device is the surface of the mirror plate covered with exposed Al/Cr on the top. It is the core of the whole system and the constraints linked to its position will determine the dimensions of all other rigid and deformable components. The second rigid element is the frame (that will also be referred to as "inner frame" in the following) that acts like a support for the mirror plate that will be actuated by electrothermal actuators located between the frame and the mirror plate. The frame itself is to be actuated within the reference frame of a fixed bulky substrate (or outer frame).

A sketch of the micro-scanner is drawn in Fig. 4.9. For a better understanding of the components constituting the micro-scanner, a color coding is used in order to distinguish the different actuators. The inner frame is actuated by an array of identical electrothermal bimorph actuators in parallel represented in red in Fig. 4.9. Right after release, the bimorph beams have an initial bending due to intrinsic stress as discussed in Section 4.2.2. Hence, the inner frame is initially tilted at an angular position of approximately 45°. The motion provided by the bimorph array on the inner frame is the motion of a draw bridge and is referred to as "pitch" in the nautical angle standard. Whereas, the mirror plate has a pure rotative motion within the inner frame controlled around a rotation axis materialized by a pair of torsion rods<sup>5</sup>. The actuators implemented to tilt the mirror plate out of the frame plane are ISC in nature and consist of two double ISC actuators in parallel located on each side of the mirror plate in opposite directions to generation a rotation motion that will be denoted as "roll" actuators because it corresponds to the third rotation with respect to yaw and pitch of the nautical angles. To enable the rotation, the same voltage signal has to be applied on both actuators in order to generate the same tilt. Applying different signals could cause opposite moments on the mirror plate, causing damage or breakage. Hence, the electrical "grounds" of the two inner actuators are connected to one common pad.

---

<sup>5</sup>The term of "rod" is used here because it refers to a gimbal-like slender structure which can be subject to several modes of vibrations. Hence, it is considered that the rod can work in torsion and bending along the vertical and lateral axes perpendicular to its length. However, the terms of bars and beams can also be used but have specific meaning in theory of mechanics: a beam is a model that contains efforts applied in traction, compression and flexion, whereas a the model of a bar is inherent to the model of a beam and only consists of traction or compression. In this manuscript, we won't make any difference between the terms "beam" and "bar".

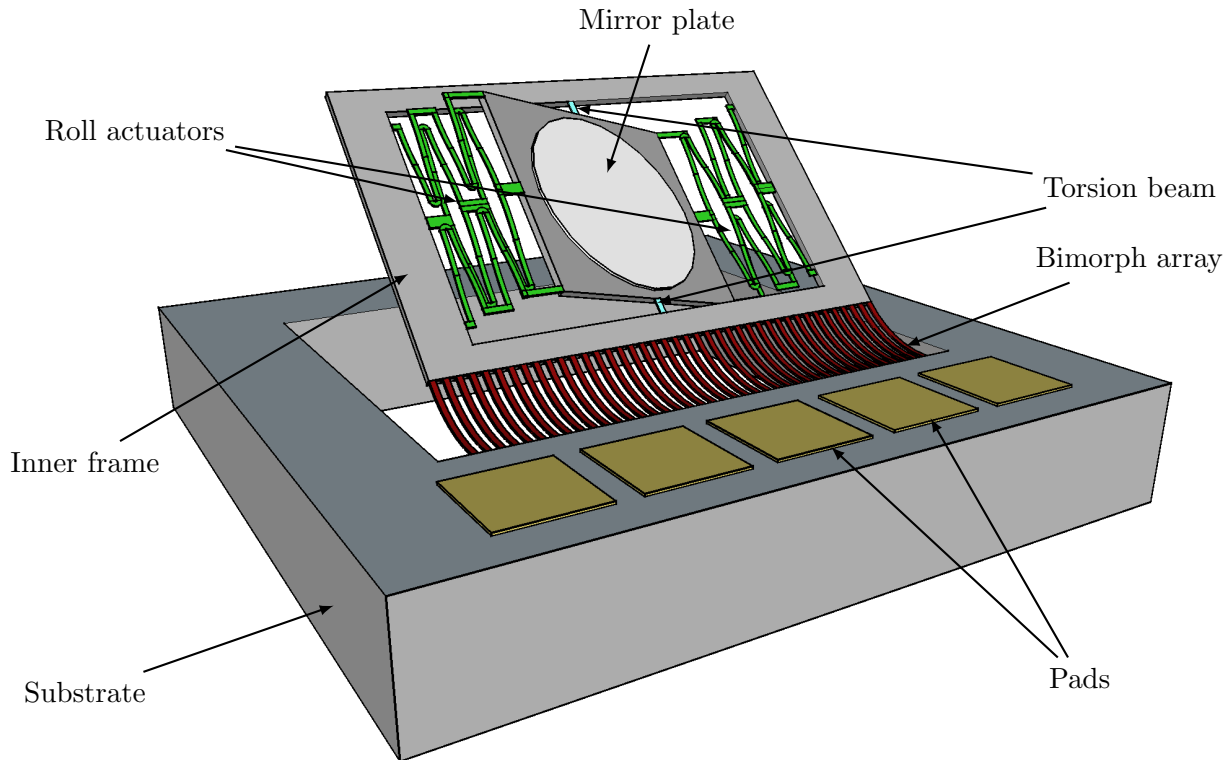


Figure 4.9: Sketch of the MOTEMS of the first batch with torsion beam.

### 4.3.1 Torsion beam

The motion of the mirror plate is constrained, in theory, to a pure rotation around the axis of roll  $\vec{r}$ . Torsion beams were widely used for the design of MEMS scanners in the literature because they are a passive structural element that is easy to dimension, fabricate and implement and provides sufficiently pure rotative motions [116, 177, 178, 182, 210, 348]. In quite a few systems, torsion beams are made of silicon [177] because of the very high performances in shear of the material. However, the process of fabrication exposed in Chapter 5 and the micro-scanner dimensions prevented from fabricating silicon torsion beams. Indeed, the main materials used for fabrication of the micro-scanner are aluminum, platinum and silicon dioxide stacked up and etched to form layers in a series of 9 masks and 11 stages. For a reason of time and simplicity, we avoided to create additional steps to form the torsion beam. As a result, the torsion beam is composed of the same materials as the rest of the micro scanners in a sandwich piling described in Fig. 4.10. In theory, apart from pure torsion, a slender rod is also expected to develop other modes of motion such as in-plane (the plane of the inner frame) horizontal mode and out-of-plane vertical and rocking modes illustrated in Fig. 4.11. For the calculation of the different modes, a few assertions need to be introduced:

**Hypothesis 1** *It is assumed that the mass of the rods is small enough compared to the mass of the mirror plate to be neglected. Indeed, the dimensions of the plate are much larger than the torsion bar.*

**Hypothesis 2** *The gradient of displacement through the bar remains small enough compared to its thickness.*

**Hypothesis 3** *No body force exerts on the bar.*

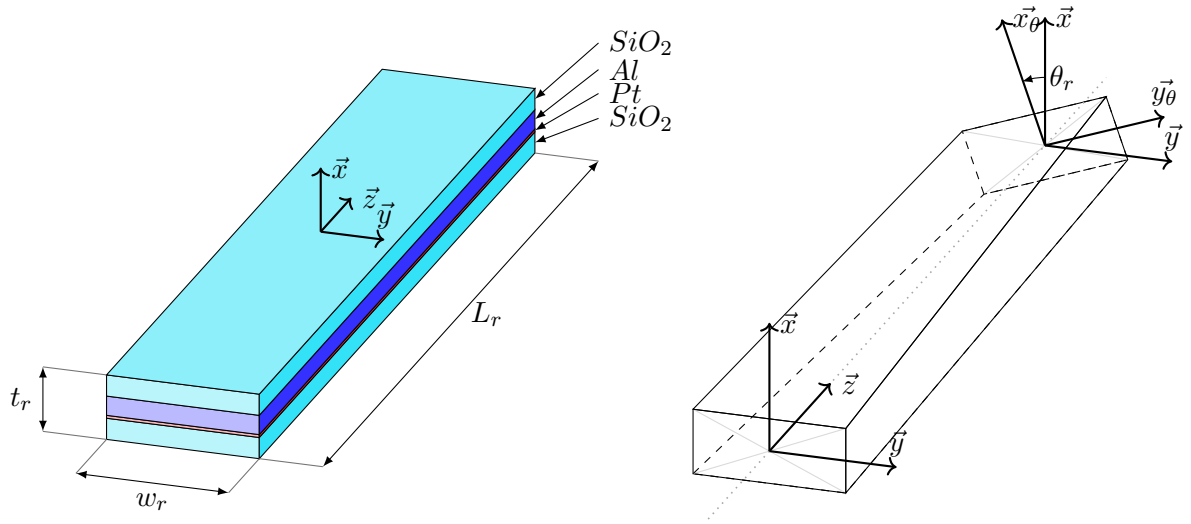


Figure 4.10: Schematic 3D view of the torsion beam as designed in the micro-scanner.

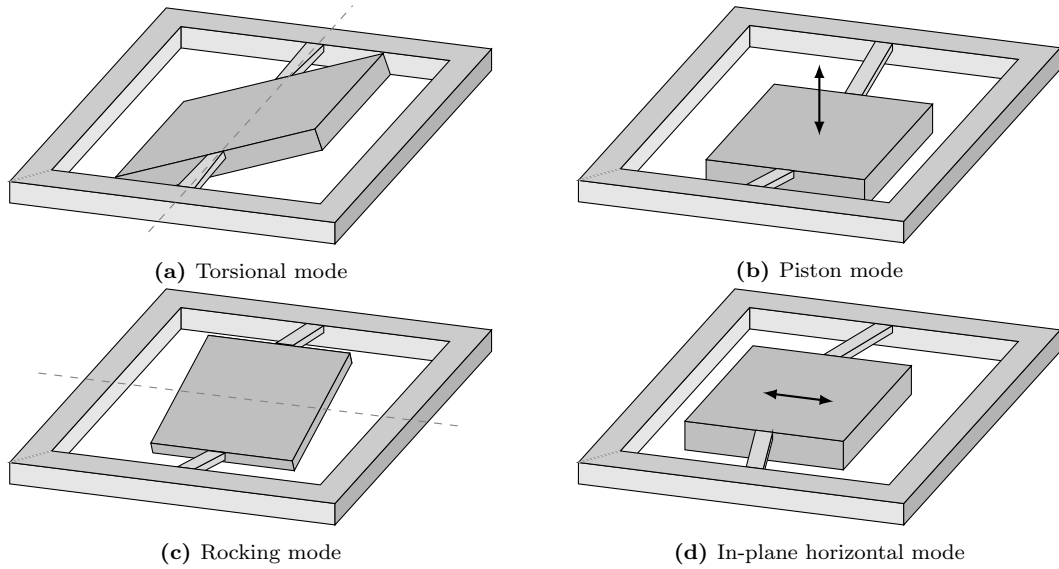


Figure 4.11: First four oscillation modes of the torsional micro-scanner.

Aluminum and silicon dioxide that compose the rod have a comparable Young's modulus which allows to make one more hypothesis:

**Hypothesis 4** *The bar is made of one isotropic, homogeneous, linear and elastic virtual material of equivalent Young's modulus  $E$  and poisson's ratio  $\nu$ .*

As a result of the hypotheses quoted above, only the linear behavior of the torsion beam will be investigated. The detailed calculation for the resolution of the stress and strain distribution of the torsion is recalled in Eq. (4.34).

$$C = \frac{\theta_m \mu I_t}{L_r} \tag{4.34}$$

The vibrating modes' stiffness and resonant frequency are given in Table 4.4 from [348].

The second moment of area<sup>7</sup> of the torsion rod concerning the torsional mode is given by the

**Table 4.4:** Resonant frequency, stiffness and other parameters of the vibrating modes of a rectangular cross-section torsion bar.

Mode	Stiffness (N m <sup>-1</sup> or N m)	Resonance frequency $\omega$ (rad s <sup>-1</sup> )	Frequency ratio $\omega_{mode}/\omega_{torsion}$	Numerical estimation <sup>6</sup>
Torsion	$k_t = \frac{2\mu I_t}{L_r}$	$\sqrt{\frac{k_t}{J_m}}$	1	-
Rocking	$k_b = \frac{E w_r t_r^3}{12 L_r^2} (4 L_r + 3 L_m)$	$\sqrt{\frac{k_b}{J_m}}$	$\sqrt{\frac{(1+\nu)(1+\frac{3L_m}{4L_r})}{3K_t}} \cdot \frac{w_m}{L_m}$	if $w_r = 22 \mu\text{m}$ , $1.19 \sqrt{1 + \frac{3L_m}{4L_r}}$ if $w_r = 28 \mu\text{m}$ , $1.18 \sqrt{1 + \frac{3L_m}{4L_r}}$ if $w_r = 38 \mu\text{m}$ , $1.16 \sqrt{1 + \frac{3L_m}{4L_r}}$
Piston	$k_b = \frac{E w_r t_r^3}{4 L_r^3}$	$\sqrt{\frac{k_b}{M_m}}$	$\frac{1}{4} \sqrt{\frac{1+\nu}{3K_t}} \cdot \frac{w_m}{L_r}$	if $w_r = 22 \mu\text{m}$ , $0.30 \frac{w_m}{L_r}$ if $w_r = 28 \mu\text{m}$ , $0.30 \frac{w_m}{L_r}$ if $w_r = 38 \mu\text{m}$ , $0.29 \frac{w_m}{L_r}$
Horizontal	$k_b = \frac{E w_r^2 t_r}{4 L_r^3}$	$\sqrt{\frac{k_b}{M_m}}$	$\frac{1}{4} \sqrt{\frac{1+\nu}{3K_t}} \cdot \frac{w_r}{t_r} \cdot \frac{w_m}{L_r}$	if $w_r = 22 \mu\text{m}$ , $1.98 \frac{w_m}{L_r}$ if $w_r = 28 \mu\text{m}$ , $2.49 \frac{w_m}{L_r}$ if $w_r = 38 \mu\text{m}$ , $3.35 \frac{w_m}{L_r}$

Roark's formula [349] and recalled in Eq. (4.35).  $J_m$  refers to the moment of inertia of the mirror plate around the axis formed by the torsion bars and is mainly composed of silicon. The matrix of inertia  $\underline{J}_m$  is expressed in Eq. (4.36) for the torsion mode and the rocking mode.

$$I_t = w_r t_r^3 K_t \text{ with } K_t = \left[ \frac{1}{3} - 0.21 \frac{t_r}{w_r} \left( 1 - \frac{t_r^4}{12 w_r^4} \right) \right] \quad (4.35)$$

$$\underline{J}_m = \frac{1}{12} M_m \begin{pmatrix} L_m^2 + w_m^2 & 0 & 0 \\ 0 & L_m^2 & 0 \\ 0 & 0 & w_m^2 \end{pmatrix}_{(\vec{x}, \vec{y}, \vec{z})} \quad \text{with } M_m = \rho_{Si} t_m L_m w_m \quad (4.36)$$

where  $\rho_{Si}$  is the density of Silicon.  $L_m$ ,  $t_m$  and  $w_m$  are the length, the thickness and the width of the mirror plate respectively. The mass of the mirror is  $M_m$ . A quick analysis of Table 4.4 yields that the torsional mode is the first mode in frequency. This is due to the low torsional spring constant of the rod. Let us also notice that the whole system introduces additional stiffnesses in the spring constant problem. These supplementary stiffnesses are caused by the electrothermal bimorph actuators that develop a spring force between the supporting inner frame (considered fixed so far) and the mirror plate. This will be taken into account after the bimorph actuator structure is presented in Section 4.3.3.2.

The goal of comparing the ratio of close modes with the torsional mode is to ensure a motion with separated modes from the mode of torsion and its harmonics in order to reject undesired movements and subsequently minimize the power dissipation. The modes following the torsion

<sup>6</sup>For the ratio of the angular frequencies of the rocking mode with the torsion mode, we assume that the mirror plate is a square, hence  $L_m = w_m$ . The material of the mirror plate is silicon and the materials constituting the beam have the same Young's modulus  $E = 70$  GPa. The thickness of the torsion beam is a parameter already determined by the fabrication process and is given in Table 4.5.

<sup>7</sup>The second moment of area is different from the moment of inertia and is expressed in m<sup>4</sup>.

in order of importance are the piston mode, the rocking mode and the in-plane horizontal mode. Although the in-plane and piston modes do not have an impact on the direction of the reflected path of the beam, the piston mode may generate artifacts in the final OCT image. The frequency of the SS-OCT A-scan is about a hundred times higher than the piston mode frequency of the mirror plate (which is in the order of the kHz) reducing the possibility of introducing a modulation in the OCT scan to the B-scan exclusively. The vertical vibrating motion may also modify the location of the focal plane of the laser beam. For a further study of the effect of this secondary mode onto the scan path consistency and the OCT image, the quality factor or the damping ratio could be estimated. However, we can easily refute this assertion observing on the one hand that the thermal cut-off frequency drawn in Fig. 4.6a occurs in the range of a few hundreds of Hz and that on the second hand, the magnitude of the vertical motion will be expectedly attenuated compared with the first resonance peak of torsion. As a result, the piston mechanical resonance peak will undergo a significant attenuation by 20 dB/decade on top of the low quality factor developed by the specific mode. The rocking mode, ranking third in the order of the frequency magnitudes deflects the beam in the perpendicular direction of the torsion leading to undesired and uncontrolled motion that may even superimpose with the mode shape of the frame due to the bimorph array contribution. It needs to be discriminated from the harmonics of the pitch mode of the frame and whose stiffness is developed in Eq. (4.32).

Columns 4 and 5 of Table 4.4 give a method of determination for the “rejection” of the undesired modes. The harmonics of the bimorph array pitch mode also requires to be taken into account. Once the parameters constituting the bar are properly chosen so that the very following vibrating mode of piston will not be interfering with the torsion mode, the steady-state behavior of the torsion beam can also be guaranteed. Indeed, unlike a bimorph beam, the material stacking order of the torsion rod will cause the residual stresses to be auto-compensated at all time, so that neither an initial intrinsic stress profile, nor an extrinsic thermal stress will arise a bending deformation of the bar: the rotation shaft formed by the virtual axis of the torsion rods is reliably fixed. A high quality factor is highly preferred to maximize the ratio “displacement range over power consumption”. The parameters chosen are listed in Table 4.5 and several designs of torsion bars are set for further tests and comparison. Other criteria will also have an impact on the dimensions of some structures such as the fabrication process for example. However, this will be discussed in the corresponding Chapter 5. The amplitude of the torsional mode is determined by the damping ratio  $\zeta = \frac{c}{2\sqrt{J_m k_t}}$  depending on the environment, the viscous damping coefficient  $c$  and the natural frequency  $\omega_t$  of the concerned mode. The quality factor of the torsional mode  $Q_t$  is directly related to the damping coefficient and a method of estimation was investigated by Buser and De Rooij [350] and Kadar *et al.* [351] from the work of Christian [352] and can be calculated by Eq. (4.37).

$$Q_t = \frac{\sqrt{k_t J_m}}{c} = \frac{\sqrt{2\pi}}{8} \frac{\omega_t \rho S_i t_m}{P} \left( \frac{R_0 T}{M_{mol}} \right)^{\frac{1}{2}} \quad (4.37)$$

where  $M_{mol}$  is the molar mass of the gas surrounding the bar,  $P$  its pressure,  $T$  its temperature, and  $R_0$  is the universal gas constant. The micro-scanner will be encapsulated in air at standard atmosphere. Temperature  $T$  should be set at  $T_0$ , although, in reality, the boundary layer in the vicinity of the torsion rod has a higher temperature and depends on the heat generated by the actuators. Hence, for a short period of time and as an estimation,  $T$  will be set as  $T_0$  in first approach, but the quality factor is proportional to the square root of the average temperature in

the torsion bar. We can as of now predict a resonance frequency shift of the torsion mode as long as the temperature of the torsion bar will fluctuate with the bias voltage applied on the inner actuators between the mirror plate and the inner frame. For a rod at the ambient temperature of 293.15 K, the quality factor of the torsional mode is estimated at 2/3, corresponding to an underdamped system. The value of the Q-factor is very far from reality as long as we considered that the rotational movement was only due to the spring constant of the torsion rod whereas actually, the electrothermal actuators also play a significant part in the total stiffness and consequently in the quality factor as indicated in Eq. (4.37).

The maximum shear stress admissible  $\tau_Y$ , given by [349, page. 401] in Eq. (4.38) is approximately equal to half of the tensile yield strength and has to remain lower than the Von Mises shear stress in torsion  $\tau_e$  given by Eq. (4.39) [353] so that:

$$\tau_e < \tau_Y = \frac{1}{2}\sigma_Y$$

$$\tau_Y = \frac{3C}{w_r t_r^2} \left[ 1 + 0.6095 \frac{t_r}{w_r} + 0.8865 \left( \frac{t_r}{w_r} \right)^2 - 1.8023 \left( \frac{t_r}{w_r} \right)^3 + 0.9100 \left( \frac{t_r}{w_r} \right)^4 \right] \quad (4.38)$$

$$\tau_e = \frac{\sqrt{3}}{2} \sqrt{\sigma_{xz}^2 + \sigma_{yz}^2} = \frac{\sqrt{3}}{4} \frac{\theta_r \mu}{L_r} \sqrt{w_r^2 + t_r^2} \quad (4.39)$$

As a result, for a given angle of the mirror plate, the Von Mises stress induced in the torsion bar increases with the length and width of the cross section and decreases with the length of the rod. Hence, assuming a maximum angle of  $+30^{\circ \text{mech}}$ , a given thickness of about  $3.3 \mu\text{m}$  and a maximum width of  $40 \mu\text{m}$ , the length of the rod has to satisfy  $L_r \geq 2.49/\tau_Y$ .

Silicon dioxide and aluminum have identical Young's modulus and the platinum heater's influence in the equivalent Young's modulus is minor. Though, the two main constituents of the torsion bar do not have comparable elastic limit and the "weaker" one may cause the beam to culminate into a breaking to the detriment of the other one. The contribution of the aluminum amid the layers of silicon dioxide brings ductility and yields a more resistant beam in motion and fatigue. The sturdiness of the aluminum "inlaid" torsion beam – tested from a former unpublished trial experiment – is illustrated in Fig. 4.12. After identical actuations on both structures, the aluminum-free beam rapidly breaks off. The two ends of the torsion beam have been filleted to reduce the high stress effect on the sharp angles between the bar and the support. The torsion beam, made of both thermal conductors and insulators (Al, Pt and SiO<sub>2</sub>) is a thermal bridge between the mirror plate and the inner frame. Comparing the thermal behavior of the torsion beam with the one of the electrothermal actuators that deflect the mirror plate, it is obvious that the thermal resistance of the torsion beam due to conduction will be much smaller than the one of the actuators. Although, the torsion beam is more convective, the resistance due to convection of the mirror plate is much smaller, the impact of the torsion beam can be neglected and the mirror plate and the inner frame are considered to be connected by a purely conductive element in the thermal model of the whole micro-scanner. At some point, the thermal resistance due to conduction of the torsion beam can be incorporated to the one of the electrothermal actuators driving the mirror plate.

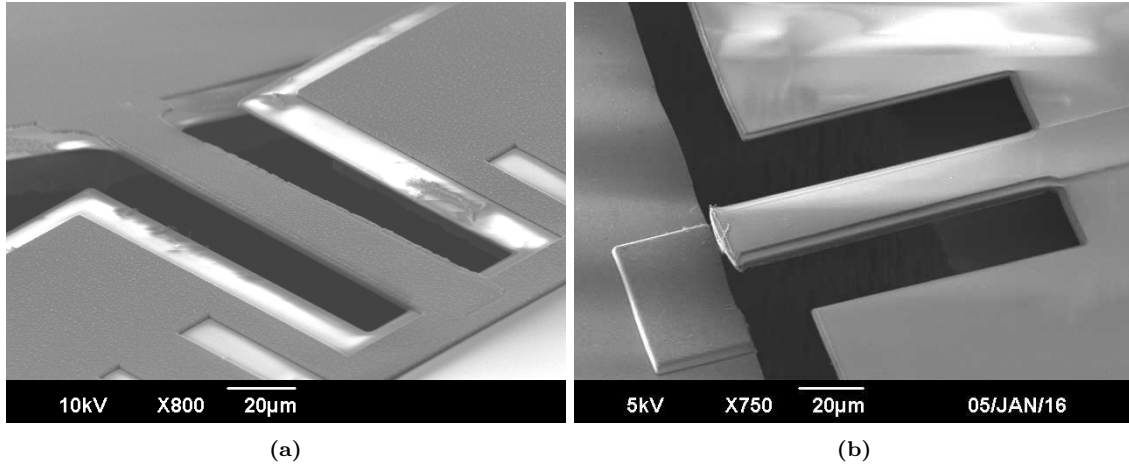


**Figure 4.12:** SEM pictures of torsion beams composed of different materials and their state after identical actuation. (a): Aluminum inlaid torsion beam. This structure is schematically described in Fig. 4.10(left). (b): Aluminum-free torsion beam.

**Table 4.5:** List of the main parameters of the mirror plate and torsion beam.

Parameter	Value	Description
Torsion beam		
$L_r$	160 $\mu\text{m}$	Length of the rod
$w_r$	28 $\mu\text{m}$	Width of the rod
$t_r$	3.46 $\mu\text{m}$	Thickness of the rod
$E_r$	70 GPa	Equivalent Young's modulus of the rod
Mirror plate		
$L_m$	950 $\mu\text{m}$	Length of the mirror plate
$w_m$	1015 $\mu\text{m}$	Width of the mirror plate
$t_m$	25 - 40 $\mu\text{m}$	Thickness of th mirror plate

### 4.3.2 Mirror coating and plate deformation

The mirror plate is used to deflect the focused incoming beam and to reinject the backreflected beam from the tissue into the OCT system. Aluminum was used as the reflecting material for a reason of compatibility with the fabrication process. Furthermore, aluminum is a satisfactory reflector for near-IR light [128, 259]. A thickness of 1.1  $\mu\text{m}$  was deposited on the upper side of the mirror plate (front side of the SOI wafer) as well as 2000 to 4000  $\text{\AA}$  on the back side of the mirror. The process of metalization is described in Chapter 5. The mirror front side layer and the actuators' high CTE layer are deposited in one step. This justifies the thickness of the aluminum on the front side. But, in fact, such a thick layer of aluminum is not required to provide a satisfactory reflectivity. It was shown that over a given threshold, the thickness of a film of aluminum in the near-IR range very slightly affects its reflectivity [354]. The reflectivity of a similar mirror plate with the same thickness of aluminum in near-IR was measured by Wu [295] between 84 and 86%. However, in order to increase the reflectivity and improve the surface quality of the mirror plates, a thin layer of Gold could be deposited during an independent step of fabrication. At all time, the mirror is considered as a rigid body without dynamic deformation. Indeed, the maximum difference between the mirror plate deflection curve and its upper average surface d as shown in Fig. 4.13 (commonly compared with the wavelength of the light beam reflected by the mirror) was estimated by Eq. (4.40) from [355] in the order of magnitude of 1 nm around a frequency of



1 kHz and can thus be neglected. Indeed, the first natural frequency of the mirror plate oscillating about its center is in the range of the MHz according to [355].

$$d = 6 \frac{M_m(1 - \nu^2)}{E} \frac{w_m^4}{t_m^3 L_m} \hat{\theta}_r \omega^2 \quad (\text{in } \mu\text{m}) \quad (4.40)$$

In Eq. (4.40),  $E$  and  $\nu$  are the Young's modulus and the Poisson's ratio of Si,  $\hat{\theta}_r$  is the angular amplitude of the mirror plate ( $\hat{\theta}_r = \theta_{max} - \theta_{min}$ ), and  $\omega$  is the circular frequency in rad/s. Finally, we conclude that the dynamic distortions of the mirror plate do not affect the optical scan.

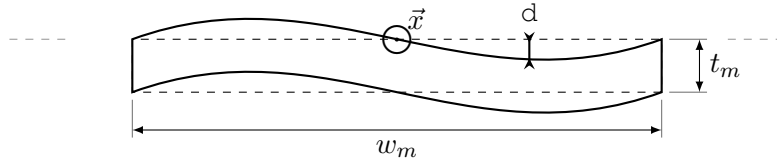


**Figure 4.13:** Mirror distortion due to dynamic torque.

However, temperature might also affect the curvature or the distortion of the plate. The temperature change oscillating from room temperature to a few hundred °C at a frequency depending on the electrical actuation frequency may create enough stress into the layers constituting the mirror plate to reshape the light beam and affect the resolution. The radius of curvature is due to the initial intrinsic stress (mainly induced by the temperature deposition of the thin films on top of the Si mirror substrate) and the stress induced by the temperature change. However, no data is available on the initial stress and radius of curvature to estimate this distortion. Plate roughness, surface quality and deformation will be characterized in Section 6.1.1.

### 4.3.3 Electrothermal actuators

#### 4.3.3.1 Bimorph array

The electrothermal bimorph array actuator will be referred to as pitch actuator for it controls the pitch motion of the micro-scanner. It is composed of 64 identical bimorph cantilevers in parallel. The 64 beams enclose a platinum heater that generates a temperature change by Joule heating relatively uniform about the span of the array [216, 217]. The Pt resistors of 2 adjacent bimorphs are connected in parallel forming 32 electrical resistors attached in series. Hence, the pitch actuator can be considered as one equivalent electrical resistor composed of 32 two-beam parallel electrical resistors in series as illustrated in Fig. 4.14 by [216]. Hence, the electrical initial resistance of one bimorph must be multiplied by a factor of 32 to obtain the total electrical initial resistance of the array. The thermal resistance due to conduction becomes the resistance of one bimorph divided by the total number of bimorphs in parallel  $N_p$ . This is also true for isolation bridges. The geometric parameters of the bimorph array are provided in Table 4.6 and a sketch of the different layers composing one bimorph cantilever from the pitch actuator is illustrated in Section 4.2.2. The fabrication process is the object of Chapter 5.

The electrical platinum path is connected to the two outer pads located on the 550  $\mu\text{m}$ -thick silicon substrate. The platinum path is continuous all the way to the pads and is coated by a thick layer of aluminum to reinforce the bonding pads. The roll actuators' pads are also located on the silicon substrate between the pitch actuator's pads. Platinum cannot be used to connected

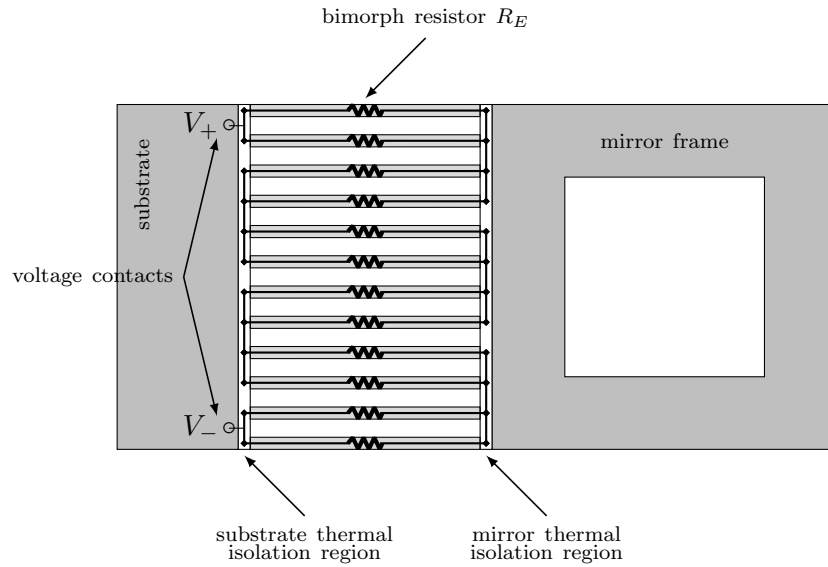


**Figure 4.14:** Top-view schematic of the bimorph array electrical path.

the roll actuators' electrical resistor to the bonding pads as far as it would directly heat up the bimorphs of the array, directly causing a cross coupling in the actuation. Therefore, in order to keep the fabrication process free from additional steps, the aluminum constituting the high CTE layer of the pitch actuator bimorphs is used to transport the current through them and to the roll actuator's heater. The aluminum and the platinum on the bimorphs of the array are not electrically connected to each other to prevent shortcuts. The two metals are insulated by a thin layer of  $\text{SiO}_2$ . First, the electrical resistivity of the aluminum is lower than the one of the platinum by a factor of 5 and second, the cross section of the aluminum layer in the bimorph is much higher than the platinum which makes the aluminum contribution to the bimorph temperature change by Joule heating negligible. The length of the bimorph cantilevers defines the initial tilt angle of the inner frame and consequently the maximum displacement of the pitch axis at the steady state. The thickness of the layers in the bimorph has been optimized using Eq. (4.24). The length has been calculated based on the model of bimorph beams described in Section 4.2.2 and according to the dynamic behavior expected due to the scanning requirements. The mass carried by the pitch actuator includes the mass of the inner frame plus the one of the mirror plate. Therefore, recalling the relation between the resonance frequency and the mass, it is natural to assign the slow scan with the pitch motion. The width and the gap between the beams depends on the fabrication release step and has to be consistent with the roll actuator so that all the actuators are released in the same time and the least stress is induced in the structure. However, the width of the beams has to be minimized: for thermal expansion occurs in an isotropical way, wide beams would bend along their width and could cause severe deformations. The nature of the endoscopic probe was chosen as side-view. Thus, the micro-scanner has to deflect the light beam by an angle of  $\pm 5^\circ$  centered around a mean angle of  $45^\circ$ . The mean angle plus half of the maximum angular course at the corresponding frequency of the scan defines the maximum initial angle of the mirror after fabrication. As we discussed about in Section 4.2.2, this parameter is due to intrinsic stress and can only be estimated based on the outcomes of former characterisations. The dimensions that were picked for the bimorph array of the first batch of micro-scanners are given in Table 4.6.

**Table 4.6:** Parameters chosen for the first design of the bimorph array actuators.

Parameter	Value
Number of bimorphs	64
Length	350 $\mu\text{m}$
Width of Al	22 $\mu\text{m}$
Width of Pt	8 $\mu\text{m}$
Thickness of Al	1.0 $\mu\text{m}$
Thickness of SiO <sub>2</sub>	1.1 $\mu\text{m}$
Thickness of Pt	1500 $\text{\AA}$

### 4.3.3.2 Meshed inverted-series-connected actuators

Most piezoelectric and electrothermal micromirrors use a single cantilever beam to generate the actuation [262]. However, as shown in Fig. 4.8, a single cantilever develops 3 dofs: 2 in translation, vertical and horizontal and 1 rotation. These 3 displacements sometimes result in issues when only the horizontal displacement is needed for actuation. Indeed, the higher the vertical displacement, the higher the horizontal and angular displacements. Fabricating a real pivot boundary in the micro world is quite a challenge. Thus, each rigid-body boundary is used as a deformable component that bends or twists to absorb the movement of the structures. Sometimes, the motions are so broad that they cause the deformable joints to break. In our design, the inner actuators are connected to the inner frame and the mirror plate via isolation bridges mainly made of SiO<sub>2</sub> for the sake of thermal insulation. Unfortunately, SiO<sub>2</sub> is a brittle material with a low breaking point and should not be used as a reliable mechanical bending part. Therefore, when large displacements are needed, it is preferable to make the actuators carry the flexibility rather than the connecting bridges.

ISC configuration was developed to tackle the lack of flexibility in the single bimorph actuators enabling high displacements without soliciting the SiO<sub>2</sub> bridges. ISC actuators enable a piston motion on the  $z$  axis free from tilt motion of the tip and an evolved version, the **double S-shaped inverted-series-connected (DSSISC)** allows to get rid of the lateral shift present in the simple ISC actuator. The first ISC actuator was proposed, developed and studied by Todd *et al.* [219] in 2005. As shown in Fig. 4.15, the ISC actuators are composed of the a series of bimorphs beam connected together in order to get rid of the unwanted dof that is the tip tilt. When the actuator is only composed of bimorphs, the total displacement of the tip can be related to the displacement of the single bimorph tip that depends itself on the voltage applied [220] and can be obtained assuming that the curvature of the two-bimorph beam constituting the ISC actuator is the same. Its expression is simply two times the displacement of one single bimorph and is given by [220, 339] in Eq. (4.41) assuming the displacement is small enough to linearize the cosine at the first order.

$$\delta_{isc} \approx \frac{L_b^2 \Delta\alpha \Delta\bar{T}}{\chi} = \frac{L_b^2 \Delta\alpha}{2\xi\chi} \left( \sqrt{\frac{4\xi\bar{R}_T}{R_{E0}} V^2 + 1} - 1 \right) \quad (4.41)$$

From Eq. (4.41), the angle of the mirror around the fixed rotation axis can be derived as follows (Eq. (4.42)):

$$\theta_r = \arcsin \frac{4\delta_{isc}}{w_m} \approx \frac{4\delta_{isc}}{w_m} \quad (4.42)$$

One of the limitations of this design was reported by Jia: the weak connection between two con-

secutive inverted bimorphs is transmitted to the whole structure causing more frequent breakages [356]. Recent designs consisted in making the connected structure sturdier by the mean of an uninterrupted layer all the way through the actuator and then sandwiching it between the other constituents that are the  $\text{SiO}_2$  and the Pt heater. An overlapping portion is introduced between each consecutive inverted and non-inverted bimorph and is made of two outer  $\text{SiO}_2$  layers and an Al layer in between enclosing the thin Pt heater layer as shown in Figs. 4.15 and 4.16. This overlapping layer is neutral in terms of stress distribution and is represented in Fig. 4.17c. Similarly to the torsion bar, the stresses are auto compensated and the overlap is a pure reinforcing component. In this case, the length of the overlapping sections  $L_{OL}$  has to be incorporated in the equation of the displacement. Taking into account that the bimorphs and the overlapping segment are multimorphs, Jia [356] used Eqs. (4.25) to (4.29) to show that the ratio of the length of the inverted and the non-inverted bimorph gives a factor of 2.1 as represented in Fig. 4.16. Hence, based on the sketch of Fig. 4.15, for small angles, the displacement of the tip of the ISC actuator with overlap yields:

$$\delta_{isc} \approx \theta_b (2.7L_{NI} + L_{OL}) \quad (4.43)$$

The cross sections resulting from the incorporation of the platinum heater in the bimorph-based

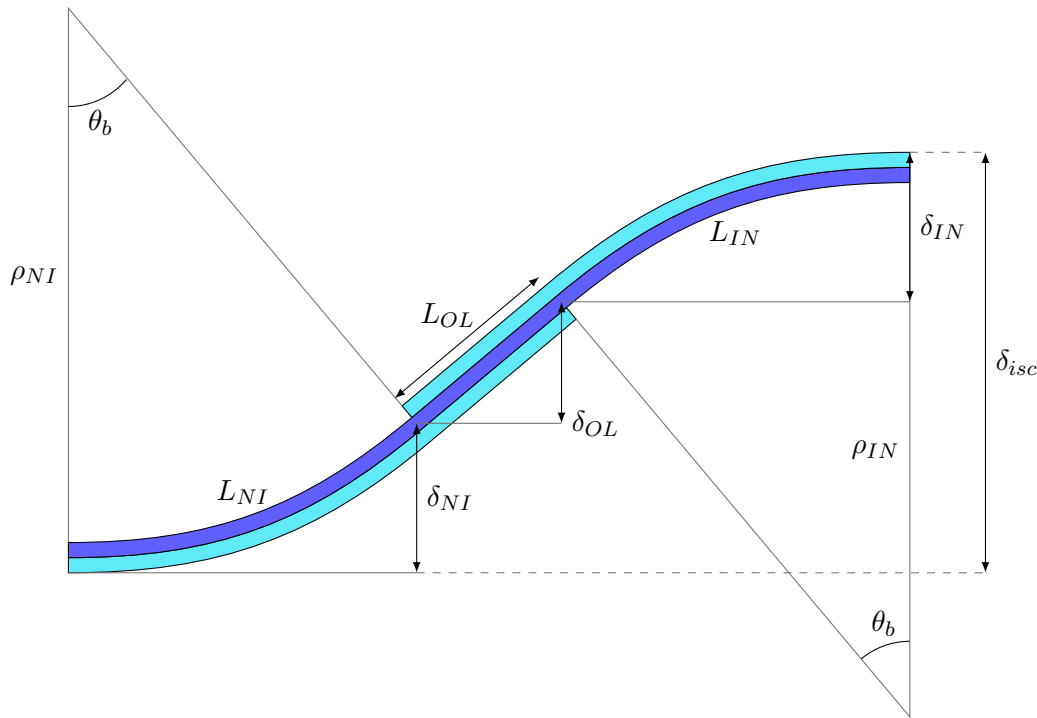


**Figure 4.15:** Deflection of the ISC structure with overlapping section and parameters for calculation.

ISC actuator are represented in Figs. 4.17a to 4.17c and are compared with the stack configuration of the torsion bar introduced in Section 4.3.1. The profiles are approximated by rectangular sections to simplify the calculations, although the shapes are process-dependent and are developed in Chapter 5. The ISC actuator has been extended to the DSSISC actuator and consists of a piling up of two ISC actuators in series as represented in Fig. 4.18 and allows to remove the second undesired dof: the lateral shift. Each bimorph beam composing the DSSISC actuator can be lumped by a linear spring under the assertion of small displacements. However, rather than subdividing each ISC structure into 3 others, a simplified manner consists of considering one

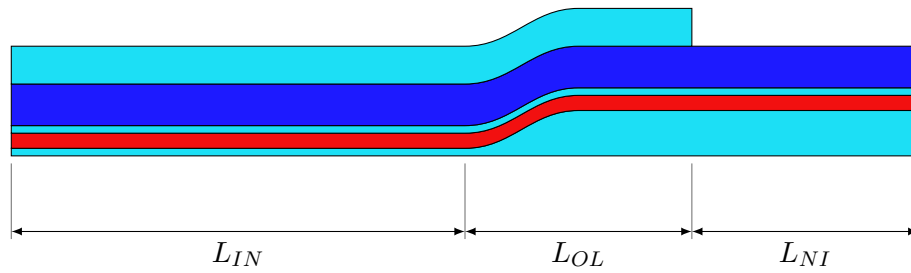


**Figure 4.16:** Schematic side view of the ISC actuator piling up order and configuration during fabrication and before release.

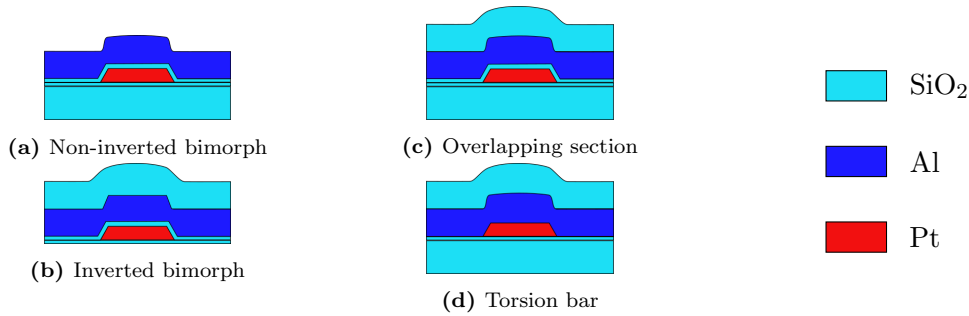


**Figure 4.17:** Schematic cross section of the (a) non-inverted bimorph, (b) inverted bimorph and (c) overlapping segment and (d) torsion beam for comparison. Courtesy from [176].

ISC structure as one cantilever beam of same width  $w_b$  and of thickness  $t_b$  as only the overlapping segments and the collarbone (segment  $c$  in Fig. 4.18) are thicker of a  $1\ \mu\text{m}$ - $\text{SiO}_2$  layer. This assertion is only available around a displacement working point which is consistent with a small temperature change. Therefore, both electrothermal and thermomechanical transfer functions of the system can be consolidated coherently to model the whole system by an electro-thermo-mechanical linear transfer function around a working point corresponding to a small change in temperature leading to a small change in position. In order to reduce the deviation of the displacement along the vertical axis, DSSISC actuators have been erected in pairs and in parallel so that the stiffness and the stability are both increased. This new structure is referred to as a “pair of DSSISC” and was widely implemented and studied in the literature [105, 127, 128, 140, 163, 219–221, 238–251, 296, 300]. Compared with actuators composed of simple pairs of DSSISC, the higher displacement required by our system specifications motivated an “evolution” of the former structure (represented in dark red in Fig. 4.19) towards a meshed structure allowing the same operational frequency for a higher displacement and twice as less space occupied as actuators exhibiting the same features [253]. The additional components completing the basic structure to form the final meshed inverted-series-connected (MISC) actuator are represented in light green in Fig. 4.19.

The actuator is an equivalent spring with a constant stiffness. As sketched in Fig. 4.20, the actuators are located on both sides of the mirror plate rotating around the torsion bar axis. They apply the same force on the mirror plate making the total equivalent spring exert a spring force stiffer by a factor of 2. As mentioned earlier, the actuators are usually made of a pair of DSSISC structures in parallel. Thus, the spring constant is divided by a factor of 2 compared to the simple DSSISC actuator studied hereafter and reported in Fig. 4.18. The stiffness of a fixed-horizontally-

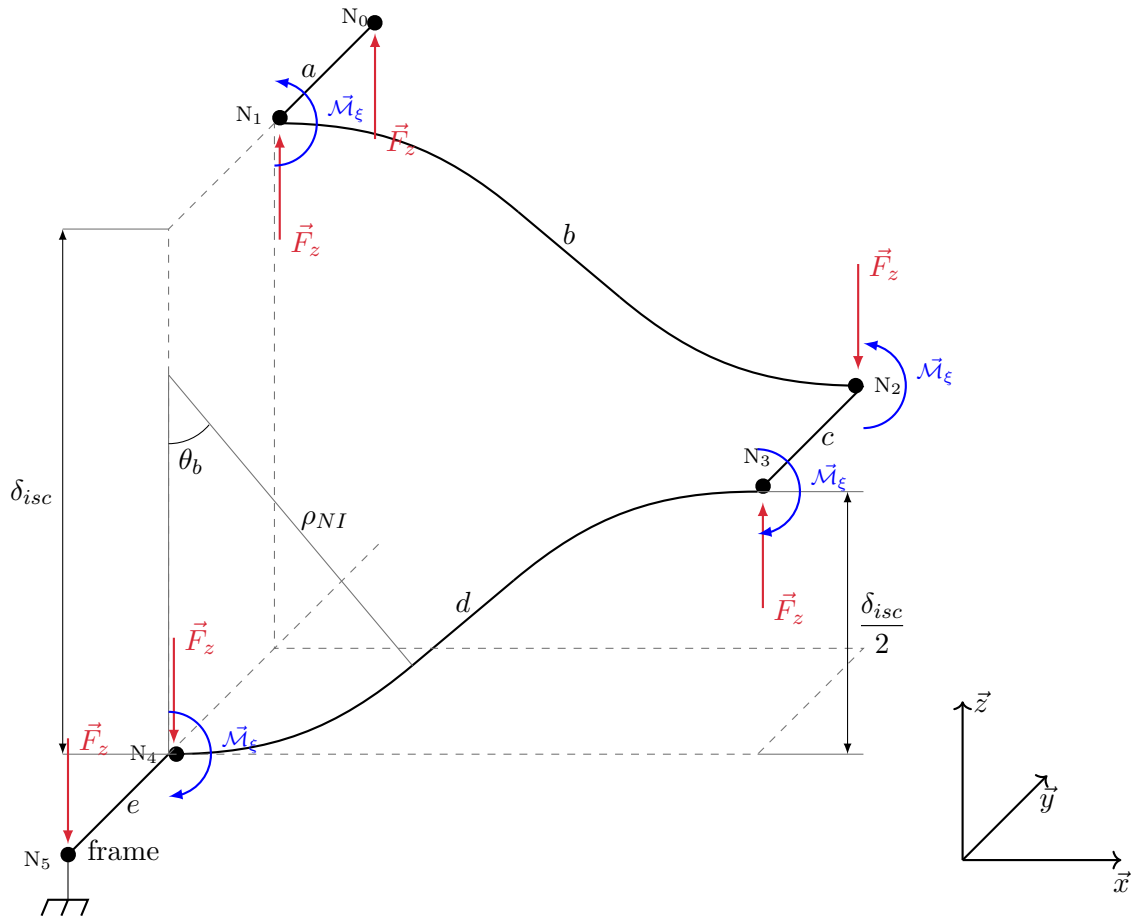


Figure 4.18: Schematic view of the split up logic of the DSSISC actuator with the segments and the nodes.

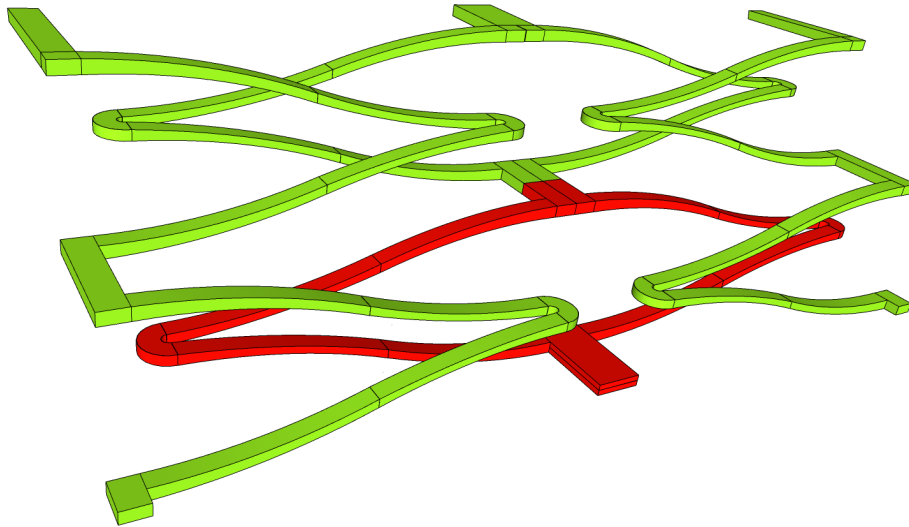


Figure 4.19: MISC actuator proposed in this work (in light green), as an evolution of the basic pair of DSSISC structure (in dark red).

guided end beam is given by:

$$\begin{cases} k_x = \frac{Ew_b t_b}{L_b} \\ k_y = \frac{Ew_b^3 t_b}{L_b^3} \\ k_z = \frac{Ew_b t_b^3}{L_b^3} \end{cases} \quad (4.44)$$

The stiffnesses associated with the vertical and the axial displacements on  $\vec{z}$  and  $\vec{y}$  respectively, increase when the length diminishes. Furthermore, the vertical stiffness  $k_z$  is proportional to the thickness of the beam to the power of three whereas the width of the beam is the parameter mainly affecting the axial stiffness  $k_y$ . The dimensions of the actuators are first limited by the space available between the mirror plate and the inner frame that have to be reasonably controlled to guarantee the size of the footprint and the fill-factor. As represented in Fig. 4.20, the force developed by the actuator is exerted between the inner frame and the mirror plate anchor points and thus varies with the angular position of the mirror plate. The equivalent stiffness of the DSSISC actuator should thus be a composition of the stiffnesses of a spring with two spring constants of the  $\vec{z}$  and  $\vec{y}$  axes respectively. In fact, analytical calculations for tilting MEMS micro-scanners used to ignore the stiffness about the axial  $\vec{y}$  axis [335, 356] so that only the piston mode frequency could be estimated from the expression of the vertical stiffness of actuators in parallel as in Eq. (4.44) replacing the term of length  $L_b$  by the length of the main slender cantilever arms. Unfortunately, the tilt mode resonance cannot be calculated the same as far as the actuator is much stiffer about the axial direction than the vertical direction. The two displacements  $\delta y$  and  $\delta z$  are linked by the angle of rotation of the mirror plate  $\theta_r$ . In order to get more into details relatively to the motion of the mirror plate, we would have to notice that the lumped single spring represented in Fig. 4.20 is composed of a series of straight and rotational springs depicting the segments of the actuator subject to bending and torsion. Indeed, as it is clearer in the 3D representation of Fig. 4.18, the actuator is a complex structure made of 5 elements including 2 main slender cantilever beams of respective length  $b$  and  $d$  working in flexion and torsion around their axis. Therefore, the effective force applied on the mirror and seen from the mirror side, is the projection of the vector directing the force of application of the lumped-actuator spring onto the vector tangeant to the displacement of the edge of the mirror plate as represented in Fig. 4.20 and expressed by Eq. (4.45).

$$F_m = \|(k_y \delta y \cdot \vec{y} + k_z \delta z \cdot \vec{z})\| \frac{\vec{F}_i}{\|\vec{F}_i\|} \cdot \vec{z}_m \quad (4.45)$$

The spring constant of the actuator (in N/m) can be converted into an angular spring constant (in N m) considering the moment generated by the actuator about the rotation axis. The relation is established in Eq. (4.46) where  $k_\theta$  is the angular spring constant due to the actuators and  $\theta_r$  the angle of rotation of the mirror plate in rad.

$$\mathcal{M}_m = F_m \frac{w_m}{2} = k_\theta \theta_r \quad (4.46)$$

To enable the displacement  $\delta z$ , the strain energy from torsion has to be included in the model as well as the bending of the connecting bridges  $a$  and  $e$  and the collarbone  $c$  [357]. For the intended OCT scan, the scanning frequency of the roll actuator has to reach at least 1 kHz. The resonance frequency of a beam of stiffness  $k_a$  is given by  $\frac{1}{2\pi} \sqrt{\frac{k_a}{M_m}}$  with  $M_m$  the moving mass at the tip of the cantilever beam. However, the resonance of the mirror plate in torsion is rather given by  $\frac{1}{2}\pi \sqrt{\frac{k_\theta}{J_m}}$ . In order to determine the rotational stiffness  $k_\theta$ , the vertical and axial stiffnesses  $k_z$  and  $k_y$  need to be calculated first. In a first time, the spring constant of the simple DSSISC actuator is calculated. The expression of the spring constant for a pair of parallel DSSISC can be readily derived by combining lumped springs as capacitors (Table 4.1). We work under the assertion of small displacements. Each node in Fig. 4.18, from  $N_0$  to  $N_5$  in our case is associated with the

corresponding torsor of forces and moments in the linked local basis  $(\vec{\delta}, \vec{\xi}, \vec{\tau})$ :

$$\mathcal{T} = \left\{ \begin{array}{c|c} F_{\delta} & \mathcal{M}_{\delta} \\ F_{\xi} & \mathcal{M}_{\xi} \\ F_{\tau} & \mathcal{M}_{\tau} \end{array} \right\}_{N_i} \quad (4.47)$$

For each segment,  $\vec{\tau}$  and  $\vec{z}$  are collinear,  $\vec{\xi}$  is collinear about the direction about the length of the segment and  $\vec{\delta}$  is the last vector forming the orthonormal base. Only the vertical efforts  $\vec{F}_z$  about  $\vec{\tau}$  and moments  $\vec{\mathcal{M}}_{\xi}$  about  $\vec{\xi}$  are represented for the sake of clarity. Furthermore, the straight forces  $\vec{F}_z$  are only represented applying on the slender segments and anchors whereas the moments  $\vec{\mathcal{M}}_{\xi}$  are represented on the short connecting arms and the collarbone.

The calculations are based on the second theorem of Castigliano developed by Fedder [357] in a model of in-plane serpentine with  $n$  nodes,  $n \in \mathbb{N}$ . In a first approach, the planar stiffnesses  $k_x$  and  $k_y$  may be determined including in-plane bending moments and forces. Then in a second stage, the vertical spring constant  $k_z$  will be calculated, including torsion and out-of-plane moments and forces. An equivalent Young's modulus is adopted about the length of the beam. We take  $E = 70$  GPa in our case.  $I_b$  and  $I_t$  are the second moments of area of the beam around the  $\vec{z}$  and  $\vec{x}$  axes respectively. The vertical external load is neglected as the mass of the micro-scanner is too small to be impacted by gravity. Only the problem in torsion for the resolution of  $k_z$  is represented in Fig. 4.18, and only the moments about the  $\vec{y}$  axis are represented for the sake of clarity. The total strain energy of the structure under torsion around the  $\vec{x}$  axis and bending in the XZ plane can be derived:

$$U_{x,y} = \frac{1}{2} \sum_i \int_0^{L_i} \frac{(\mathcal{M}_{\tau})_i^2}{E(I_{\tau})_i} d\zeta \quad (4.48)$$

$$U_z = \frac{1}{2} \sum_i \int_0^{L_i} \frac{(\mathcal{M}_{\xi})_i^2}{E(I_{\xi})_i} + \frac{(\mathcal{M}_{\delta})_i^2}{\mu(I_{\delta})_i} d\zeta \quad (4.49)$$

where the second moment of area for the bending in the  $(\vec{\xi}O\vec{\delta})$  and  $(\vec{\xi}O\vec{\tau})$  plane are given in Eqs. (4.50) and (4.51) and the torsion in the  $(\vec{\delta}O\vec{\tau})$  plane from Timoshenko and Goodier [358](p. 278) or from the Roark's formula [349] is given by Eq. (4.35) and recalled here in Eq. (4.52).

$$I_{\tau} = \frac{w_b t_b^3}{12} \quad (4.50)$$

$$I_{\delta} = \frac{w_b^3 t_b}{12} \quad (4.51)$$

$$\begin{aligned} I_{\xi} &= \frac{1}{3} w_b t_b^3 \left[ 1 - \frac{192}{\pi^5} \frac{t_b}{w_b} \left( \sum_{n=1,3,5,\dots}^{\infty} \frac{1}{n^5} \tanh \left[ \frac{n\pi}{2} \frac{t_b}{w_b} \right] \right) \right] \\ &= w_b t_b^3 \left[ \frac{1}{3} - 0.21 \frac{t_b}{w_b} \left( 1 - \frac{t_b^4}{12w_b^4} \right) \right] \end{aligned} \quad (4.52)$$

The boundary conditions are developed in [357] and the stiffnesses for a single DSSISC actuator are given by Eqs. (4.53) and (4.54) where the value of the parameters  $a$ ,  $b$ ,  $c$ ,  $d$  and  $e$  specified



in Fig. 4.18 are provided in Table 4.7.

$$k_y = \frac{NUM_y}{DEN_y}, \quad (4.53)$$

where

$$\begin{aligned} NUM_y &= 3EI_\tau(a^4 + 8a^3b + 4a^3c + 4a^3e + 12a^2bc + 6a^2c^2 + 12a^2ce + 6a^2e^2 + 12abc^2 + 4ac^3 + 12ac^2e \\ &\quad + 12ace^2 + 4ae^3 + 12b^2c^2 + 8bc^3 + 12bc^2e + 12bce^2 + 8be^3 + c^4 + 4c^3e + 6c^2e^2 + 4ce^3 + e^4) \\ DEN_y &= (b^2(2a^4b + 3a^4c + 4a^3b^2 + 8a^3bc + 8a^3be + 12a^3ce + 6a^2b^2c + 12a^2bc^2 + 24a^2bce + 12a^2be^2 \\ &\quad + 36a^2c^2e + 18a^2ce^2 + 15ab^2c^2 + 26abc^3 + 24abc^2e + 24abce^2 + 8abe^3 + 3ac^4 + 36ac^3e \\ &\quad + 36ac^2e^2 + 12ace^3 + 6b^3c^2 + 13b^2c^3 + 15b^2c^2e + 6b^2ce^2 + 4b^2e^3 + 2bc^4 + 26bc^3e + 12bc^2e^2 \\ &\quad + 8bce^3 + 2be^4 + 3c^4e + 3ce^4)) \end{aligned}$$

$$k_z = \frac{12EGI_\delta I_\xi [2EI_\delta b + GI_\xi(a + c + e)] [EI_\delta(a + c + e) + 2GI_\xi b]}{DEN_z} \quad (4.54)$$

$$\begin{aligned} DEN_z &= E^3 I_\delta^3 (12b^2(4a^3 + 8a^2c + 4a^2e + 2abc + 5ac^2 + 4ace + 2bce + c^3 + c^2e)) \\ &\quad + E^2 GI_\delta^2 (4I_\xi b(8a^4 + 29a^3c + 20a^3e + 24a^2b^2 + 3a^2bc + 42a^2c^2 + 57a^2ce + 18a^2e^2 + 4ab^3 \\ &\quad + 24ab^2c + 3abc^2 + 6abce + 29ac^3 + 60ac^2e + 39ace^2 + 8ae^3 + 4b^3c + 4b^3e + 6b^2c^2 + 3bc^2e \\ &\quad + 3bce^2 + 8c^4 + 23c^3e + 24c^2e^2 + 11ce^3 + 2e^4)) + EG^2 I_\delta (I_\xi^2(a^5 + 5a^4e + a^3(64b^2 + 10e^2) \\ &\quad + a^2(8b^3 + 96b^2e + 10e^3) + a(16b^3e + 48b^2e^2 + 5e^4) + 8b^5 + 8b^3e^2 + 16b^2e^3 + c^5 + c^4(5a + 5e) \\ &\quad + c^3(10a^2 + 20ae + 64b^2 + 10e^2) + c^2(10a^3 + 30a^2e + 168ab^2 + 30ae^2 + 8b^3 + 120b^2e + 10e^3) \\ &\quad + c(5a^4 + 20a^3e + 168a^2b^2 + 30a^2e^2 + 16ab^3 + 192ab^2e + 20ae^3 + 16b^3e + 72b^2e^2 + 5e^4) + e^5)) \\ &\quad + G^3 I_\xi^3 (2b(a + c + e)(a^3 + 3a^2c + 3a^2e + 3ac^2 + 6ace + 3ae^2 + 2b^3 + c^3 + 3c^2e + 3ce^2 + e^3)) \end{aligned}$$

With the parameters chosen for the micro-scanner and specified in Table 4.7, Eqs. (4.53) and (4.54)

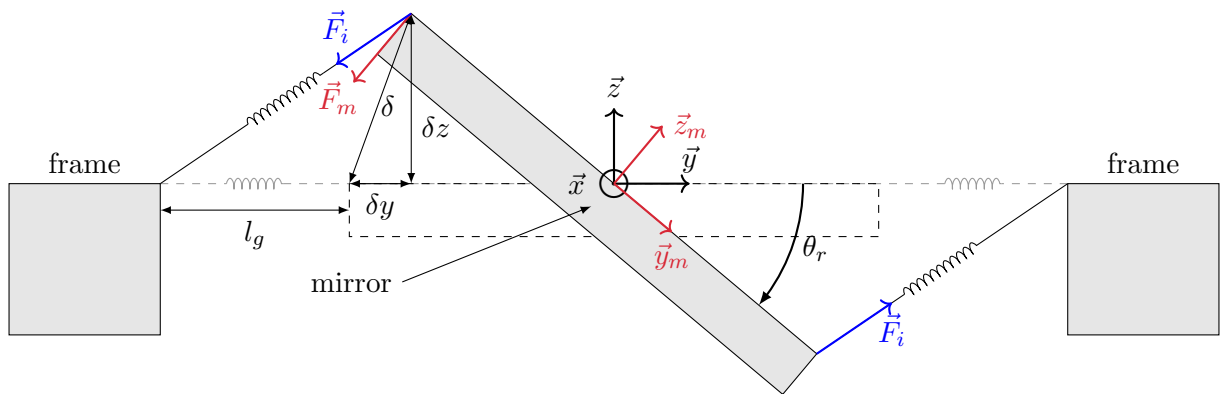


**Figure 4.20:** Side-view geometric schematic of mirror plate motion within the inner frame. The actuators are symbolized by springs. The springs in gray depict the actuators as they are initially during fabrication and after release of the micromirror. The mirror is represented in an out-of-plane position.

yield  $k_y = 14 \text{ N m}$  and  $k_z = 345 \text{ m N m}$ . These results are coherent with the beam dimensions as long as the width is much higher than the thickness and hence the vertical spring is more flexible than the axial spring. Let us write down the expression of the displacements of the virtual springs

$\delta_y$  and  $\delta_z$ :

$$\begin{aligned}\delta y &= \frac{w_m}{2}(1 - \cos \theta_r) \\ \delta z &= \frac{w_m}{2} \sin \theta_r \\ \delta &= \sqrt{\delta y^2 + \delta z^2} = \frac{w_m}{\sqrt{2}} \sqrt{1 - \cos \theta_r}\end{aligned}\quad (4.55)$$

Combining Eqs. (4.33), (4.45) and (4.55) readily yields an expression for the rotational spring constant  $k_\theta$  due to the contribution of the stiffnesses  $k_y$  and  $k_z$  of the simple **DSSISC** actuator:

$$\begin{aligned}k_\theta(\theta_r) &= \frac{F_m w_m}{2\theta_r} = \frac{w_m}{2\theta_r} \sqrt{\frac{(k_y \delta y)^2 + (k_z \delta z)^2}{(l_g + \delta y)^2 + (\delta z)^2}} ((l_g + \delta y) \sin \theta_r + \delta z \cos \theta_r) \\ &= \frac{w_m^2}{4\theta_r} \sqrt{\frac{k_y^2 (1 - \cos \theta_r)^2 + k_z^2 \sin^2 \theta_r}{l_g^2 + \frac{w_m}{2}(1 - \cos \theta_r)(2l_g + w_m)}} \left( l_g + \frac{w_m}{2} \sin \theta_r \right)\end{aligned}\quad (4.56)$$

Finally, as discussed in Section 4.3.1, the total equivalent spring constant necessarily includes the stiffness of the torsion rod calculated in Table 4.4. The total angular stiffness of the torsion mode of the mirror plate  $k_m$  actuated by a pair of parallel **DSSISC** located on both sides of the mirror plate around the axis of rotation materialized with two torsion bars is given by Eq. (4.57).

$$k_m = 2k_r + 4k_\theta(\theta_r) \quad (4.57)$$

To derive an expression for the resonance frequency, the value of the stiffness to be taken into account is the sum of the torsion bars stiffness  $2k_r$  and of the mean of the angular stiffness due to the actuators  $4\langle k_\theta \rangle$  between the upper and the lower angular positions of vibration of the mirror plate:  $\theta_{max}$  and  $\theta_{min}$  respectively. The calculation of  $\langle k_\theta \rangle$  can be performed graphically: indeed, as plotted in Fig. 4.21, the average stiffness is the slope of the chord jointing the utmost stiffnesses with respect to  $\theta_{max}$  and  $\theta_{min}$  centered on the average angle  $\langle \theta_r \rangle$ . Its expression is given by:

$$\langle k_\theta \rangle = \frac{k_\theta(\theta_{max}) - k_\theta(\theta_{min})}{2} \quad (4.58)$$

and finally, the corresponding eigen frequency is given by:

$$f_m = \frac{1}{2\pi} \sqrt{\frac{4\langle k_\theta \rangle + 2k_r}{J_m}} \quad (4.59)$$

From Eq. (4.59) we can conclude that, first, the resonance frequency is not a constant parameter, but varies with the tilt angle of the plate. The resonance frequency of the tilt mode of the mirror plate due to both the torsion bar and the **ISC** actuators has been plotted in Fig. 4.22 for 3 different widths of the torsion bar. Second, the mass of the mirror plays an important part in the speed of scan. Indeed, it is mostly composed of Si, and during the final release step of fabrication the Si thickness can fluctuate by  $\pm 2 \mu\text{m}$  from an average thickness depending on the etching time.  $2 \mu\text{m}$  corresponds to about  $\pm 9\%$  of error in the final thickness and yields about  $\pm 3\%$  of error on the resonance frequency. Calculating the total stiffness based on Eq. (4.44) assuming  $L_b = a+b+c+d+e$  yields 20% of error on the tilt mode resonance frequency. Let us also notice that although the torsion bar has a smaller impact on the tilt resonance frequency than the **ISC** actuators have, the

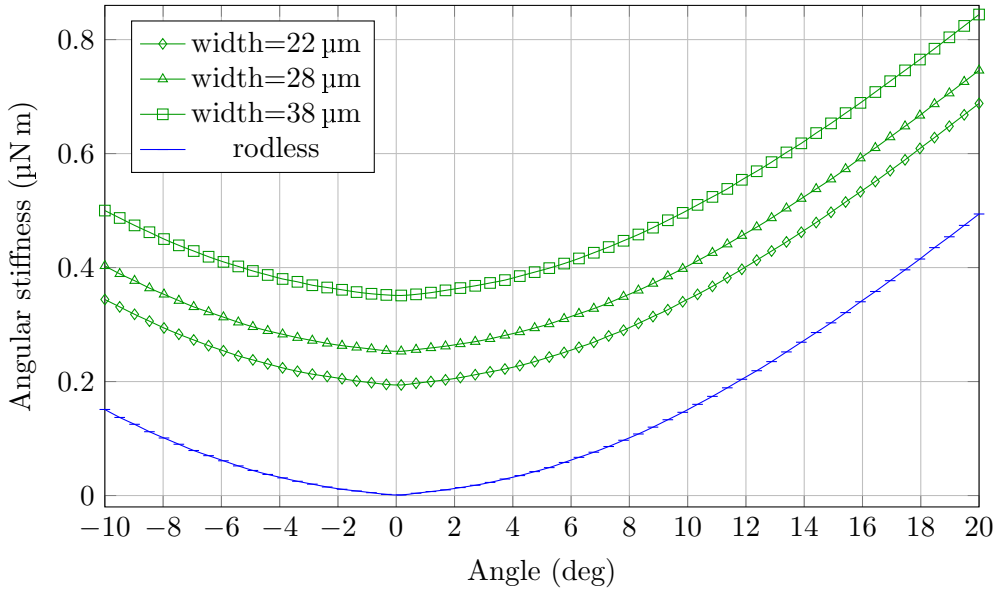


**Figure 4.21:** Variation of angular stiffness  $k_m$  with respect to angle of mirror for three different width of torsion bar. The “rodless” labelled curve is the stiffness of the actuators without the torsion bar.

width of the torsion bar still affects the frequency of the mode. Figure 4.23 shows the simulation result of the resonance frequency with respect to the thickness of the mirror (characterized by the thickness of the device layer).

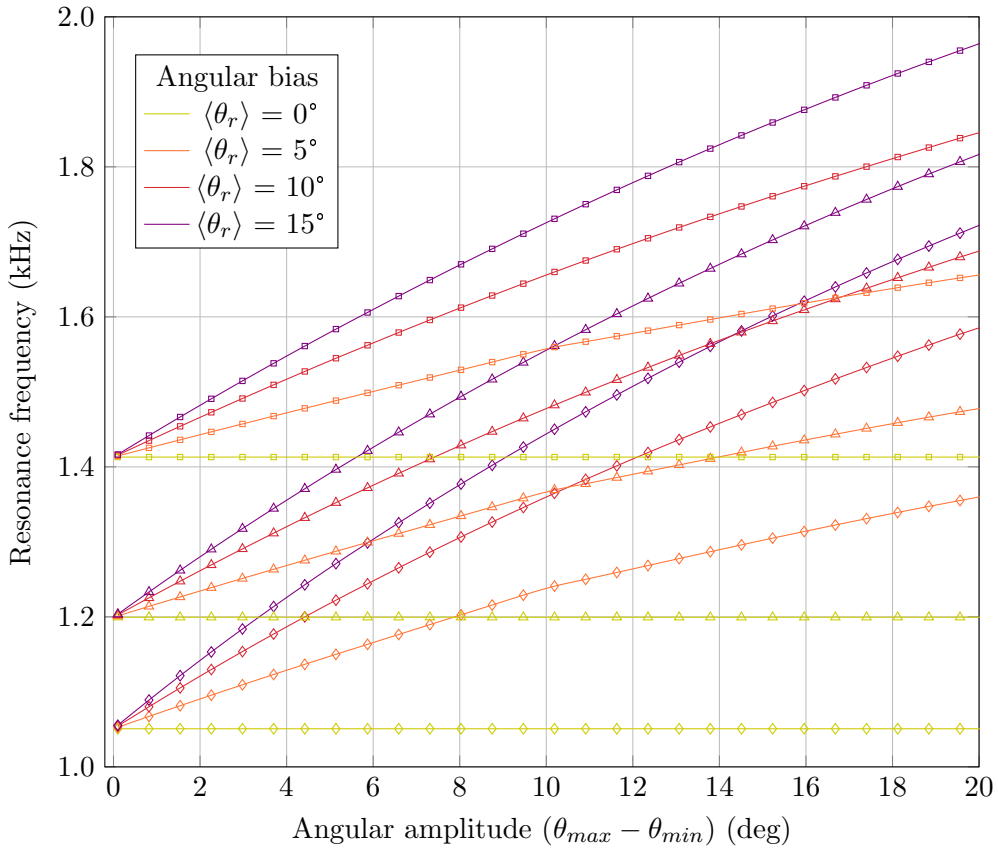


**Figure 4.22:** Resonance frequency versus amplitude of vibration of the mirror plate for four different average angles and three different widths of torsion bar denoted by their curve marks:  $\diamond$ : width= $22 \mu\text{m}$ ,  $\triangle$ : width= $28 \mu\text{m}$  and  $\square$ : width= $38 \mu\text{m}$ .

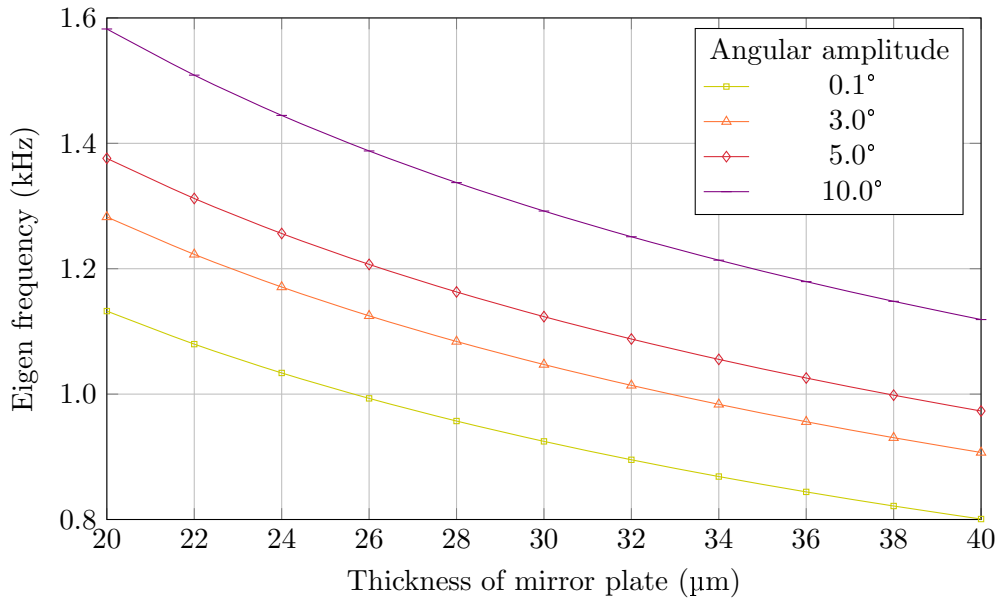


**Figure 4.23:** Resonance frequency variation with respect to thickness of the mirror plate for different angular amplitudes centered around an initial angular offset of  $18^\circ$ .

Finally, a few conclusions deserve to be pointed out: first, we conclude that for a torsion bar of width  $w_r \geq 22 \mu\text{m}$ , the target resonance frequency of 1 kHz is reached if the thickness of the mirror plate  $t_m \leq 26 \mu\text{m}$  for an angular amplitude of  $0.1^\circ$  (and the plate thickness can be as thick as  $38 \mu\text{m}$  for an amplitude of  $5^\circ$ ) because the tilt mode resonance frequency decreases with the thickness of the plate. Second, the resonance frequency of the mirror plate's pure roll mode increases with the bias angle  $\langle \theta_r \rangle$  and the vibration amplitude peak to peak ( $\theta_{max} - \theta_{min}$ ).

The actuator proposed in this work is based on the **ISC** structure. As a pair of parallel **DSSISC** actuators already measures up the requirements in frequency, we kept an identical order of magnitude for the stiffness of ours. However, given the space available in the footprint of the micro-scanner, a specific configuration of the **ISC** actuators can lead to a displacement comparatively increased by a factor of 2 along the vertical axis ending up into a larger angle range. Subsequently, the force generated to compensate the moment from the torsion bar is also increased. The **MISC** actuator consists of a pair of **double inverted-series-connected actuators of second generation (DISC)** arranged in parallel about one side of the mirror plate. Figure 4.24 displays a comprehensive view of the different structures based on the **ISC** structure and their lumped spring equivalence.

The frequency is high enough to match the scan requirements for the **OCT** image. However, the angular displacement can be increased to cover a broader **ROI**. The design proposed to increase the performance in displacement of the former **ISC** scanners includes two **DISC**<sup>8</sup> in parallel on both sides of the mirror plate. As the cumbersomeness of the actuators is often a subject that matters in the microworld, a few authors have tried to benefit from the spare region surrounding the mirror plates in the literature [215, 218] either reducing the footprint and the fill factor either filling up the gap with further actuators in order to modify the initial behavior of the micromirror. In our project, the **MISC** actuators have been introduced in order to duplicate the total displacement [176]. The available space has been filled by a set of 2 more actuators than the **DISC** structures without

<sup>8</sup>Refer to Section 3.3.

decreasing the fill factor nor increasing the footprint of the final device. The MISC structure is schematically rendered in Figs. 4.19 and 4.24d.

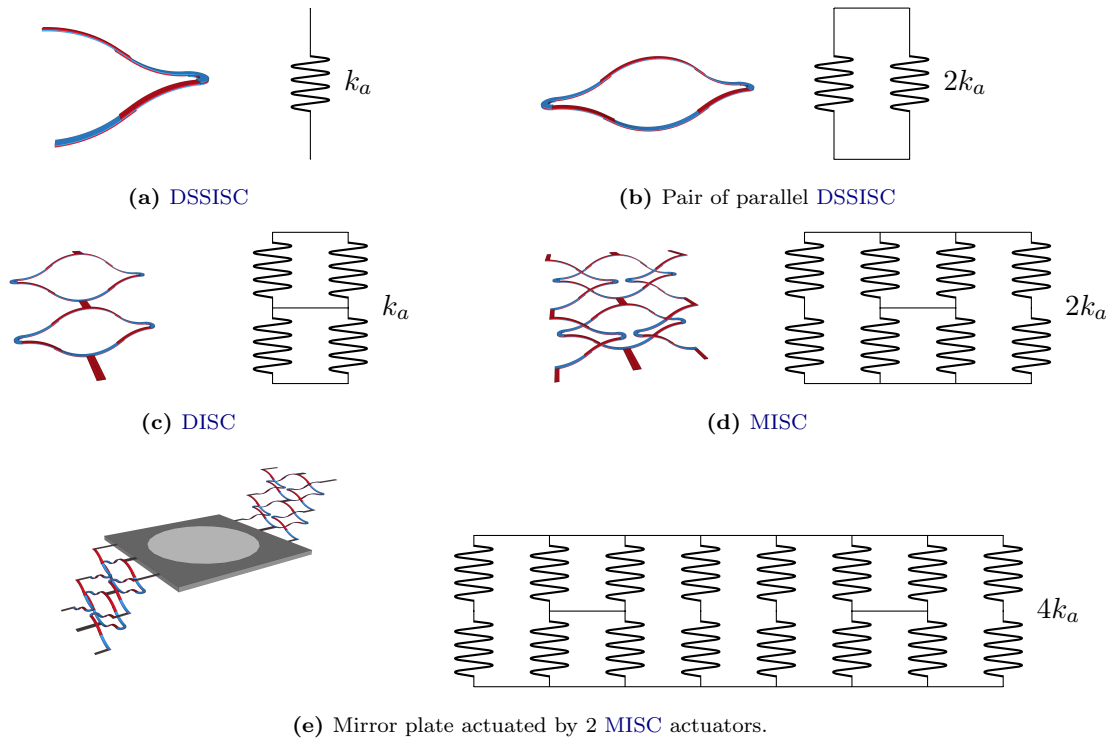


**Figure 4.24:** Evolution of the ISC-based actuators and their LEM equivalence in term of mechanical spring constant.

The maximum admissible stress on the actuators is located about the corners between the collarbones and the slender arms of the structure [165]. The Von Mises stress can be calculated by Eq. (4.60).

$$\sigma_e = \frac{1}{\sqrt{2}} \sqrt{(\sigma_{11} - \sigma_{22})^2 + (\sigma_{22} - \sigma_{33})^2 + (\sigma_{33} - \sigma_{11})^2 + 6(\sigma_{12}^2 + \sigma_{23}^2 + \sigma_{31}^2)} < \sigma_Y \quad (4.60)$$

The electrothermal actuators were designed so that the stress usually located at the corners is minimized. A curved shape is adopted for the collarbones of the actuators and finally extended to every right-angled boundary in further designs. Filleted corners are also very appreciated to facilitate the flux of electrons in electrical paths. The improvements brought in the designs are highlighted in the Section 4.3.5. The first batch of fabrication provided one type of device for characterization and further improvements. Even though, many test devices were also part of the first wafer batch and were also used as test samples. The main structure will be referred to as Tor1.x micro-scanner which is represented in Fig. 4.9. The following batches and mirror types will be introduced in the next Section 4.3.5.

#### 4.3.4 Thermal model

In the design presented earlier, it is crucial to study the electrothermal behavior of the whole structure because it is composed of two axes that are not necessarily totally uncoupled one from another. Thermally speaking, our design is similar to the structures designed in the group BML from generations A3 to A5 as well as the generations with stoppers (see Section 3.3). Jain *et al.* [232] reported a model of an electrothermal micromirror with an in-frame mirror plate. The

**Table 4.7:** Recap table of the main parameters of the **MISC** actuators.

Parameter	Value	Description
<b>ISC</b> actuator		
$L_{IN}$	176 $\mu\text{m}$	Length of the inverted segment
$L_{NI}$	88 $\mu\text{m}$	Length of the non- inverted segment
$L_{OL}$	88 $\mu\text{m}$	Length of the overlapping segment
$w_b$	14 $\mu\text{m}$	Width of the actuator
$t_b$	2.64 $\mu\text{m}$	Equivalent thickness of the actuator
<b>DSSISC</b> actuator		
$a$	30 $\mu\text{m}$	Length of short connecting arm
$b$	352 $\mu\text{m}$	Length of slender arms
$c$	30 $\mu\text{m}$	Length of the collarbone
$d$	352 $\mu\text{m}$	Length of slender arms
$e$	80 $\mu\text{m}$	Length of short connecting arm

thermal behavior of the micromirror was investigated and modeled by an **LEM** at the steady state. However, the model proposed is “valid when only one of the two actuators is activated” [232]. As discussed earlier in Section 4.2.1.2, the substrate is considered as a thermal well set at the ambient temperature  $T_0$ . It is the “coldest point” of the micro-scanner system. Unlike the thermal study of a single electrothermal actuator, the study of the whole micro-scanner is more complex because the “hottest point” of the system will be shifted towards the inner actuators. In order to simplify our model, let us distinguish three cases:

**Case 1.** Only the bimorph array is actuated. The maximum temperature node is located at  $\hat{x}$  of the base of the bimorph. The thermal resistance seen on the left (substrate) of the bimorph array is smaller than the resistance seen on the right (inner frame) which yields a balancing factor of the pitch actuator  $f_{pitch}$  greater than 0.5. More than half of the heat flow generated by Joule heating will go to the substrate whereas  $(1 - f_{pitch}) \times 100\%$  flows from the maximum temperature node to the inner frame. Most of it is accumulated into the inner frame and dissipated by convection in the surrounding air at the ambient temperature. We can take for granted that most of the heat flow will be dissipated before reaching the inner actuators because the inner frame is much more subject to convection than conduction. Finally, the micro-scanner is well cooled down and the thermal influence of the pitch actuator over the inner roll actuator will remain small enough to be ignored.

**Case 2.** Only the inner **MISCs** are actuated. As shown in Fig. 4.9, the micro-scanner is symmetric from a thermal approach. Indeed **MISC** actuators are thermally identical so that they can be substituted for one single equivalent thermal resistor instead. As the heat generation stems from the inner actuator, the maximum temperature will be located on the node belonging to the equivalent resistor. Unfortunately, the inner frame and the mirror plate have comparable sizes, and thus comparable thermal behaviors. Therefore, about a half of the generated power will dissipates through the mirror plate – that conducts into itself and acts as an accumulator – while the other half will take the other path, through the inner frame, across the pitch actuator until it reaches the “ground” of the system: the substrate that has the lowest temperature. In this case, a coupling can be predicted caused by the roll actuator onto the pitch actuator.

**Case 3.** Both pitch and roll actuators are actuated simultaneously. It is a superposition of the two first cases and the value of the heat flows can be added up. However, we need to notice that the maximum temperature positions will be shifted. Finally, taking into account the conclusion that were brought up for each of the two first cases, the present case can be simplified by case 2 as the essential parameter that really matters in the analysis of the whole micro-scanner is the value of the heat flow that goes through the pitch actuator when the roll actuator is driven.

Figure 4.25 shows a LEM schematic of the thermal behavior of the whole micro-scanner for steady-state analysis. The electrical circuit is not represented in Fig. 4.25, but the electrical initial

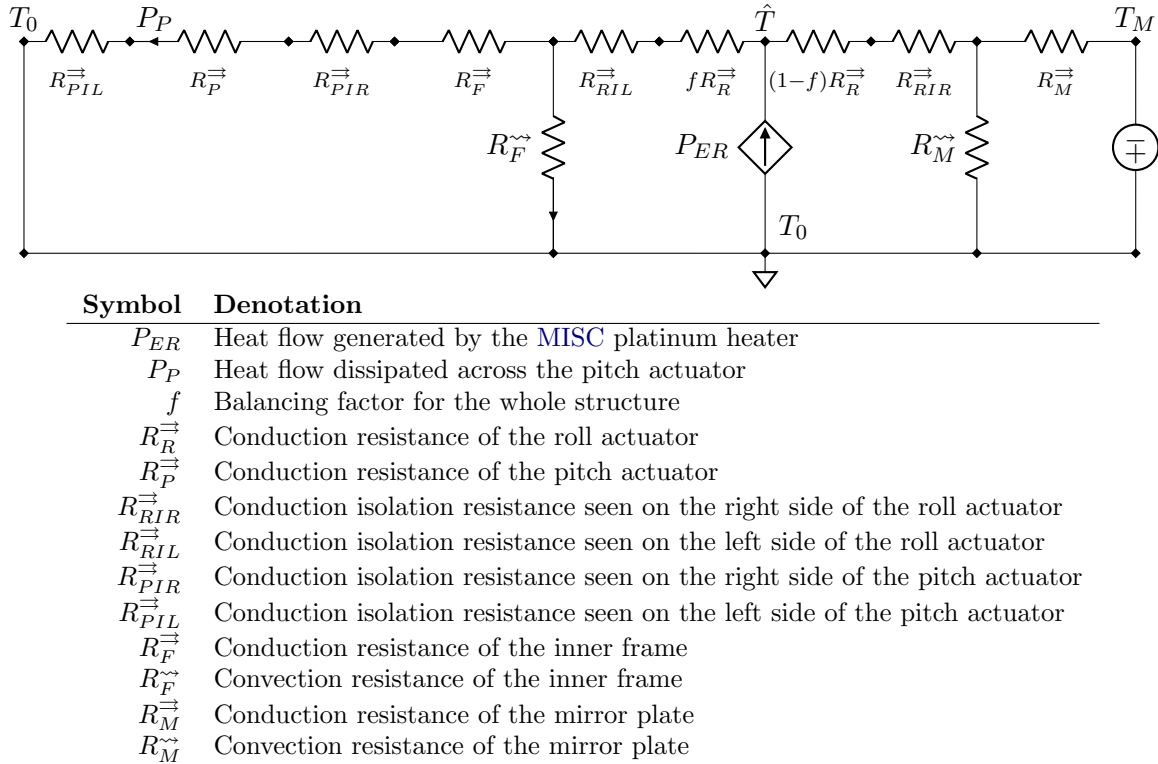


**Figure 4.25:** Schematic LEM of the thermal behavior of the micro-scanner in case 2 with symbols nomenclature.

resistance is calculated on the length of the platinum heater across the MISC actuators.  $T_M$  is the temperature of the mirror plate supposed to be different from the ambient temperature. However, for the calculations, we'll assume that  $T_M = T_0$  as in [217]. The heat flow generated by the heater dissipates on both sides of the point of maximum temperature  $\hat{T}$  and through the bimorph array that is considered completely passive as mentioned in the second case. In fact, one does not require to utilize the heater to generate an increase of temperature as long as an external source of heat can also be used [319]. In our case, the heat generation of the roll actuator mingles with the bimorph array. The amount of heat flow received by the bimorph array  $P_P$  will couple the two orthogonal scan directions, impacting directly the OCT image. One challenge in the design of the micro-scanner is to dimension properly the components in order to ensure a thermal behavior sufficiently uncoupled to be able to control the motion of the micromirror. One criterion is the ratio between the heat flow crossing the pitch actuator and the total generated power by the roll actuator's heater  $P_P/P_{ER}$ , independent from the applied voltage. From the resolution of the LEM, we extracted the evolution of the ratio mentioned earlier with respect to the value of the four

most significant resistances constituting the circuit. It was shown that the resistances that impact the ratio are mainly the resistance of the frame due to conduction and convection, the resistance of the isolation bridge between the pitch actuator on the frame and moderately the resistance of the isolation between the roll actuator and the frame as plotted in Fig. 4.26. Each resistance value is tuned independently from the others that keep a given initial approximate value. The value of the resistances was plotted within a range of  $10^3$  to  $10^5$   $\text{K W}^{-1}$  which is conceivable but for  $R_{PIR}^{\leftrightarrow}$  because the equivalent isolation bridge of the bimorph array is divided by the number beams and is usually in the range of a few tens or hundreds of  $\text{K W}^{-1}$  only.  $R_F^{\leftrightarrow}$  and  $R_F^{\rightsquigarrow}$  are the most opportune parameters to be tuned in order to minimize the heat flow ratio. Indeed, the resistance of the frame by convection and conduction fluctuates of 55% and 53% respectively within the range specified above, reaching independently ratios as low as 4%. Tuning these two resistances could allow to decrease even more this ratio. The size, the thickness, the material of the frame has been optimized consequently in our design and parameters are summarized in Table 4.5. The effect of fabrication process on the variation of the thermal behavior also exist and has been briefly mentioned by Pal and Xie [318].

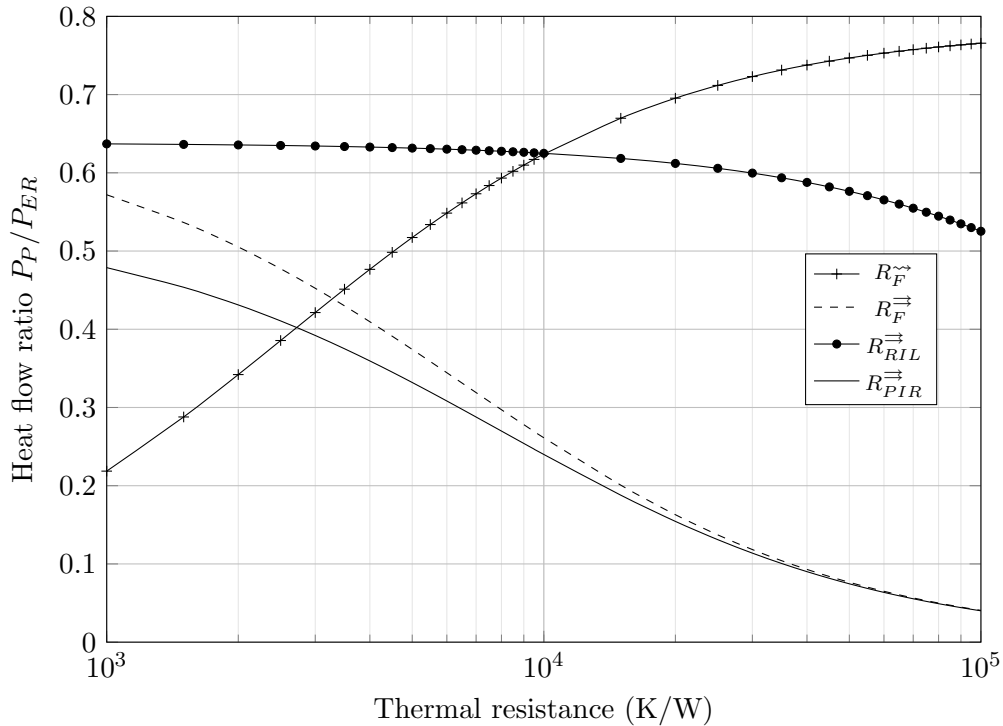


Figure 4.26: Variation of the heat flow ratio  $P_P/P_{ER}$  for different values of four thermal resistances of the structure.

### 4.3.5 Improvements

#### 4.3.5.1 Gold pads

A few improvements were made to the initial MISC structure and are strongly recommended for future designs based on the structure proposed in this work. After the last step of fabrication, the micro-scanner has to be packaged. Typically, a dual in-line package (DIP) or a custom printed circuit board (PCB) is used to connect the pads of the chip to a macro environment for interfacing with a signal generator for instance. The packaging method will be described in Chapter 6. The tool



used to implement the pad-to-pad connection is called a wire-bonder and consists of interconnecting pads together by a thin metal wire by a process described in Chapter 6. Commonly used materials are the copper, aluminum and gold. Most wire bonders are equipped with gold wires because it doesn't oxidize and stays compatible with most materials. Depending on the wire-bonding tool, the contact between the gold wire and the aluminum can be fragile or lose adhesion. A better way to ensure adhesion between the wire and the pad is to uniformize the materials. Hence, one of the improvements that was made concerning the pads is the gold coating on top of the aluminum constituting the original pads. The realization and the results will be discussed in Chapter 5.

#### 4.3.5.2 Mechanical 45° stopper mechanism

It is not the object of this section to present the characterization of the Tor1.x in order to highlight quantitatively the shortcomings arising from the first batch of fabrication. However, a combination of thermal and mechanical cross-coupling stemmed from the biased estimation of the thermal resistances due to the difference in the parameters of the bulk and the thin films has been observed and discussed in Chapter 6. Thermal and mechanical cross couplings are causing the micro-scanner to behave differently from the model expectations: the actuators are not completely independent one from another in terms of motion and entailed a cross coupling between the axes. A solution in the design has been suggested to tackle the mechanical coupling issue [287, 300]. Duan *et al.* implemented a mechanical “stopper” to prevent the uncontrolled motion of the inner frame in the reference frame of the Si substrate. The so-called stopper is a mechanism that locks the pitch rotation by making the edge of the inner frame lean onto the vertical wall of the handle layer of the SOI wafer [300]. Another version of stoppers has been reported to lock the inner frame along a vertical plane [287] (see Fig. 4.27a) but is inadapted in our case. An illustration of Duan *et al.*'s stopper is shown in Fig. 4.27b and compared with the mechanism proposed in this work, which corresponds to a different rotation of the inner frame [359]. The principle of the stopper mechanism is sketched in Fig. 4.28 in two steps depicting the states before and after release of the device in Fig. 4.28a and Fig. 4.28b respectively. The device layer slanting against the handle layer

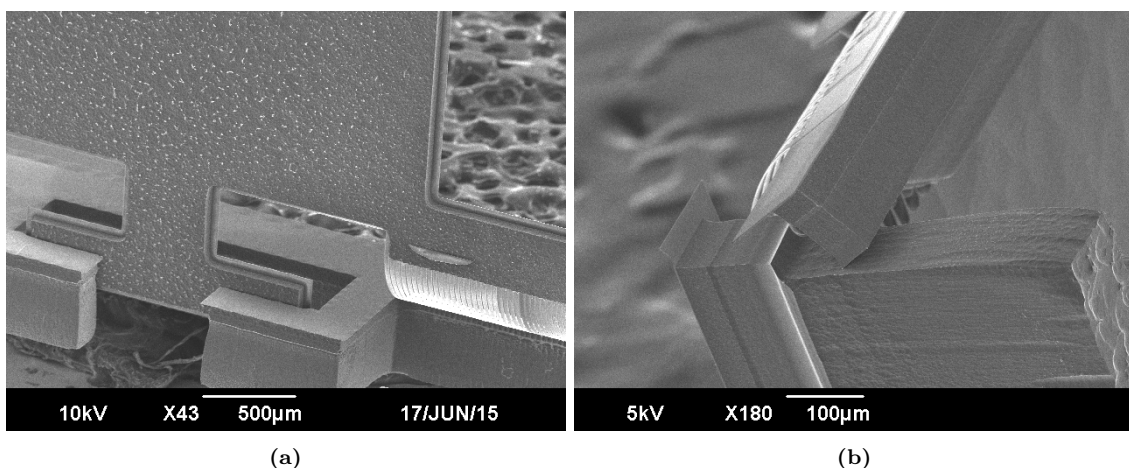


**Figure 4.27:** Comparison of two types of stopper mechanisms used for MEMS technology. (a): Vertical stopper from [287]. (b): Bending down slanting stopper. Courtesy of Duan *et al.*.

of the SOI wafer wedges the inner frame at a fixed angular position that can hardly be modified after release. The moving arm of the stopper latch is as thick as the device layer in order to avoid buckling and ensure the quality of the contact. Unlike the vertically slanting stopper of [287], in

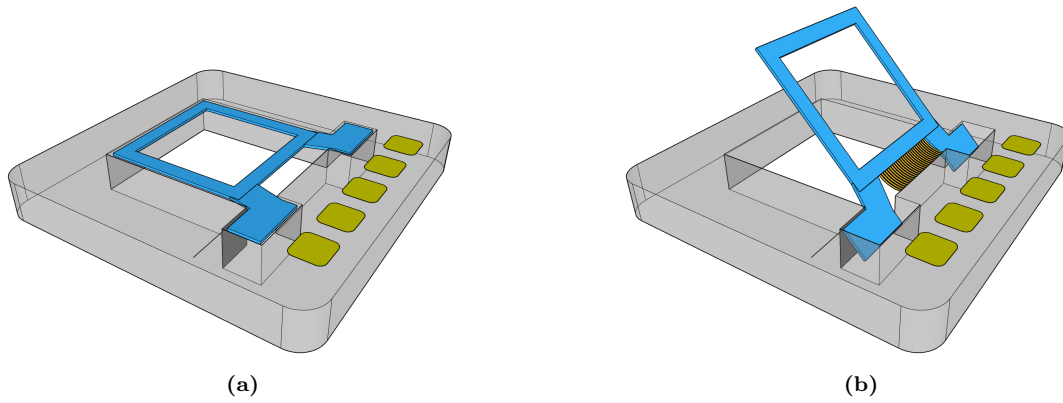


**Figure 4.28:** Schematic view of mechanical stopper mechanism. Frame is represented in green (a) before and (b) after release.

our case, the nature of the contact between the device layer and the vertical wall of the handle layer is a line as shown in Figs. 4.27b and 4.28. During operation, the stopper has to be glued so that the motion of the inner frame is definitely locked in displacement and the inner frame becomes one rigid body with the substrate. As mentioned in Section 2.5, this angle has to be as close as possible to  $45^\circ$  to be able to use most of the effective part of the reflective surface and deflect the light beam along a perpendicular optical axis towards the sample observed in side-viewing mode. The value of the length of each bimorph was set at  $300\ \mu\text{m}$  based on former studies conducted within the BML group who worked with identical tools in the NRF cleanroom facility. This position depends and the final thickness of the device layer, on the dimensions of the hinged latch and on its location within the outer frame. Figures 4.28 and 4.29 are complementary and illustrates the geometrical principle of the stopper mechanism developed in this work. It is assumed

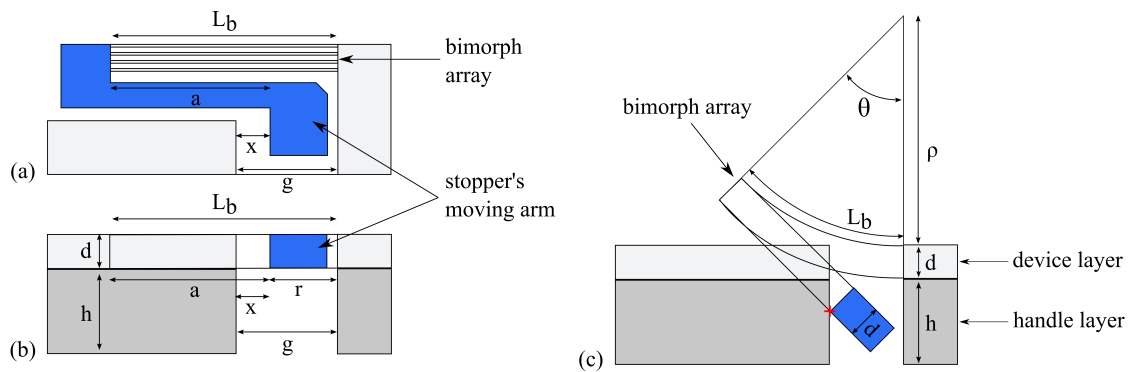


**Figure 4.29:** Sketch of the geometry of the stopper mechanism and its dimensions for the calculation of the latch lock angle. (a): Layout top view of the latch and the actuators. (b): Side view of the stopper before release of the device. (c): Side view of the stopper slanting on the vertical wall of the handle layer after release.

that the initial tilt elevation of the inner frame (without stopper) is greater than  $45^\circ$ , otherwise the device layer won't touch the handle layer and the stopper will be useless. The dimensions and the position of the mechanical stopper within the substrate (see Fig. 4.29a,b) stem from the desired angle of tilt after release (Fig. 4.29c). The angle can be accurately controlled and the standard deviation of the frame angle of the different chips within a batch significantly reduced. Knowing that the length of the bimorphs equals the radius of curvature multiplied by the target angle  $\theta_b$  and based on the relations given in Eq. (4.61), we derive an equation of inequalities defining a

range of dimensions for the tunable parameters of the stopper in Eq. (4.62).

$$\begin{cases} (\rho_b + d)\theta_b = a - x + g \\ g = r + x \end{cases} \quad (4.61)$$

$$\forall \theta_b \in [0, \frac{\pi}{2}], \quad 0 < a - a_{min} < \frac{d + h}{\sin \theta_b} \quad (4.62)$$

with  $a_{min} = (\rho_b + d)(1 - \cos \theta_b) - d$ . The length of the moving arm is calculated at  $307 \mu\text{m}$ ,  $r$  is a parameter specified in Fig. 4.29 and the  $x$  gap equals  $32.5 \mu\text{m}$  at a distance  $a$  of  $187 \mu\text{m}$ . The isotropic etching of the Si by DRIE cause the dimensions to differ from the layout dimensions: lengths diminish and gaps increase causing the tilt angle to soar rapidly. Errors of  $10 \mu\text{m}$  and  $30 \mu\text{m}$  yield 17% and 44% of error in the final angle respectively [300]. However, the center value of  $45^\circ$  is not critical and can fluctuate without affecting the OCT image. We know from the optical model that a mechanical angle below  $37.3^\circ$  will block the light beam reflected off the mirror. Unlike Duan *et al.*'s probe design, the parameter limiting the maximum tilt angle in our case is the height of the center of the mirror plate with respect to the top surface of the device layer of the SOI. In the literature, most reflective prisms used for circumferential scans in side-viewing probes are tilted by a angle smaller (or greater) than  $45^\circ$  to reduce backreflections from the interface with the tissue or with the capsule diopters. Although such a tilt modifies the direction of the observation, it does not affect the quality of the images [96, 123]. The calculations of Duan *et al.* led to an overshoot angle of  $17^\circ$  from the initially expected  $45^\circ$  value with a variation of  $\pm 3.7\%$ . In conclusion a safety index has to be included in the model, predicting variations of the thickness of the outer wall from 20 to  $30 \mu\text{m}$ .

Another issue that has to be highlighted, is the decrease of *dofs* of the micro-scanner due to the introduction of the mechanical stopper. The Tor1.x device originally had 2 *dofs* provided by the pitch and roll axes. Unfortunately, the mechanical stopper limits the motion to a single rotation on the roll axis. This limitation motivated the design of a novel micro-scanner including a mechanical stopper and allowing 2 *dofs* in rotation around the pitch and roll axes.

### 4.3.5.3 Increasing the degrees of freedom

Two new devices including stopper mechanisms were realized in a second batch of fabrication. SEM pictures of these devices are shown in Figs. 4.30a and 4.30b and will be referred to as Tor2.x and Quad2.0 respectively. The micro-scanner Tor2.x is the evolution of Tor1.x but was downgraded to a single *dof* around the torsion beams axis because the stopper locked the pitch *dof*. This micromirror can only be used for a 2D probe to perform a B-scan OCT image. The Quad2.0 is also an outcome of the second batch of fabrication and allows 3D OCT images, by means of 4 ISC actuators within the inner frame and actuating the mirror plate in tip-tilt and piston mode as many micro-scanners designed formerly [221]. In conclusion, the Tor1.x has 2 *dofs*, the Tor2.x has 1 *dof* and the Quad2.0 has 3. As the Quad2.0 is very similar to the work of Duan *et al.* [300], its principle of actuation will not be described in details in this manuscript. We invite the reader to refer to Refs. [59, 105, 128, 163, 251, 296, 300].

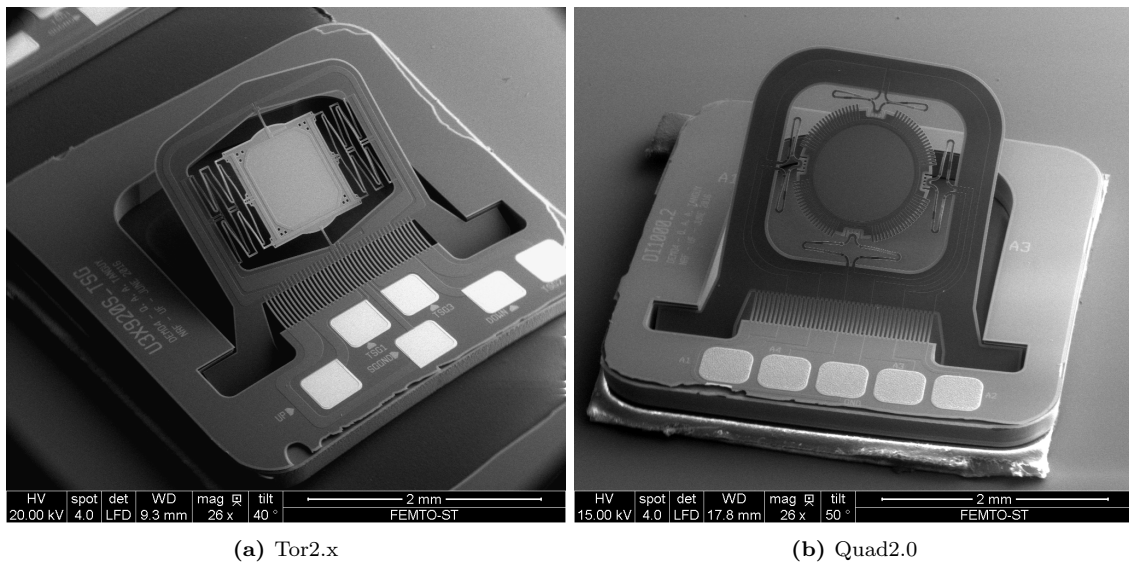


**Figure 4.30:** SEM pictures of the two main devices (a) Tor2.x and (b) Quad2.0 of the second batch of fabrication.

## 4.4 Conclusion

We have seen in this chapter several designs developed purposely to match the specifications defined earlier. Analytical models have been established to describe the electrothermal and thermomechanical behaviors of single bimorph beams in a first time and complex bimorph-based actuators in a second time. The accuracy of the models was reported to be sufficiently close to the FEM simulations and experimental results obtained by the authors who have demonstrated their efficiency in the literature. Hence, we relied on the analytical models to design the micro-scanner. The two last designs result from the enhancements brought to the first version of micro-scanners in order to improve the performances and to remove the axis cross-coupling, potentially hindering the quality of the 2D scan performed by combination of the motion of the two axes. The first version of the micro-scanner was designed to reach minimum mechanical angles of  $5^\circ$  for a fast-scan frequency around 1 kHz about the roll axis, and a slow-scan frequency of 200 Hz about the pitch axis. The design was extended to provide much larger angles than the very requirements so that additional scans with similar scanned area can be performed for different angular offsets and then merged to reconstruct a larger scan cluster.

### Chapter summary

After establishing the models of the electrothermal micro-scanner, parameters have been tuned in regard to the specifications. The devices still remain to be fabricated at the wafer level by batch fabricated in cleanroom. The micro-scanners were fabricated in two different cleanrooms because of the framework of this work realized under an exchange program between the [university of Franche-Comté \(UFC\)](#) and the [UF](#). The process of each step of fabrication will be presented in the next chapter as well as the technologies and related risks.



## Chapter 5

# Fabrication

**A**FTER the theoretical design and the simulations presented in the former chapter, the micro-scanner still remains to take shape. Regarding the small size of the MEMS device, it was fabricated by “microfabrication” in appropriate microscale facilities. Before introducing the very core of microfabrication processes, flow charts were established to ensure the feasibility, the compatibility between the materials themselves and considering the capability of the different tools available. The validation of the flow chart entails the design of the photomasks, essential for each step’s photolithography. Two main batches of fabrication were carried out and will be detailed in this chapter. The first batch, fabricated in the NRF of the UF in the USA was based on a relatively mature flow chart developed over the last ten years in the BML group of the UF. This flow chart and the fabrication corresponding processes are presented in a first section (Section 5.1) by order of fabrication step. The role of each step, the process, the results are detailed and the possible engendered risks are also mentionned in Appendix A. In terms of flow chart and fabrication process, our contribution also claims a few novelties intended to enhance the optical characteristics, the packaging and the embedded controlability of the device. These novelties will be presented separately in a second section (Section 5.2) and were implemented during the second batch.

Most of the processes dedicated to the fabrication of the electrothermal actuator technology were well mastered in the NRF through a long optimization process of the past 15 years of development of these devices. Hence, the processes implemented in the first batch of fabrication have nothing of a novelty. Nevertheless, being able to master all these steps properly and reproduce them also requires substancial skills and adaptability from the operator. Transferring these technologies from one cleanroom (NRF) to another (MIMENTO) is no less of a pain in the butt. Finally, on top of these processes present in the first batch, a few novel processes were entirely developed to improve the performance of the devices, facilitate their integration and increase their optical adaptability for further integration. These novel processes are described in the flow chart of the second batch of fabrication. They consist of depositing selectively a reflective layer on the back side of the mirror plate, patterning a microscale embedded strain gauge sensor system and plating the pads with gold.

## 5.1 Base device fabrication process

### 5.1.1 Flow chart and layout

The first batch of fabrication was performed on a 4" SOI wafer. The process of photolithography is detailed in Appendix B.1 and introduces all the necessary terms that will be widely used in the following of the present chapter. SOI wafers are composed of:

- a thick layer of on the “back side” of the wafer called the “handle layer”, and used to bring stiffness by increasing the thickness of the support in order to – as indicated – handle the wafer safely. For 4" wafers, this layer is recommended to have a thickness greater than 200  $\mu\text{m}$ .
- a thin layer on the “front side” called “device layer”, which will “support” the device intended to be fabricated,
- and an intermediate ultra-thin dielectric layer made of  $\text{SiO}_2$ , and called the “buried oxide (BOX) layer” (and which will simply be referred to as “BOX” in the following) whose thickness vary widely depending on the application.

In our case, the handle layer and the device layer are both made of single-crystal silicon (SCS) of orientation  $\langle 100 \rangle$  and have a respective thickness of 500  $\mu\text{m}$  and 30  $\mu\text{m}$ . The BOX has a thickness of 1  $\mu\text{m}$ . As at last, the micro devices will be connected to an electrical ground either for nominal operation either for testing, the wafer is P-doped and has a resistivity of 1-30  $\Omega\text{ cm}$ . These parameters are summarized in Table 5.1. The flow chart is established in the light of the specifications

**Table 5.1:** Summary of the main parameters of the SOI wafer used for the batch of fabrication of the device Tor1.x.

	Device layer	BOX	Handle layer
Diameter	100 $\pm$ 0.2 m m		
Thickness	30 $\mu\text{m}$	1 $\mu\text{m}$	500 $\mu\text{m}$
Resistivity	1-20 $\Omega\text{ cm}$	-	1-30 $\Omega\text{ cm}$
Edge exclusion	<5 mm	-	
Finish	Polished	-	Polished
Type/Dopant	P/Boron	-	P/Boron

defined by the dimensions, the static and dynamic behavior of the micro-scanner, the materials required, their compatibility between each other and regarding the machines and the possibility of implementation in the microscale facility. Finally, the flow chart was made as simple as possible to avoid complexifying even more the process which already requires a relatively large amount of steps.

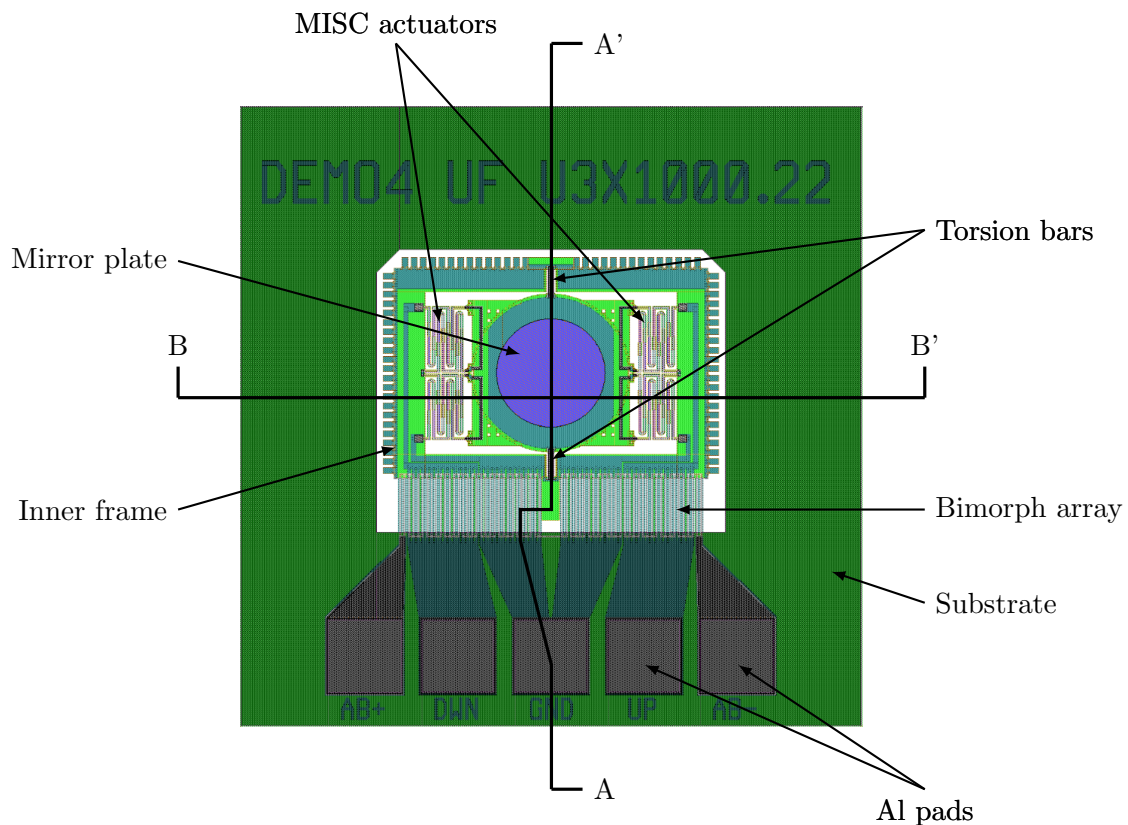
The flow chart of the first batch of fabrication is composed of 7 major stages described very briefly in Table 5.2 – in order to provide a guidance outline of the steps and a reference for the photomask names used in the following – and more thoroughly in Sections 5.1.3 to 5.1.9. The wafers of the first batch of fabrication hold 317 chips with an exclusion ring of 5 mm and two alignment marks.

A general layout is given for the three structures presented in this manuscript for an overview of what they look like. However, specific areas of the layout will be closely displayed accordingly for

**Table 5.2:** Chronological list of steps of fabrication of the device Tor1.x with the corresponding color code of materials.

Step	Description	Mask I.D.	
	Wafer clean up	-	
1	SiO <sub>2</sub>	OXD1	Light Blue
	Insulation	-	Light Blue
2	Platinum sputtering	PT	Red
	Insulation	-	Light Blue
3	Via opening	VIA	
4	Aluminum evaporation	ALU1	Blue
5	SiO <sub>2</sub>	OXD2	Light Blue
6	Back side pit	BSD	
7	Release	-	

each step of fabrication where a comparison between the layout and the result of the fabrication can be appreciated. Finally, one subsection will be dedicated to one major step of fabrication. Apart from the first step of cleaning-up, all the other major steps (where a photomask is to be used) will be illustrated by a sketch of the cross section of one chip displaying the advancement by the change in the layers. In the current section, the sketches will represent the fabrication process of the Tor1.x and will split into a left cross section represented by the segment [AA'] and a right cross section depicted by the segment [BB'] in Fig. 5.1. The purpose of such a representation is to show both the torsion beam and the actuators. For the sake of simplicity, only *DSSISC* actuators will be drawn instead of *MISC*.

**Figure 5.1:** Layout of the Tor1.x micro-scanner fabricated and presented in the current work.



### 5.1.2 Preliminary clean-up stage

Before processing the SOI wafer anyhow, especially when its container has been opened and that it has been taken out for a while or for any other doubtful reason, it is necessary to clean it up thoroughly. The purpose of the present stage is to remove the traces of organic components and oxydation on both surface of the substrate. First, the wafer is dipped into a solution of Piranha before introduction of the second species. Piranha is made of 3 parts of sulfuric acid ( $H_2SO_2$ ) dosed out at 49% and 1 part of hydrogen peroxide ( $H_2O_2$ ) poured in this order. Unlike the common preconception, the solution of Piranha must be prepared by pouring the sulfuric acid first, followed by the hydrogen peroxide dribbled gently in a glass beaker, and not the other way! This is a hint for safety concerning this operation. After the insertion of the two compounds, an exothermic reaction will occur and can reach a high temperature. A “boiling” will also happen, and the wafer should be introduced in the beaker immediatly. The wafer should not be left in the solution for too long. Usually, 5 minutes are enough to allow an efficient result. Since the Piranha is a strong oxidizing agent and hydroxylates the surface in contact, an additional clean-up phase will follow using **buffered hydrofluoric acid (BHF)** in order to remove the oxydation on the substrate caused by the Piranha. The BHF has a contrary effect to the hydrophilic effect of the Piranha and will make the surface hydrophobic so that one knows when the wafer can be removed from the BHF solution. The wafer must be abundantly washed using deionized water and blown thoroughly with  $N_2$  to drive off all the water after each step. Before the next operation, the substrate was dried in an oven at a temperature of  $120\text{ }^\circ\text{C}$  for about a quarter-hour.

### 5.1.3 First layer of silicon dioxide - OXD1

The very first pattern to lie on the wafer is a layer of  $SiO_2$  constituting the bottom layer of the non-inverted, the overlapping segment of the bimorph and the inferior layer of the torsion bar. It also defines the “rigid” part which will stay in the footprint at the end. These regions are the mirror plate, the thermal bridges, the inner frame and the outer frame (substrate) as illustrated by Fig. 5.2.

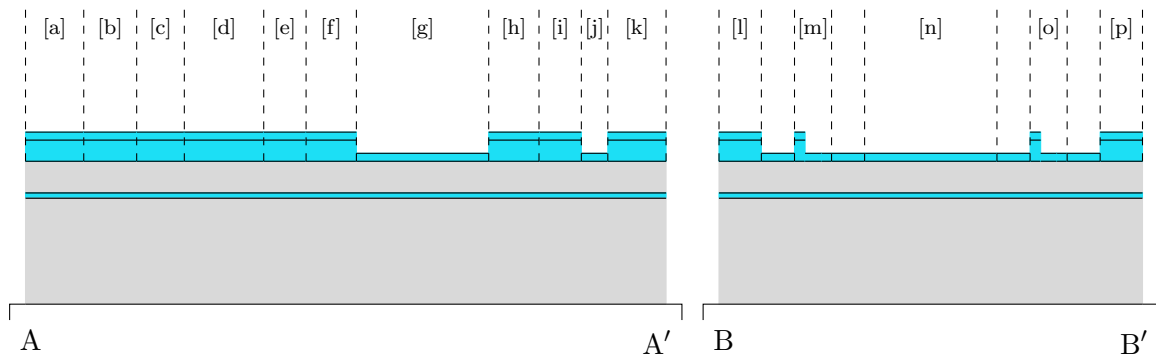


**Figure 5.2:** Schematic view of the fabrication step (OXD1) of the first batch. [a,k]: Substrate; [b]: Pads; [c]: Space between the pads and the bimorph array; [d]: Bimorph array; [e,i,l,p]: Inner frame; [f,h]: Torsion bar; [g,n]: Mirror plate; [j]: Gap between the substrate and the inner frame; [m]: ISC-based actuators; [o]: ISC-based actuators.

Then,  $1.1\text{ }\mu\text{m}$  of  $SiO_2$  was deposited by **plasma-enhanced chemical vapor deposition (PECVD)** on the front side of the wafer at a temperature of  $300\text{ }^\circ\text{C}$  to maximize the stress. The tool used is a STS<sup>®</sup>310PC.

After metrological verification of the thickness of the deposited layer of  $\text{SiO}_2$  with a maximum tolerance of 4% of error, a photolithography of positive photoresist (PR) AZ1512 is performed on the top side using the mask ⟨OXD1⟩. Then the wafer is dipped into a solution of buffered oxide etchant (BOE) to wet etch  $1.1\ \mu\text{m}$  of  $\text{SiO}_2$  until the Si underneath is exposed. In microfabrication, the BOE is another name of the BHF. It is a wet etchant primarily used to etch  $\text{SiO}_2$  and silicon nitride. The term of BOE is generally used when a dilution is performed which allows a better controllability of the etch rate. For this step, a solution of BOE with a volume ratio of 6:1 is used. Such a volume ratio means that the BOE comprises 6 doses of 40% ammonium fluoride ( $\text{NH}_4\text{F}$ ) to 1 dose of 49% HF<sup>1</sup>. Unlike concentrated HF (49% in water)<sup>2</sup> which peels off the PR, BOE is adapted for this type of wet etch on polymer after a photolithography. BOE was especially used for this step because of the gentle slope profile it leaves on the edges of the patterns unlike a dry etch method that creates curved or straight walls by isotropy or anisotropy. This slope profile is preferred for a reason of compatibility with the following step. Indeed, in the next step, the Pt heater will lie directly on the  $\text{SiO}_2$  and requires a profile of slight slope to ensure the continuity of the electrical path.

BOE 6:1 has an etch rate of about 90 nm/min at 21 °C. The wafer is kept in the BOE 6:1 for about 11 min until the Si underneath is reached. A profilometer of the brand Dektak<sup>®</sup> is used to measure the remaining thickness of  $\text{SiO}_2$  on the wafer and ensure the device layer is reached. The result before PR strip is shown in Fig. 5.3a and the layout of the corresponding area is provided in Fig. 5.3b for comparison.

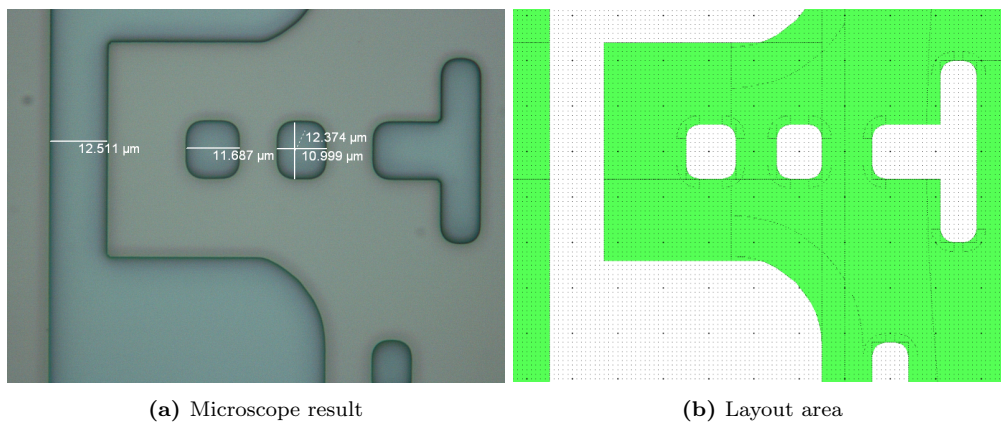


**Figure 5.3:** Image of step ⟨OXD1⟩ on the region of the thermal bridge after BOE wet etch and before PR strip. The region corresponds to the SEM picture shown in Fig. 5.15h. (a): Optical microscope. (b): Corresponding layout area.

Then, the PR on the wafer is stripped in a solution of PRS-3000 heated at 70 °C. The wafer is then dried using a  $\text{N}_2$  gun and baked in oven for an hour at 150 °C.

At last, a thin layer of 50 nm is deposited by the same process described at the beginning of this step as an insulation layer between the exposed Si of the device layer and the next material which will be deposited on top to avoid shortcuts.

<sup>1</sup>Implicitly 40%  $\text{NH}_4\text{F}$  in water and 49% HF in water.

<sup>2</sup>The maximum concentration authorized in cleanroom for HF is 49%.

### 5.1.4 Platinum heater - PT

The heater which generates the increase in temperature in the bimorph actuators is made of platinum. A thin and narrow path is deposited at the location of the actuators and is thickened on the thermal bridges to reduce electrical and thermal resistance and thus its self-influence in the transmission of heat by Joule heating in these regions. The schematic step is illustrated below.

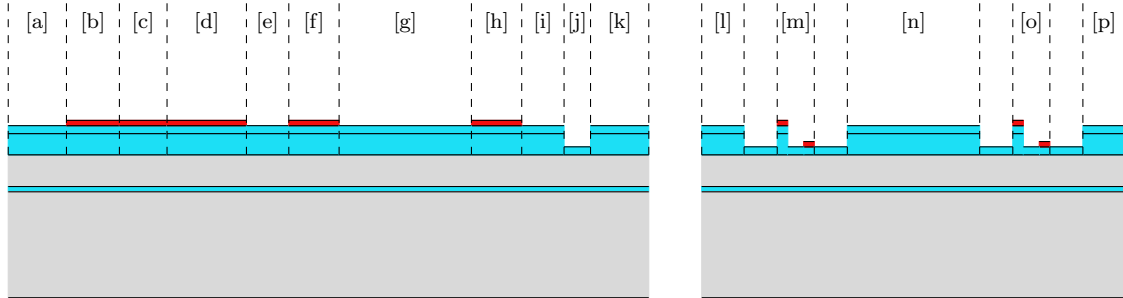


**Figure 5.4:** Schematic view of the fabrication step (PT) of the first batch. [a,k]: Substrate; [b]: Pads; [c]: Space between the pads and the bimorph array; [d]: Bimorph array; [e,i,l,p]: Inner frame; [f,h]: Torsion bar; [g,n]: Mirror plate; [j]: Gap between the substrate and the inner frame; [m]: ISC-based actuators; [o]: ISC-based actuators.

The Pt is patterned using a method called lift-off, described in Appendix B.2. A photolithography is performed with the (PT) mask and the negative PR AZnLOF2035. When spun at 3000 rpm for more than 40 s, the film of AZnLOF2035 has a thickness of  $3.5 \mu\text{m}$  leaves an undercut of typically  $\sim 0.7 \mu\text{m}$ .

To ensure the compatibility of the Pt onto the layer of  $\text{SiO}_2$  underneath, thin adhesion layers of  $150 \text{ \AA}$  of chrome are deposited in sandwich underneath and above the Pt layer of  $1500 \text{ \AA}$ . These 3 layers are deposited in the same run by a process of sputtering, using a Kurt J. Lesker Multi-Source RF and DC sputter system in RF mode. Sputtering was preferred to evaporation because it creates films of better quality (amid the available tools in the NRF), denser, is easier to use than evaporation tools and the thickness is better controlled because more repeatable.

After deposition, the Pt on the PR is lifted off dipping the wafer into a solution of 1-methyl-2-pyrrolidinone (NMP) at  $70^\circ\text{C}$  until all the Pt has lifted off. An ultrasonic bath can be used if necessary to help lifting off.

As a result of the two former fabrication steps, an SEM is shown in Fig. 5.5 where we can see the Pt lying onto the gentle slope of the  $\text{SiO}_2$  pattern underneath.

An overview of Pt sputter of the Tor1.x and a close-up on the actuators is shown in Figs. 5.6a and 5.6b respectively and compared with their respective layouts in Figs. 5.6d and 5.6e. Another view of the actuators of another structure is also compared with its corresponding SEM picture in Figs. 5.6c and 5.6f.

We notice when comparing Figs. 5.6b and 5.6e that the width of the Pt paths is greater after being sputtered in reality than in the dimensions drawn in the layout of about  $1 \mu\text{m}$  in total. This is due to the large angle of the deposition cone of the sputter method and must be taken into account when designing the masks.

### 5.1.5 Second insulation layer opening - VIA

The (VIA) step consists of defining the regions of the devices which will be directly interconnected with the following layer deposited directly after this step. Indeed, the next step is the deposition

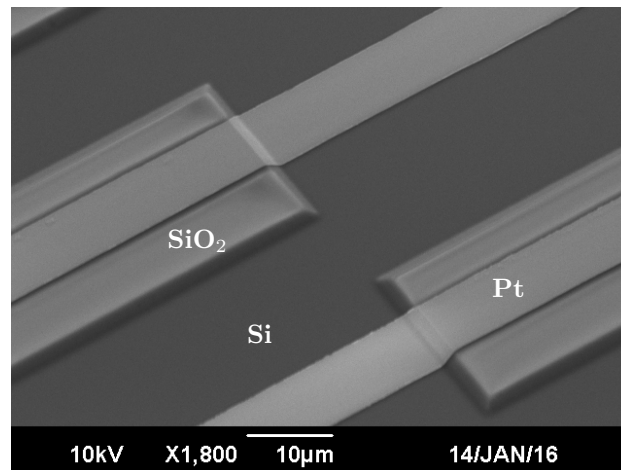


**Figure 5.5:** SEM picture of the Pt heater continuous electrical path deposited on top of the first layer of SiO<sub>2</sub>.

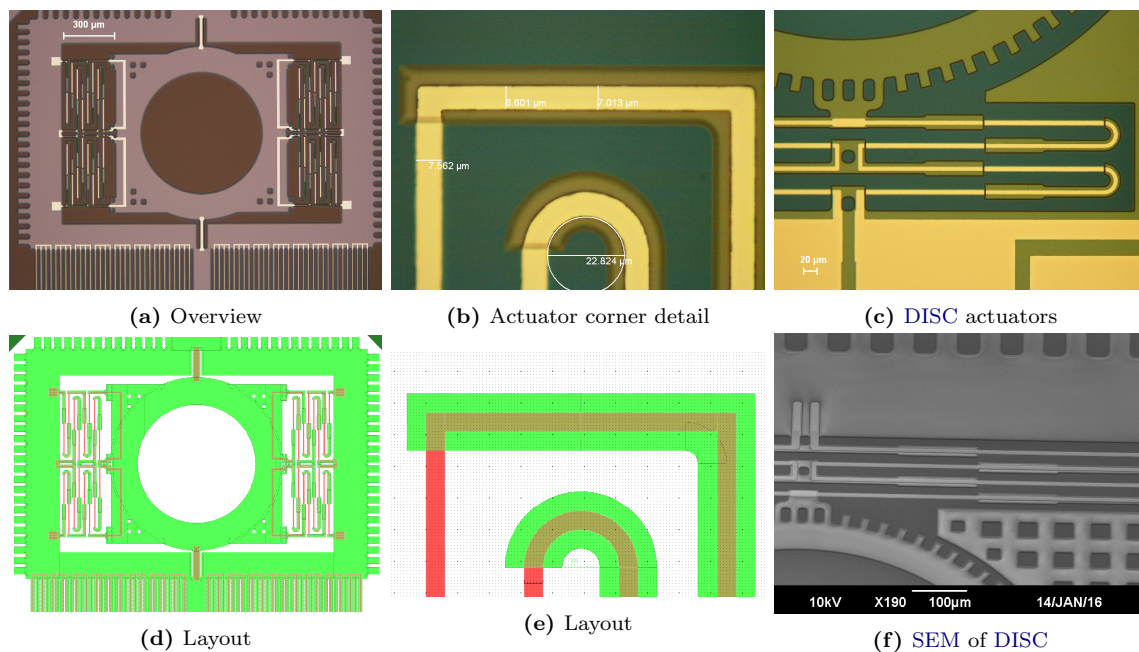


**Figure 5.6:** Results of the Pt sputtering by microscope and SEM and comparison with the layout.

of the aluminum; to avoid shortcircuiting the Pt with the Al on the bimorph, any contact must be prohibited: the SiO<sub>2</sub> insulation layer will not be “opened”. Whereas, on the torsion beam, the electrical Pt/Al connections and the pads, the two metals need to be in contact: the insulation layer must be “opened” to allow this contact.

A thin insulation layer of 50 nm is deposited by PECVD in a similar way as described in Section 5.1.3 followed by a positive photolithography using AZ 1512 with the mask (VIA). The SiO<sub>2</sub> is “opened” by dry etch using a Unaxis<sup>©</sup> SLR reactive-ion etch (RIE)/inductive-coupled plasma (ICP) through the whole thickness of the insulation layer.

### 5.1.6 Top side layer of aluminum - ALU1

The Al of the bimorphs, torsion bars, pads and mirror is deposited all in one single step.

A photolithography of negative PR, analogous to the photolithography performed for the Pt is realized. However, as the thickness of Al to be deposited is 1.0 µm, a thicker PR such as AZ nLOF

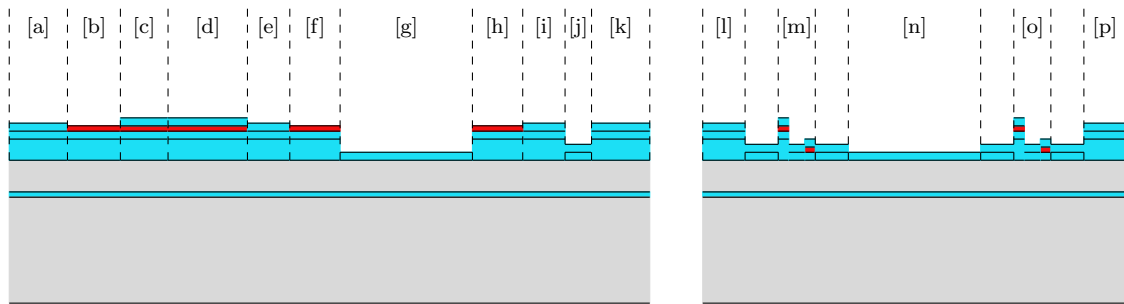


**Figure 5.7:** Schematic view of the fabrication step (VIA) of the first batch. [a,k]: Substrate; [b]: Pads; [c]: Space between the pads and the bimorph array; [d]: Bimorph array; [e,i,l,p]: Inner frame; [f,h]: Torsion bar; [g,n]: Mirror plate; [j]: Gap between the substrate and the inner frame; [m]: ISC-based actuators; [o]: ISC-based actuators.

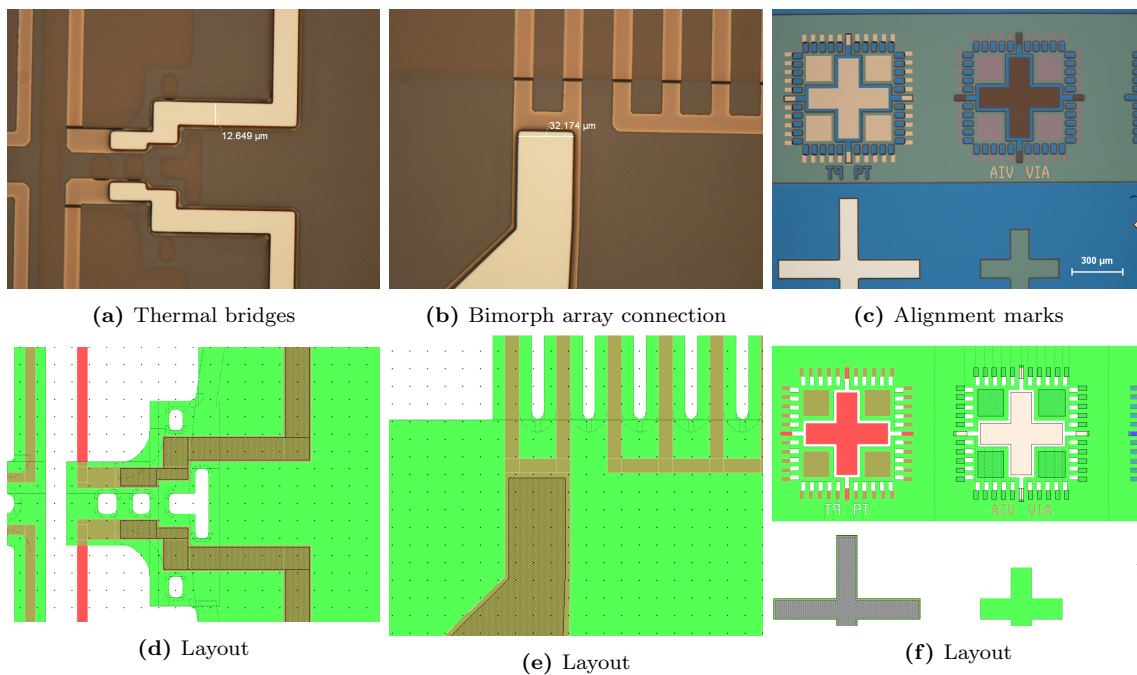


**Figure 5.8:** Results of step (VIA) seen under optical microscope in different regions of the device and corresponding layout areas.

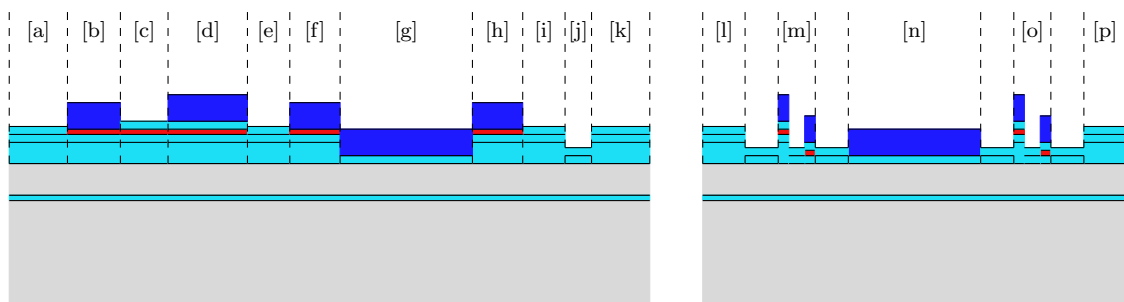


**Figure 5.9:** Schematic view of the fabrication step (ALU1) of the first batch. [a,k]: Substrate; [b]: Pads; [c]: Space between the pads and the bimorph array; [d]: Bimorph array; [e,i,l,p]: Inner frame; [f,h]: Torsion bar; [g,n]: Mirror plate; [j]: Gap between the substrate and the inner frame; [m]: ISC-based actuators; [o]: ISC-based actuators.

2070 can be employed instead of the AZ nLOF 2035 to facilitate the lift-off. Al can be deposited by sputter or evaporation. In our case, an e-beam physical vapor deposition evaporator was used to deposit  $1\ \mu\text{m}$  of Al with  $150\ \text{\AA}$  of Cr underneath and on top of it with a rotation of the wafer of 10 rpm without heating. Finally a lift-off is performed. At this step, if the PR has difficulties

lifting off, a longer dipping time in NMP is highly recommended instead of using ultrasound which may damage the structures as shown in Figs. 5.10b and 5.10c. A layout of the corresponding area is given to spot the region (at the base of the bimorph array actuators) in Fig. 5.10a. An overview of the structure after lift-off and oven bake is shown with its layout in Figs. 5.10d and 5.10e. After several trials of deposition of such a thick layer of Al with different tools, one problem persisted and deserves to be pointed out here. Although the Al is protected by a layer of Cr, an oxidation occurred and is visible under the form of black dots evenly scattered on the surface as highlighted in Fig. 5.10f. To tackle this problem, one solution proposed is to use AlCu instead of pure Al, which would prevent from any oxidation and preserve the quality of the surface.

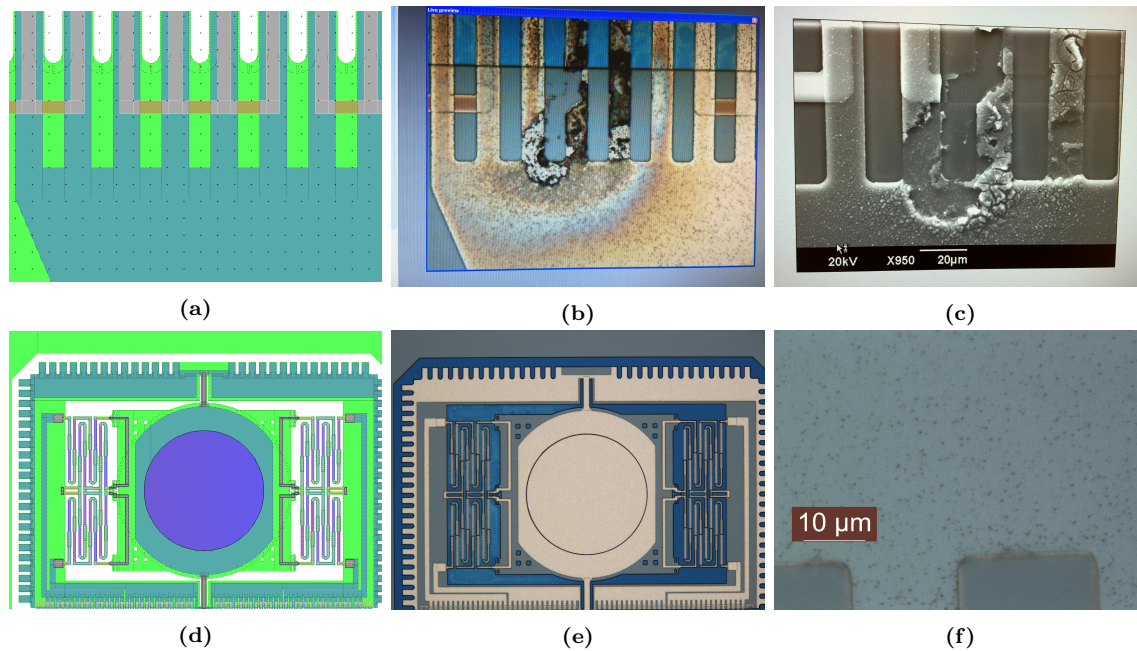


**Figure 5.10:** Fabrication results of step (ALU1). (a): Base of bimorph array layout. (b): Microscope image of parts burned by arcing on the same region. (c): SEM picture of the same region. (d): Overview layout of the device. (e): Microscope view of the corresponding region. (f): Black dots on aluminum.

### 5.1.7 Second layer of silicon dioxide - OXD2

This step might be one of the more tedious and risky steps for the process. The second layer of  $\text{SiO}_2$  composes the bimorph, the thermal bridges and the areas where the device layer's Si needs to remain. The gaps around the inner frame and the actuators will be etched through until the device layer is reached.

A thick layer of  $\text{SiO}_2$  is deposited on the top side of the wafer by PECVD and will be dry etched after a photolithography by RIE until the surface of the device layer is exposed altogether at the “opened” areas which appear in white on the layouts provided. The photolithography uses a positive PR. However, the thickness of the PR has to be thick enough to allow the RIE to etch until the end before the PR is all consumed. Indeed the etch rate of the  $\text{SiO}_2$  and of the PR are comparable. Two different standard operating procedures (SOPs) are proposed and summarized in Table 5.3 where the etch rates of the  $\text{SiO}_2$  and the PR are also indicated.

We notice that if we use a slow etch SOP, the etch rate of the PR is very close to the one of the  $\text{SiO}_2$ . Hence, the thickness of the PR must be greater than the one of the  $\text{SiO}_2$  to be etched. Though, the maximum thickness of  $\text{SiO}_2$  that must be etched is located on the overlapping segments

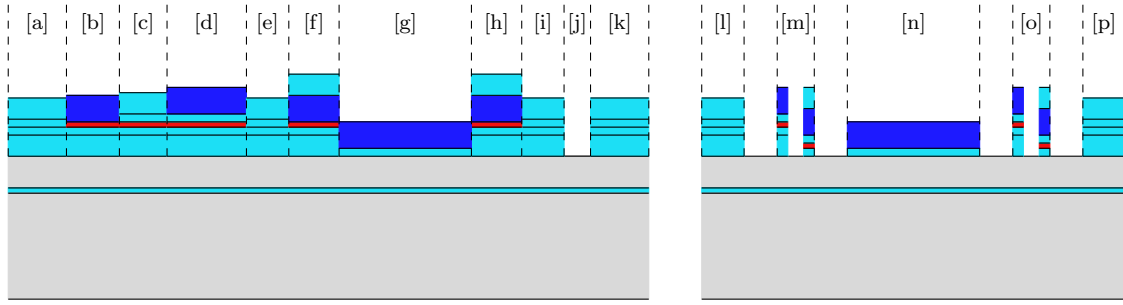


**Figure 5.11:** Schematic view of the fabrication step  $\langle\text{OXD2}\rangle$  of the first batch. [a,k]: Substrate; [b]: Pads; [c]: Space between the pads and the bimorph array; [d]: Bimorph array; [e,i,l,p]: Inner frame; [f,h]: Torsion bar; [g,n]: Mirror plate; [j]: Gap between the substrate and the inner frame; [m]: ISC-based actuators; [o]: ISC-based actuators.

**Table 5.3:** Comparison of two  $\text{SiO}_2$  slow and fast etching SOPs.

Fast $\text{SiO}_2$		Slow $\text{SiO}_2$	
Parameters	Etch rates ( $\text{\AA}/\text{min}$ )	Parameters	Etch rates ( $\text{\AA}/\text{min}$ )
CF <sub>4</sub> flow=30 sccm	SiO <sub>2</sub> =580	CHF <sub>3</sub> flow=45 sccm	SiO <sub>2</sub> =130
CHF <sub>3</sub> flow=20 sccm	PR=470	O <sub>2</sub> flow=5 sccm	PR=120
Ar=50 sccm		Pressure=200 mTorr	
Pressure=100 mTorr		RIE power=100 W	
RIE power=150 W			

of the MISC actuators and on every part where the  $\text{SiO}_2$  pattern of the  $\langle\text{OXD1}\rangle$  is larger than the pattern of the  $\langle\text{OXD2}\rangle$ , and accounts for the thickness of  $\langle\text{OXD1}\rangle$  plus  $\langle\text{OXD2}\rangle$  plus the thickness of the two insulation layers. To determine this thickness a last element has to be taken into account: the two following steps are dry anisotropic and isotropic Si etch phases comprising a very reactive gas ( $\text{SF}_6$ ) supposed to react with the Si exclusively. However, the etch rate of the  $\text{SF}_6$  on the  $\text{SiO}_2$  is not negligible and will thin down the thickness of  $\text{OXD2}$   $\text{SiO}_2$  on the top of the actuators thereby modifying their mechanical deflection and thermal properties.

The solution suggested to tackle this problem is to perform this step with all the former ones and all the following ones on a test wafer to test and estimate which thickness of  $\text{SiO}_2$  will fit the step of  $\langle\text{OXD2}\rangle$  to keep a final thickness close enough to the target of  $1.1\ \mu\text{m}$  on top of the bimorphs at the very end. After optimizing the thickness, we found out that a thickness of  $1.4\ \mu\text{m}$  of  $\text{SiO}_2$  yielded satisfactory results.

To go back to the topic in hand, the total thickness of  $\text{SiO}_2$  equals  $2.6\ \mu\text{m}$ . This entails that the thickness of PR must be greater than this value. Unfortunately, the typical thickness of AZ 1512 is optimized between 1 and  $2\ \mu\text{m}$  and suffer from homogeneity or pattern quality if spun more slowly to get a thicker film. A thicker PR such as AZ 9260 with a thickness of  $6.5\ \mu\text{m}$  was used instead. After a vigorous descum, the  $\text{SiO}_2$  is etched by RIE and before stripping the PR, the electrical connections on the Al pads must be verified.

Large areas are etched faster than narrow ones; thus, the Al of the mirror plate and the pads will be exposed first. Extra time is required to complete etching the remaining  $\text{SiO}_2$  in the narrow areas and corners. During this “overetching” time, black silicon may be created, by scattering of the exposed Al onto the Si exposed of the device layer. Black silicon is an undesirable side effect of RIE and can be efficiently avoided when the PR is rebaked before dry etch. Figure 5.12a show black silicon on the device layer around the MISC actuators after  $\langle\text{OXD2}\rangle$  dry etch phase and its corresponding layout in Fig. 5.12b.

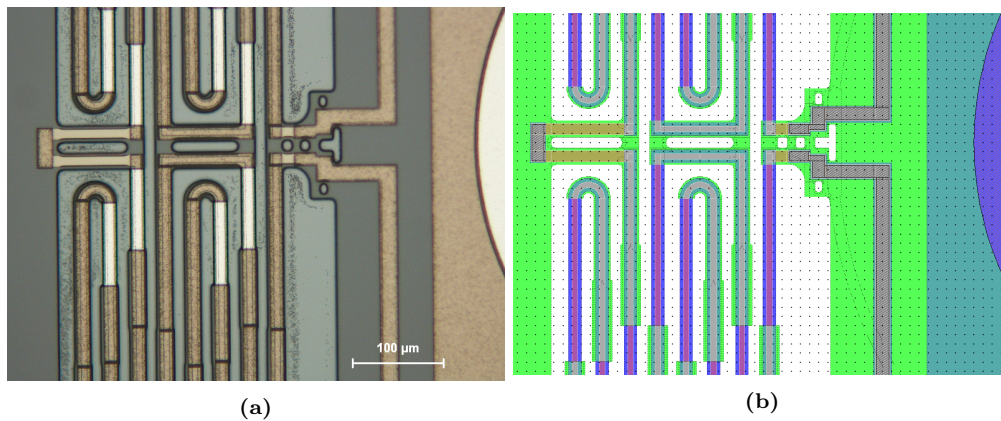


**Figure 5.12:** Fabrication results of step <OXD2>. (a): Black silicon around the MISC actuator area. (b): Corresponding layout.

### 5.1.8 Back side pit carving - BSD

This “pre-release” step is probably as tedious as the former one, as it requires going through several risky stages. Before releasing the microdevices from the top side, the thickness of the wafer must be thinned down from the back side until reaching the BOX. Once the BOX is exposed, it will be removed allowing a highly smooth surface quality under the mirror plate (the back side of the mirror).

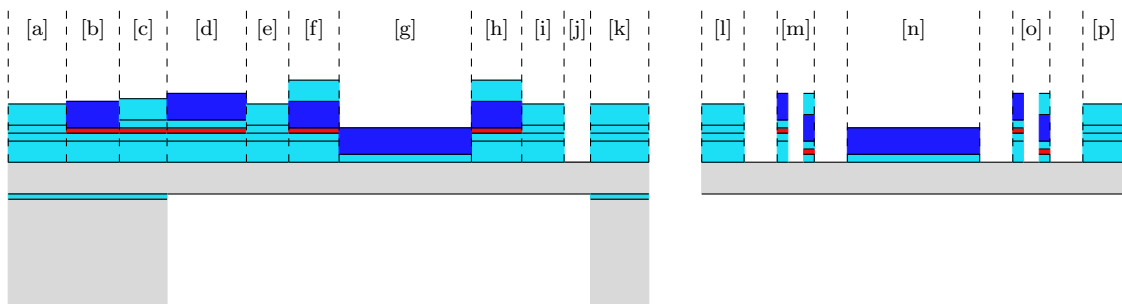


**Figure 5.13:** Schematic view of the fabrication step <BSD> of the first batch. [a,k]: Substrate; [b]: Pads; [c]: Space between the pads and the bimorph array; [d]: Bimorph array; [e,i,l,p]: Inner frame; [f,h]: Torsion bar; [g,n]: Mirror plate; [j]: Gap between the substrate and the inner frame; [m]: ISC-based actuators; [o]: ISC-based actuators.

Before starting any process on the back side of the SOI wafer, the front side must be protected. Generally, a “carrier” wafer is utilized to protect the front side and carry the SOI wafer from the beginning to the end of the step. Indeed, at the end of the step, the boundary between each chip will be strongly weakened and on the edge of being taken apart. At that point, the SOI wafer is very fragile and the role of the carrier wafer becomes compulsory. Figure 5.14a show the profile of the back side with the large pits and the deep and narrow grooves hanging on to 30 μm of Si.

Four different methods of bonding were tested using Fomblin<sup>®</sup> PFPE oil, Crystalbond<sup>™</sup>, dry and wet PR. According to the author, the best method is the one using wet PR. Once the carrier supports the SOI wafer, a photolithography with a thick positive PR AZ 9260 is performed on the back side with the mask <BSD>. The handle layer is etched anisotropically by DRIE in a tool from STS<sup>®</sup> all the way down to the BOX. The BOX is etched by RIE and the stack of wafers is dipped into a powerful solvent to remove the PR between the two wafers. Aceton, PR strip or NMP can be used.

The results are shown in Fig. 5.14b from the backside where some chips were already separated



from the wafer, and a cluster from the front side is also shown in Fig. 5.14c.

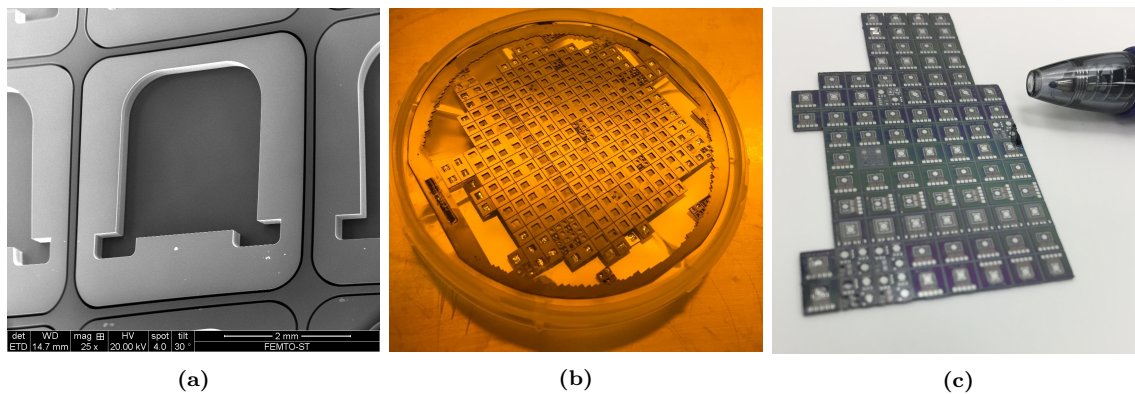


**Figure 5.14:** Fabrication results of step (BSD). (a): Profile of the back side of the SOI wafer. (b): State of the wafer after separation of some structures from the wafer. (c): Cluster of micromirrors ready for final release step.

### 5.1.9 Release - REL

The last step of the fabrication process of the first batch of fabrication consists in releasing the micromirrors from their substrate. The release stage is performed in two steps and can be carried out at the wafer level (if the layout allows to do so) or at the chip level. If performed at the wafer level, one or a few chips are fixed to a thermal tape stucked on an oxidized carrier wafer as shown in Figs. 5.15a and 5.15b. We used a Nitto<sup>®</sup> thermal tape which loses its taping effect at a temperature of 180 °C. The first step consists of an anisotropic DRIE through the device layer (about 30 μm). It is followed by a second step whose purpose is to remove the Si of the device layer beneath the actuators and the torsion bar to “release” them literally. Otherwise, the device won’t pop up and the mirror will remained unmovable as shown in the two steps of release in Fig. 5.15c where some Si remains under the torsion beam and in Fig. 5.15d where all the silicon has been removed and the tilt is apparent. The release time has an influence on the initial tilt angle and may be optimized after several preliminary trials. SEM pictures of the released device and its different specific parts are shown in Figs. 5.15e to 5.15h.

## 5.2 Complementary fabrication tips

The second batch of fabrication comprising the devices Tor2.x and Quad2.0 represented in Fig. 5.16 brought up a few additional novelties. A dual-reflective mirror plate was fabricated; gold was deposited on the pads to improve the adherence with the wire bonder gold wire; and a Ni/Cr-based strain gauge was monolithically embedded on the torsion beams of the micro-scanner in order to replace external sensors used to monitor the displacement of the mirror for potential feedback controls. These improvements are presented in the following subsections. First a rectified flow chart is provided in Table 5.4 enabling to integrate all the modifications in one batch. Then each novelty is detailed one by one.

### 5.2.1 Flow chart

Four additional steps were inserted in the flow chart of the second batch compared to the first one. The wafers used for the second batch has room for 273 chips, possesses an exclusion ring

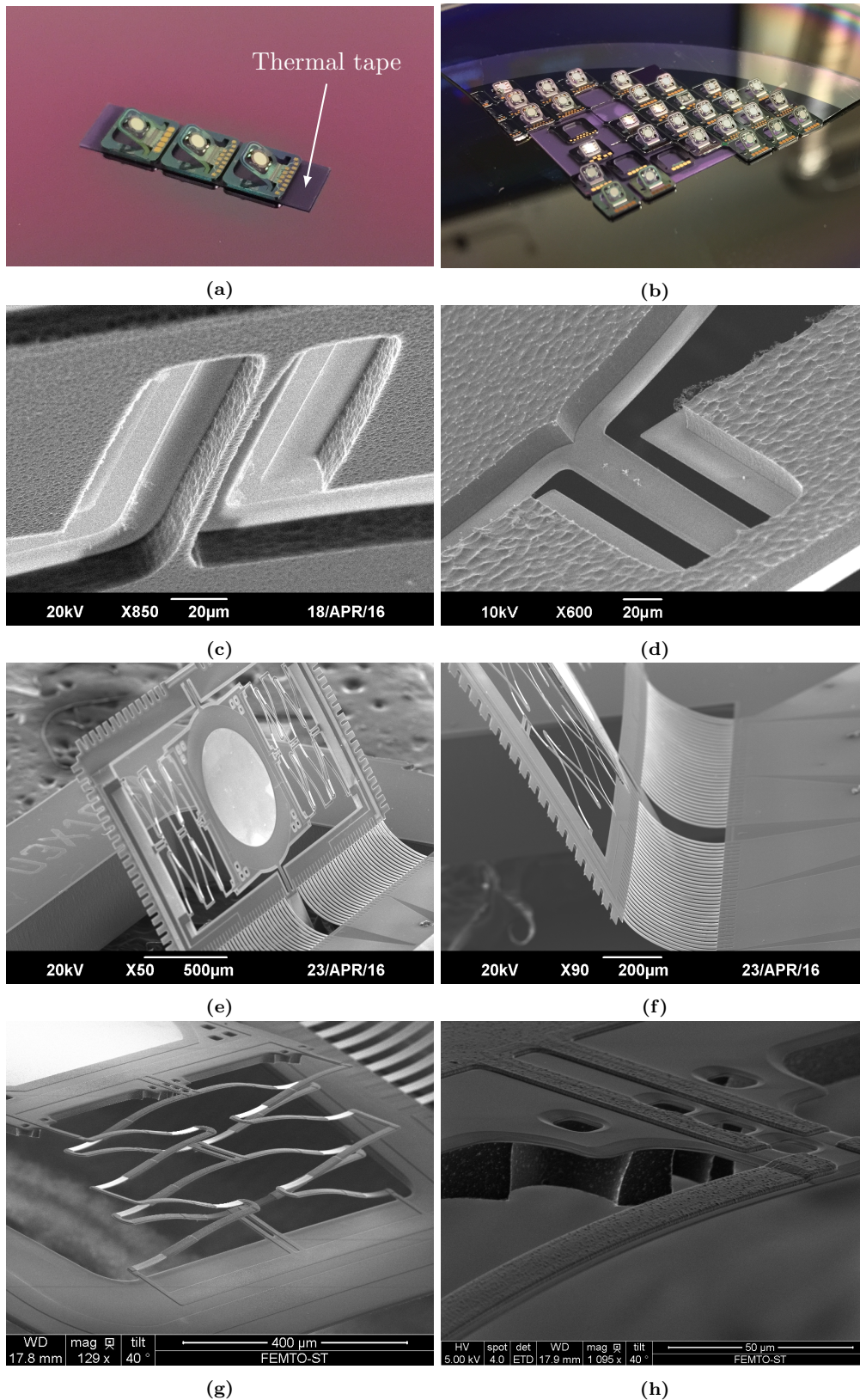


**Figure 5.15:** Fabrication results of step (REL). (a): Three micro-scanners stuck on thermal tape after release and before being removed from the carrier wafer. (b): Bigger amount of devices after release. (c): Unreleased torsion bar. (d): Released torsion bar. (e): Front side SEM view of the Tor1.x. (f): Close-up view of the Tor1.x bimorph array. (g): Close-up of the MISC actuators. (h): Thermal insulation bridge between MISC actuators and mirror plate.

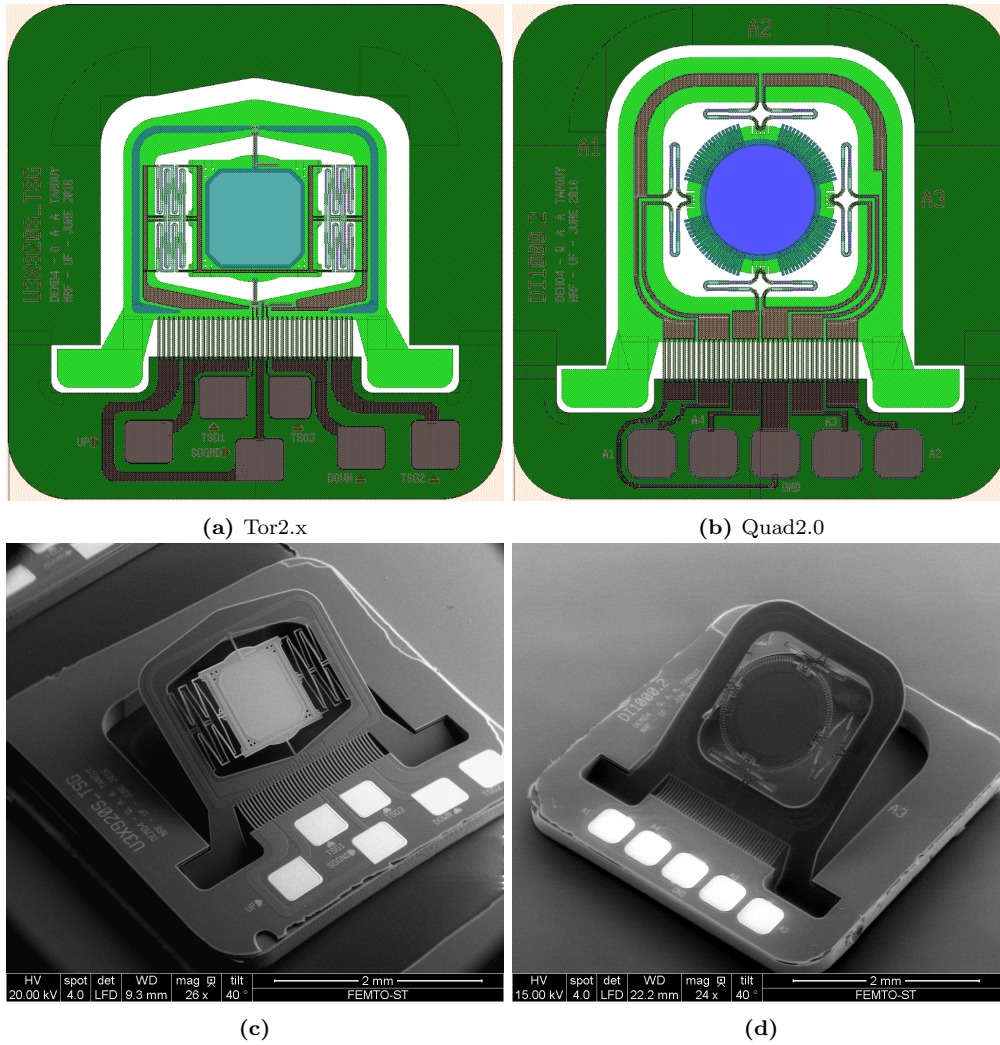


**Figure 5.16:** Layout of the (a) Tor2.x and (b) Quad2.0 micro-scanner fabricated and presented in the current work and their corresponding SEM pictures (c) and (d).

of 8 mm, 2 alignment marks and 3 visual alignment marks for macro positioning. The 3 macro alignment marks are used to align the mask of the mirror back side aluminum photolithography. Two different techniques for this specific step are presented in Section 5.2.3.

### 5.2.2 Gold pads - AUP

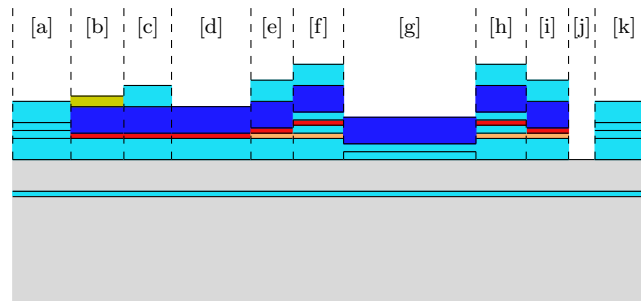
Most wire-bonders<sup>3</sup> are equipped with gold wires because it is the most flexible material and suits a very wide variety of processes. Formerly, the pads of our chips used to be made of Al (with 150 Å of Cr on top), and making gold wires adhere on Al is not always an easy task. Hence, to gain time and money in the wire bonding step, a thin gold coat was deposited right on top of Al pads. The step is represented below:

It is recommended to deposit at least 2500 Å of gold for bonding pads. In addition this step must be performed as the very last operation on the front side of the wafer to prevent potential diffusion of gold into other materials. A thickness of 3000 Å of gold was deposited by sputter in a Plassys<sup>®</sup> MP700S with an adherence layer of Cr of 150 Å deposited underneath only.

<sup>3</sup>The term of wire bonder, although not defined yet, is a tool in micro technologies used to bond pads of small size with a micro wire. The process will be presented more in details in Section 5.3.

**Table 5.4:** Chronological list of steps of fabrication of the device Tor1.x with the corresponding color code of materials.

Step	Description	Mask I.D.	
	Wafer clean up	-	
1	SiO <sub>2</sub>	OXD1	Light Blue
	Insulation	-	Light Blue
2	Platinum sputtering	PT	Red
	Insulation	-	Light Blue
3	Via opening	VIA	
4	Aluminum front side	ALU1	Blue
5	SiO <sub>2</sub>	OXD2	Light Blue
5a	Gold pads sputtering	AUP	Yellow
6	Back side pit	BSD	
6a	Aluminum back side	ALU2	Blue
7	Release	-	

**Figure 5.17:** Schematic view of the fabrication step (AUP) of the second batch. [a,k]: Substrate; [b]: Pads; [c]: Space between the pads and the bimorph array; [d]: Bimorph array; [e,i,l,p]: Inner frame; [f,h]: Torsion bar; [g,n]: Mirror plate; [j]: Gap between the substrate and the inner frame; [m]: ISC-based actuators; [o]: ISC-based actuators.

Unfortunately, in reality this step was realized before the deposition by PECVD of SiO<sub>2</sub> at 300 °C and despite the 300 Å-thick Cr layer between the gold and the aluminum, diffusion still occurred. The compound resulting from the diffusion has not been analyzed by spectrometer to identify the constituent and the proportions, however, we reckon AuAl<sub>2</sub> (also known under the name of “purple plague”) replaced the Al/Au pads because of its purplish tint under white light. Although purple plague is known as affecting significantly the adherence, the roughness and reducing the resistivity, the pads of our devices could be saved. More detail will be provided in Section 5.3.

An SEM picture of the pads where diffusion occurred is shown in Fig. 5.18a and Fig. 5.18b more in a close-up.

### 5.2.3 Second mirror aluminum layer - ALU2

The only purpose of the second layer of Al is to make the back side<sup>4</sup> of the mirror reflective. Although two different methods were considered to realize this step, by hard mask and using dry PR, only one of them led to acceptable results. This step is performed right after the BOX has finished etching.

<sup>4</sup>The “back side” denotes the side which is exposed after the removal of the BOX; not the one on the top side of the device layer.

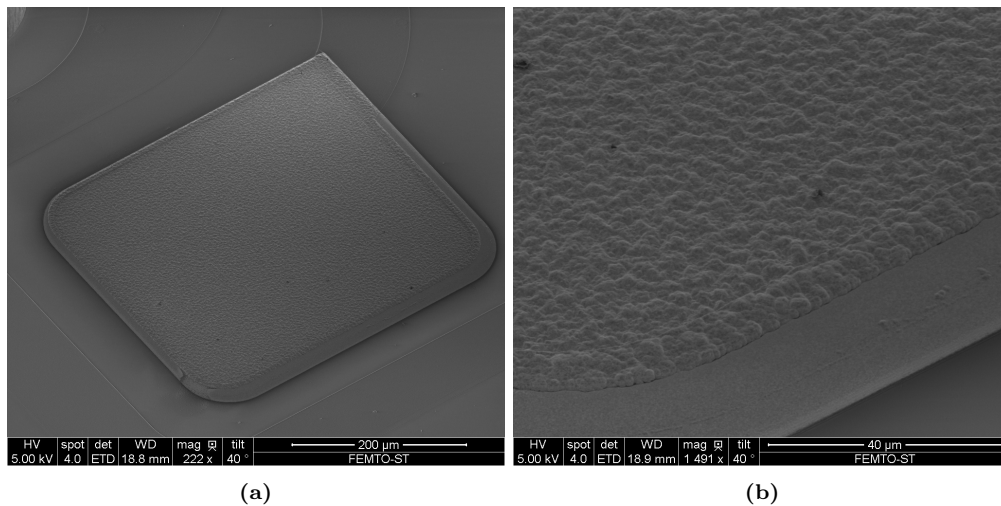


**Figure 5.18:** Fabrication results of step (AUP). (a): SEM overview of an  $\text{AuAl}_2$  pad subject to diffusion. (b): Close-up of the pad, roughness detail.

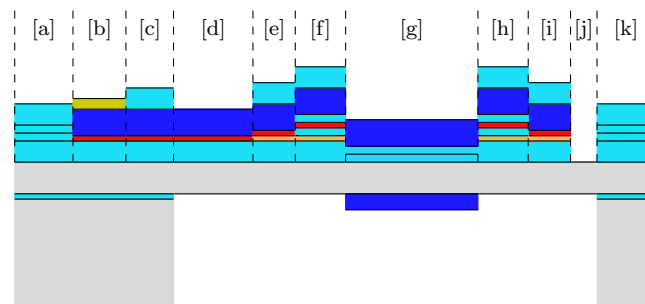


**Figure 5.19:** Schematic view of the fabrication step (ALU2) of the second batch. [a,k]: Substrate; [b]: Pads; [c]: Space between the pads and the bimorph array; [d]: Bimorph array; [e,i,l,p]: Inner frame; [f,h]: Torsion bar; [g,n]: Mirror plate; [j]: Gap between the substrate and the inner frame; [m]: ISC-based actuators; [o]: ISC-based actuators.

The advantage of using dry PR is that it can be laminated evenly, even over deep cavities where a standard photolithography would most likely fail. Although a deposition by spray coating could be a possible trade off, the method remained untested. A recap schematic is shown in Fig. 5.19.

The dry PR used is a  $50\ \mu\text{m}$  thick DuPont™ WBR 2000 series dry negative PR film. The film is laminated on the back side of the handle layer after removal of the polyethylene layer and with the appropriate lamination conditions prescribed by DuPont™ at  $85\ ^\circ\text{C}$ . After a bake in oven of 20 min at  $65\ ^\circ\text{C}$ , the back side of the SOI wafer is aligned under a microscope with a glass photomask or an emulsion thin film mask and exposed with a dose of  $400\ \text{mJ}/\text{cm}^2$  at  $365\ \text{nm}$ . A post-bake must be performed at  $70\ ^\circ\text{C}$  for 30 min and the PR is developed in a custom solution of  $\text{K}_2\text{CO}_3$  at 1.0 wt% for about 160 s. Then, the wafer is rinsed and dried very gently, taking care of the fragile film hanging over the cavities. No post-development bake nor descum is recommended. A photograph of this step is shown in Fig. 5.20a where the subsiding of the hanging film over the cavities around the holes is apparent. Finally,  $150\ \text{\AA}$  of Cr,  $4000\ \text{\AA}$  of Al and  $150\ \text{\AA}$  of Cr again are evaporated on the substrate without heating. The wafer is stripped, and the fabrication process gets back to the last step of release.

A picture taken by microscope showing the position and the dimension of the mirror plate is given in Fig. 5.20b before starting the release process from the front side. The radius of the mirror disk shown on this picture measures  $400\ \mu\text{m}$  on the layout. We can observe an actual reduction

of the real radius of 1.9% mainly due to the subsiding and the wet rinsing. The back side of the mirror plate is shown in Fig. 5.20c before complete release of the in-frame mirror.

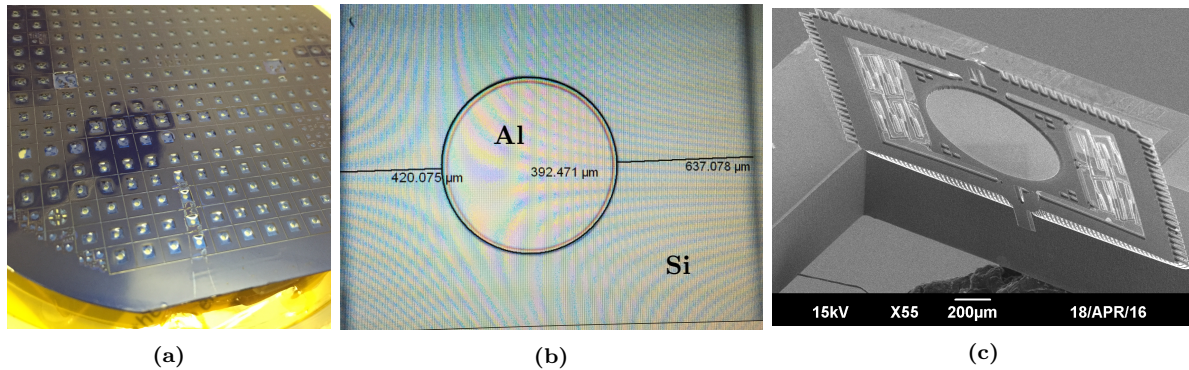


**Figure 5.20:** Fabrication results of step (ALU2) using dry PR. (a): Dry PR after lamination and photolithography on the back side of the SOI wafer. (b): Microscope image of the back side of the mirror plate aluminum reflective layer and measures. (c): SEM picture of the back side of the mirror plate before complete release of the torsion bars and inner MISC actuators.

### 5.3 Packaging

In a first time, a “packaging” was designed for tests and characterization of the micromirrors. Such an interface is necessary for interconnection with the macroworld and safe handling out of a cleanroom. A custom support was designed to bond the chips and connect the pads with external devices such as function generators to generate voltages and drive the micro-scanners. A thick PCBs was custom-made with a main gold bonding pad of the size of the micro-scanners rounded by a series of gold connection pads to connect the pads of the micro-scanners by wire-bonding. The PCBs designed is shown in Fig. 5.21. The PCB holder only has a routing function and the small gold pads are connected to white 5 contact right angle wire-to-board connectors. Each PCB is equipped with 2 connectors. One connector is for the driving signals and the other one for the strain gauge sensors.

First a micro-scanner is carefully handled and glued onto the central hollow pad with a layer of 2 mil of silver epoxy in between. Then, the whole PCB with the micro-scanner on it is baked at 80 °C for 3 h for epoxy annealing. The micro-scanners failed to be wire bonded using a conventional 1 mil thick gold wire as shown in Fig. 5.21b. Indeed, the stress on the pads is disproportionned for the low adherence of the pads, and as a result, the pads are pulled off until the SiO<sub>2</sub> underneath. Hence, a 17 μm gold wire was used instead in order to decrease the stress on the pads. It was also implemented with lower parameters and a smaller ball than usual as specified in Table 5.5 for the TPT<sup>®</sup> HB16 tool. Furthermore, the ball bond was performed on the PCB gold pads and the wedge bond on the device pads. This method gave a yield of about 2/3 of successful wire bonding (see Fig. 5.21c).

A sketched in Fig. 5.22, the PCB has a size of 10 mm x 79.5 mm with a thinner end to fix the micro-scanner facing the lateral edge. The characterization will consist of testing the thermomechanical behavior of the micro-scanner but also its performance for imaging. Hence, an optical setup with dimensions as close as possible to the final embedded system must be adopted in characterization setup. Therefore, the micro-scanner is located the closest to the edge to minimize the distance between the optical components and the center of the mirror plate which will determine

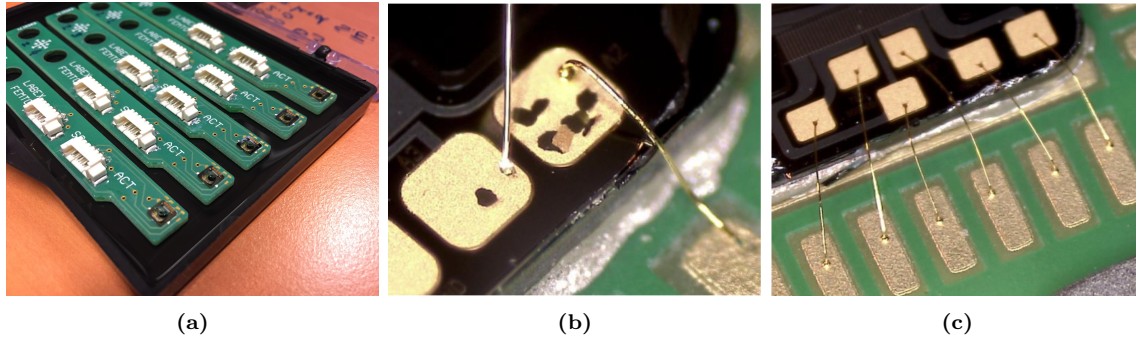


**Figure 5.21:** Custom bonding PCBs fabricated for experiments and characterization. (a): Reduced-size narrow PCB holders in a gel pack for transportation. (b): Failed trials with 25  $\mu\text{m}$  gold wire. (c): Successful trials with 17  $\mu\text{m}$  gold wire.

**Table 5.5:** Summary of the parameters used for the 17  $\mu\text{m}$  wire bonding SOP using the TPT<sup>®</sup> HB16 tool.

Parameter	Value		Ball bond	Wedge bond
Looph	500	US	120 m W	150 m W
Yway	500	Time	200 m s	200 m s
Temperature	120 °C	Force	300 m N	300 m N
Up CO	400			

the working distance, the focal length and the DOF of the imaging setup. The results of the characterization and of the imaging are given in Chapter 6.

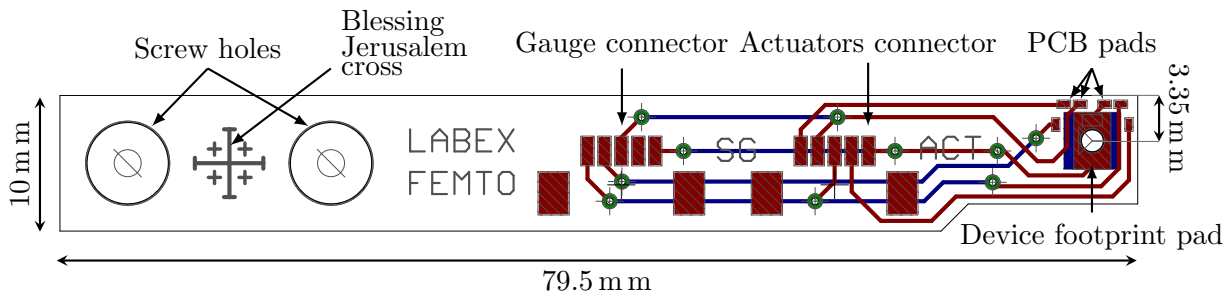


**Figure 5.22:** Sketch of the micro-scanner holder PCB used for characterizations and testing.

The big gold pad referred to as “device footprint pad” in the sketch Fig. 5.22 has the same footprint as the micro-scanner, and is used as a thermal and electrical ground for the device. Its center matches the vertical of the center of the released mirror plate when the inner frame is tilted at  $45^\circ$ . Thus, the distance between the edge of the PCB and the center of the micro-scanner’s mirror plate is 3.35 mm. The hole in the footprint pad allows the alignment of a light beam through the PCB. This way, both sides of the mirror plate can be exploited: one side can be used for imaging (OCT for example) and the other side for optical position tracking for a feedback control for instance.

## 5.4 Conclusion

Two series of fabrication were carried out for two different batches of micro-scanners. The device Tor1.x is the main outcome of the first batch and is composed of 6 photomasks and 7 major steps whereas the Tor2.x and Quad2.0 brought four additional novelties all integrated in the second

batch requiring 9 masks and 11 steps of fabrication. The first batch was well developed in the NRF and does not present particular risks nor hazards for the fabrication. The second series of fabrication is much more risky because of the introduction of the very oxidizing *Karma* alloy used for the strain gauge which reduces the access to a few tools used to guarantee the quality of the photolithographies. Furthermore, the second batch was realized in a different cleanroom and most processes had to be completely re-developed from scratch. Finally, the micro-scanners were packaged onto a custom macro interface to undergo further tests. The design of the holding PCB conceived for characterization and imaging was presented, as well as the wire-bonding stage. Despite the damage caused to the pads due to a phenomenon of diffusion, most of the devices could be saved and will be used for testing in a first place before being integrated to the Mirau micro-interferometer.

#### Chapter summary

The chapter presented in three sections the fabrication process of the first and the second batches of fabrication and the packaging design and procedure. For each step, a sketch of the state of progress is provided as well as the risks and recommendations of the author. At last the interface between the devices fabricated and the instrumentations of the macro world is introduced and will be used in the all the characterizations, imaging and other experiments which will be presented in the following chapter.





## Chapter 6

# Characterization and integration

THE static and dynamic behaviors of the fabricated micro-scanners are compared to the model predictions as much as possible, in order to evaluate the general performances attained. The ability of the devices to perform imaging is tested on Lissajous scans. Finally, the first steps of integration of the probe with the Mirau micro-interferometer are presented. To characterize the micro-scanners, the PCB described in Chapter 5 was used as a holder to handle and adjust the position of the device. It was also employed as an interface with the instrumentations required in several setups to characterize the electrothermomechanical behavior of the devices under static and dynamic conditions.

### 6.1 Characterization of the micro-scanner

After the last step of fabrication, the devices from the first batch (Tor1.x), which do not have a mechanical stopper, were characterized under a microscope with an initial angle of  $70^{\circ}_{\text{mech}}$ . This is due to a necessary overetch time to release the structures due to a difference in the width of the actuators and the torsion bars themselves as well as in the difference in the size of the space around them. Indeed, the isotropic etch time of the final step of release determines the quantity of Si etched underneath the actuators and the torsion bar. If these two elements are not released in the same time, the etching time may be extended causing at some point the  $\text{SiO}_2$  to be thinned down. When the  $\text{SiO}_2$  is deposited at  $300^{\circ}\text{C}$  and cools down to ambient temperature, the pattern is unchanged in its dimensions causing the layer to develop a high tensile stress. Then, as the aluminum is deposited without stress on top of the highly stressed  $\text{SiO}_2$ , the bimorph bends up because the tensile stress is intrinsic to the lower layer. If the  $\text{SiO}_2$  layer is thinned down *a fortiori*, its surface is reduced and the stress is consequently increased, thereby causing the bending angle to be larger, which explains that the initial angle is higher than expected [360].

So far, only the Tor1.x, shown in Fig. 6.1a, has been characterized and the results of the characterization will be presented in this chapter. The second batch's Tor2.x and Quad2.0 will be characterized later and presented in a future work.

This section of characterization is divided in 4 subsections. First, the general features of the device and its static behavior (when a **direct current (DC)** signal is applied on the actuators) are characterized. Then, the experimental setup used to drive the micro-scanner and track its position dynamically is detailed, and finally a characterization of the dynamic behavior and the frequency response of the device are provided. A last section will take care of presenting the integration

process of the micro-scanner with the Mirau micro-interferometer.

### 6.1.1 Optical characteristics

A topographic characterization was conducted on the surface of the micromirror (highlighted in Fig. 6.1b) to screen the surface quality of the mirror in order to evaluate the impact on the quality of the optical signal obtained in the final integrated system. For a matter of time, only the upper surface was investigated. The upper surface reflective layer deposition is the sixth last fabrication step, much more impacted by the physical and chemical processes and treatments of the last steps (RIE, DRIE, bonding, ...) than the back-side reflective layer which is the second last step. The mirror quality of the back side should then be much higher than the one of the front side. A Polytec MEMS Analyzer MSA 500 was used to realize a topography of the mirror plate. The outcome of the topography is shown in Fig. 6.1c.

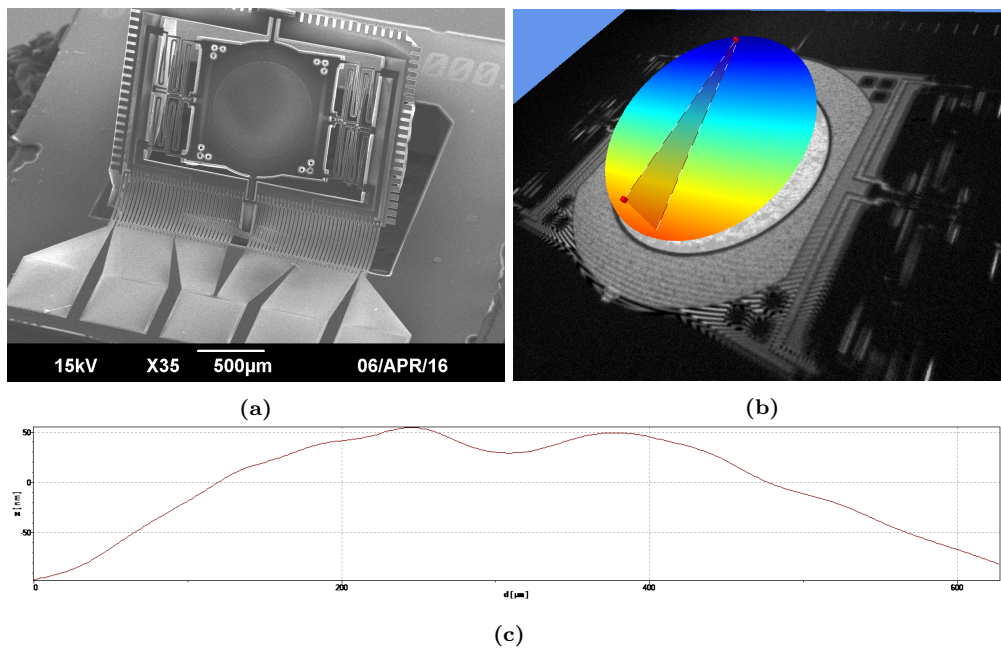


**Figure 6.1:** Tor1.x (a) SEM picture, (b) topography front-side surface of the mirror plate and (c) topographic profile curve.

The topography was realized on the effective part of the mirror which does not overlap the  $\text{SiO}_2$ , where the flatness is the better. The radius of curvature was measured at  $\sim 1.3$  m corresponding to  $\lambda/6$  and the roughness is below 10 nm. This quality will not deteriorate the laser beam too much (at least it is acceptable for the back side where mere dynamic angular position tracking will be realized by laser reflection onto a [position sensing detector \(PSD\)](#)).

### 6.1.2 General features and static behavior

The electrical resistances of the pitch and roll actuators were measured after release at 1.34 k $\Omega$  and 1.07 k $\Omega$ , respectively. It was observed that the resistance before and after release could be significantly different. Furthermore, the resistance varies with temperature as well as with aging. A brief study of the resistance shift of the heater was reported by Chen *et al.* [361] who showed that the heater resistance decreased no more than 6% for a typical MEMS device subject to 100 million scan cycles. In our devices, the heating resistance of the actuators was a bit underestimated

because of the biased value of the resistivity of the bulky Pt  $\rho_{Pt}$  found in the literature. The value of the heater resistance was fit on the measured value of the resistance at ambient temperature in order to derive an appropriate resistivity for thin films of Pt. This value was calculated at  $314 \times 10^{-9} \Omega \text{ m}$ . The resistance change trend is well estimated by the model, and is compared to the experimental measurements in Fig. 6.2.

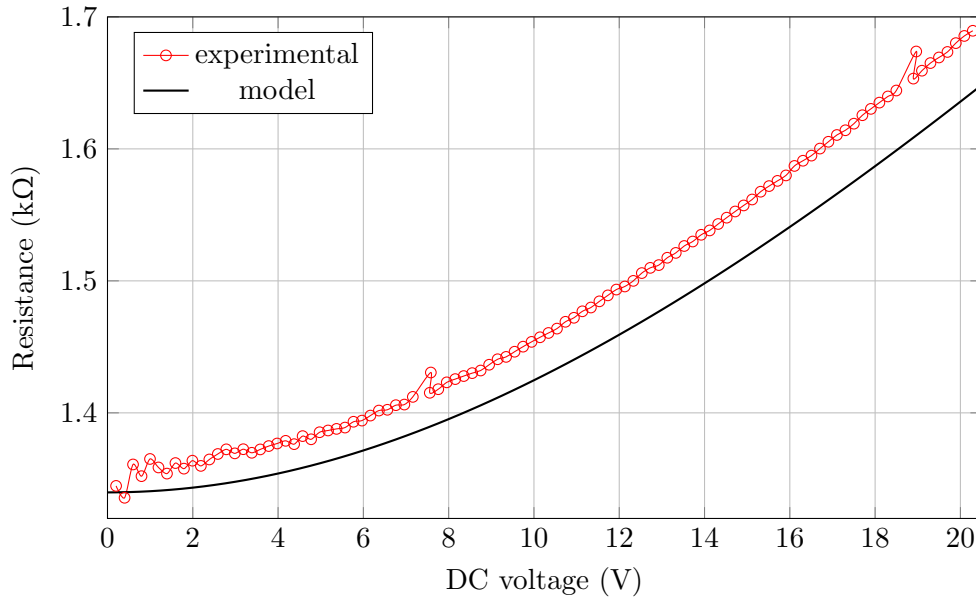


**Figure 6.2:** Comparison of resistance change upon actuation obtained experimentally and from the model.

The device chips were arranged vertically and observed under a microscope to measure the absolute angle of rotation of the inner frame and the mirror plate when the actuators are independently driven at different DC voltages using a power generator. Figure 6.3 shows the static angular behavior of each actuators independently with respect to different actuation voltages. The inner frame deflects over  $32^\circ$  in total from an initial angle of  $70^\circ$  to a maximum angle of  $38^\circ$  for a limit voltage of  $16 V_{DC}$  corresponding to  $178 \text{ mW}$ . The mirror plate declines from  $18^\circ$  to  $-4^\circ$  achieving a maximum total angular scan range of  $22^\circ$  at  $16.5 V_{DC}$ , *i.e.*  $188 \text{ mW}$  for the Tor1.28<sup>1</sup>. A negative angle for the roll actuators refers to when the mirror plate is crossed the plane of the inner frame (for a negative  $\theta_r$  in Fig. 4.20).

The power consumed due to Joule heating is calculated, multiplying the known voltage applied and the current measured through the actuators using an ammeter. The real power is compared with the power estimated by the model of Eq. (4.11b), with and without considering the convection in Fig. 6.4.

Barely no difference is noticeable between the power trends calculated by the model with and without convection. This is mostly due to the fact that the resistances due convection in our design are much higher than the ones due to conduction. And hence, the influence of the convection is bypassed by conduction. A very slight discrepancy is visible between the models and the experimental results at “high” voltage (over  $15 V_{DC}$ ). This can be explained by the increase of the non-linearity of the parameters with respect to temperature such as the TCR that was supposed constant at all time. A similar behavior can be observed even more seriously in the curve

<sup>1</sup>The two-digit figure located after the dot in the formalism of the micro-scanner’s type (Tor1.x, Tor2.x) replacing the “x” refers to the width of the torsion bar in  $\mu\text{m}$ .

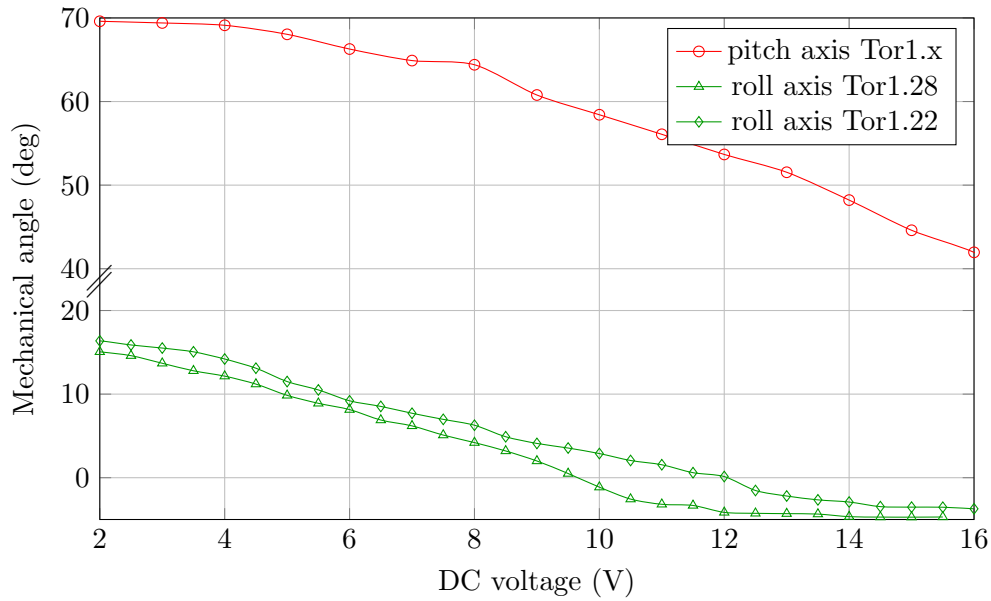


**Figure 6.3:** Absolute static angular displacement of the inner frame and the mirror plate vs. DC voltage applied.

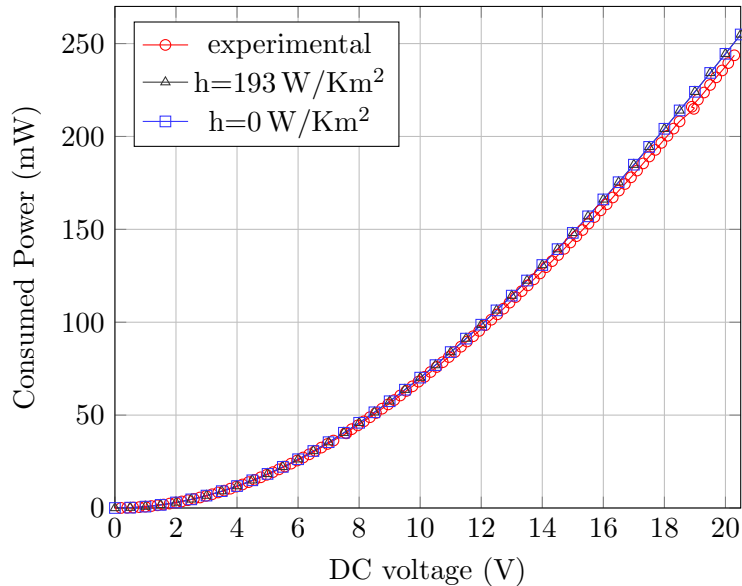


**Figure 6.4:** Power consumption of the actuators due to Joule heating vs. voltage applied.

of the optical angular displacement shown in Fig. 6.5a. The experimental curve was compared with the model and exhibits about 15% of error at  $12 V_{DC}$ .

The average and maximum temperature change on the bimorph beams is extracted from the model and plotted in Fig. 6.5b. The balancing factor calculated equals 7.8, which is still acceptable for the distribution uniformity. The highest temperature reached on the bimorph transducer of the pitch axis is estimated at about 380 K at  $20 V_{DC}$ . The temperature was not measured nor estimated on the roll axis because the main problem that occurred due to temperature was located on the bimorph array: indeed, an overheating at the base of the bimorph array actuators caused the aluminum to burn. This defect modified the properties of the aluminum and damaged the actuators making the micro-scanner unusable. This phenomenon was also reported by Pal and Xie and can be seen in [315].

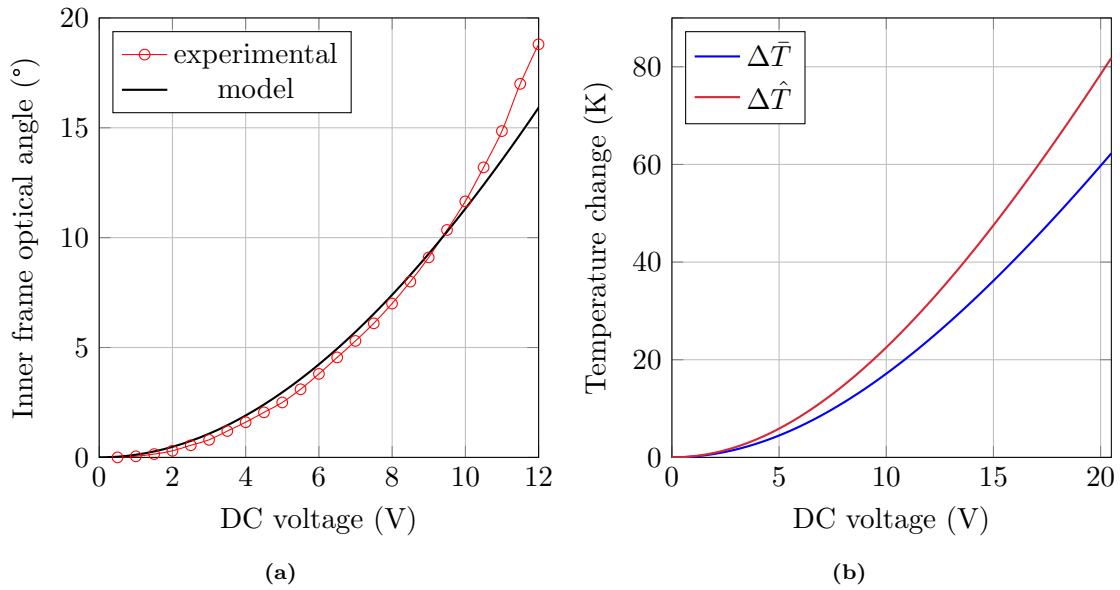


**Figure 6.5:** DC characterization of (a) optical angular pitch displacement of the inner frame compared with the model results and (b) corresponding calculated average temperature change  $\Delta\bar{T}$  and maximum temperature change  $\Delta\hat{T}$  across a bimorph actuator.

### 6.1.3 Experimental setups

A sketch of the optical setup is given in Fig. 6.6. It was used for most characterization experiments where the static or dynamic relative position of the mirror is sought as well as for dynamic scan and imaging.

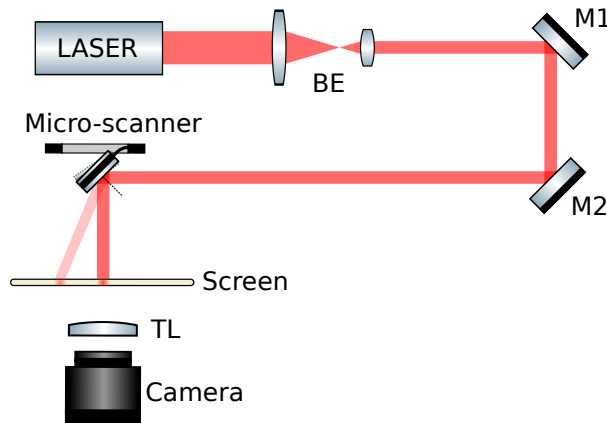


**Figure 6.6:** Sketch of the experimental optical setup used for characterization of the micro-scanner.

In order to work as close as possible to the operational conditions, we use a 632.8 nm laser beam of 5 mW directed precisely onto the micro-scanner that reflects it on a diffusing screen. The diameter of the laser beam is reduced to about 0.5 mm using a 4F doublet of lenses denoted as “beam expander” (BE) in the sketch. A pair of fixed mirrors M1 and M2 are used to direct the light beam along the X and Y directions (perpendicular to the optical path), towards the center of the micromirror. Then, upon actuation of the micro-scanner, the beam is deflected on one side of a diffusing screen observed by an ultrahigh-speed camera Phantom<sup>®</sup> Miro M120 on the other side. A focusing lens is also employed between the screen and the camera to adjust the size of the image and the resolution. Then, the images captured by the camera are collected and processed

by a computer.

The micromirror interfaced through the PCB holder, is connected to custom wires used to route the proper ports to the corresponding actuators to be driven. This way, several micro-scanners can be very easily interchanged, and only the wire connector needs to be reconnected. The Tor1.x, for instance, is composed of 2 axes, 3 actuators (1 for the pitch and 2 for the roll motion) and 5 pads: 2 for the pitch actuator, 2 for each roll actuator plus one more for their common ground. The roll actuators are interconnected in parallel and 2 operational amplifier (OA) are used to amplify the signal by a factor of 2 from a NI data acquisition (DAQ) card itself driven by a program coded in Python. The OAs are used because the current delivered from the DAQ is too low to drive the micro-scanners. A voltage regulator is used instead of a current OA setup. The schematic electrical circuit of the OA is shown in Fig. 6.7.

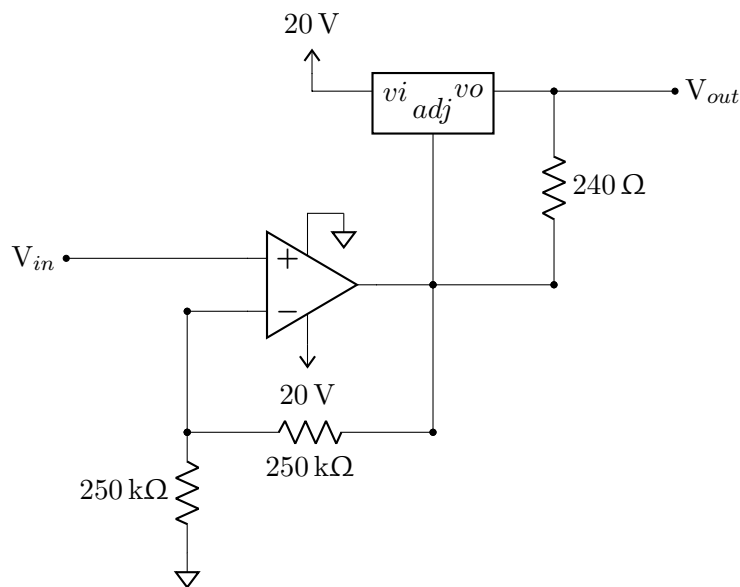


Figure 6.7: Sketch of the OA electrical circuit.

A picture of the custom OA PCB is shown in Fig. 6.8b and comprises 4 channels to be adaptable to both Tor and Quad designs with 2 and 4 actuators respectively. The board is also powered by a voltage generator in 20 V. The DAQ, shown in Fig. 6.8a is connected to the computer and the analog outputs are connected to the OA card via BNC to SMA cables. Finally, the last element of the chain, the micro-scanner PCB holder is connected to the custom routing wires (red) to the OA as shown in Fig. 6.8c.

The voltage regulator and the OA are components from LT<sup>®</sup>. The  $V_{in}$  is connected to an analog output of the DAQ and the  $V_{out}$  to one of the actuator ports. The signal is amplified by a factor of 2 and because of the voltage regulator, a lower saturation occurs below 2 V.

#### 6.1.4 Dynamic behavior and frequency response

The setup described in the former section was used for the characterization of the time and frequency response of the micro-scanner. A Polytec MEMS Analyzer MSA 500 was used to measure the deviations on the torsion bars for a frequencies ranging from 0.5 Hz to 4 kHz. The region around the torsion bars is chosen as the ideal area where to observe the motions of the whole structure, because movements linked to the two *dofs* in pitch and roll are present. Series of measures of

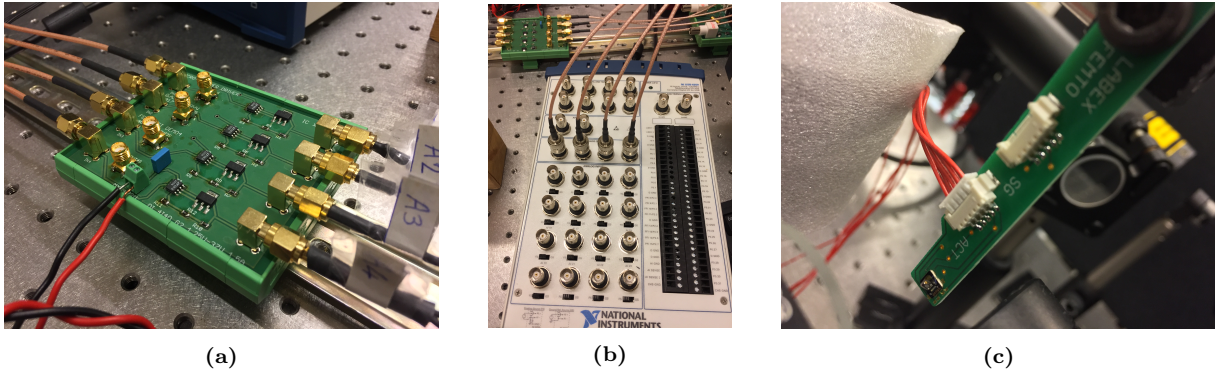


**Figure 6.8:** Elements constituting the driving setup. (a): Custom OA PCB. (b): DAQ with four connection cables for the Quad2.0. (c): micro-scanner PCB holder and routing wire connected.

frequency response were carried out for three different widths of torsion bars of the Tor1.x type. For each type, a voltage white noise signal of frequencies ranging in a bandwidth of 4 kHz was applied on each actuators (one after another) with a bias voltage of 1.5 V and around a working point for an amplitude of  $0.2 V_{pp}$ .

The gain and phase of the Tor1.28 are given in Fig. 6.9 when the white noise is applied on the pitch actuator (denoted by “Tor1.28 pitch” and in red in Section 6.1.4) and when the noise is applied on the roll actuator (referred to as “Tor1.28 roll” in green in Section 6.1.4). The magnitude in dB is only given for estimation. Two resonance frequencies can be observed when the pitch bimorph array is driven: the first one at 205 Hz is the pure pitch motion (the draw bridge movement of the inner frame) and the second one identified at 2.881 kHz is a tilt mode of the inner frame around the roll axis. This latter high-frequency mode, which is unwanted, is very overdamped and does not influence the scan of the micro-scanner. Four resonance frequencies are observed when the roll actuator is driven. The first and the fourth resonance are superimposed with the first and the second one of the former experiment, when the pitch actuator is driven. The fact that the first resonance peak is also identified at 205 Hz witnesses the coupling effect of the inner actuators on the outer one. The second peak at 1.286 kHz corresponds to the pure tilt motion of the mirror plate keeping the inner frame idle. The absence of coupling from the outer pitch actuator towards the inner actuators can be pointed out here: indeed the heat flow direction is directed from the inside of the micro-scanner to the outside, to the bulky silicon substrate acting like a thermal well. Finally, the third mode measured at 1.586 kHz, is a cross-coupling between the roll axis tilt and the pitch axis flapping. This mode is highly undesired and motivated the implementation of the mechanical stopper to mechanically bypass the influence of one axis over the other one.

The resonance frequencies of each type of micro-scanner are summarized in Table 6.1 and are consistent with the increase in frequency of the pure tilt mode dependence with the width of the torsion bars. The resonances of mode #2 are compared with the model in Table 6.1 (in red and in parentheses) and appear to be relatively close to the experimental values of frequency. The resonance frequency of the inner frame flapping mode stays relatively constant with this parameter.

For the third and fourth modes, the frequency decreases between the Tor1.22 and Tor1.28 and increase again between the Tor1.28 and the Tor1.38. These resonance modes were not modeled, however, an analytical model to determine the peak value of the cross-coupling mode could be the topic of a future work in order to increase the gap between the pure tilt mode and the coupled mode and to prevent it from being in the vicinity of the harmonics of the first pitch mode. Indeed,



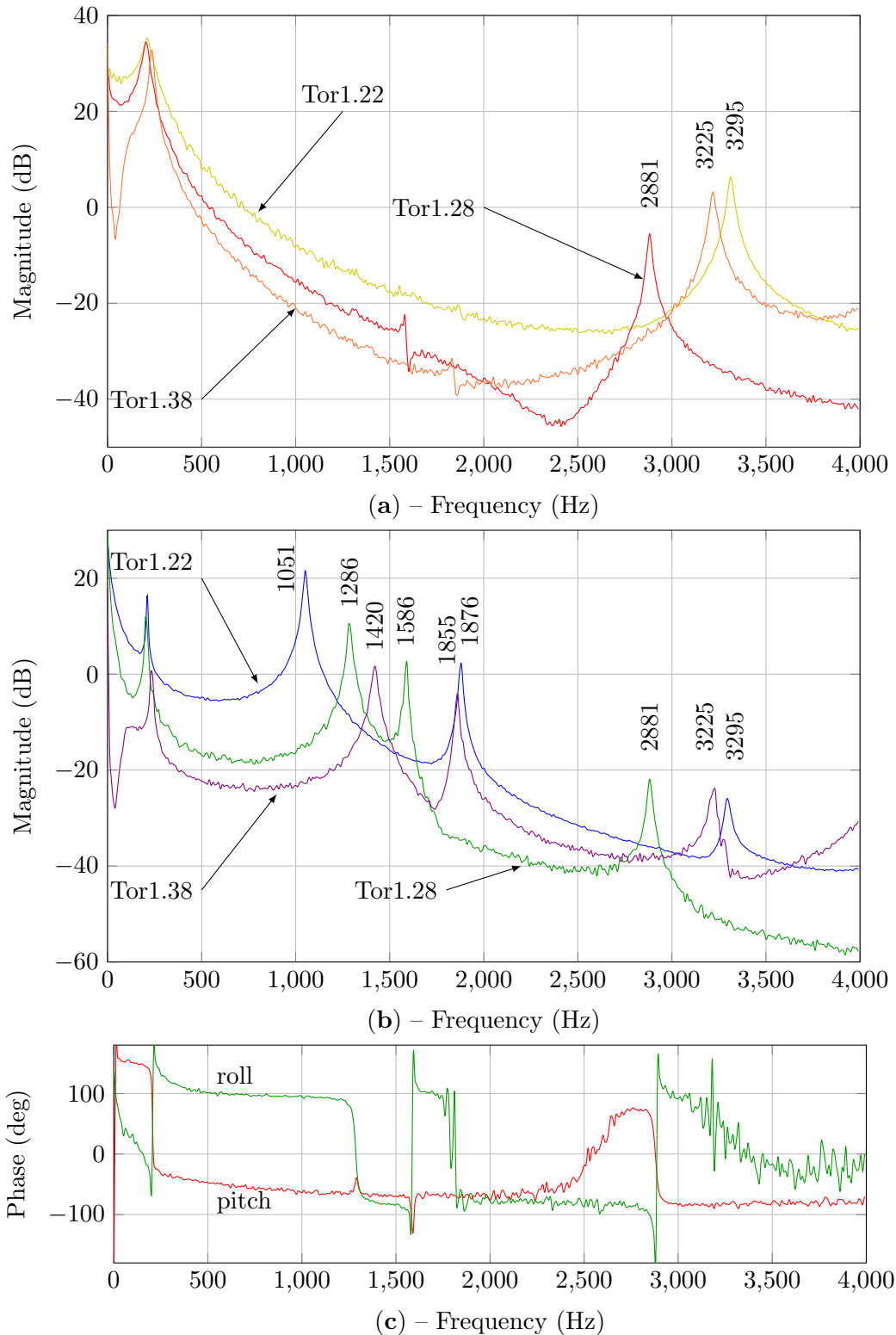


**Figure 6.9:** Bode diagrams of three different types of Tor1.x, when (a) the pitch actuator is driven, (b) the roll actuators are driven and (c) the phase of the Tor1.28 for the pitch and roll axes.

harmonics were also observed when a sine signal is applied on the roll axis.

We can conclude from the frequency response curves that the cross-coupling is only unilateral: from the inner actuators to the outer bimorph array actuator at the frequency corresponding to the torsional mode of the mirror plate. Hence, the motions about the two axes of the micro-scanner

**Table 6.1:** Summary of the measured resonance frequencies in Hz of the main modes constituting the frequency response of the three types of Tor1.x and of the model resonance of the pure tilt mode in red.

Mode	Tor1.22	Tor1.28	Tor1.38
Pure pitch #1	211	205	235
Pure tilt #2	1051 (1056)	1286 (1204)	1420 (1417)
Cross coupling #3	1876	1586	1855
Last peak #4	3295	2881	3225

can be overcome by applying a sine signal of the frequency of the second mode on the roll actuator and a sine signal of the frequency of the first mode on the pitch actuator. One should still be careful doing so, in order to avoid damaging the pitch actuator: indeed, the temperature induced on the pitch actuator array is a function of the sum of the maximum voltage applied on both actuators and can thus quickly culminate into an overheat.

A shift of the resonance peaks was observed for different bias voltages as described in Chapter 4. An experiment of measurement of this shift is shown in Fig. 6.10 with the Tor1.22 for a white noise in input with an amplitude of  $0.2 V_{pp}$ . A zoom in of the second and third modes is also given in Fig. 6.10b and Fig. 6.10c to highlight the shift in frequency. For the second mode (pure tilt), the resonance frequency drops when the offset voltage increases, whereas it is the contrary for the cross-coupling mode. This figure reveals the non-linearity of the system with respect to the frequency of the signal applied.

The shift of the second mode (the pure tilt of the mirror plate) can be understood noticing that first, when the bias voltage  $V_{bias}$  increases, the average angle  $\langle \theta_r \rangle$  (represented in Fig. 4.20) decreases as shown in Fig. 6.3. Second, as the equivalent stiffness of the roll actuators also diminishes when the bias angle decreases (when the angle remains positive however) as shown by the simulations in Fig. 4.22, finally, it is consistent that the eigen frequency decreases when the input bias voltage increases.

In the Tor1.x designs, one of the reasons for the implementation of torsion bars is the removal of the piston dof that used to be problematic in the first generations of electrothermal MEMS scanners (see Chapter 3). We demonstrate that the “piston” dof of the mirror plate inside the inner frame is completely ineffectual by the fact that the torsion beam prevents the bending mode of the torsion rods from happening. In Fig. 6.11, we compared the frequency responses of 2 Tor1.22 for the same input applied on the roll axis. In the first Tor1.22, the torsion bars have been purposely ripped out, using a needle and a fine positioning system to reach the area of the torsion bars precisely without damaging the rest of the structure. The second micromirror is “normal”, *i.e.* not damaged.

A description of the modes labeled [a] to [g] in Fig. 6.11 is given in Table 6.2. In addition to the existing modes present in the “normal” Tor1.22, the Tor1.22 without torsion rods also exhibits mirror plate rocking coupled modes. The modes of pure pitch of the inner frame, pure roll of the mirror plate as well as the 2 other coupled modes are still present in the rod-less device. While the frame pitch mode frequency remains almost unchanged, the roll mode is shifted towards a lower frequency. This can be explained by the fact the contribution of the stiffness due to the torsion rod is withdrawn yielding a smaller stiffness and thus a lower frequency. The 2 coupled modes have their frequency increased and are highly attenuated. The pure roll mode of the mirror splits into its shifted rod-less counterpart and into an attenuated peak composed of a weak torsion of the inner frame and a large tilt of the mirror plate. The [b] and the [f] undesired modes completely

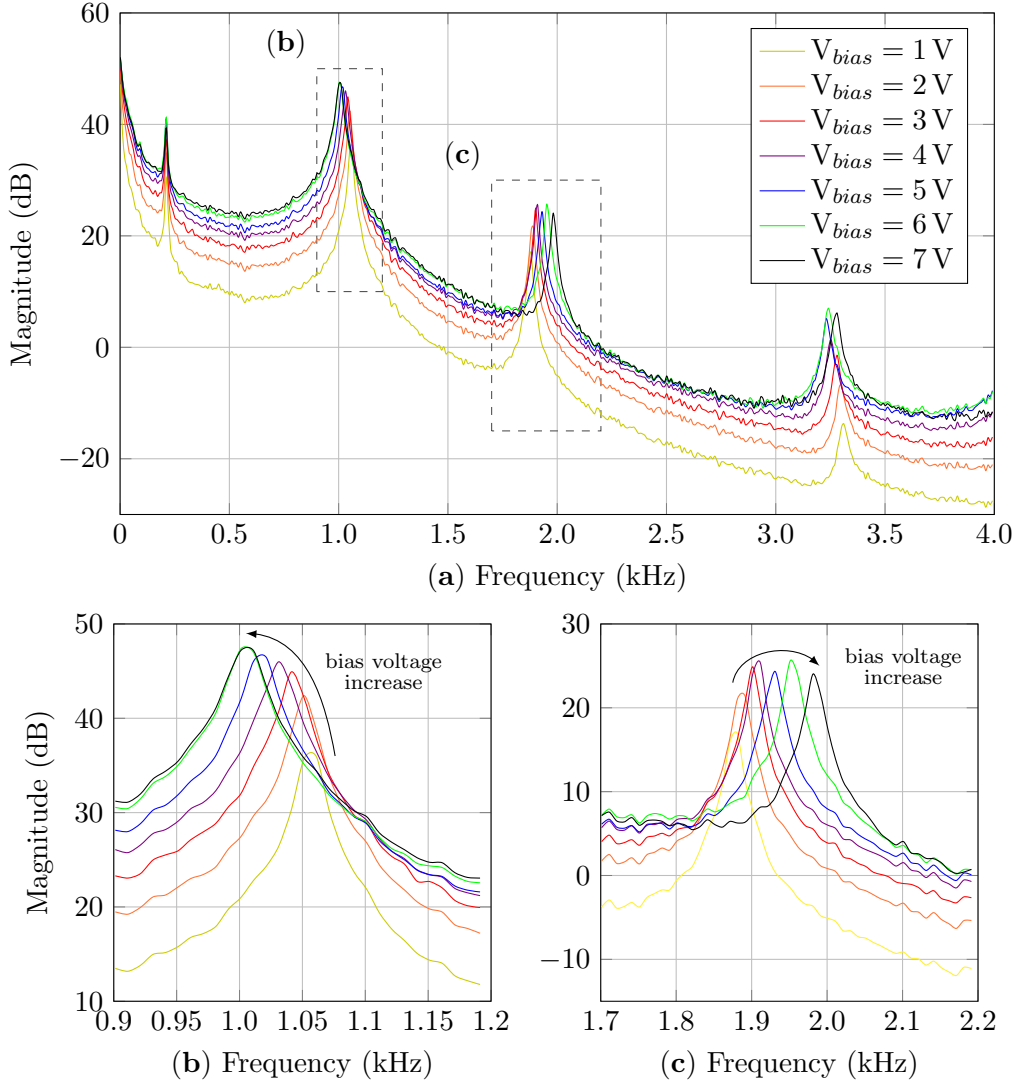


**Figure 6.10:** Frequency response of the Tor1.22 for a voltage input on the roll actuator of amplitude  $0.2V_{pp}$  and varying offsets. (a): Frequency response over a bandwidth of 4 kHz and zoomed-in insets of the pure tilt mode response and third coupled mode given in (b) and (c), respectively.

disappear in the unbroken rod situation. The indisputable differences between the two situations supports the argument of steadiness of the mirror plate within the inner frame and the elimination of the possible piston and rocking modes due to the torsion bars.

**Table 6.2:** Summary and description of the different vibrating modes of the Tor1.22 without torsion rods.

Label	Freq.	Motion	
		Inner frame	Mirror plate
[a]	191	pure pitch	idle
[b]	513	pitch	large tilt
[c]	886	idle	pure tilt
[d]	990	weak torsion	large tilt
[e]	2,054	torsion	medium rocking/piston <sup>2</sup>
[f]	2,147	idle	large rocking/piston
[g]	3,474	pitch	large tilt, medium rocking/piston

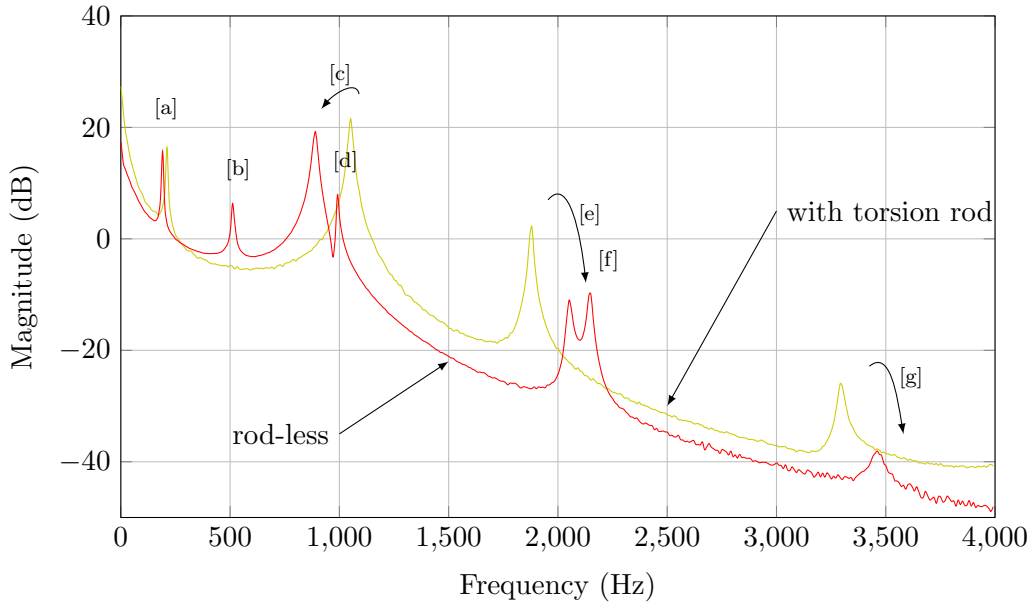


Figure 6.11: Frequency response comparison of Tor1.22 with and without torsion bars.

### 6.1.5 Lissajous scan for imaging

In this section, the Tor1.28 micro-scanner was tested dynamically to evaluate its capability to perform imaging by sweeping Lissajous scan patterns. Because of the cross coupling occurring between the roll and the pitch actuators of the Tor1.x devices, a Lissajous pattern was preferred to perform the 2D scan (composed of the B-scan and the C-scan) of the OCT image. First, the Lissajous is most “simple” type of pattern to implement with a scanner, and second, the axis cross coupling is significantly attenuated around the resonance frequencies (concerning the pure pitch and pure roll modes) of the micromirror. Although a raster scan is more adapted for data collection and post-treatment, it exhibits a non negligible coupling between the slow and fast axes and was thus proscribed in this study. Other types of scans based on more complex input have not been studied yet, however, they may ensue from a control study of the micro-device in a future work.

In a first time, the Lissajous scan is characterized to evaluate whether the performances achieved in terms of speed (real-time imaging capability), area dimension and cover rate, and resolution match the specifications established in Chapter 2. In a second time, a study on repeatability and tracking is carried out, in order to determine the degree of control required by the micro-scanner to provide images reliable enough to be used in OCT imaging.

#### 6.1.5.1 Lissajous scan dynamic study

The micro-scanner was actuated at its resonance frequencies on both axes. The trajectory of the Lissajous scan performed was acquired by the ultrahigh-speed camera at 30 kfps. An example of area scanned with the Tor1.28 for a duration of 200 ms is shown in Fig. 6.12<sup>3</sup>.

From this figure, a slight distortion can be identified on the Y axis and is due to the coupling between the two axes. However, the shape of the Lissajous remains relatively rectangular and

<sup>2</sup>The mention “rocking piston” was referred to as such because at this day, due to the lack of information of the precise motion of the whole mirror plate, the mode shape remains partially undefined.

<sup>3</sup>Notice that the scanned area has been scaled down considering the experimental angular range of  $\pm 5^\circ$  (along the X axis) towards an area ( $870 \mu\text{m}^2 \times 310 \mu\text{m}^2$ ) corresponding to the scanned zone if the micromirror was integrated in the endoscopic probe (same angle applied to a working distance of 5 mm).

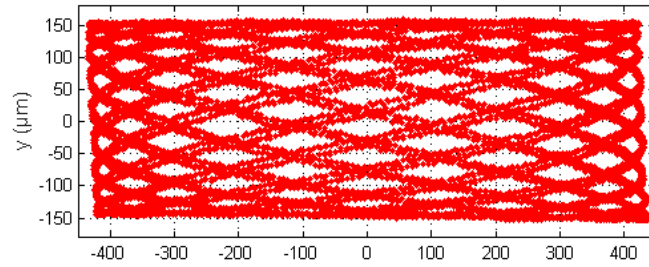


**Figure 6.12:** Lissajous scan pattern for a duration of 200 ms.

a scanning area can be extracted from it with a proper cover rate within a decent time. The micro-scanner was driven at frequencies close to respective resonance frequencies of 205 Hz and 1.445 kHz for the slow and fast scan and the pitch and roll axes. For each frame, the coordinate of the centroid of the laser spot was retrieved and the superposition of all the cartesian points is shown in Fig. 6.13a, Fig. 6.13b and Fig. 6.13c after acquisition times of respectively 4 ms, 16 ms and 45 ms.

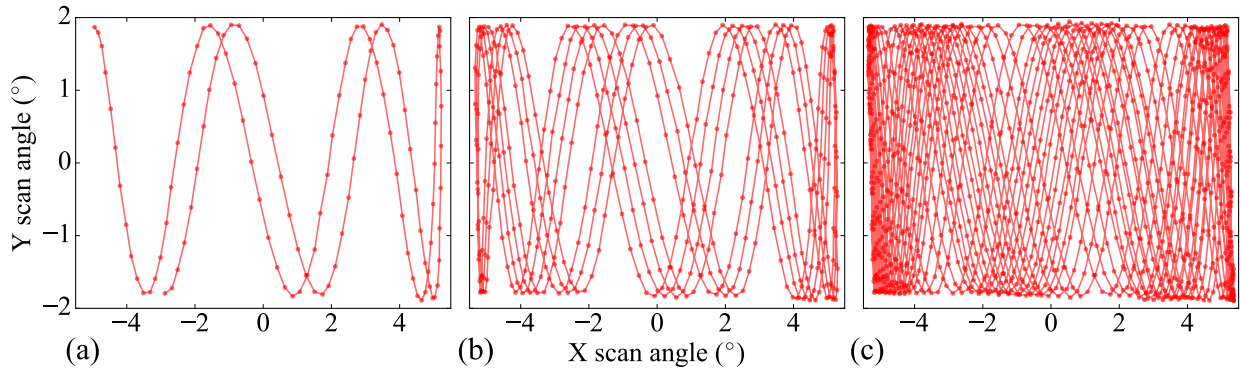


**Figure 6.13:** Lissajous patterns obtained by sine excitations of frequencies 205 Hz and 1.445 kHz for the slow scan on the pitch axis and the fast scan on the roll axis, respectively, in elapsed times of (a) 4 ms, (b) 16 ms and (c) 45 ms.

Furthermore, 100 kHz repetition rate is roughly the performance achieved by most commercial **SS-OCT** systems today [80] and most of **OCT** implementations based on point-scanning imaging beams are actually limited by the laser sweep rate. Hence, drawn trajectories are retrieved and filled with pixels (3 times more than initially collected) which would correspond to such an A-scan rate of 90 kHz. Subsequently, by considering that the system resolution is about 10  $\mu\text{m}$  [83], each pixel has a footprint of 20  $\mu\text{m}$ . The duration required to fill up the field of view can then be derived. In the following, the Lissajous scan is slightly cropped to keep a **ROI** of 270  $\mu\text{m} \times 770 \mu\text{m}$ . Figure 6.14 reports the proportion of the field of view consequently illuminated as a function of time.

At the specified frequencies, for a duration of 45 ms of scan, corresponding to an imaging frequency of 22 Hz, 99% of an area of 270  $\mu\text{m} \times 770 \mu\text{m}$  was covered. It can be underlined that 22 Hz can be considered as quasi real-time imaging frequency. In Lissajous scan, the “corners” of the scan pattern are superimposed in the trajectory. Because of the edge passing “high density”, a large amount of pixels are averaged: for instance, 95% of the area can be covered for an imaging frequency of 5 Hz with a 9 time averaging and 99% at 10 Hz with a 3 time averaging.

As an illustration, the following figure reports the number of times one area is illuminated

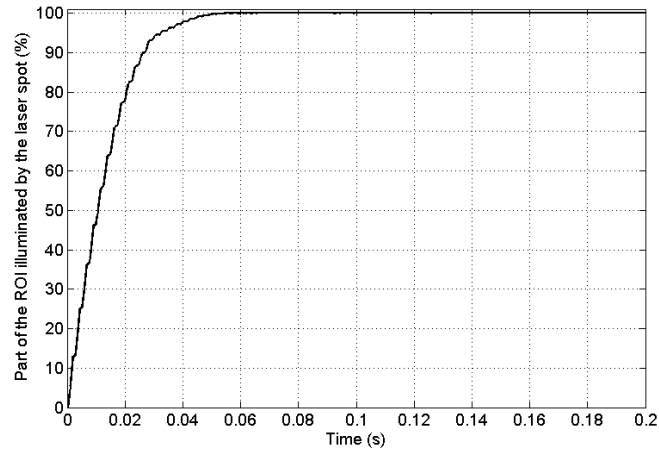


**Figure 6.14:** Cover rate of the Lissajous scan pattern versus acquisition time.

during 100 ms (*i.e.* for 10 Hz of imaging frequency for which 99% of the ROI is illuminated at least 3 times). It can be seen that the averaging in many parts can be over 10 times.

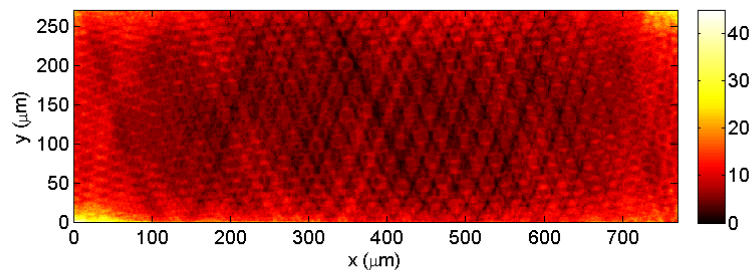


**Figure 6.15:** Cover density of the laser spot in times of passing.

We believe that this estimation is an argument in favor of paces compatible with real time imaging. Especially, because an improvement of imaging frequency, FOV or resolution can furthermore be obtained by a higher A-scan rate than the considered 90 kHz, allowing using larger angles, or an objective of higher NA. It can be underlined that much higher A-scan rates have been reported, *e.g.* speeds of up to 1 MHz by electrically pumped vertical cavity surface-emitting lasers (VCSELs) at around 1310 nm center wavelength [362].

Without considering the post-processing hardware acquisition time limitations, the micro-scanner can achieve real-time 3D scans with the swept source employed in the setup of this work.

#### 6.1.5.2 Tracking and repeatability study

The quality of the OCT image directly depends on the quality of the 2D scan (excluding the A-scan which only depends on the swept source), *i.e.* the ability to determine accurately “enough” the location of the laser spot in time and space. The purpose of this section is to evaluate this accuracy. For a reason of lack of time, the Tor1.x micro-scanner was studied only in open-loop. The criterion of determination of the “quality” of the scan is the error between the real output and the predicted output. The predicted output is obtained after a linear “rectification” of the real inputs of the system identified and optimized by an estimate ARX221<sup>4</sup> model to fit the best the system. The

<sup>4</sup>ARX refers to AutoRegressive with eXogenous terms, and the three figures of the suffix 221 refer to the polynomial order of the denominator of the transfer function, the polynomial order of the numerator of the transfer function

correction system, prefigured in Fig. 6.16 is a MIMO system between, on the one hand, the driving signals of the slow and fast scans, and on the other hand, the weighted centroid of the angular position of the laser spot projected on the vertical and the horizontal axes of the screen. Indeed, no matter how different is the output from the input, if this difference is sufficiently repeatable, then it can be compensated in a “rectification model” including the electrothermomechanical system of the micro-scanner, the geometrical distortions and rotations, the cross coupling and other linear or nonlinear non-random phenomena that may affect the output, for the given set of input signal frequencies. It does not include the disturbances due to air flux, noise, or other disturbances which would require a close-loop control to be compensated and is only available for the considered frequencies.

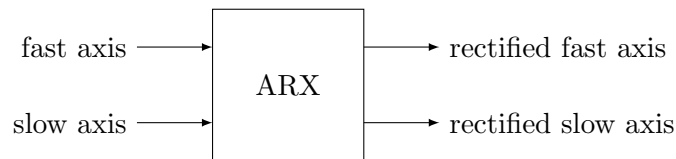


**Figure 6.16:** Schematic of the compensation model of the micro-scanner system for a given set of input signal frequencies.

Detailing the transfer function of the corrector ARX system will not bring much more information, nor will plotting the transfer function frequency response make enough sense, as long as it is valid only for the given scan frequency and is completely irrelevant for the rest of the frequency range.

The angular positions of the rectified inputs, and the measured laser spots angular positions in 2D, sampled at the same frequency, are plotted in Fig. 6.17. An “edge effect” is clearly apparent on this figure, due to the nature of the Lissajous scan, where the speed of scan slows down at the peaks of the sine signals of both axes, thereby increasing the spots “passing” density. Although the cover density is much lower in the central area of the scan, this will not affect the outcome of the imaging, if the largest “uncovered” surface included within the scan area remains smaller than the spatial resolution. The distribution of the absolute error function between the predicted and the measured angular position of the laser spots is given in Fig. 6.18a along each axis separately. As we could expect, these distributions are gaussian. The mean absolute error of the slow axis is  $-0.001^\circ$  and its standard deviation equals  $0.027^\circ$  while the mean absolute error and standard deviation of the fast axis are calculated at  $0.011^\circ$  and  $0.051^\circ$ , respectively.

The absolute 2D error is the norm between the predicted position and the measured position of the laser spot in the plane of scan. In that plane, the scanned area is  $870 \mu\text{m}^2 \times 310 \mu\text{m}^2$  as mentioned earlier in Section 6.1.5.1. The 2D error is a  $\chi^2$  distribution of standard deviation  $5.0 \mu\text{m}$  and mean  $6.5 \mu\text{m}$  (though it does not make much sense of calculating the mean of a  $\chi^2$  distribution).

From Figs. 6.18a and 6.18b, we can conclude that: first, the differences between the scan pattern input and the measured pattern are repeatable enough so that they can be compensated by a linear correction in open loop; and second, the differences between the rectified input and the measured output (*i.e.* the uncompensated phenomena) are small enough to obtain a sufficient quality for OCT imaging without implementing feedback control in close loop in the first place. Inside the body, other considerations will have to be taken in account for the integrated endoscopic

---

and the input-output delay, respectively.

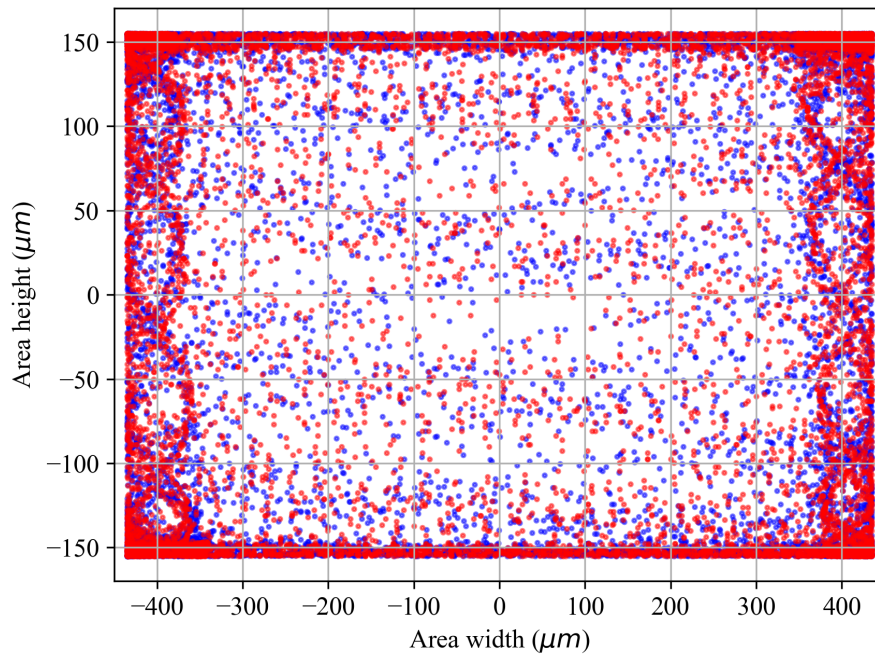


**Figure 6.17:** 2D rectified laser spot angular position (in blue, in background) and measured positions (in red, in foreground).

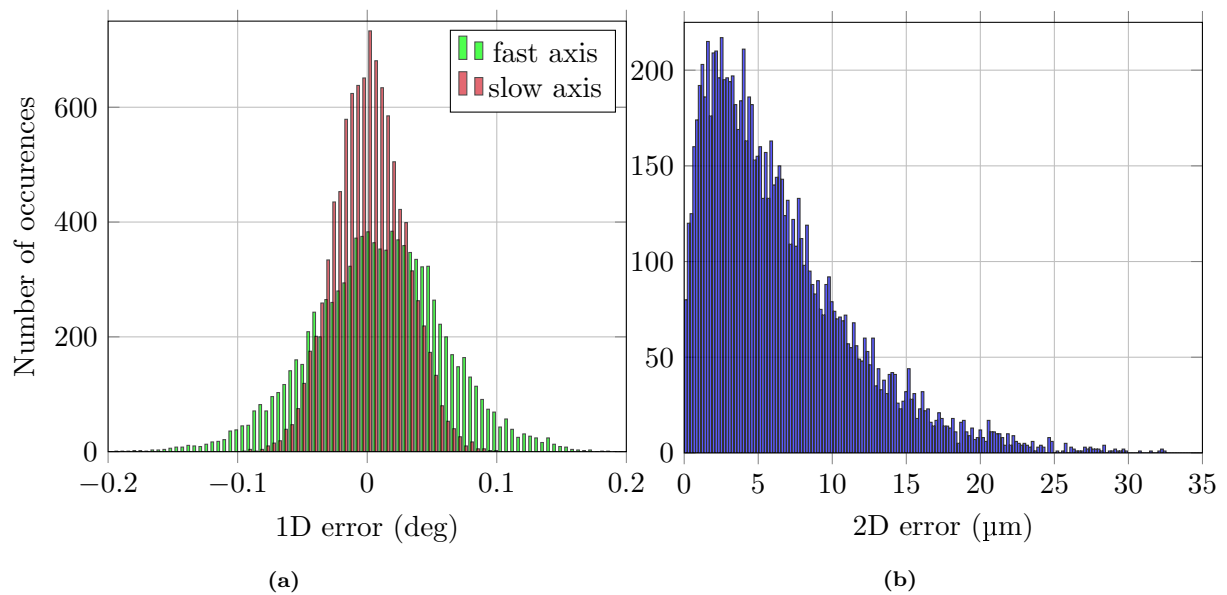


**Figure 6.18:** Histograms of distribution of the absolute angular error (a) in 1D (with respect to each axis), and (b) in 2D.

system such as the general body organ motion, heart beat, breathing movements, etc. We believe most of them can also be pre-compensated in open loop, however, for uncompensable phenomena, a close-loop control may be the last resort.

The idea of developing integrated strain gauge was to provide the possibility of a feedback control even in the very confined space of the encapsulated endoscopic probe where it would be cumbersome to include another type of sensing mechanism. Compared to microscale sensing systems that have been implemented for dynamic position tracking of electrothermal MEMS scanners



[363, 364], the strain gauge sensing mechanism proposed in this work offers the undisputable advantage of taking up no space at all, as long as it is fully integrated. Unfortunately, no opportunity of characterizing the strain gauges was possible for a reason of lack of time again. A thorough characterization will be realized in a future work.

## 6.2 Integration of the MOEMS probe head

This section will consist in describing the different steps of the process of consolidation of the MEMS micro-scanner with the Mirau micro-interferometer. A schematic view of the result expected is provided in Fig. 6.19 showing the released Quad2.0, the micro-interferometer (of same footprint), a flexible PCB for electrical pad connections, the GRIN and focusing lenses, and a portion of the focused laser beam (only to depict the deflection of the light) and a cylindrical/spherical transparent capsule.

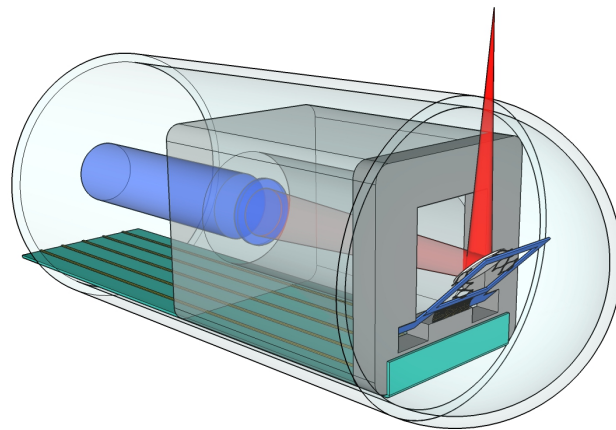


**Figure 6.19:** Schematic overview of the fully integrated MOEMS probe's head without the continuum robot arm.

All assembly steps were performed using a semi-automatic chip-bonder TPT HB70 tool. This machine allows to pick a component with a programmable motorized vacuum pick-up tool as shown in Fig. 6.20a. The substrate is maintained by a vacuum chuck and the base stage can be displaced in X and Y directions. The alignment of the interferometer-chip and the micro-scanner was made using a high-resolution camera with an adjustable viewing angle. A special electrically-heated vacuum chuck was installed on the XY stage (see Fig. 6.20b) for the assembly process detailed in the following.

The interferometer-chip and the micro-scanner were assembled using an adhesive thermally conductive silver Epoxy paste. The Epoxy glue was laminated manually on the BS side of the interferometer-chip resulting in a uniform layer of about 2 mil in thickness. The central hollow and transparent part of the interferometer chip was protected by a Teflon<sup>™</sup> cover during lamination to keep it off the glue.

The manual lamination process is described in Fig. 6.21. A glass slide is wrapped by 2 layers of Teflon<sup>™</sup> tape (of 1 mil each) as shown in Fig. 6.21. Then, a razor blade, is pulled back along the glass and tamps the glue all along the gap formed between the layers of tape. The beam splitter side of the interferometer chip is brought into contact with the Epoxy stripe and is transferred to

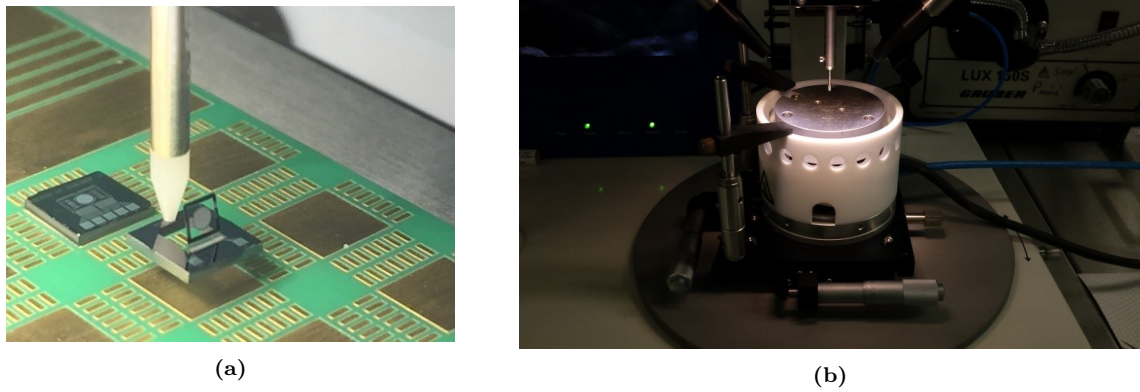


**Figure 6.20:** (a) Micro-mirror handled by a vacuum pick-up tool. (b) Heated vacuum chuck.

the exposed surface on the chip. After removing the central protection of the BSP, the Epoxy film is structured and the interferometer-chip is ready for assembly with the micro-scanner.

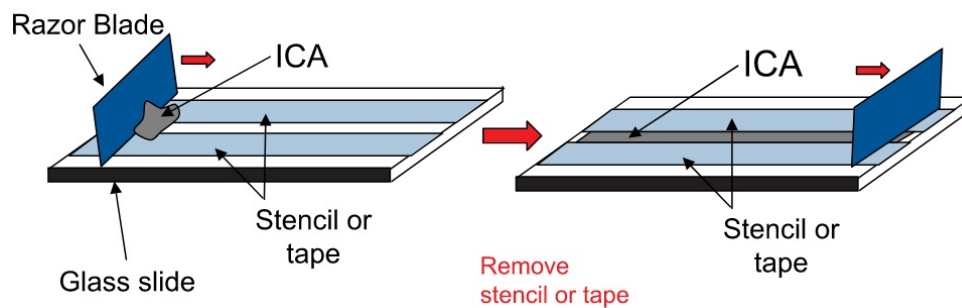


**Figure 6.21:** Fabrication of a thin and uniform layer of Epoxy glue.

In a first time, the two components are aligned manually so that the optical axis of each component is consistent with the other one.

The micro-scanner can not be handled by the pick-up tool in its very centre because of the fragile structure of the micromirror, thinned down in this location. During the assembly, the distribution of the force applied by the pick-up tool is not uniform. This may result in a slight tilt of the micro-scanner as well as an excessive local flow of Epoxy out of the joint. In order to improve this uniformity, the bonding force was applied by the pick-up tool in several points around the micromirror. Figure 6.22 shows the micro-scanner bonded onto the interferometer-chip.



**Figure 6.22:** Micro-scanner bonded to the interferometer-chip.

Before the assembly of the flexible PCB, small dots of Epoxy glue (200 - 250  $\mu\text{m}$  in diameter) were deposited on the contact pads of the micro-scanner as shown in Fig. 6.23a The interferometer-

scanner structure is maintained in a horizontal position and the flexible PCB is bent before the assembly. In this way, bending of the PCB after the connection is avoided to prevent breaking it off. Since the bending is carried out manually, a special attention should be paid to obtain an angle of  $90^\circ$  (see Fig. 6.23b).

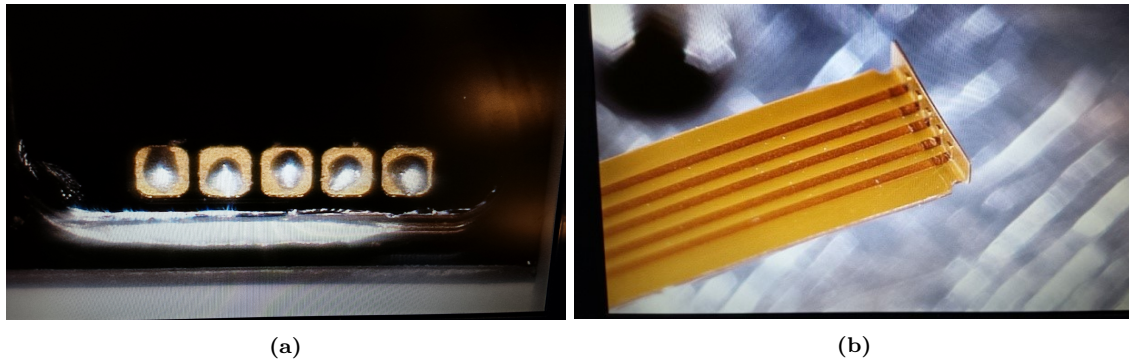


**Figure 6.23:** Preparation the step of bonding of the custom flexible PCB onto the micro-scanner's pads. (a): Epoxy glue drops are deposited on the pads. (b): The flexible PCB is folded at  $90^\circ$ .

Because of the horizontal position of the interferometer-scanner structure, the contact pads are located in the lateral side. Therefore, an external camera or microscope was installed in front of the structure in order to have a lateral view (Figure 6.24a). Once the contact pads of the PCB are aligned with the pads of the micro-scanner as in Fig. 6.24b, a small force is applied with the pick-up tool to ensure a good contact. Then, the chuck is heated to  $80^\circ\text{C}$ - $100^\circ\text{C}$  during 2 - 3 hours for the curing of the Epoxy glue.

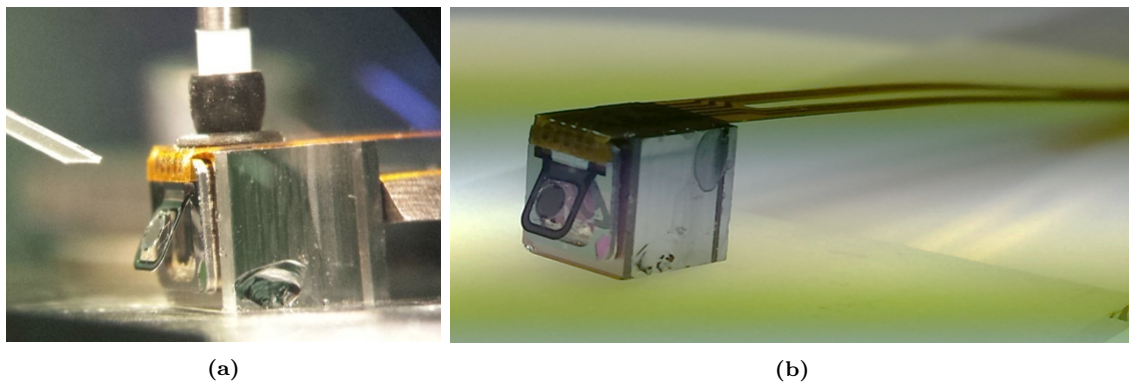


**Figure 6.24:** Views of the interferometer-scanner chip with the vacuum tool handling the flexible PCB. (a): *End face* view, with the capillary used to apply contact pressure.

The flexible PCB could be successfully bonded onto the released micro-scanner. Next steps will consist in encapsulating the integrated head and aligning and connecting the GRIN lens and the SMF to the Mirau micro-interferometer.

### 6.3 Conclusion

Among the 3 different designs of micro-scanners which were proposed in this work, we only had time to characterize the Tor1.x type of the first batch of fabrication. The Tor1.x allows large angular displacements for relatively low voltages, despite the underestimated prediction value of the electrical resistance. Furthermore, it was demonstrated that the model established in Chapter 4

could be trusted to predict the static behavior of the micro-scanner within a range of actuation close to the initial position. The experimental setup built for the dynamic characterization, was detailed and the dynamic behavior of the Tor1.x with 3 different width of torsion bar was investigated. As described roughly by the model, the increase of the pure tilt mode frequency with the width of the torsion rods is observed. The frequency shifts of the different modes of vibration of the Tor1.x are also observed for different angular offsets. Although, this shift seems nonlinear, the model describes a linear phenomenon in the corresponding bias voltage experimental range. In conclusion of the modeling of the vibrating modes of the micro-scanner investigated compared with the experimental characterization, the model should probably be improved, taking into account the nonlinearities due to the shape of the actuators and the positive feedback of the temperature change in the static and dynamic response as well as the aging of the system. The assertions of linearity and small displacements established may also be revised and evolve towards a nonlinear approach [365]. The use of the torsion rod in the design introduced appears to be an efficient way of reducing the number of degrees of freedom to the bare essential motions. The presence of the torsion bars significantly reduces the influence of the undesired modes in the system. The rocking/piston modes even completely disappear from the frequency response, which proves the motion selectivity of the rod in pure torsion. When the axes of the Tor1.x are driven at the frequency of the 2 main modes of pure tilt and pitch, the axes become sufficiently “decoupled” to be able to perform a Lissajous scan in open loop, whose discrepancies with the actual scanned pattern can be compensated to obtain a satisfactory quality of image achieving paces compatible with real-time imaging (or close to real-time imaging if averaging is performed). Although, the Tor1.x meets the specifications required to do OCT imaging for EGC detection, the general performances of this micro-scanner – such as the coupling which still remains slightly present and the possibility of tracking and controlling dynamically the angular position of the mirror plate – could be improved using the novel design of the Tor2.x and Quad2.0 which remained untested so far. Their characterization will be the object of a future work.

A trial of integration of the interferometer-scanner chip was realized. Unfortunately, further efforts will be needed to improve the process and allow a characterization of the integrated MOEMS probe head.

**Chapter summary**

In this chapter, the Tor1.x type of the electrothermal designs presented in this thesis work was characterized in its 3 variants. The experimental static measures and the static model appeared to be close enough to be trusted within a range around to the initial position of the mirror plate after release. Although the dynamic models could predict the overall behavior of the micro-scanner, a few discrepancies were observed and would need to be improved taking into account the mechanically and thermally-induced nonlinearities. An experimental Lissajous scan was performed to evaluate the capability of the device to perform imaging according to the specifications to build an OCT demonstrator. Finally, the result of the imaging scan were quantified and it was concluded that the Tor1.x micro-scanner could provide satisfactory results although it still remains to be tested after integration to the Mirau micro-interferometer and *in vivo*. The other designs of micro-scanners may be useful to continue improving the performances of the scan and will therefore be investigated in a future work as well as the integration and the photonic characterizations.

# General conclusion and prospects

**D**RIVEN by promising stakes, the development of endoscopic probes for *in vivo* imaging has tremendously progressed over the last fortnight, although no clinical demonstrator of early stage GI cancer detection has conquered the market yet. Instigators in this field have not achieved sufficient trade-offs to overcome the decisive threshold of performance, to engage in a procedure for clinical market acceptance. Indeed, improving probes performance and reliability in the desired operating environment as well as bringing down their cost below \$25 per piece remains relatively challenging and prevents from moving on.

This thesis work was part of the context of the DEMO4 project (2014-2017), financed by the LabEx Action funding source, and aided by the US National Science Foundation in parallel. It focused on the conception of an electrothermal micro scanning device for vertical integration to a Mirau micro-interferometer within a endo-microscopic OCT probe for early stage stomach and esophagus cancers detection.

This work benefited from the experience acquired by the researchers and Ph.D. students from the AS2M and Micro Nano Sciences & Systems (MN2S) departments of FEMTO-ST in robotics, optics and micro-fabrication, and from the BML group of the UF in the design and simulations of the electrothermal behavior of the micro-device, the integration of OCT probes know-how, as well as the micro-fabrication development at the NRF. The work done by Todd [231], Wu [335] and Duan [59] constituting the cornerstones of this work deserve to be brought forth.

The outcome of this thesis work is the conception of the central electrothermal MOEMS micro-scanner. It demonstrates large optical angular displacement ranges (up to  $64^\circ$ ) for low actuation voltages (less than  $17V_{DC}$ ) making it interesting for a much wider range of applications than just OCT imaging. The best architecture reaches resonance frequencies of 1420 Hz in rotational mode and allows a relatively exploitable decoupling to perform imaging. The micro-scanner was fabricated within a set footprint of  $4\text{ mm}^2 \times 4\text{ mm}^2$  and its design results from the application specifications.

In this context, imaging methods, probe architectures and actuation types were studied in order to build a list of specifications on which to base the design of the micromachine.

SS-OCT was adopted as the optical imaging modality because of its competitive characteristics. OCT provides a high axial resolution, and the lateral resolution can be tuned by adjusting the architecture of the interferometer so that isotropic resolutions can be achieved. It allows non-invasive, radiation-free and inexpensive 3D imaging, very appreciated to encourage patients to

mass preventive diagnoses. Breakthroughs in Optics have kept improving the performances of swept sources, able to provide paces compatible with real-time 3D imaging.

Defining the architecture of the endoscopic probe is crucial, as it will set most of the specifications of the system. A side-viewing layout was preferred for stomach imaging stability and esophagus luminal configuration. Distal actuation presents numerous advantages over proximal actuation. Not only, the working distance and the lateral resolution are significantly higher, but also the pullbacks, limiting the system speed and causing non-uniform rotations, can be avoided. Pullback-free distal actuations can benefit from 2D rotations using MEMS scanners, proscribing exorbitantly expensive micromotors for good. With this architecture, imaged volumes of  $770\ \mu\text{m}^3 \times 270\ \mu\text{m}^3 \times 202\ \mu\text{m}^3$  at least, are claimed to be acquired at 5 Hz with a 9 time averaging and a 95% cover rate at working distances of 1.05 m and axial and lateral resolutions of  $5.2\ \mu\text{m}$  and  $10.7\ \mu\text{m}$ , respectively. The MOEMS probe is incorporated at the distal nozzle of a continuum robot arm enabling accurate positioning inside the human body. It comprises a MEMS scanner of footprint  $4\ \text{m}^2 \times 4\ \text{m}^2$  vertically integrated onto a 5.3 m m-long Mirau micro-interferometer. Such a level of integration of a distal MEMS scanning device with a Mirau micro-interferometer is the first novelty claimed in this work. The cost of building a monolithic micro-interferometer is the inaccessibility of the different components and the non-modularity after manufacture. Probably for this reason, integrated interferometer-based probes are still uncommon. Yet, this configuration is much more insensitive to the influence of the environment stemmed from uncompensated path length differences, and eventually leads to enhanced image qualities.

The speeds of acquisition of volumetric OCT images are first limited by the sweep rate of the optical source and the related type of B-scan. To keep the benefits of real-time imaging without degrading the resolution, B-scans have to be as fast as possible without exceeding thresholds higher than 22 fps.

A 2D MEMS micro scanning device has been designed to take up the challenge. Although electrostatic and piezoelectric actuations are far from expectations, due to their small displacement range and high driving voltage, hazardous for human *in vivo* operations; electromagnetic and electrothermal actuations appeared to be in competition as the candidates for the micro-scanner's actuators. Finally, because of the poor modularity of electromagnetic actuators, very cumbersome, the presence of hysteresis and the complexity of assembly, bimorph-based electrothermal technology turned out being the best compromise.

Despite the slow time responses inherent to low thermal establishment time constants, actuators need not reach frequencies much higher than 1 kHz to scan 3D volumes with a sweep rate of about 100 kHz, implemented in our system.

The electrothermal MEMS micro-scanner was designed to be vertically integrated directly onto the beam splitter of the Mirau micro-interferometer. The mirror plate included into an inner frame, itself linked to the bulk substrate in a gimbal-like way, is coated by a reflective layer of aluminum and oriented in an initial position of about  $45^\circ$  from its substrate and the optical path axis of the interferometer to scan along a perpendicular axis towards the tissue. A combination of ISC-based actuators were conceived in purpose, to develop the necessary force and displacement to reach resonance frequencies in the vicinity of 1 kHz and a few hundred Hz. An original architecture using torsion bars was implemented to remove unnecessary dofs, bring local stability to the mirror plate in the vibrating tilt mode, and offer the possibility of implementing embedded novel torsional strain gauge sensors (remained untested so far though), for potential dynamic close-loop control.

To underline the influence of the torsion bar in the behavior of the micro-scanners, three different versions of width of torsion bars were designed, showing a significant difference in the frequency response and the location of the pure pitch and roll modes. Contrarily to the assertions of a linear “temperature-displacement” dynamic behavior – claimed in most models of the literature – , first, a model describing the nonlinear phenomenon was proposed – yet still needs to undergo further improvements to be accurate – and second, the nonlinearity of the electrothermal actuation was brought forth in experimental series of characterization. The role of the torsion bars – whose role is to stabilize the rotation of the mirror plate around the roll axis and prevent rocking and piston vibrations, undesired for the scan imaging – was successfully demonstrated.

A thermal cross-coupling was observed in the first version of the micro-scanners and justifies the need for the novel auto-positioning stopper mechanism brought up in the second version. The dof reduction due to the introduction of the mechanical stopper entailed the evolution towards a third version comprising four actuators.

Finally, we demonstrated that the Tor1.x version of the micro-scanners measured up the expectations in terms of imaging, and could be further used to perform OCT 3D imaging. Reliable open-loop compensations can be easily implemented and allow satisfactory corrections (less than  $0.012^\circ$  or error at worst) of the predicted positions of the laser spot on the sample area. As long as the Lissajous scan axis scanning frequency remains close enough to its respective resonance frequency, experimental results revealed that the cross-coupling was insignificant enough so that the linear open-loop corrections could generate an image sufficiently close to reality.

As it was underlined at multiple occasions in the content of this manuscript, different tasks would deserve further investigation.

The two last versions of the micro-scanners: the Tor2.x and Quad2.0 were left uncharacterized. Nevertheless, based on the work of other research, these structures might demonstrate very promising performances, as long as they were design to remedy the drawbacks pointed out in the Tor1.x version. The dynamic characterization of the strain gauges also adds grist to the mill, with the engendered challenge of providing the possibility of a cumbersome dynamic embedded sensing. A close-loop control could hence be carried out to compensate the disturbances linked to the *in vivo* environment, and eventually improve the OCT image quality drastically.

The use of mosaicing, to spread the area of observation and increase the chances of detection abnormalities, could be envisioned

More efforts will focus on the integration, to allow finalizing the MOEMS probe and start the combination with the continuum robot arm, and the characterization of the SS-OCT imaging.

Finally, all this work is far from being tossed in the garbage heap of history. Indeed, a new Ph.D. position (2018-2020) will follow on from the DEMO4 project, and takes over the photonic aspects of the imaging system, the work of integration, characterization and commercialization of the endoscopic OCT probe.

Furthermore, a new project, called “ROBOT” (Robotics and OCT for optical BiOpsy in the digestive Tract) (2018-2020), leveraged the DEMO4 project’s accomplishment, to develop a new concept of clinical demonstrator.

Beyond the field of OCT imaging, electrothermal MEMS scanners could be exploited for a multitude of other applications such as fluorescence microscopy. Another application could be



laser excision for surgery, using the surface of the micromirror to deflect the light emitted from a powerful laser to ablate or cauterize specific areas. The main challenge of this application would be to minimize the heat energy absorbed by the mirror plate, developing a high reflectivity coating. Further researches are still ongoing at the UF on the development of electrothermal MEMS micro-scanners in two-photon microscopy and lidars.

# Appendices



# Appendix A

## Fabrication risks & recommendations

**E**ACH fabrication step developed in Chapter 5 may presents risks or be completed with recommendations. These additional information are listed hereafter for each respective step.

### **Preliminary clean-up stage**

- The order of insertion of the two species constituting the Piranha must be respected.
- This operation must be performed under an extrator hood. Furthermore, in addition to the typical outfit normally required in cleanroom, the user must wear a specific gown, over-gloves and a safety helmet.
- **BHF** attacks glass! The **BHF** must be poured in a plastic beaker. Glass beakers are absolutely forbidden.
- Used solutions must be disposed of in provided containers.

### **First layer of silicon dioxide - OXD1**

- **BOE** must be poured in a plastic beaker.
- As for the first step, a specific protection outfit must be worn to handle the **BOE**.
- It is highly recommended to make preliminary tests to measure the etch rate of the **BOE** 6:1 on a test wafer before processing the **SOI** wafer.

### **Platinum heater - PT**

- A descum should be performed before deposition of the Pt by sputter to avoid stingers or arcing during lift-off. Parameters used for the descum are 300 W, 60 s and 300 sccm.
- A thin **PR** such as AZ nLOF 2035 can be used regarding the low thickness of Pt to be deposited. A thinner **PR** will provide better patterns and resolution.

### **Second insulation layer opening - VIA**

- This step is particularly subject to wafer breakage inside the tools. Most tools require an edge exclusion of **PR** over several m.m. It is highly recommended to design an edge exclusion ring in the ⟨VIA⟩ mask. Otherwise a manual edge exclusion must be performed and may dissolve patterned **PR** close to the edge.

- Before stripping the PR, it is also highly recommended to check the electrical connection using a probe station for instance to make sure the RIE has etched all the way through.

#### **Top side layer of aluminum - ALU1**

- As mentioned, Al/Cu is recommended instead of pure Al.
- Ultrasounds are not recommended as long as they could damage the Al in several areas because of the power overage of ultrasounds.
- A first trial on a test wafer is a good way to estimate the final thickness obtained with the given SOP. Indeed, if the Al is too thin or too thick in the end, it is not possible to rectify the thickness by adding nor etching matter anymore.

#### **Second layer of silicon dioxide - OXD2**

- A thick PR must be used to preserve the SiO<sub>2</sub>-covered areas during the whole etch time. The PR must be rebaked to avoid black silicon as much as possible.
- Preliminary tests can be made on a test wafer in order to determine the proper thickness of SiO<sub>2</sub> to be deposited.
- An edge exclusion ring of 5 mm is recommended to avoid breaking the wafer inside the RIE tool.
- Before PR stripping, the electrical connection is a criterion to check to ensure the SiO<sub>2</sub> has finished to etch.

#### **Back side pit carving - BSD**

- The bonding between the SOI wafer and the carrier must be dry enough to prevent degasing and breaking the wafer during the DRIE jeopardizing the stake of the step, and wet enough to avoid burning the PR and hindering it from being stripped in the solvents (Aceton does not dissolve burnt PR).

#### **Release - REL**

- Once released, the micro-scanners are very fragile, they must be handled with care and stored in gel packs for transportation.

#### **Karma strain gauge - KAR**

- The use of ultrasounds is prohibited for this step as the features are too small to hold such a high power.
- Oxidizing processes are prohibited until the deposition of the second layer of SiO<sub>2</sub>. During that time, ashers cannot be used.

#### **Strain gauge insulation opening - VIA**

- As the *Karma* structures, including the pads, are too small to be xxx by a probe station needle, there is no way to ckeck the electrical connection to verify the SiO<sub>2</sub> layer has etched altogether.

**Gold pads - AUP**

- This step must be performed after all steps that require high temperature operations to prevent diffusion.

**Second mirror aluminum layer - ALU2**

- As the shape of dry PR film may be subject to deformation due to the hollow opening after development, a hard mask may be considered to carry out this step instead.
- The aluminum deposited needs not be as thick as the front-side reflective layer, yet it must be thick enough to possess a sufficient reflectivity, uniformity and smoothness.
- It is important to keep low temperatures during the whole step, especially when using dry PR (solvent-free) to avoid burning the film. This would cause the PR to be undissolvable in solvents.



# Appendix B

## Photolithography

### B.1 Basic principle

The term of photolithography comes from the greek and is formed of three particles:  $\phi\omega\tau\omicron\varsigma$  (photo): “light”,  $\lambda\iota\theta\omicron\varsigma$  (litho): “stone” and  $\gamma\rho\alpha\phi\epsilon\iota\omega$  (graphy): “writing”. Photolithography is also called optical lithography because the term of “lithography” is more widely understood. Photolithography is a microfabrication process used to pattern selectively a material to be deposited or already present on the bulk of a substrate using a PR polymer resin. A photomask is used to selectively hide and expose parts of a thin film of PR coated onto a substrate. Then a light source (generally ultraviolet light) illuminates the PR with the photomask precisely aligned on top of it (The alignment and the exposure are performed in the same machine) and modifies the chemical structure of the exposed PR as shown in Fig. B.1a. Then a chemical solution called “developer” is

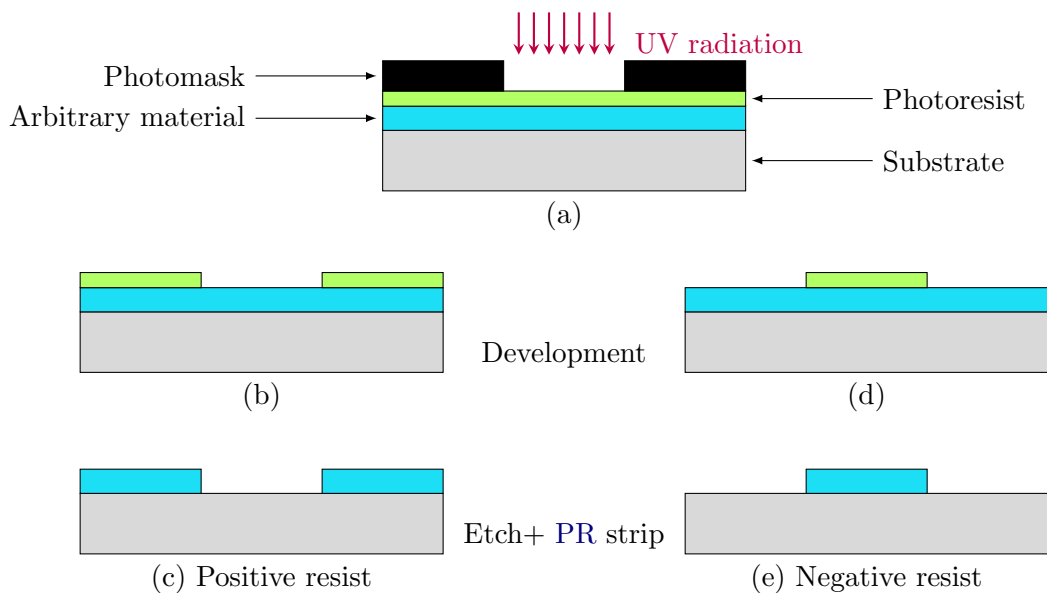


**Figure B.1:** Schematic diagram of a photolithography with positive and negative PR.

used to remove the parts of the PR pattern that can be dissolved in the developer. PRs that become soluble when exposed are known as “positive” whereas those that do not, are known as “negative” as illustrated by Fig. B.1b and Fig. B.1d respectively. Figure B.1c and Figure B.1e show respectively the etching process of a material by the use of a positive and a negative photolithography and after stripping the PR.



Another process using a photolithography, suitable for material deposition is called lift-off and is presented briefly in Appendix B.2.

## B.2 Lift-off principle

The lift-off process consists in depositing a material (usually by sputter or evaporation) using a patterned film of negative PR and lifting it off to keep the material deposited on the developed areas only. Negative PR is always preferred when performing a lift-off because of the shape of the walls on the edge of the patterns and the possibility to have an undercut to facilitate the resin to lift-off even after thick depositions. Figure B.2 summarizes the lift-off process and highlights the advantages of using a positive resin.

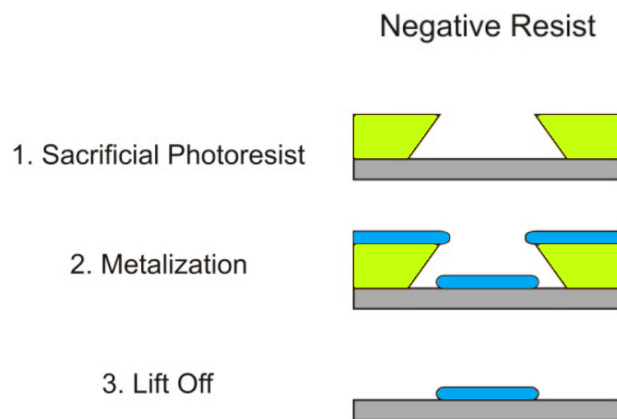


**Figure B.2:** Schematic diagram of a lift-off process comparing the use of a positive and a negative PR.

In the first case, the positive PR has a slight slope profile on the edges of the pattern. This is called an overcut. During lift-off, the solvent has difficulties to attain the PR altogether covered by the metal deposited and perfectly uninterrupted. Furthermore, even if the PR finally lifts off, some PR may stick to the metal and the substrate et create stingers on the edges. The common phenomenon of arcing may also occur during ultrasonic or any other powerful treatment and cause the structures to be damaged.

On the contrary, in the second case of negative PR, the profile of the resin is “inverted” from the first case. The undercut prevents the metal from sticking on the edges and allows the solvent to penetrate to the PR enabling a clean and efficient lift-off.

# Bibliography

- [1] Institut National du Cancer. Les cancers en France en 2015 - L'essentiel des faits et chiffres. 2015, 2015.
- [2] American Cancer Society. Cancer Facts and Figures 2017. Technical report, 2017. URL [↗](#).
- [3] Z. Uhry, N. Leone, N. Voirin, L. Roche, F. Binder-Foucard, A-S. Woronoff, P. Delafosse, L. Remontet, N. Bossard. Projection de l'incidence et de la mortalité par cancer en France métropolitaine en 2015. *Rapport technique*, 129:1–2, 2015.
- [4] Kimberly D. Miller, Rebecca L. Siegel, Chun Chieh Lin, Angela B. Mariotto, Joan L. Kramer, Julia H. Rowland, Kevin D. Stein, Rick Alteri, and Ahmedin Jemal. Cancer treatment and survivorship statistics, 2016. *CA: a cancer journal for clinicians*, 66(4):271–89, jul 2016. ISSN 1542-4863. doi: 10.3322/caac.21349. URL [↗](#).
- [5] Graeme W. Morgan, Robyn Ward, and Michael Barton. The contribution of cytotoxic chemotherapy to 5-year survival in adult malignancies. *Clinical Oncology*, 16(8):549–560, 2004. ISSN 09366555. doi: 10.1016/j.clon.2004.06.007.
- [6] Paul Sexton, Peter McAnena, John O'Dea, Eoin Bambury, Edel McGarry, and Oliver McAnena. What Is the Diameter of the Gastroesophageal Junction Produced During Nissen Fundoplication Surgery. *AGA Abstracts Gastroenterology*, 144(5):S–853, may 2013. ISSN 00165085. doi: 10.1016/S0016-5085(13)63171-6. URL [↗](#).
- [7] Xin-En Huang, Kazuo Tajima, Nobuyuki Hamajima, Yasuhiro Kodera, Yoshitaka Yamamura, Jin Xiang, Suketami Tominaga, and Shinkan Tokudome. Effects of Dietary, Drinking, and Smoking Habits on the Prognosis of Gastric Cancer. *Nutrition and Cancer*, 38(1):30–36, sep 2000. ISSN 0163-5581. doi: 10.1207/S15327914NC381\_5. URL [↗](#).
- [8] E Brambilla, W D Travis, T V Colby, B Corrin, and Y Shimosato. The new World Health Organization classification of lung tumours. *The European respiratory journal*, 18(6):1059–1068, 2001. ISSN 0903-1936. doi: 10.1183/09031936.01.00275301. URL [↗](#).
- [9] Bryan J. Dicken, David L. Bigam, Carol Cass, John R Mackey, Anil A Joy, and Stewart M Hamilton. Gastric Adenocarcinoma Review and Considerations for Future Directions. *Ann Surg*, 241(1):27–39, 2005. ISSN 0003-4932. doi: 10.1097/01.sla.0000149300.28588.23. URL [↗](#).
- [10] Masaki Kitajima. Gastric Cancer: Introduction. *Gastric Cancer*, 12(SUPPL. 1):1–2, 2009. ISSN 14363291. doi: 10.1007/s10120-008-0491-6. URL [↗](#).

- [11] Joong-min Park, W Ryu, Jong-han Kim, Sung-soo Park, Chong-suk Kim, and Young-jae Mok. Prognostic Factors for Advanced Gastric Cancer: Stage-stratified Analysis of Patients who Underwent Curative Resection. *Cancer Res Treat*, 38(January 1993):13–18, 2006. URL [↗](#).
- [12] Understanding stomach cancer - The basics. URL [↗](#).
- [13] M J Bowles and I S Benjamin. ABC of the upper gastrointestinal tract: Cancer of the stomach and pancreas. *BMJ (Clinical research ed.)*, 323(7326):1413–6, dec 2001. ISSN 0959-8138. URL [↗](#).
- [14] Anne Kathrin Diesing, Constanze Nossol, Heidi Faber-Zuschratter, Werner Zuschratter, Lydia Renner, Olga Sokolova, Michael Naumann, and Hermann Josef Rothkötter. Rapid interaction of helicobacter pylori with microvilli of the polar human gastric epithelial cell line NCI-N87. *Anatomical Record*, 296(12):1800–1805, 2013. ISSN 19328486. doi: 10.1002/ar.22818.
- [15] Won Jin Im, Min Gyu Kim, Tae Kyung Ha, and Sung Joon Kwon. Tumor Size as a Prognostic Factor in Gastric Cancer Patient. *Journal of gastric cancer*, 12(3):164–172, sep 2012. ISSN 2093-5641. doi: 10.5230/jgc.2012.12.3.164. URL [↗](#).
- [16] Hong-Mei Wang, Chang-Ming Huang, Chao-Hui Zheng, Ping Li, Jian-Wei Xie, Jia-Bin Wang, Jian-Xian Lin, and Jun Lu. Tumor size as a prognostic factor in patients with advanced gastric cancer in the lower third of the stomach. *World journal of gastroenterology*, 18(38):5470–5, oct 2012. ISSN 2219-2840. doi: 10.3748/wjg.v18.i38.5470. URL [↗](#).
- [17] María Blanca Piazuolo and Pelayo Correa. Gastric cancer: Overview. *Colombia Médica*, 44(3):192–201, 2013. ISSN 1657-9534. URL [↗](#).
- [18] Robert Michael Kwee and Thomas Christian Kwee. Imaging in local staging of gastric cancer: A systematic review, may 2007. ISSN 0732183X. URL [↗](#).
- [19] Victor Pasechnikov, Sergej Chukov, Evgeny Fedorov, Ilze Kikuste, and Marcis Leja. Gastric cancer: Prevention, screening and early diagnosis, oct 2014. ISSN 22192840. URL [↗](#).
- [20] Surgery A Pennathur, Blair A Jobe, James D Luketich, Arjun Pennathur, Michael K Gibson, James D Luketich, Arjun Pennathur, Michael K Gibson, and Blair A Jobe. Oesophageal carcinoma. *Seminar 400 www.thelancet.com Lancet*, 381(381):400–12, feb 2013. ISSN 1474-547X. doi: 10.1016/S0140-6736(12)60643-6. URL [↗](#).
- [21] V. Backman, M. B. Wallace, L. T. Perelman, J. T. Arendt, R. Gurjar, M. G. Müller, Q. Zhang, G. Zonios, E. Kline, J. a McGilligan, S. Shapshay, T. Valdez, K. Badizadegan, J. M. Crawford, M. Fitzmaurice, S. Kabani, H. S. Levin, M. Seiler, R. R. Dasari, I. Itzkan, J. Van Dam, and M. S. Feld. Detection of preinvasive cancer cells. *Nature*, 406(6791):35–36, 2000. ISSN 0028-0836. doi: 10.1038/35017638.
- [22] Brett E. Bouma, Guillermo J. Tearney, Carolyn C. Compton, and Norman S. Nishioka. High-resolution imaging of the human esophagus and stomach in vivo using optical coherence tomography. *Gastrointestinal Endoscopy*, 51(4):467–474, apr 2000. ISSN 00165107. doi: 10.1016/S0016-5107(00)70449-4. URL [↗](#).

- [23] J F Botet, C J Lightdale, A G Zauber, H Gerdes, S J Winawer, C Urmacher, and M F Brennan. Preoperative staging of gastric cancer: comparison of endoscopic US and dynamic CT. *Radiology*, 181(2):426–32, 1991. ISSN 0033-8419. doi: 10.1148/radiology.181.2.1924784. URL [↗](#).
- [24] Don Wayne Fawcett. An atlas of fine structure: the cell, its organelles, and inclusions., 1966.
- [25] Kyung Myung Sohn, Jae Mun Lee, Sung Yong Lee, Bo Young Ahn, Seung Man Park, and Kyoung Mee Kim. Comparing MR imaging and CT in the staging of gastric carcinoma. *American Journal of Roentgenology*, 174(6):1551–1557, jun 2000. ISSN 0361803X. doi: 10.2214/ajr.174.6.1741551. URL [↗](#).
- [26] Woonggyu Jung, Daniel T McCormick, Yeh-Chan Ahn, Ali Sepehr, Matt Brenner, Brian Wong, Norman C Tien, and Zhongping Chen. In vivo three-dimensional spectral domain endoscopic optical coherence tomography using a microelectromechanical system mirror. *Optics letters*, 32(22):3239–3241, nov 2007. ISSN 0146-9592. doi: 10.1364/OL.32.003239. URL [↗](#).
- [27] Benjamin J. Vakoc, Dai Fukumura, Rakesh K. Jain, and Brett E. Bouma. Cancer imaging by optical coherence tomography: preclinical progress and clinical potential. *Nature Reviews Cancer*, 12(5):363–368, apr 2012. ISSN 1474-175X. doi: 10.1038/nrc3235. URL [↗](#).
- [28] Gaspar Delso and Sibylle Ziegler. PET/MRI system design, mar 2009. ISSN 16197070. URL [↗](#).
- [29] Cui Lei, Liming Huang, Yanlin Wang, Yiling Huang, and Huang Yurong. Comparison of MRI and endoscope ultrasound detection in preoperative T/N staging of gastric cancer. *Molecular and Clinical Oncology*, 1(4):699–702, jul 2013. ISSN 2049-9450. doi: 10.3892/mco.2013.103. URL [↗](#).
- [30] Peter K. H. Roschmann. High-frequency coil system for a magnetic resonance imaging apparatus, 1988. ISSN 0730-725X. URL [↗](#).
- [31] Brian A. Baertlein, Özlem Özbay, Tamer Ibrahim, Robert Lee, Ying Yu, Allahyar Kangarlu, and Pierre Marie L Robitaille. Theoretical model for an MRI radio frequency resonator. *IEEE Transactions on Biomedical Engineering*, 47(4):535–546, 2000. ISSN 00189294. doi: 10.1109/10.828153.
- [32] Joo Hee Kim, Geerard L. Beets, Myeong Jin Kim, Alfons G H Kessels, and Regina G H Beets-Tan. High-resolution MR imaging for nodal staging in rectal cancer: Are there any criteria in addition to the size? *European Journal of Radiology*, 52(1):78–83, 2004. ISSN 0720048X. doi: 10.1016/j.ejrad.2003.12.005.
- [33] Joon Il Choi, Ijin Joo, and Jeong Min Lee. State-of-the-art preoperative staging of gastric cancer by MDCT and magnetic resonance imaging. *World Journal of Gastroenterology*, 20(16):4546–4557, apr 2014. ISSN 22192840. doi: 10.3748/wjg.v20.i16.4546. URL [↗](#).
- [34] Lutz Schmitz, Uwe Reinhold, Erhard Bierhoff, and Thomas Dirschka. Optical coherence tomography: its role in daily dermatological practice. *JDDG: Journal der Deutschen Dermatologischen Gesellschaft*, 11(6):499–507, jun 2013. ISSN 16100379. doi: 10.1111/ddg.12073. URL [↗](#).

- [35] Gregory Zuccaro. The use of endoscopic ultrasound in esophageal disease, mar 2007. ISSN 15547914. URL [↗](#).
- [36] Francesco Giganti, Elena Orsenigo, Paolo Giorgio Arcidiacono, Roberto Nicoletti, Luca Albarello, Alessandro Ambrosi, Annalaura Salerno, Antonio Esposito, Maria Chiara Petrone, Damiano Chiari, Carlo Staudacher, Alessandro Del Maschio, and Francesco De Cobelli. Pre-operative locoregional staging of gastric cancer: is there a place for magnetic resonance imaging? Prospective comparison with EUS and multidetector computed tomography. *Gastric Cancer*, 19(1):216–225, 2016. ISSN 14363305. doi: 10.1007/s10120-015-0468-1.
- [37] David M Shotton. Confocal scanning optical microscopy and its applications for biological specimens. *Journal of Cell Science*, 94:175–206, 1989. ISSN 0021-9533.
- [38] J B Pawley. *Handbook of biological confocal microscopy*. Springer Science Business Media, Madison, 3 edition, 1996. ISBN 987-0-387-25921-5.
- [39] Adaobi Nwaneshiudu, Christiane Kuschal, Fernanda H. Sakamoto, R. Rox Anderson, Kathryn Schwarzenberger, and Roger C. Young. Introduction to Confocal Microscopy. *Journal of Investigative Dermatology*, 132(12):1–5, 2012. ISSN 0022202X. doi: 10.1038/jid.2012.429. URL [↗](#).
- [40] R. Rezakhaniha, A. Agianniotis, J. T C Schrauwen, A. Griffa, D. Sage, C. V C Bouten, F. N. Van De Vosse, M. Unser, and N. Stergiopoulos. Experimental investigation of collagen waviness and orientation in the arterial adventitia using confocal laser scanning microscopy. *Biomechanics and Modeling in Mechanobiology*, 11(3-4):461–473, 2012. ISSN 16177959. doi: 10.1007/s10237-011-0325-z.
- [41] L. V. Wang. Tutorial on photoacoustic microscopy and computed tomography. *Journal of Selected Topics in Quantum*, 14(1):171–179, 2008. doi: 10.1109/JSTQE.2007.913398. URL [↗](#).
- [42] Junjie Yao and Lihong V Wang. Photoacoustic Microscopy. *Laser Photon Rev*, 7(5):1–36, 2014. ISSN 1863-8880. doi: 10.1002/lpor.201200060.Photoacoustic.
- [43] Jeff W. Lichtman and Jose-Angel Conchello. Fluorescence microscopy. *Nature Methods*, 2(12):910–919, 2005. ISSN 15487091. doi: 10.1038/nmeth817.
- [44] Peter T.C. So, Elijah Y.S. Yew, and Christopher Rowlands. High-throughput nonlinear optical microscopy. *Biophysical Journal*, 105(12):2641–2654, 2013. ISSN 00063495. doi: 10.1016/j.bpj.2013.08.051. URL [↗](#).
- [45] Aaron M. Streets, Ang Li, Tao Chen, and Yanyi Huang. Imaging without fluorescence: nonlinear optical microscopy for quantitative cellular imaging. *Anal. Chem.*, 86(17):8506–8513, 2014. doi: 10.1021/ac5013706.
- [46] S Yue, M. N. Slipchenko, and J.-X. Cheng. Multimodal nonlinear optical microscopy. *Laser Photon Rev*, 5(4):496–512, 2001. doi: 10.1002/lpor.201000027. URL [↗](#).

- [47] David Huang, Eric A Swanson, Charles P Lin, Joel S Schuman, William G Stinson, Warren Chang, Michael R Hee, Thomas Flotte, Kenton Gregory, Carmen A Puliafito, and James G. Fujimoto. Optical Coherence Tomography HHS Public Access. *Science*. November, 22 (2545035):1178–1181, nov 1991. ISSN 0036-8075. doi: 10.1002/jcp.24872.The. URL [↗](#).
- [48] Benjamin Potsaid, Bernhard Baumann, David Huang, Scott Barry, Alex E Cable, Joel S Schuman, Jay S Duker, and James G Fujimoto. Ultrahigh speed 1050nm swept source/Fourier domain OCT retinal and anterior segment imaging at 100,000 to 400,000 axial scans per second. *Optics express*, 18(19):20029–48, 2010. ISSN 1094-4087. doi: 10.1364/OE.18.020029. URL [↗](#).
- [49] Nam Hyun Cho, Kibeom Park, Ruchire Eranga Wijesinghe, Yong Seung Shin, Woonggyu Jung, and Jeehyun Kim. Development of real-time dual-display handheld and bench-top hybrid-mode SD-OCTs. *Sensors (Switzerland)*, 14(2):2171–2181, jan 2014. ISSN 14248220. doi: 10.3390/s140202171. URL [↗](#).
- [50] Woonggyu Jung, Jeehyun Kim, Mansik Jeon, Eric J Chaney, Charles N Stewart, and Stephen A Boppart. Handheld optical coherence tomography scanner for primary care diagnostics. *IEEE Transactions on Biomedical Engineering*, 58(3 PART 2):741–744, mar 2011. ISSN 00189294. doi: 10.1109/TBME.2010.2096816. URL [↗](#).
- [51] Thilo Gambichler, Georg Moussa, Michael Sand, Daniel Sand, Peter Altmeyer, and Klaus Hoffmann. Applications of optical coherence tomography in dermatology, nov 2005. ISSN 09231811. URL [↗](#).
- [52] Luigi Vignali, Emilia Solinas, and Enzo Emanuele. Research and Clinical Applications of Optical Coherence Tomography in Invasive Cardiology: A Review. *Current Cardiology Reviews*, 10(4):369–376, nov 2014. ISSN 1573403X. doi: 10.2174/1573403X10666140604120753. URL [↗](#).
- [53] F Feldchtein, V Gelikonov, R Iksanov, G Gelikonov, R Kuranov, A Sergeev, N Gladkova, M Ourutina, D Reitze, and J Warren. In vivo OCT imaging of hard and soft tissue of the oral cavity. *Optics express*, 3(6):239–250, sep 1998. ISSN 1094-4087. doi: 10.1364/OE.3.000239. URL [↗](#).
- [54] N. Weber, H. Zappe, and A. Seifert. Endoscopic optical probes for linear and rotational scanning. In *Proceedings of the IEEE International Conference on Micro Electro Mechanical Systems (MEMS)*, pages 1065–1068, 2013. ISBN 9781467356558. doi: 10.1109/MEMSYS.2013.6474433.
- [55] G. Zuccaro, N. Gladkova, J. Vargo, F. Feldchtein, E. Zagaynova, D. Conwell, G. Falk, J. Goldblum, J. Dumot, J. Ponsky, G. Gelikonov, B. Davros, E. Donchenko, and J. Richter. Optical coherence tomography of the esophagus and proximal stomach in health and disease. *American Journal of Gastroenterology*, 96(9 SUPPL.):2633–2639, 2001. ISSN 00029270. doi: 10.1016/S0002-9270(01)02681-8.
- [56] James G Fujimoto and W Drexler. Introduction to Optical Coherence Tomography. *Optical Coherence Tomography*, (1):1–39, 2008.

- [57] Alexander Ng and Justiaan Swanevelder. Resolution in ultrasound imaging. *Continuing Education in Anaesthesia, Critical Care and Pain*, 11(5):186–192, oct 2011. ISSN 17431816. doi: 10.1093/bjaceaccp/mkr030. URL [↗](#).
- [58] Nathaniel M. Fried and Arthur L. Burnett. Novel methods for mapping the cavernous nerves during radical prostatectomy. *Nature Reviews Urology*, 12(8):451–460, aug 2015. ISSN 1759-4812. doi: 10.1038/nrurol.2015.174. URL [↗](#).
- [59] Can Duan. *Planar and Integrated MEMS Micromirrors Based Endoscopic Optical Coherence Tomography*. PhD thesis, University of Florida, 2016.
- [60] Michael F Byrne and Paul S Jowell. Gastrointestinal imaging: endoscopic ultrasound. *Gastroenterology*, 122(6):1631–1648, 2002. ISSN 0016-5085. doi: 10.1053/gast.2002.33576.
- [61] Sherif El Saadany, Wael Mayah, Ferial El Kalla, and Tawfik Atta. Endoscopic Ultrasound Staging of Upper Gastrointestinal Malignancies. *Asian Pacific journal of cancer prevention : APJCP*, 17(5):2361–7, 2016. ISSN 1513-7368. URL [↗](#).
- [62] Jingjing Sun and Huikai Xie. MEMS-based endoscopic optical coherence tomography, 2011. ISSN 16879384. URL [↗](#).
- [63] A. F. Fercher, K. Mengedoht, and W. Werner. Eye-length measurement by interferometry with partially coherent light. *Optics Letters*, 13(3):186–188, mar 1988. ISSN 0146-9592. doi: 10.1364/OL.13.000186. URL [↗](#).
- [64] Wolfgang Drexler and James G. Fujimoto. *Biological and Medical Physics , Biomedical Engineering Biological and Medical Physics , Biomedical Engineering*. 2008. ISBN 9783540775492. doi: 10.1007/978-1-4614-2146-7.
- [65] Yoshifumi Nakamura, Shuichi Makita, Masahiro Yamanari, Masahide Itoh, Toyohiko Yatagai, and Yoshiaki Yasuno. High-speed three-dimensional human retinal imaging by line- field spectral domain optical coherence tomography. *Optics Express*, 15(12):7103–7116, jun 2007. ISSN 1094-4087. doi: 10.1364/OE.15.007103. URL [↗](#).
- [66] Eduardo A. Novais, Mehreen Adhi, Eric M. Moulton, Ricardo N. Louzada, Emily D. Cole, Lennart Husvogt, ByungKun Lee, Sabin Dang, Caio V.S. Regatieri, André J. Witkin, Caroline R. Bauman, Joachim Hornegger, Vijaysekhar Jayaraman, James G. Fujimoto, Jay S. Duker, and Nadia K. Waheed. Choroidal Neovascularization Analyzed on Ultrahigh-Speed Swept-Source Optical Coherence Tomography Angiography Compared to Spectral-Domain Optical Coherence Tomography Angiography. *American Journal of Ophthalmology*, 164: 80–88, apr 2016. ISSN 18791891. doi: 10.1016/j.ajo.2016.01.011. URL [↗](#).
- [67] V. Jayaraman, G.D. Cole, M. Robertson, A. Uddin, and A. Cable. High-sweep-rate 1310nm MEMS-VCSEL with 150nm continuous tuning range. *Electronics Letters*, 48(14):867, 2012. ISSN 00135194. doi: 10.1049/el.2012.1552. URL [↗](#).
- [68] Ratheesh Kumar Meleppat, Murukeshan Vadakke Matham, and Seah Leong Key. Optical frequency domain imaging with a rapidly swept laser in the 815-870 nm range. *International Conference on Optical and Photonic Engineering*, 9524(July):95242R, 2015. ISSN 1094-4087. doi: 10.1364/OE.14.005937. URL [↗](#).

- [69] G. J. Tearney, M. E. Brezinski, J. G. Fujimoto, N. J. Weissman, S. A. Boppart, B. E. Bouma, and J. F. Southern. Scanning single-mode fiber optic catheter–endoscope for optical coherence tomography: erratum. *Optics Letters*, 21(12):912, 1996. ISSN 0146-9592. doi: 10.1364/OL.21.000912. URL [↗](#).
- [70] Hiram G. Bezerra, Marco A. Costa, Giulio Guagliumi, Andrew M. Rollins, and Daniel I. Simon. Intracoronary Optical Coherence Tomography: A Comprehensive Review. *Clinical and Research Applications*, 2009. ISSN 19368798. URL [↗](#).
- [71] Bryden C. Quirk, Robert A. McLaughlin, Andrea Curatolo, Rodney W. Kirk, Peter B. Noble, and David D. Sampson. In situ imaging of lung alveoli with an optical coherence tomography needle probe. *Journal of Biomedical Optics*, 16(3):036009, 2011. ISSN 10833668. doi: 10.1117/1.3556719. URL [↗](#).
- [72] Michael V Sivak, Kenji Kobayashi, A Joseph, Andrew M Rollins, Richard C K Wong, Gerard A Isenberg, and Joseph Willis. High-resolution endoscopic imaging of the GI tract using optical coherence tomography. *Gastrointestinal Endoscopy*, 51(4):474–, 2000. doi: 10.1067/mge.2000.103679.
- [73] G. J. Tearney, S. A. Boppart, B. E. Bouma, M. E. Brezinski, N. J. Weissman, J. F. Southern, and J. G. Fujimoto. Scanning single-mode fiber optic catheter-endoscope for optical coherence tomography. *Optics letters*, 21(7):543–545, apr 1996. ISSN 0146-9592. doi: 10.1364/OL.21.000543. URL [↗](#).
- [74] B E Bouma and G J Tearney. Power-efficient nonreciprocal interferometer and catheter for optical coherence tomography. *Optics Letters*, 24(8):531–533, 1999. ISSN 0146-9592.
- [75] Victor X.D. Yang, Maggie L. Gordon, Shou-jiang Tang, Norman E. Marcon, Geoffrey Gardiner, Bing Qi, Stuart Bisland, Emily Seng-Yue, Stewart Lo, Julius Pekar, Brian C. Wilson, and I. Alex Vitkin. High speed, wide velocity dynamic range Doppler optical coherence tomography (Part III): in vivo endoscopic imaging of blood flow in the rat and human gastrointestinal tracts. *Optics Express*, 11(19):2416, 2003. ISSN 1094-4087. doi: 10.1364/OE.11.002416. URL [↗](#).
- [76] S a Boppart, B E Bouma, C Pitris, G J Tearney, J G Fujimoto, and M E Brezinski. Forward-imaging instruments for optical coherence tomography. *Optics letters*, 22(21):1618–1620, 1997. ISSN 0146-9592. doi: 10.1364/OL.22.001618.
- [77] Jigang Wu, Michael Conry, Chunhui Gu, Fei Wang, Zahid Yaqoob, and Changhuei Yang. Paired-angle-rotation scanning optical coherence tomography forward-imaging probe. *Optics letters*, 31(9):1265–7, may 2006. ISSN 0146-9592. doi: 10.1364/OL.31.001265. URL [↗](#).
- [78] Maciej Wojtkowski. High-speed optical coherence tomography: basics and applications. *Applied optics*, 49(16):D30–D61, 2010. ISSN 0003-6935. doi: 10.1364/AO.49.000D30. URL [↗](#).
- [79] Muneki Nakada, Chongho Chong, Atsushi Morosawa, Keiji Isamoto, Takuya Suzuki, Hiroyuki Fujita, and Hiroshi Toshiyoshi. Optical coherence tomography by all-optical MEMS



- fiber endoscope. *IEICE Electronics Express*, 7(6):428–433, 2010. ISSN 13492543. doi: 10.1587/elex.7.428.
- [80] Thomas Klein and Robert Huber. High-speed OCT light sources and systems [Invited]. *Biomedical Optics Express*, 8(2):828, 2017. ISSN 2156-7085. doi: 10.1364/BOE.8.000828. URL [↗](#).
- [81] Lin Liu, Lei Wu, Jingjing Sun, Elaine Lin, and Huikai Xie. Miniature endoscopic optical coherence tomography probe employing a two-axis microelectromechanical scanning mirror with through-silicon vias. *Journal of biomedical optics*, 16(2):026006, 2011. ISSN 10833668. doi: 10.1117/1.3533323. URL [↗](#).
- [82] Henry L. Fu, Yuxin Leng, Michael J. Cobb, Kevin Hsu, Joo Ha Hwang, and Xingde Li. Flexible miniature compound lens design for high-resolution optical coherence tomography balloon imaging catheter. *Journal of Biomedical Optics*, 13(6):060502, 2008. ISSN 10833668. doi: 10.1117/1.3037340. URL [↗](#).
- [83] Przemyslaw Struk, Sylwester Bargiel, Luc Froehly, Maciej Baranski, Nicolas Passilly, Jorge Albero, and Christophe Gorecki. Swept source optical coherence tomography endomicroscope based on vertically integrated mirau micro interferometer: Concept and technology. *IEEE Sensors Journal*, 15(12):7061–7070, dec 2015. ISSN 1530437X. doi: 10.1109/JSEN.2015.2469547. URL [↗](#).
- [84] Alexandre R. Tumlinson, Jennifer K. Barton, Boris Povazay, Harald Sattman, Angelika Unterhuber, Rainer A. Leitgeb, and Wolfgang Drexler. Endoscope-tip interferometer for ultrahigh resolution frequency domain optical coherence tomography in mouse colon. *Optics express*, 14(5):1878–1887, 2006. ISSN 1094-4087. doi: 10.1364/OE.14.001878. URL [↗](#).
- [85] F J Wallace. Fiber Optic Endoscopy. *The Journal of urology*, 90:324–334, sep 1963. ISSN 00225347. URL [↗](#).
- [86] Chen D. Lu, Martin F. Kraus, Benjamin Potsaid, Jonathan J. Liu, WooJhon Choi, Vijaysekhar Jayaraman, Alex E. Cable, Joachim Hornegger, Jay S. Duker, and James G. Fujimoto. Handheld ultrahigh speed swept source optical coherence tomography instrument using a MEMS scanning mirror. *Biomedical Optics Express*, 5(1):293–311, jan 2013. ISSN 2156-7085. doi: 10.1364/BOE.5.000293. URL [↗](#).
- [87] Mouloud Ourak, Brahim Tamadazte, and Nicolas Andreff. Partitioned camera-OCT based 6 DOF visual servoing for automatic repetitive optical biopsies. *IEEE International Conference on Intelligent Robots and Systems*, 2016-Novem(3):2337–2342, 2016. ISSN 21530866. doi: 10.1109/IROS.2016.7759364.
- [88] Michalina J. Gora, Melissa J. Suter, Guillermo J. Tearney, and Xingde Li. Endoscopic optical coherence tomography: technologies and clinical applications [Invited]. *Biomedical Optics Express*, 8(5):2405, 2017. ISSN 2156-7085. doi: 10.1364/BOE.8.002405. URL [↗](#).
- [89] Zahid Yaqoob, Jigang Wu, Emily J McDowell, Xin Heng, and Changhuei Yang. Methods and application areas of endoscopic optical coherence tomography. *Journal of Biomedical Optics*, 11(6):063001, 2006. ISSN 1083-3668. doi: 10.1117/1.2400214. URL [↗](#).

- [90] T.-H. Tsai, J G Fujimoto, and Hiroshi Mashimo. Endoscopic optical coherence tomography for clinical gastroenterology. *Diagnostics*, 4(2):57–93, may 2014. ISSN 2075-4418. doi: 10.3390/diagnostics4020057. URL [↗](#).
- [91] Peter H Tran, David S Mukai, Matthew Brenner, and Zhongping Chen. In vivo endoscopic optical coherence tomography by use of a rotational microelectromechanical system probe. *Optics letters*, 29(11):1236–8, 2004. ISSN 0146-9592. doi: 10.1364/OL.29.001236. URL [↗](#).
- [92] P R Herz, Y Chen, a D Aguirre, K Schneider, P Hsiung, J G Fujimoto, K Madden, J Schmitt, J Goodnow, and C Petersen. Micromotor endoscope catheter for in vivo, ultrahigh-resolution optical coherence tomography. *Optics letters*, 29(19):2261–2263, 2004. ISSN 0146-9592. doi: 10.1364/OL.29.002261.
- [93] Jianping Su, Jun Zhang, Linfeng Yu, and Zhongping Chen. In vivo three-dimensional micro-electromechanical endoscopic swept source optical coherence tomography. *Optics express*, 15(16):10390–10396, aug 2007. ISSN 1094-4087. doi: 10.1364/OE.15.010390. URL [↗](#).
- [94] Shoude Chang, Erroll Murdock, Youxin Mao, Costel Flueraru, and John Disano. Stationary-fiber rotary probe with unobstructed 360 view for optical coherence tomography. *Optics letters*, 36(22):4392–4, nov 2011. ISSN 1539-4794. doi: 10.1364/OL.36.004392. URL [↗](#).
- [95] Tianyuan Chen, Ning Zhang, Tiancheng Huo, Chengming Wang, Jing-gao Zheng, Tieying Zhou, and Ping Xue. Tiny endoscopic optical coherence tomography probe driven by a miniaturized hollow ultrasonic motor. *Journal of Biomedical Optics*, 18(8):086011, aug 2013. ISSN 1083-3668. doi: 10.1117/1.JBO.18.8.086011. URL [↗](#).
- [96] X Li, C Chudoba, T Ko, C Pitris, and J G Fujimoto. Imaging needle for optical coherence tomography. *Optics letters*, 25(20):1520–1522, 2000. ISSN 0146-9592. doi: 10.1364/OL.25.001520.
- [97] D. Lorensen, X. Yang, R. W. Kirk, B. C. Quirk, R. A. McLaughlin, and D. D. Sampson. Ultrathin side-viewing needle probe for optical coherence tomography. *Opt. Lett.*, 36(19):3894, 2011. ISSN 0146-9592. doi: 10.1364/OL.36.003894.
- [98] Aaron D. Aguirre, Paul R. Hertz, Yu Chen, James G. Fujimoto, Wibool Piyawattanametha, Li Fan, and Ming C. Wu. Two-axis MEMS scanning catheter for ultrahigh resolution three-dimensional and en face imaging. *Optics express*, 15(5):2445–2453, 2007. ISSN 1094-4087. doi: 10.1364/OE.15.002445. URL [↗](#).
- [99] Yingtian Pan, Huikai Xie, and Gary K. Fedder. Endoscopic optical coherence tomography based on a microelectromechanical mirror. *Optics Letters*, 26(24):1966, 2001. ISSN 0146-9592. doi: 10.1364/OL.26.001966. URL [↗](#).
- [100] Shanshan Gu-Stoppel, Thorsten Giese, Hans-Joachim Quenzer, Ulrich Hofmann, and Wolfgang Benecke. PZT-Actuated and -Sensed Resonant Micromirrors with Large Scan Angles Applying Mechanical Leverage Amplification for Biaxial Scanning. *Micromachines*, 8(7):215, jul 2017. ISSN 2072-666X. doi: 10.3390/mi8070215. URL [↗](#).

- [101] Eakkachai Pengwang, Kanty Rabenorosoa, Micky Rakotondrabe, and Nicolas Andreff. Scanning micromirror platform based on MEMS technology for medical application. *Micromachines*, 7(2):1–29, 2016. ISSN 2072666X. doi: 10.3390/mi7020024.
- [102] T.H. Tsai, B.M. Potsaid, M. Kraus, J.J. Liu, Chao Zhou, Joachim Hornegger, and J.G. Fujimoto. Piezoelectric transducer based miniature catheter for ultrahigh speed endoscopic optical coherence tomography. *Biomedical Optics Express*, 2(8):2438–2448, 2011. ISSN 16057422. doi: 10.1117/12.875815. URL [↗](#).
- [103] Kristin H Gilchrist, Ryan P McNabb, Joseph A Izatt, and Sonia Grego. Piezoelectric scanning mirrors for endoscopic optical coherence tomography. *Journal of Micromechanics and Microengineering*, 19(9):1–11?, sep 2009. ISSN 0960-1317. doi: 10.1088/0960-1317/19/9/095012. URL [↗](#).
- [104] Yeong Hyeon Seo, Kyungmin Hwang, and Ki Hun Jeong. Compact OCT endomicroscopic catheter using flip-chip bonded Lissajous scanned electrothermal MEMS fiber scanner. *Proceedings of the IEEE International Conference on Micro Electro Mechanical Systems (MEMS)*, pages 518–521, 2017. ISSN 10846999. doi: 10.1109/MEMSYS.2017.7863457.
- [105] Can Duan, Xiaoyang Zhang, Donglin Wang, Zhengwei Zhou, Peng Liang, Antonio Pozzi, and Huikai Xie. An endoscopic forward-viewing OCT imaging probe based on a two-axis scanning mems mirror. *2014 IEEE 11th International Symposium on Biomedical Imaging (ISBI)*, pages 1397–1400, 2014. doi: 10.1109/ISBI.2014.6868139. URL [↗](#).
- [106] Leo. Beiser. *Unified Optical Scanning Technology*. Wiley-Interscience, 2003. ISBN 0471316547. URL [↗](#).
- [107] S R Chinn, E a Swanson, and J G Fujimoto. Optical coherence tomography using a frequency-tunable optical source. *Optics letters*, 22(5):340–342, 1997. ISSN 0146-9592. doi: 10.1364/OL.22.000340.
- [108] Hiroshi Miyajima, Kenzi Murakami, and Masahiro Katashiro. MEMS optical scanners for microscopes. *IEEE Journal on Selected Topics in Quantum Electronics*, 10(3):514–527, 2004. ISSN 1077260X. doi: 10.1109/JSTQE.2004.828487.
- [109] Y. Zhang, M. L. Akins, K. Murari, J. Xi, M.-J. Li, K. Luby-Phelps, M. Mahendroo, and X. Li. A compact fiber-optic SHG scanning endomicroscope and its application to visualize cervical remodeling during pregnancy. *Proceedings of the National Academy of Sciences*, 109(32):12878–12883, 2012. ISSN 0027-8424. doi: 10.1073/pnas.1121495109.
- [110] Ning Zhang, Tsung-Han Tsai, Osman O Ahsen, Kaicheng Liang, Hsiang-Chieh Lee, Ping Xue, Xingde Li, and James G Fujimoto. Compact piezoelectric transducer fiber scanning probe for optical coherence tomography. *Optics letters*, 39(2):186–8, 2014. ISSN 1539-4794. doi: 10.1364/OL.39.000186. URL [↗](#).
- [111] Hyeon-Cheol Park, Yeong-Hyeon Seo, and Ki-Hun Jeong. Lissajous fiber scanning for forward viewing optical endomicroscopy using asymmetric stiffness modulation. *Optics express*, 22(5):5818–25, 2014. ISSN 1094-4087. doi: 10.1364/OE.22.005818. URL [↗](#).

- [112] M J Everett, S A Meyer, and Y Zhou. Patterned spinning disk based optical phase shifter for spectral domain optical coherence tomography, 2008. URL [↗](#).
- [113] Gaddum Duemani Reddy and Peter Saggau. Fast three-dimensional laser scanning scheme using acousto-optic deflectors. *Journal of biomedical optics*, 10(6):064038, 2005. ISSN 1083-3668. doi: 10.1117/1.2141504. URL [↗](#).
- [114] Paul A. Kirkby, K. M. Naga Srinivas Nadella, and R. Angus Silver. A compact acousto-optic lens for 2D and 3D femtosecond based 2-photon microscopy. *Optics Express*, 18(13):13720, 2010. ISSN 1094-4087. doi: 10.1364/OE.18.013720. URL [↗](#).
- [115] Khaled Aljaseem, Armin Werber, Andreas Seifert, and Hans Zappe. Fiber optic tunable probe for endoscopic optical coherence tomography. *Journal of Optics A: Pure and Applied Optics*, 10:044012, 2008. ISSN 1464-4258. doi: 10.1088/1464-4258/10/4/044012.
- [116] Khaled Aljaseem, Luc Froehly, Andreas Seifert, and Hans Zappe. Scanning and tunable micro-optics for endoscopic optical coherence tomography. *Journal of Microelectromechanical Systems*, 20(6):1462–1472, 2011. ISSN 10577157. doi: 10.1109/JMEMS.2011.2167656.
- [117] Yuhe Shao and David L Dickensheets. MOEMS 3-D scan mirror for single-point control of beam deflection and focus. *Journal of Micro/Nanolithography, MEMS, and MOEMS*, 4(4):41502–41507, 2005. ISSN 1932-5150. doi: 10.1117/1.2107127.
- [118] Melissa J. Suter, Benjamin J. Vakoc, Patrick S. Yachimski, Milen Shishkov, Gregory Y. Lauwers, Mari Mino-Kenudson, Brett E. Bouma, Norman S. Nishioka, and Guillermo J. Tearney. Comprehensive microscopy of the esophagus in human patients with optical frequency domain imaging. *Gastrointestinal Endoscopy*, 68(4):745–753, 2008. ISSN 00165107. doi: 10.1016/j.gie.2008.05.014.
- [119] Jiefeng Xi, Li Huo, Yicong Wu, Michael J Cobb, Joo Ha Hwang, and Xingde Li. High-resolution OCT balloon imaging catheter with astigmatism correction. *Optics letters*, 34(13):1943–1945, 2009. ISSN 0146-9592. doi: 10.1364/OL.34.001943.
- [120] W Kang, H Wang, Y Pan, M W Jenkins, G A Isenberg, A Chak, M Atkinson, D Agrawal, Z Hu, and A M Rollins. Endoscopically guided spectral-domain OCT with double-balloon catheters. *Optics express*, 18(16):17364–17372, 2010. ISSN 1094-4087. doi: 10.1364/OE.18.017364. URL [↗](#).
- [121] Kaicheng Liang, Giovanni Traverso, Hsiang-Chieh Lee, Osman Oguz Ahsen, Zhao Wang, Benjamin Potsaid, Michael G Giacomelli, Vijaysekhar Jayaraman, Ross Barman, Alex E Cable, Hiroshi Mashimo, Robert Langer, and James G. Fujimoto. Ultrahigh speed en face OCT capsule for endoscopic imaging. *Biomedical Optics Express*, 6(4):1146, 2015. ISSN 2156-7085. doi: 10.1364/BOE.6.001146. URL [↗](#).
- [122] Michalina J. Gora, Jenny S. Sauk, Robert W. Carruth, Kevin A. Gallagher, J. Melissa, Norman S. Nishioka, Lauren E. Kava, Mireille Rosenberg, Brett E. Bouma, Guillermo J. Tearney, Melissa J. Suter, Norman S. Nishioka, Lauren E Kava, Mireille Rosenberg, Brett E Bouma, and Guillermo J Tearney. Tethered capsule endomicroscopy enables less invasive

- imaging of gastrointestinal tract microstructure. *Nature medicine*, 19(2):238–40, feb 2013. ISSN 1546-170X. doi: 10.1038/nm.3052. URL [↗](#).
- [123] Victor X.D. Yang, You X. Mao, Nigel Munce, Beau Standish, Walter Kucharczyk, Norman E. Marcon, Brian C. Wilson, and I. Alex Vitkin. Interstitial Doppler optical coherence tomography. *Opt.Lett.*, 30(0146-9592 (Print)):1791–1793, jul 2005. ISSN 0146-9592. doi: 10.1364/OL.30.001791. URL [↗](#).
- [124] Robert A. McLaughlin, Bryden C. Quirk, Andrea Curatolo, Rodney W. Kirk, Loretta Scolaro, Dirk Lorenser, Peter D. Robbins, Benjamin A. Wood, Christobel M. Saunders, and David D. Sampson. Imaging of breast cancer with optical coherence tomography needle probes: Feasibility and initial results. *IEEE Journal on Selected Topics in Quantum Electronics*, 18(3):1184–1191, 2012. ISSN 1077260X. doi: 10.1109/JSTQE.2011.2166757.
- [125] Woonggyu Jung, Daniel T. McCormick, Jun Zhang, Lei Wang, Norman C. Tien, and Zhongping Chen. Three-dimensional endoscopic optical coherence tomography by use of a two-axis microelectromechanical scanning mirror. *Applied Physics Letters*, 88(16), 2006. ISSN 00036951. doi: 10.1063/1.2195092.
- [126] Y Xu, J Singh, C S Premachandran, a Khairyanto, K W S Chen, N Chen, C J R Sheppard, and M Olivo. Design and development of a 3D scanning MEMS OCT probe using a novel SiOB package assembly. *Journal of Micromechanics and Microengineering*, 18(12):125005, 2008. ISSN 0960-1317. doi: 10.1088/0960-1317/18/12/125005.
- [127] Sean R. Samuelson, Lei Wu, Jingjing Sun, Se Woon Choe, Brian S. Sorg, and Huikai Xie. A 2.8-mm imaging probe based on a high-fill-factor MEMS mirror and wire-bonding-free packaging for endoscopic optical coherence tomography. *Journal of Microelectromechanical Systems*, 21(6):1291–1302, 2012. ISSN 10577157. doi: 10.1109/JMEMS.2012.2209404.
- [128] Can Duan, Quentin Tanguy, Antonio Pozzi, and Huikai Xie. Optical coherence tomography endoscopic probe based on a tilted MEMS mirror. *Biomedical Optics Express*, 7(9):3345–3354, 2016. ISSN 2156-7085. doi: 10.1364/BOE.7.003345. URL [↗](#).
- [129] Tianshi Wang, Tom Pfeiffer, Evelyn Regar, Wolfgang Wieser, Heleen van Beusekom, Charles T Lancee, Geert Springeling, Ilona Krabbendam, Antonius F W van der Steen, Robert Huber, and Gijs van Soest. Heartbeat OCT: in vivo intravascular megahertz-optical coherence tomography. *Biomedical optics express*, 6(12):5021–32, 2015. ISSN 2156-7085. doi: 10.1364/BOE.6.005021. URL [↗](#).
- [130] Utkarsh Sharma and Jin U. Kang. Common-path optical coherence tomography with side-viewing bare fiber probe for endoscopic optical coherence tomography. *Review of Scientific Instruments*, 78(11), 2007. ISSN 00346748. doi: 10.1063/1.2804112.
- [131] Bryden C. Quirk, Robert A. McLaughlin, Alex M. Pagnozzi, Brendan F. Kennedy, Peter B. Noble, and David D. Sampson. Optofluidic needle probe integrating targeted delivery of fluid with optical coherence tomography imaging. *Optics letters*, 39(10):2888–91, may 2014. ISSN 1539-4794. doi: 10.1364/OL.39.002888. URL [↗](#).

- [132] Tomas Tuma, John Lygeros, V Kartik, Abu Sebastian, and Angeliki Pantazi. High-speed multiresolution scanning probe microscopy based on Lissajous scan trajectories. *Nanotechnology*, 23:185501, 2012. ISSN 0957-4484. doi: 10.1088/0957-4484/23/18/185501.
- [133] Alexandre R Tumlinson, Lida P Hariri, Urs Utzinger, and Jennifer K Barton. Miniature endoscope for simultaneous optical coherence tomography and laser-induced fluorescence measurement. *Applied optics*, 43(1):113–121, 2004. ISSN 0003-6935. doi: 10.1364/AO.43.000113.
- [134] Wibool Piyawattanametha, P. R. Patterson, Dooyoung Hah, Hiroshi Toshiyoshi, and M. C. Wu. Surface- and Bulk- Micromachined Two-Dimensional Scanner Driven by Angular Vertical Comb Actuators. *2003 IEEE/LEOS International Conference on Optical MEMS*, 14(6):1329–1338, 2005. doi: 10.1109/OMEMS.2003.1233483.
- [135] Sommaire D U Dossier. Santé et sécurité du travail, risques électriques. Technical report, 2007. URL [↗](#).
- [136] Dominique Finon. L 'électricité. (1996):1–5, 2005.
- [137] Ki Hean Kim, B. Hyle Park, Gopi N. Maguluri, Tom W. Lee, Fran J. Rogomentich, Mirela G. Bancu, Brett E. Bouma, Johannes F. de Boer, and Jonathan J. Bernstein. Two-axis magnetically-driven MEMS scanning catheter for endoscopic high-speed optical coherence tomography. *Optics express*, 15(26):18130–18140, dec 2007. ISSN 1094-4087. doi: 10.1364/OE.15.018130. URL [↗](#).
- [138] Takayuki Naono, Takamichi Fujii, Masayoshi Esashi, and Shuji Tanaka. A large-scan-angle piezoelectric MEMS optical scanner actuated by a Nb-doped PZT thin fil. *Journal of Micromechanics and Microengineering*, 24(1):015010, 2014. ISSN 09244247. doi: 10.1016/j.sna.2015.06.029.
- [139] Jingjing Sun, Shuguang Guo, Lei Wu, Lin Liu, Se Woon Choe, Brian S Sorg, and Huikai Xie. 3D in vivo optical coherence tomography based on a low-voltage, large-scan-range 2D MEMS mirror. *Optics express*, 18(12):12065–12075, 2010. ISSN 1094-4087. doi: 10.1364/OE.18.012065.
- [140] Donglin Wang, Can Duan, Xiaoyang Zhang, Zhao Yun, Antonio Pozzi, and Huikai Xie. Common-path optical coherence tomography using a microelectromechanical-system-based endoscopic probe. *Appl. Opt.*, 55(25):6930–6935, 2016. ISSN 0003-6935. doi: 10.1364/AO.55.006930. URL [↗](#).
- [141] Ankur Jain, Anthony Kopa, Yingtian Pan, Gary K. Feeder, and Huikai Xie. A two-axis electrothermal micromirror for endoscopic optical coherence tomography. *IEEE Journal on Selected Topics in Quantum Electronics*, 10(3):636–642, may 2004. ISSN 1077260X. doi: 10.1109/JSTQE.2004.829194. URL [↗](#).
- [142] Stephen Jacobsen. A proposal for the development of Micro Electromechanical Systems. Technical report, The center for engineering design, University of Utah, Salt lake city, 1986.

- [143] Byeong Ha Lee, Eun Jung Min, and Young Ho Kim. Fiber-based optical coherence tomography for biomedical imaging, sensing, and precision measurements. *Optical Fiber Technology*, 19(6 PART B):729–740, 2013. ISSN 10685200. doi: 10.1016/j.yofte.2013.07.011. URL [↗](#).
- [144] Chen D. Lu, Martin F. Kraus, Benjamin Potsaid, Jonathan J. Liu, Woojhon Choi, Vijaysekhar Jayaraman, Alex E. Cable, Joachim Hornegger, Jay S. Duker, and James G. Fujimoto. Handheld ultrahigh speed swept source optical coherence tomography instrument using a MEMS scanning mirror. *Biomedical Optics Express*, 5(1):293–311, 2013. ISSN 2156-7085. doi: 10.1364/BOE.5.000293. URL [↗](#).
- [145] Ming C. Wu. Micromachining for optical and optoelectronic systems. *Proceedings of the IEEE*, 85(11):1833–1856, 1997. ISSN 00189219. doi: 10.1109/5.649660.
- [146] M.C. Wu, L.-Y. Lin, S.-S. Lee, and K.S.J. Pister. Micromachined free-space integrated micro-optics, 1995. ISSN 09244247. URL [↗](#).
- [147] Richard S. Muller. Surface-micromachined microoptical elements and systems. *Proceedings of the IEEE*, 86(8):1705–1720, 1998. ISSN 00189219. doi: 10.1109/5.704276.
- [148] S Bargiel, K Rabenorosoa, C Clévy, C Gorecki, and P Lutz. Towards micro-assembly of hybrid MOEMS components on a reconfigurable silicon free-space micro-optical bench. *Journal of Micromechanics and Microengineering*, 20(4):045012, 2010. ISSN 0960-1317. doi: 10.1088/0960-1317/20/4/045012. URL [↗](#).
- [149] Niklas Weber, Hans Zappe, and Andreas Seifert. A tunable optofluidic silicon optical bench. *Journal of Microelectromechanical Systems*, 21(6):1357–1364, 2012. ISSN 10577157. doi: 10.1109/JMEMS.2012.2206565.
- [150] Niklas Weber, Dominik Spether, Andreas Seifert, and Hans Zappe. Highly compact imaging using Bessel beams generated by ultraminiaturized multi-micro-axicon systems. *Journal of the Optical Society of America A*, 29(5):808, 2012. ISSN 1084-7529. doi: 10.1364/JOSAA.29.000808.
- [151] Hyeon-Cheol Park, Cheol Song, Minseok Kang, Yong Jeong, and Ki-Hun Jeong. Forward imaging OCT endoscopic catheter based on MEMS lens scanning. *Optics Letters*, 37(13):2673, 2012. ISSN 0146-9592. doi: 10.1364/OL.37.002673.
- [152] Hyeon-Cheol Park, Cheol Song, and Ki-Hun Jeong. Micromachined lens microstages for two-dimensional forward optical scanning. *Optics express*, 18(15):16133–8, 2010. ISSN 1094-4087. doi: 10.1364/OE.18.016133. URL [↗](#).
- [153] Justine Lullin, Sylwester Bargiel, Patrice Lemoal, Stéphane Perrin, Jorge Albero, Nicolas Passilly, Luc Froehly, Franck Lardet-Vieudrin, and Christophe Gorecki. An electrostatic vertical microscanner for phase modulating array-type Mirau microinterferometry. *Journal of Micromechanics and Microengineering*, 25(11):115013, 2015. ISSN 0960-1317. doi: 10.1088/0960-1317/25/11/115013. URL [↗](#).
- [154] Maciej Baranski. *Thèse de doctorat*. PhD thesis, UFC, 2008.

- [155] Robert J. Webster and Bryan A. Jones. Design and Kinematic Modeling of Constant Curvature Continuum Robots: A Review. *The International Journal of Robotics Research*, 29(13):1661–1683, 2010. ISSN 0278-3649. doi: 10.1177/0278364910368147. URL [↗](#).
- [156] Mohamed Taha Chikhaoui, Kanty Rabenorosoa, and Nicolas Andreff. Towards Clinical Application of Continuum Active Micro-endoscope Robot based on EAP Actuation. *Surgetica*, 2014.
- [157] Mohamed Taha Chikhaoui, Kanty Rabenorosoa, and Nicolas Andreff. Kinematics and performance analysis of a novel concentric tube robotic structure with embedded soft micro-actuation. *Mechanism and Machine Theory*, 104:234–254, 2016. ISSN 0094114X. doi: 10.1016/j.mechmachtheory.2016.06.005. URL [↗](#).
- [158] Adolf Friedrich Fercher, Wolfgang Drexler, C K Hitzenberger, and Lass. optical coherence tomography - Principles and Applications. pages 238–303, 2003.
- [159] Alexey N. Bashkatov, Elina A. Genina, Vyacheslav I. Kochubey, Anna A. Gavrilova, Sergey V. Kapralov, Veniamin A. Grishaev, and Valery V. Tuchin. Optical properties of human stomach mucosa in the spectral range from 400 to 2000 nm: Prognosis for gastroenterology. *Medical Laser Application*, 22(2):95–104, 2007. ISSN 16151615. doi: 10.1016/j.mla.2007.07.003.
- [160] Christophe Gorecki, Franck Chollet, Eric Bonnotte, and Hideki Kawakatsu. Silicon-based integrated interferometer with phase modulation driven by surface acoustic waves. *Optics Letters*, 22(23):1784, 1997. ISSN 0146-9592. doi: 10.1364/OL.22.001784. URL [↗](#).
- [161] Utkarsh Sharma, Nathaniel M. Fried, and Jin U. Kang. All-fiber common-path optical coherence tomography: Sensitivity optimization and system analysis. *IEEE Journal on Selected Topics in Quantum Electronics*, 11(4):799–805, 2005. ISSN 1077260X. doi: 10.1109/JSTQE.2005.857380.
- [162] Michael A. Choma, Audrey K. Ellerbee, Changhui Yang, Tony L. Creazzo, and Joseph A. Izatt. Spectral-domain phase microscopy. 30(10):1162–1164, 2005.
- [163] Can Duan, Jingjing Sun, Sean R. Samuelson, and Huikai Xie. Probe alignment and design issues of microelectromechanical system based optical coherence tomography endoscopic imaging. *Applied optics*, 52(26):6589–98, 2013. ISSN 1539-4522. doi: 10.1364/AO.52.006589. URL [↗](#).
- [164] M. Oliva, D. Michaelis, P. Dannberg, M. Józwick, K. Liewski, M. Kujawiska, and U. D. Zeitner. TwymanGreen-type integrated laser interferometer array for parallel MEMS testing. *Journal of Micromechanics and Microengineering*, 22(1), 2012. ISSN 09601317. doi: 10.1088/0960-1317/22/1/015018. URL [↗](#).
- [165] Justine Lullin. *Design , simulation and fabrication of a vertical microscanner for phase modulation interferometry - Application to optical coherence tomography system for skin imaging*. PhD thesis, UFC, 2016.



- [166] Jan Niehues, Peter Lehmann, and Weichang Xie. Low coherent Linnik interferometer optimized for use in nano-measuring machines. *Measurement Science and Technology*, 23(12):125002, 2012. ISSN 0957-0233. doi: 10.1088/0957-0233/23/12/125002. URL [↗](#).
- [167] Wei Xu, Alain Bosseboeuf, Fabien Parrain, and Emile Martincic. Design of a long range bidirectional MEMS scanner for a tunable 3D integrated Mirau interferometer. *DTIP 2014 - Symposium on Design, Test, Integration and Packaging of MEMS/MOEMS*, (April), 2014. doi: 10.1109/DTIP.2014.7056655.
- [168] J. Albero, S. Bargiel, N. Passilly, P. Dannberg, M. Stumpf, U. Zeitner, C. Rousselot, K. Gastinger, and C. Gorecki. Micromachined array-type Mirau interferometer for MEMS metrology. *2011 16th International Solid-State Sensors, Actuators and Microsystems Conference, TRANSDUCERS'11*, pages 546–549, 2011. ISSN 0960-1317. doi: 10.1109/TRANSDUCERS.2011.5969709.
- [169] Wei Xu. *Modeling and fabrication of tunable 3D integrated Mirau micro-interferometers* To cite this version : *Modélisation et fabrication de microinterféromètres Mirau accordables intégrés 3D Modeling and fabrication of tunable 3D integrated Mirau micro-interferom.* PhD thesis, 2015.
- [170] S A Boppart. Optical coherence tomography: Technology and applications for neuroimaging. *Psychophysiology*, 40(4):529–541, 2003. ISSN 0048-5772. doi: 10.1111/1469-8986.00055.
- [171] P H Tomlins and R K Wang. Theory, developments and applications of optical coherence tomography. *Journal of Physics D: Applied Physics*, 38(15):2519–2535, 2005. ISSN 0022-3727. doi: 10.1088/0022-3727/38/15/002. URL [↗](#).
- [172] K Kobayashi, Joseph a Izatt, Manish D Kulkarni, Joseph Willis, and Michael V Sivak. High-resolution cross-sectional imaging of the gastrointestinal tract using optical coherence tomography : preliminary results. *Gastrointestinal endoscopy*, 47(6):515–523, 1998.
- [173] Desmond C. Adler, Yu Chen, Robert Huber, Joseph Schmitt, James Connolly, and James G. Fujimoto. Three-dimensional endomicroscopy using optical coherence tomography. *Nature Photonics*, 1(12):709–716, 2007. ISSN 1749-4885. doi: 10.1038. URL [↗](#).
- [174] Wei Cai, Fan Wu, Guangyi Shang, and Nan Yao. Surface modifications with Lissajous trajectories using atomic force microscopy. 113102(2015):1–4, 2016. ISSN 0003-6951. doi: 10.1063/1.4931087. URL [↗](#).
- [175] A. Bazaie, Yuen K. Yong, and S. O.Reza Moheimani. High-speed Lissajous-scan atomic force microscopy: Scan pattern planning and control design issues. *Review of Scientific Instruments*, 83(6), 2012. ISSN 00346748. doi: 10.1063/1.4725525.
- [176] Quentin A A Tanguy, Sylwester Bargiel, Huikai Xie, Nicolas Passilly, Magali Barthès, Olivier GaiFFE, Jaroslaw Rutkowski, Philippe Lutz, and Christophe Gorecki. Design and Fabrication of a 2-Axis Electrothermal MEMS Micro-Scanner for Optical Coherence Tomography. *Micromachines MDPI*, 8(5):146, 2017.

- [177] Kurt E. Petersen. Silicon Torsional Scanning Mirror. *IBM Journal of Research and Development*, 24(5):631–637, 1980. ISSN 0018-8646. doi: 10.1147/rd.245.0631.
- [178] Hiroshi Toshiyoshi and Hiroyuki Fujita. Electrostatic micro torsion mirrors for an optical switch matrix. *Journal of Microelectromechanical Systems*, 5(4):231–237, 1996. ISSN 10577157. doi: 10.1109/84.546402.
- [179] Dooyoung Hah, Hiroshi Toshiyoshi, and Ming C Wu. Design of Electrostatic Actuators for MOEMS Applications. *SPIE*, 4755(1):200–207, 2002. ISSN 0277786X. doi: 10.1117/12.462812. URL [↗](#).
- [180] David Kallweit and Hans Zappe. Fabrication of bulk-Si micromirrors with an integrated tilt sensing mechanism. *Journal of Micromechanics and Microengineering*, 16(2):463–469, feb 2006. ISSN 0960-1317. doi: 10.1088/0960-1317/16/2/033. URL [↗](#).
- [181] John T. W. Yeow, V. X.D. Yang, A. Chahwan, M. L. Gordon, B. Qi, I. A. Vitkin, B. C. Wilson, and A. A. Goldenberg. Micromachined 2-D scanner for 3-D optical coherence tomography. *Sensors and Actuators, A: Physical*, 117(2):331–340, jan 2005. ISSN 09244247. doi: 10.1016/j.sna.2004.06.021. URL [↗](#).
- [182] Ofir Degani, Eran Socher, Ariel Lipson, Tomer Leitner, Dan J. Setter, Shmuel Kaldor, and Yael Nemirovsky. Pull-in study of an electrostatic torsion microactuator. *Journal of Microelectromechanical Systems*, 7(4):373–378, 1998. ISSN 10577157. doi: 10.1109/84.735344. URL [↗](#).
- [183] Dong Yan, Alyssa Apsel, and Amit Lal. Fabrication and electromechanical characterization of silicon on insulator based electrostatic micro-scanners. *Smart Materials and Structures*, 14(4):775–784, aug 2005. ISSN 0964-1726. doi: 10.1088/0964-1726/14/4/037. URL [↗](#).
- [184] Yanhui Bai, John T. W. Yeow, and Brian C Wilson. Design, fabrication, and characteristics of a MEMS micromirror with sidewall electrodes. *Journal of Microelectromechanical Systems*, 19(3):619–631, jun 2010. ISSN 10577157. doi: 10.1109/JMEMS.2010.2044139. URL [↗](#).
- [185] Pin Hsu Kao, Ching Liang Dai, Cheng Chih Hsu, and Chyan Chyi Wu. Manufacture of micromirror arrays using a CMOS-MEMS technique. *Sensors*, 9(8):6219–6231, aug 2009. ISSN 14248220. doi: 10.3390/s90806219. URL [↗](#).
- [186] Jason M. Zara, S Yazdanfar, K D Rao, J a Izatt, and S W Smith. Electrostatic micromachine scanning mirror for optical coherence tomography. *Optics letters*, 28(8):628–630, 2003. ISSN 0146-9592. doi: 10.1364/OL.28.000628.
- [187] Jason M. Zara and S. W. Smith. Optical scanner using a MEMS actuator. *Sensors and Actuators, A: Physical*, 102(1-2):176–184, dec 2002. ISSN 09244247. doi: 10.1016/S0924-4247(02)00302-3. URL [↗](#).
- [188] Jason M. Zara, Joseph A. Izatt, K. Divakara Rao, Siavash Yazdanfar, and Stephen W. Smith. Scanning mirror for optical coherence tomography using an electrostatic MEMS actuator. In *Proceedings - International Symposium on Biomedical Imaging*, volume 2002-Janua, pages 297–300. IEEE, 2002. ISBN 078037584X. doi: 10.1109/ISBI.2002.1029252. URL [↗](#).

- [189] Mingching Wu and Weileun Fang. A molded surface-micromachining and bulk etching release (MOSBE) fabrication platform on (1 1 1) Si for MOEMS. *Journal of Micromechanics and Microengineering*, 16(2):260–265, feb 2006. ISSN 0960-1317. doi: 10.1088/0960-1317/16/2/010. URL [↗](#).
- [190] Ulrich Hofmann, Joachim Janes, and Hans Joachim Quenzer. High-Q MEMS resonators for laser beam scanning displays. *Micromachines*, 3(2):509–528, jun 2012. ISSN 2072666X. doi: 10.3390/mi3020509. URL [↗](#).
- [191] Hiroshi Miyajima, Nobuyoshi Asaoka, Toshihiko Isokawa, Masanori Ogata, Yukihiro Aoki, Masaharu Imai, Osamu Fujimori, Masahiro Katashiro, and Kazuya Matsumoto. A mems electromagnetic optical scanner for a commercial confocal laser scanning microscope. *Journal of Microelectromechanical Systems*, 12(3):243–251, 2003. ISSN 10577157. doi: 10.1109/JMEMS.2003.809961.
- [192] Victor Farm Guoo Tseng, Jiping Li, Xiaoyang Zhang, Jinling Ding, Qiao Chen, and Huikai Xie. An electromagnetically actuated micromirror with precise angle control for harsh environment optical switching applications. *Sensors and Actuators, A: Physical*, 206:1–9, feb 2014. ISSN 09244247. doi: 10.1016/j.sna.2013.11.025. URL [↗](#).
- [193] Guo Dung John Su, Chen Wei Chiu, and Fukang Jiang. Vertical micromirrors integrated with electromagnetic microactuators for two-dimensional optical matrix switches. *IEEE Photonics Technology Letters*, 17(9):1860–1862, sep 2005. ISSN 10411135. doi: 10.1109/LPT.2005.852642. URL [↗](#).
- [194] Chang Liu, Thomas Tsao, Gwo Bin Lee, Jeremy T S Leu, Yong W Yi, Yu Chong Tai, and Chih Ming Ho. Out-of-plane magnetic actuators with electroplated permalloy for fluid dynamics control. *Sensors and Actuators, A: Physical*, 78(2):190–197, dec 1999. ISSN 09244247. doi: 10.1016/S0924-4247(99)00238-1. URL [↗](#).
- [195] Jack W. Judy and Richard S. Muller. Magnetically actuated, addressable microstructures. *Journal of Microelectromechanical Systems*, 6(3):249–255, 1997. ISSN 10577157. doi: 10.1109/84.623114.
- [196] Jonathan J. Bernstein, William P. Taylor, John D. Brazzle, Christopher J. Corcoran, Gregory Kirkos, Jefferson E. Odhner, Ajay Pareek, Marc Waelti, and Marvin Zai. Electromagnetically actuated mirror arrays for use in 3-D optical switching applications. *Journal of Microelectromechanical Systems*, 13(3):526–535, jun 2004. ISSN 10577157. doi: 10.1109/JMEMS.2004.828705. URL [↗](#).
- [197] Si-Hong Ahn and Yong-Kweon Kim. Silicon scanning mirror of two DOF with compensation current routing. *Journal of Micromechanics and Microengineering*, 14(11):1455–1461, nov 2004. ISSN 0960-1317. doi: 10.1088/0960-1317/14/11/004. URL [↗](#).
- [198] Mu Can-Jun, Zhang Fei-Ling, and Wuya-Ming. High-Speed and Large-Scale Electromagnetically Actuated Resonant MEMS Optical Scanner. *Chinese Physics Letters*, 24(12):3574–3577, dec 2007. ISSN 0256-307X. doi: 10.1088/0256-307X/24/12/077. URL [↗](#).

- [199] Hsueh-An Yang, Tsung-Lin Tang, Sheng Ta Lee, and Weileun Fang. A Novel Coil-less Scanning Mirror Using Eddy Current Lorentz Force and Magnetostatic Force. *Journal of Microelectromechanical Systems*, 16(3):511–520, jun 2007. ISSN 1057-7157. doi: 10.1109/JMEMS.2007.896708. URL [↗](#).
- [200] Yixiang Wang, Hong Ding, Xianhao Le, and Jin Xie. A MEMS piezoelectric in-plane resonant accelerometer with two-stage micro-leverage mechanism. In *2016 IEEE 11th Annual International Conference on Nano/Micro Engineered and Molecular Systems, NEMS 2016*, volume 254, pages 455–459, feb 2016. ISBN 9781509019472. doi: 10.1109/NEMS.2016.7758289. URL [↗](#).
- [201] Hyo Jin Nam, Young Sik Kim, Seong Moon Cho, Yougjoon Yee, Jong Uk Bu, Sung Jin Kim, and Young Ho Cho. Low voltage PZT actuated tilting micromirror with hinge structure. In *2002 IEEE/LEOS International Conference on Optical MEMs, OMEMS 2002 - Conference Digest*, pages 89–90. IEEE, 2002. ISBN 0780375955. doi: 10.1109/OMEMS.2002.1031457. URL [↗](#).
- [202] A Donoso and O Sigmund. Optimization of piezoelectric bimorph actuators with active damping for static and dynamic loads. *Structural and Multidisciplinary Optimization*, 38(2): 171–183, 2009. ISSN 1615147X. doi: 10.1007/s00158-008-0273-0. URL [↗](#).
- [203] Metin Sitti, Domenico Campolo, Joseph Yan, Ronald S. Fearing, Tao Su, David Taylor, and Timothy D. Sands. Development of PZT and PZN-PT based unimorph actuators for micromechanical flapping mechanisms. *Proceedings - IEEE International Conference on Robotics and Automation*, 4:3839–3846, 2001. ISSN 10504729. doi: 10.1109/ROBOT.2001.933216. URL [↗](#).
- [204] Yiping Zhu, Wenjing Liu, Kemiao Jia, Wenjun Liao, and Huikai Xie. A piezoelectric unimorph actuator based tip-tilt-piston micromirror with high fill factor and small tilt and lateral shift. *Sensors and Actuators, A: Physical*, 167(2):495–501, 2011. ISSN 09244247. doi: 10.1016/j.sna.2011.03.018. URL [↗](#).
- [205] Jeffrey J. Dosch and Daniel J. Inman. Self-Sensing Piezoelectric Actuator for Collocated Control. *Journal of Intelligent Material Systems and Structures*, 3(January):166–185, jan 1992. ISSN 1045-389X. doi: 10.1177/1045389X9200300109. URL [↗](#).
- [206] Chunyou Zhang, Lihua Wang, Xiaoqiang Wu, and Weijin Gao. A novel optimal configuration of sensor and actuator using a non-linear integer programming genetic algorithm for active vibration control..pdf. (37), 2017. ISSN 1045-389X. doi: 10.1177/1045389X16685439.
- [207] A H Meitzler, H F Tiersten, A W Warner, D Berlincourt, G A Couquin, and F S Welsh III. IEEE standard on piezoelectricity, 1988.
- [208] Ping Ge and Musa Jouaneh. Modeling hysteresis in piezoceramic actuators. *Precision Engineering*, 17(3):211–221, jul 1995. ISSN 01416359. doi: 10.1016/0141-6359(95)00002-U. URL [↗](#).
- [209] J. Tsaur, R. Maeda, and S. Matsumoto. 2D micro scanner actuated by sol-gel derived double layered PZT. *Technical Digest. MEMS 2002 IEEE International Conference. Fifteenth IEEE*

- International Conference on Micro Electro Mechanical Systems (Cat. No.02CH37266)*, pages 548–551, 2002. ISSN 1084-6999. doi: 10.1109/MEMSYS.2002.984330. URL [↗](#).
- [210] Cheng Liang Pan, Yu Ting Ma, Jing Yin, Fan Rang Kong, and Zhi Hua Feng. Miniature orthogonal optical scanning mirror excited by torsional piezoelectric fiber actuator. *Sensors and Actuators, A: Physical*, 165(2):329–337, feb 2011. ISSN 09244247. doi: 10.1016/j.sna.2010.10.013. URL [↗](#).
- [211] Wenjing Liu, Yiping Zhu, Kemiao Jia, Wenjun Liao, Yongming Tang, Baoping Wang, and Huikai Xie. A tip-tilt-piston micromirror with a double S-shaped unimorph piezoelectric actuator. *Sensors and Actuators, A: Physical*, 193:121–128, 2013. ISSN 09244247. doi: 10.1016/j.sna.2012.12.038. URL [↗](#).
- [212] Werner Riethmoller and Wolfgang Benecke. Thermally Excited Silicon Microactuators. *IEEE Transactions on Electron Devices*, 35(6):758–763, 1988. ISSN 15579646. doi: 10.1109/16.2528.
- [213] Shane Truman Todd and Huikai Xie. An electrothermomechanical lumped element model of an electrothermal bimorph actuator. *Journal of Microelectromechanical Systems*, 17(1): 213–225, 2008. ISSN 10577157. doi: 10.1109/JMEMS.2007.908754.
- [214] Lei Wu and Huikai Xie. A large vertical displacement electrothermal bimorph microactuator with very small lateral shift. *Sensors and Actuators, A: Physical*, 145-146(1-2):371–379, 2008. ISSN 09244247. doi: 10.1016/j.sna.2007.10.068.
- [215] Lin Liu, Sagnik Pal, and Huikai Xie. MEMS mirrors based on a curved concentric electrothermal actuator. *Sensors and Actuators, A: Physical*, 188:349–358, 2012. ISSN 09244247. doi: 10.1016/j.sna.2012.03.021. URL [↗](#).
- [216] Shane Truman Todd and Huikai Xie. Steady-state 1D electrothermal modeling of an electrothermal transducer. *Journal of Micromechanics and Microengineering*, 16(3):665–665, 2005. ISSN 0960-1317. doi: 10.1088/0960-1317/16/3/C01. URL [↗](#).
- [217] Sagnik Pal and Huikai Xie. A parametric dynamic compact thermal model of an electrothermally actuated micromirror. *Journal of Micromechanics and Microengineering*, 19(6):065007, 2009. ISSN 0960-1317. doi: 10.1088/0960-1317/19/6/065007. URL [↗](#).
- [218] Sagnik Pal and Huikai Xie. A curved multimorph based electrothermal micromirror with large scan range and low drive voltage. *Sensors and Actuators, A: Physical*, 170(1-2):156–163, 2011. ISSN 09244247. doi: 10.1016/j.sna.2011.06.011. URL [↗](#).
- [219] Shane Truman Todd, Ankur Jain, Hongwei Qu, and Huikai Xie. A 3-D Micromirror Utilizing inverted-Series-Connected Electrothermal Bimorph Actuators for Piston and Tilt Motion. 34 (1998):27–28, 2005.
- [220] Shane Truman Todd, Ankur Jain, Hongwei Qu, and Huikai Xie. A multi-degree-of-freedom micromirror utilizing inverted-series-connected bimorph actuators. *Journal of Optics A: Pure and Applied Optics*, 8(7):S352–S359, 2006. ISSN 1464-4258. doi: 10.1088/1464-4258/8/7/S10. URL [↗](#).

- [221] Kemiao Jia, Sagnik Pal, and Huikai Xie. An electrothermal tip-tilt-piston micromirror based on folded dual s-shaped bimorphs. *Journal of Microelectromechanical Systems*, 18(5):1004–1015, oct 2009. ISSN 10577157. doi: 10.1109/JMEMS.2009.2023838. URL [↗](#).
- [222] Ankur Jain, Hongwei Qu, Shane Truman Todd, and Huikai Xie. A thermal bimorph micromirror with large bi-directional and vertical actuation. *Sensors and Actuators, A: Physical*, 122(1 SPEC. ISS.):9–15, 2005. ISSN 09244247. doi: 10.1016/j.sna.2005.02.001.
- [223] Authors Lingfeng Zhou, Zhiming Chen, Jin Cheng, Yingtao Ding, and Huikai Xie. Investigation of dynamic thermal behaviors of an electrothermal micromirror Abstract. *Sensors and Actuators: A. Physical*, 2017. ISSN 09244247. doi: 10.1016/j.sna.2017.06.002. URL [↗](#).
- [224] Xiaoyang Zhang, Liang Zhou, and Huikai Xie. A fast, large-stroke electrothermal MEMS mirror based on Cu/W bimorph. *Micromachines*, 6(12):1876–1889, dec 2015. ISSN 2072666X. doi: 10.3390/mi6121460. URL [↗](#).
- [225] Ankur Jain and Huikai Xie. A single-crystal silicon micromirror for large bi-directional 2D scanning applications. *Sensors and Actuators, A: Physical*, 130-131(SPEC. ISS.):454–460, aug 2006. ISSN 09244247. doi: 10.1016/j.sna.2005.10.030. URL [↗](#).
- [226] Ephraim Garcia and Nicolae Lobontiu. Induced-strain multimorphs for microscale sensory actuation design. *Smart Materials and Structures*, 13(4):725–732, 2004. ISSN 0964-1726. doi: 10.1088/0964-1726/13/4/010.
- [227] R. A. Buser, N. F. de Rooij, H. Tischhauser, A. Dommann, and G. Staufert. Biaxial scanning mirror activated by bimorph structures for medical applications. *Sensors and Actuators: A. Physical*, 31(1-3):29–34, 1992. ISSN 09244247. doi: 10.1016/0924-4247(92)80076-F.
- [228] J. Buhler, J. Funk, O. Paul, E. P. Steiner, and H. Baltes. Thermally actuated CMOS micromirrors, 1995. ISSN 09244247.
- [229] Liudi Jiang, R. Cheung, J. Hedley, M. Hassan, A. J. Harris, J. S. Burdess, M. Mehregany, and C. A. Zorman. SiC cantilever resonators with electrothermal actuation. *Sensors and Actuators, A: Physical*, 128(2):376–386, 2006. ISSN 09244247. doi: 10.1016/j.sna.2006.01.045.
- [230] M. Sinclair. A high frequency resonant scanner using thermal actuation. *Technical Digest. MEMS 2002 IEEE International Conference. Fifteenth IEEE International Conference on Micro Electro Mechanical Systems (Cat. No.02CH37266)*, pages 698–701, 2002. ISSN 1084-6999. doi: 10.1109/MEMSYS.2002.984366.
- [231] Shane Truman Todd. *Electrothermomechanical modeling of a 1-D electrothermal MEMS micromirror*. PhD thesis, 2005. URL [↗](#).
- [232] Ankur Jain, Shane Truman Todd, and Huikai Xie. An electrothermally-actuated, dual-mode micromirror for large bi-directional scanning. *IEDM Technical Digest. IEEE International Electron Devices Meeting, 2004.*, pages 1–4, 2004. ISSN 01631918. doi: 10.1109/IEDM.2004.1419060.

- [233] S. Schweizer, S. Calmes, M. Laudon, and Ph Renaud. Thermally actuated optical microscanner with large angle and low consumption. *Sensors and Actuators, A: Physical*, 76(1-3): 470–477, 1999. ISSN 09244247. doi: 10.1016/S0924-4247(99)00012-6.
- [234] S. Schweizer, P. Cousseau, G. Lammel, S. Calmes, and Ph Renaud. Two-dimensional thermally actuated optical microprojector. *Sensors and Actuators, A: Physical*, 85(1):424–429, 2000. ISSN 09244247. doi: 10.1016/S0924-4247(00)00384-8.
- [235] Sagnik Pal and Huikai Xie. Analysis and Simulation of Curved Bimorph Microactuators. 2 (September):2–5, 2010.
- [236] Sagnik Pal and Huikai Xie. Design and fabrication of 2D fast electrothermal micromirrors with large scan range and small center shift. pages 2550–2553, 2011. doi: 10.1109/TRANSDUCERS.2011.5969768.
- [237] Huikai Xie, Ankur Jain, Tuqiang Xie, Yingtian Pan, and G.K. Fedder. A single-crystal silicon-based micromirror with large scanning angle for biomedical applications. *Conference on Lasers and Electro-Optics, 2003. CLEO '03.*, pages 1–3, 2003. ISSN 10945695. doi: 10.1109/CLEO.2003.1298114.
- [238] Kemiao Jia, Sagnik Pal, Lei Wu, Douglas Hamilton, and Huikai Xie. Dental optical coherence tomography employing miniaturized MEMS-based imaging probe. *2009 IEEE/LEOS International Conference on Optical MEMS and Nanophotonics, OPTMEMS 2009*, 2:1–2, 2009. doi: 10.1109/OMEMS.2009.5338637.
- [239] Lin Liu, Erkang Wang, Xiaoyang Zhang, Yiqi Tang, and Huikai Xie. Confocal microendoscopic 3D imaging using MEMS scanners for both lateral and axial scans. *Proceedings of the IEEE International Conference on Micro Electro Mechanical Systems (MEMS)*, (c): 1085–1088, 2013. ISSN 10846999. doi: 10.1109/MEMSYS.2013.6474438.
- [240] Xiaoyang Zhang, Boxiao Li, Xingde Li, and Huikai Xie. A robust, fast electrothermal micromirror with symmetric bimorph actuators made of copper/tungsten. In *Transducers' 15*, pages 912–915, 2015. ISBN 9781479989553.
- [241] Xiaoyang Zhang, Liang Zhou, Can Duan, Dong Zheng, Sanjeev Koppal, Quentin Tanguy, and Huikai Xie. A Wide-angle Immersed MEMS Mirror and Its Application in Optical Coherence Tomography. *International Conference on Optical MEMS and Nanophotonics*, pages 8–9, 2016. ISSN 21605041. doi: 10.1109/OMN.2016.7565908.
- [242] Donglin Wang, Linlai Fu, Xin Wang, Zhongjian Gong, Sean R. Samuelson, Can Duan, Hongzhi Jia, Junshan Ma, and Huikai Xie. Endoscopic swept-source optical coherence tomography based on a two-axis microelectromechanical system mirror. *Journal of biomedical optics*, 18(8):1–5, 2013. ISSN 1560-2281.
- [243] Donglin Wang, Peng Liang, Sean R. Samuelson, Hongzhi Jia, Junshan Ma, and Huikai Xie. Correction of image distortions in endoscopic optical coherence tomography based on two-axis scanning MEMS mirrors. *Biomedical Optics Express*, 4(10):2066, 2013. ISSN 2156-7085. doi: 10.1364/BOE.4.002066. URL [↗](#).

- [244] Hao Zhang, Dacheng Xu, Xiaoyang Zhang, Qiao Chen, Huikai Xie, and Suiqiong Li. Model-based angular scan error correction of an electrothermally-actuated mems mirror. *Sensors (Switzerland)*, 15(12):30991–31004, 2015. ISSN 14248220. doi: 10.3390/s151229840.
- [245] Huikai Xie, Kemiao Jia, and Sean R. Samuelson. Development HFF large-aperture micromirrors agile optical phased arrays. (February), 2010.
- [246] Lei Wu, Sean R. Samuelson, Jingjing Sun, Se Woon Choe, Brian S. Sorg, and Huikai Xie. A 2.8-mm imaging probe based on a high-fill-factor MEMS mirror and wire-bonding-free packaging for endoscopic optical coherence tomography. *Journal of Microelectromechanical Systems*, pages 33–36, 2011. ISSN 10577157. doi: 10.1109/JMEMS.2012.2209404.
- [247] Kemiao Jia and Huikai Xie. High-fill-factor, tip-tilt-piston micromirror array with hidden bimorph actuators and surface mounting capability. 10(3):67–68, 2009.
- [248] Kemiao Jia, Sean R. Samuelson, and Huikai Xie. Single-wafer solution and optical phased array application of micro-mirror arrays with high fill factor and large sub-apertures. *Proceedings of the IEEE International Conference on Micro Electro Mechanical Systems (MEMS)*, pages 180–183, 2010. ISSN 10846999. doi: 10.1109/MEMSYS.2010.5442537.
- [249] Kemiao Jia, Sean R. Samuelson, and Huikai Xie. High-fill-factor micromirror array with hidden bimorph actuators and TipTilt-Piston capability. *Journal of Microelectromechanical Systems*, 20(3):573–582, 2011. ISSN 10577157. doi: 10.1109/JMEMS.2011.2127449.
- [250] Jingjing Sun, Can Duan, Sean Samuelson, and Huikai Xie. Design and Characterization of MEMS Based Optical Coherence Tomography Endoscopic Probe. 2(c):3–5, 2012.
- [251] Can Duan, Donglin Wang, Zhengwei Zhou, Peng Liang, Sean Samuelson, Antonio Pozzi, and Huikai Xie. Swept-source common-path optical coherence tomography with a MEMS endoscopic imaging probe. *SPIE BiOS*, 8934:89342N, 2014. ISSN 16057422. doi: 10.1117/12.2036574. URL [↗](#).
- [252] Kemiao Jia and Huikai Xie. Multi-axis electrothermal scanning micromirror with low driving voltage. *Conference on Lasers and Electro-Optics, 2007, CLEO 2007*, 14:4–5, 2007. ISSN 21622701. doi: 10.1109/CLEO.2007.4452788.
- [253] Sean R. Samuelson and Huikai Xie. A large piston displacement MEMS mirror with electrothermal ladder actuator arrays for ultra-low tilt applications. *Journal of Microelectromechanical Systems*, 23(1):39–49, 2014. ISSN 10577157. doi: 10.1109/JMEMS.2013.2290994.
- [254] Wei Wang, Sean R. Samuelson, Jiapin Chen, and Huikai Xie. Miniaturizing fourier transform spectrometer with an electrothermal micromirror. *IEEE Photonics Technology Letters*, 27(13):1418–1421, 2015. ISSN 10411135. doi: 10.1109/LPT.2015.2423637.
- [255] H. Xie, S. Lan, D. Wang, W. Wang, J. Sun, H. Liu, J. Cheng, J. Ding, Z. Qin, Q. Chen, H. Kang, and Z. Tian. Miniature fourier transform spectrometers based on electrothermal MEMS mirrors with large piston scan range. *2015 IEEE SENSORS - Proceedings*, 2015. doi: 10.1109/ICSENS.2015.7370315.



- [256] W. Wang, Q. Chen, D. Wang, L. Zhou, and H. Xie. A bi-directional large-stroke electrothermal MEMS mirror with minimal thermal and temporal drift. *Proceedings of the IEEE International Conference on Micro Electro Mechanical Systems (MEMS)*, pages 331–334, 2017. ISSN 10846999. doi: 10.1109/MEMSYS.2017.7863408.
- [257] J Singh, J H S Teo, Y Xu, C S Premachandran, N Chen, R Kotlanka, M Olivo, and C J R Sheppard. A two axes scanning SOI MEMS micromirror for endoscopic bioimaging. *Journal of Micromechanics and Microengineering*, 18(2):025001, 2007. ISSN 0960-1317. doi: 10.1088/0960-1317/18/2/025001.
- [258] C. S. Premachandran, Ahmad Khairyanto, Kelvin Chen Wei Sheng, Janak Singh, Jason Teo, Xu Yingshun, Chen Nanguang, Colin Sheppard, and Malini Olivo. Design, fabrication, and assembly of an optical biosensor probe package for OCT (optical coherence tomography) application. *IEEE Transactions on Advanced Packaging*, 32(2):417–422, 2009. ISSN 15213323. doi: 10.1109/TADVP.2009.2013658.
- [259] X J Mu, G Y Zhou, H H Feng, Y S Xu, A B Yu, and C W Tan. Procedia Engineering A 3mm Endoscopic Probe with Integrated MEMS Micromirror for Optical Coherence Tomography Bioimaging. *Engineering*, 00(2009):5–8, 2010.
- [260] Xiaojing Mu, Guangya Zhou, Hanhua Feng, Yingshun Xu, Aibin Yu, C. W. Tan, Kelvin Wei Sheng Chen, Jin Xie, and Fook Siong Chau. A 3mm Endoscopic Probe with Integrated MEMS Micromirror for Optical Coherence Tomography Bioimaging. *Sensors and Actuators, A: Physical*, 168(1):202–212, 2010. ISSN 09244247. doi: 10.1016/j.sna.2011.03.040. URL [↗](#).
- [261] Xiaojing Mu, Winston Sun, Hanhua Feng, Aibin Yu, Kelvin Wei Sheng Chen, Chit Yaw Fu, and Malini Olivo. MEMS micromirror integrated endoscopic probe for optical coherence tomography bioimaging. *Sensors and Actuators, A: Physical*, 168(1):202–212, 2011. ISSN 09244247. doi: 10.1016/j.sna.2011.03.040. URL [↗](#).
- [262] U. Izhar, A. B. Izhar, and S. Tatic-Lucic. A multi-axis electrothermal micromirror for a miniaturized OCT system. *Sensors and Actuators, A: Physical*, 167(2):152–161, 2011. ISSN 09244247. doi: 10.1016/j.sna.2011.04.003. URL [↗](#).
- [263] M. Lara-Castro, A. Herrera-Amaya, M.A. Escarola-Rosas, M. Vázquez-Toledo, F. López-Huerta, L.A. Aguilera-Cortés, and A.L. Herrera-May. Design and modeling of polysilicon electrothermal actuators for a MEMS mirror with low power consumption. *Micromachines*, 8(7):203, 2017. ISSN 2072666X. doi: 10.3390/mi8070203.
- [264] Huikai Xie, Jingjing Sun, and Lei Wu. Optical micro-endoscopes for 3D in-vivo imaging. *Proceedings of SPIE*, 2:71682O–71682O–9, 2009. ISSN 1605-7422. doi: 10.1117/12.808577. URL [↗](#).
- [265] Lei Wu and H Xie. A lateral-shift-free and large-vertical-displacement electrothermal actuator for scanning micromirror/lens. *TRANSDUCERS and EUROSENSORS '07 - 4th International Conference on Solid-State Sensors, Actuators and Microsystems*, pages 1075–1078, 2007. doi: 10.1109/SENSOR.2007.4300320.

- [266] Lei Wu and Huikai Xie. A lateral-shift-free LVD microlens scanner for confocal microscopy. *2007 IEEE/LEOS International Conference on Optical MEMS and Nanophotonics, OMENS*, 3:141–142, 2007. doi: 10.1109/OMEMS.2007.4373880.
- [267] Lei Wu, S. B. Maley, S. R. Dooley, T. R. Nelson, P. F. McManamon, and Huikai Xie. A large-aperture, piston-tip-tilt micromirror for optical phase array applications. *Proceedings of the IEEE International Conference on Micro Electro Mechanical Systems (MEMS)*, pages 754–757, 2008. ISSN 10846999. doi: 10.1109/MEMSYS.2008.4443766.
- [268] Lei Wu, A. Pais, S. R. Samuelson, Shuguang Guo, and Huikai Xie. A Miniature Fourier Transform Spectrometer by a Large-Vertical-Displacement Microelectromechanical Mirror. pages 4–6, 2009. ISSN 21622701. URL [↗](#).
- [269] Lei Wu, A. Pais, S. R. Samuelson, Shuguang Guo, and Huikai Xie. A mirror-tilt-insensitive fourier transform spectrometer based on a large vertical displacement micromirror with dual reflective surface. *TRANSDUCERS 2009 - 15th International Conference on Solid-State Sensors, Actuators and Microsystems*, pages 2090–2093, 2009. doi: 10.1109/SENSOR.2009.5285647.
- [270] Lei Wu and Huikai Xie. Large-aperture, rapid scanning MEMS micromirrors for free-space optical communications. *2009 IEEE/LEOS International Conference on Optical MEMS and Nanophotonics, OPTMEMS 2009*, 2(c):131–132, 2009. doi: 10.1109/OMEMS.2009.5338553.
- [271] Lei Wu and Huikai Xie. A tunable microlens with 0.9 mm scan range and small lateral shift. *2009 IEEE/LEOS International Conference on Optical MEMS and Nanophotonics, OPTMEMS 2009*, (c):69–70, 2009. doi: 10.1109/OMEMS.2009.5338591.
- [272] Lei Wu and Huikai Xie. A millimeter-tunable-range microlens for endoscopic biomedical imaging applications. *IEEE Journal of Quantum Electronics*, 46(9):1237–1244, 2010. ISSN 00189197. doi: 10.1109/JQE.2010.2048304.
- [273] Lei Wu, Sarah Dooley, Edward A. Watson, Paul F. McManamon, and Huikai Xie. A tip-tilt-piston micromirror array for optical phased array applications. *Journal of Microelectromechanical Systems*, 19(6):1450–1461, 2010. ISSN 10577157. doi: 10.1109/JMEMS.2010.2076777.
- [274] S. Pal and H. Xie. A process for fabricating robust electrothermal micromirrors with customizable thermal response time and power consumption. *International Conference on Optical MEMS and Nanophotonics*, pages 157–158, 2011. ISSN 21605033. doi: 10.1109/OMEMS.2011.6031066.
- [275] Jingjing Sun, Shuguang Guo, Lei Wu, Se-Woon Choe, Brian Sorg, and Huikai Xie. In vivo 3D and Doppler OCT imaging using electrothermal MEMS scanning mirrors. 7594:759405–759405–8, 2010. ISSN 0277786X. doi: 10.1117/12.847237. URL [↗](#).
- [276] Jingjing Sun, Sung Jin Lee, Lei Wu, Malisa Sarntinoranont, and Huikai Xie. Refractive index measurement of acute rat brain tissue slices using optical coherence tomography. *Optics Express*, 20(2):1084, 2012. ISSN 1094-4087. doi: 10.1364/OE.20.001084. URL [↗](#).

- [277] Lin Liu, Lei Wu, Peter Zory, and Huikai Xie. Fiber-optic confocal microscope with an electrothermally-actuated, large-tunable-range microlens scanner for depth scanning. *Proceedings of the IEEE International Conference on Micro Electro Mechanical Systems (MEMS)*, 2:827–830, 2010. ISSN 10846999. doi: 10.1109/MEMSYS.2010.5442280.
- [278] Lin Liu, Lei Wu, Jingjing Sun, Elaine Lin, and Huikai Xie. Miniature endoscopic optical coherence tomography probe employing a two-axis microelectromechanical scanning mirror with through-silicon vias. *Journal of biomedical optics*, 16(2):026006, 2011. ISSN 10833668. doi: 10.1117/1.3533323.
- [279] Lin Liu and Huikai Xie. Three-dimensional confocal scanning microscope using an MEMS mirror for lateral scan and an MEMS lens scanner for depth scan. *International Conference on Optical MEMS and Nanophotonics*, 4(c):158–159, 2012. ISSN 21605033. doi: 10.1109/OMEMS.2012.6318851.
- [280] Lin Liu and Huikai Xie. 3-D confocal laser scanning microscopy based on a full-MEMS scanning system. *IEEE Photonics Technology Letters*, 25(15):1478–1480, 2013. ISSN 10411135. doi: 10.1109/LPT.2013.2267794.
- [281] Lin Liu, Erkang Wang, Xiaoyang Zhang, Wenxuan Liang, Xingde Li, and Huikai Xie. MEMS-based 3D confocal scanning microendoscope using MEMS scanners for both lateral and axial scan. 2015. doi: 10.1016/j.sna.2013.09.035.MEMS-BASED.
- [282] Xiaoyang Zhang, Rui Zhang, Sanjeev Koppal, Lisa Butler, Xiang Cheng, and Huikai Xie. MEMS mirrors submerged in liquid for wide-angle scanning. pages 847–850, 2015.
- [283] Xiaoyang Zhang, Can Duan, Lin Liu, Xingde Li, and Huikai Xie. A non-resonant fiber scanner based on an electrothermally-actuated MEMS stage. *Sensors and Actuators, A: Physical*, 233:239–245, 2015. ISSN 09244247. doi: 10.1016/j.sna.2015.07.001.
- [284] Xiaoyang Zhang, Sanjeev J. Koppal, Rui Zhang, Liang Zhou, Elizabeth Butler, and Huikai Xie. Wide-angle structured light with a scanning MEMS mirror in liquid. *Optics Express*, 24(4):3479, 2016. ISSN 1094-4087. doi: 10.1364/OE.24.003479. URL [↗](#).
- [285] W Wang, J Chen, A S Zivkovic, C Duan, and H Xie. A silicon based fourier transform spectrometer based on an open-loop controlled electrothermally MEMS mirror. *IEEE Transducers*, pages 212–215, 2015.
- [286] Wei Wang, Jiapin Chen, Aleksandar S. Zivkovic, Quentin A. A. Tanguy, and Huikai Xie. A Compact Fourier Transform Spectrometer on a Silicon Optical Bench with an Electrothermal MEMS Mirror. *Journal of Microelectromechanical Systems*, 25(2):347–355, 2016. ISSN 10577157. doi: 10.1109/JMEMS.2016.2522767.
- [287] Wei Wang, Jiapin Chen, Q A Tanguy, and Huikai Xie. A Monolithic Michelson Interferometer with a Large Piston MEMS Micromirror. *International Conference on Optical MEMS and Nanophotonics*, 3(c):2–3, 2016. ISSN 21605041. doi: 10.1109/OMN.2016.7565818.
- [288] Wei Wang, Jiapin Chen, Aleksandar S. Zivkovic, and Huikai Xie. A fourier transform spectrometer based on an electrothermal MEMS mirror with improved linear scan range. *Sensors (Switzerland)*, 16(10), 2016. ISSN 14248220. doi: 10.3390/s16101611.

- [289] Shuguang Guo, Lei Wu, Jingjing Sun, Lin Liu, and Huikai Xie. Three-Dimensional Optical Coherence Tomography Based on a High-Fill-Factor Microelectromechanical Mirror. *Osa/Dh/Fts/Hise/Ntm/Ota*, 2(c):8–10, 2009.
- [290] Shuguang Guo, Jingjing Sun, Antonio Pozzi, Hang Yin Ling, Lei Wu, Lin Liu, and Huikai Xie. 3D polarization-sensitive optical coherence tomography of canine meniscus based on a 2D high-fill-factor microelectromechanical mirror. *Proceedings of the 31st Annual International Conference of the IEEE Engineering in Medicine and Biology Society: Engineering the Future of Biomedicine, EMBC 2009*, pages 1445–1448, 2009. ISSN 1557170X. doi: 10.1109/IEMBS.2009.5332914.
- [291] Fengtian Han, Wei Wang, Xiaoyang Zhang, and Huikai Xie. Modeling and control of a large-stroke electrothermal MEMS mirror for fourier transform microspectrometers. *Journal of Microelectromechanical Systems*, 25(4):750–760, 2016. ISSN 10577157. doi: 10.1109/JMEMS.2016.2565388.
- [292] Fengtian Han, Wei Wang, Xiaoyang Zhang, and Huikai Xie. Miniature Fourier transform spectrometer with a dual closed-loop controlled electrothermal micromirror. *Optics Express*, 24(20):750–760, oct 2016. ISSN 1094-4087. doi: 10.1364/OE.24.022650. URL [↗](#).
- [293] Xiaoyang Zhang, Lin Liu, Wenxuan Liang, Xingde Li, and Huikai Xie. An electrothermal/electrostatic dual driven MEMS scanner with large in-plane and out-of-plane displacement. *International Conference on Optical MEMS and Nanophotonics*, (August):13–14, 2013. ISSN 21605033. doi: 10.1109/OMN.2013.6659035.
- [294] Xiaoyang Zhang, Liang Zhou, Hsdwphqw R I Ohfwulfd, Rpsxwhu Qjqlqhulqj, and R I Orulgd. Xiaoyang Zhang, Liang Zhou, and HuikaiXie. 17(January):71–74, 2016.
- [295] Lei Wu. Electrothermal micromirror with dual-reflective surfaces for circumferential scanning endoscopic imaging. *Journal of Micro/Nanolithography, MEMS, and MOEMS*, 8(1):013030, 2009. ISSN 1932-5150. doi: 10.1117/1.3082186. URL [↗](#).
- [296] Can Duan, Wei Wang, Xiaoyang Zhang, Jinling Ding, Qiao Chen, Antonio Pozzi, and Huikai Xie. A 45 deg-tilted 2-axis scanning micromirror integrated on a silicon optical bench for 3D endoscopic optical imaging. In *Proceedings of the IEEE International Conference on Micro Electro Mechanical Systems (MEMS)*, volume 2, pages 948–951, 2015. ISBN 978-1-4799-7955-4. doi: 10.1109/MEMSYS.2015.7051117.
- [297] Tuqiang Xie, Huikai Xie, Gary K. Fedder, and Yingtian Pan. Endoscopic optical coherence tomography with new MEMS mirror. *Transactions of the Korean Institute of Electrical Engineers*, 39(21), 2003.
- [298] Huikai Xie, Shane Todd, Ankur Jain, and Gary K Fedder. Single-Crystal Silicon Based Electrothermal MEMS Mirrors for Biomedical Imaging Applications. chapter 3. 2006.
- [299] Huikai Xie, Jingjing Sun, Shuguang Guo, and Lei Wu. 3D endoscopic optical coherence tomography based on rapid-scanning MEMS mirrors. 7634(c):76340X–76340X–6, 2009. doi: 10.1117/12.853201. URL [↗](#).

- [300] Can Duan, Wei Wang, Xiaoyang Zhang, Liang Zhou, Antonio Pozzi, and Huikai Xie. A self-aligned 45°-tilted two-axis scanning micromirror for side-view imaging. *Journal of Microelectromechanical Systems*, 25(4):799–811, 2016. ISSN 10577157. doi: 10.1109/JMEMS.2016.2562011.
- [301] Yingtian Pan, Z. G. Wang, Z. L. Wu, Ankur Jain, and Huikai Xie. Diagnosis of biological tissue morphology and function with endoscopic optical coherence tomography. *Engineering in Medicine and Biology Conference*, pages 7217–7220, 2005. ISSN 1557-170X (Print)1557-170X (Linking). doi: 10.1109/IEMBS.2005.1616175.
- [302] Ankur Jain and Huikai Xie. A tunable microlens scanner with large-vertical-displacement actuation. pages 92–95, 2005.
- [303] Ankur Jain and Huikai Xie. An electrothermal SCS micromirror for large Bi-directional 2-D scanning. *The 13th International Conference on Solid-State Sensors, Actuators and Microsystems, 2005. Digest of Technical Papers. TRANSDUCERS '05.*, pages 988–991, 2005. doi: 10.1109/SENSOR.2005.1496621. URL [↗](#).
- [304] Ankur Jain and Huikai Xie. An electrothermal microlens scanner with low-voltage large-vertical-displacement actuation. *IEEE Photonics Technology Letters*, 17(9):1971–1973, 2005. ISSN 10411135. doi: 10.1109/LPT.2005.853223.
- [305] Ankur Jain and Huikai Xie. Endoscopic Microprobe with a LVD Microlens Scanner for Confocal Imaging. (June 2003):168–169, 2006. doi: 10.1109/OMEMS.2006.1708318.
- [306] Ankur Jain and Huikai Xie. Microendoscopic Confocal Imaging Probe Based on. 13(2): 228–234, 2007.
- [307] Shane Truman Todd and Huikai Xie. An Analytical Electrothermal Model of a 1-D Electrothermal MEMS Micromirror. pages 344–353, 2004. doi: 10.1117/12.582136. URL [↗](#).
- [308] Lei Wu and Huikai Xie. A Large Rotation Angle Electrothermal Micromirror with Integrated Platinum Heater. *Optical MEMS*, pages 106–107, 2006.
- [309] Lei Wu and Huikai Xie. 124-degree Rotation Angle Electrothermal Micromirror With Integrated Platinum Heater. *IEEE Journal on Selected Topics in Quantum Electronics*, 13(2): 316–320, 2007. ISSN 1077260X. doi: 10.1109/JSTQE.2007.894066.
- [310] Lei Wu, L Fu, A Jain, Toshi Nishida, M Gu, and Huikai Xie. An Endoscopic Nonlinear Optical Imaging Probe Based on 2-D Micromirror. *Sensors (Peterborough, NH)*, pages 908–909, 2007.
- [311] Lei Wu and Huikai Xie. A Dual Reflective Electrothermal MEMS Micromirror for Full Circumferential Scanning Endoscopic Imaging. 6885, 2008. ISSN 0277786X. doi: 10.1117/12.769621. URL [↗](#).
- [312] Lei Wu and Huikai Xie. A scanning micromirror with stationary rotation axis and dual reflective surfaces for 360 deg forward-view endoscopic imaging. *TRANSDUCERS 2009 - 15th International Conference on Solid-State Sensors, Actuators and Microsystems*, pages 2222–2225, 2009. doi: 10.1109/SENSOR.2009.5285589.

- [313] Sagnik Pal, Kemiao Jia, and Huikai Xie. An Electrothermal Micromirror with High Linear Scanning Efficiency. pages 914–915, 2007. doi: 10.1109/LEOS.2007.4382707.
- [314] Sagnik Pal, Kemiao Jia, Sarah Maley, and Huikai Xie. Reduced order thermal modeling of a one-dimensional electrothermally actuated micromirror device. *Proceedings of SPIE*, 6885: 1–11, 2008. ISSN 0277786X. doi: 10.1117/12.769590. URL [↗](#).
- [315] Sagnik Pal and Huikai Xie. Repeatability study of an electrothermally actuated micromirror. *IEEE International Reliability Physics Symposium Proceedings*, pages 549–556, 2009. ISSN 15417026. doi: 10.1109/IRPS.2009.5173309.
- [316] Sagnik Pal and Huikai Xie. Maximization of constant velocity scan range of electrothermally-actuated micromirror by pulse width modulated drive. *2009 IEEE/LEOS International Conference on Optical MEMS and Nanophotonics, OPTMEMS 2009*, pages 55–56, 2009. doi: 10.1109/OMEMS.2009.5338600.
- [317] Sagnik Pal and Huikai Xie. Dynamic Compact Thermal Model of an Electrothermal Micromirror Based on Transmission Line Theory. 2:589–592, 2010.
- [318] Sagnik Pal and Huikai Xie. Distributed and lumped element models for a bimorph-actuated micromirror. *Journal of Micromechanics and Microengineering*, 20(4):045020, 2010. ISSN 0960-1317. doi: 10.1088/0960-1317/20/4/045020. URL [↗](#).
- [319] Sagnik Pal and Huikai Xie. Pre-shaped open loop drive of electrothermal micromirror by continuous and pulse width modulated waveforms. *IEEE Journal of Quantum Electronics*, 46(9):1254–1260, 2010. ISSN 00189197. doi: 10.1109/JQE.2010.2050864.
- [320] Sagnik Pal and Huikai Xie. Analysis and fabrication of curved multimorph transducers that undergo bending and twisting. *IEEE Sensors*, pages 667–670, 2011. ISSN 10577157. doi: 10.1109/JMEMS.2012.2203104.
- [321] Sagnik Pal, Sean R Samuelson, and Huikai Xie. Novel Mechanisms for Millimeter Range Piston Actuation of Vertical Micromirrors and Microlenses. 18:97–98, 2012.
- [322] Sagnik Pal and Huikai Xie. Analysis and fabrication of curved multimorph transducers that undergo bending and twisting. *Journal of Microelectromechanical Systems*, 21(5):1241–1251, 2012. ISSN 10577157. doi: 10.1109/JMEMS.2012.2203104.
- [323] Sagnik Pal and Huikai Xie. Fabrication of robust electrothermal MEMS devices using aluminum–tungsten bimorphs and polyimide thermal isolation. *Journal of Micromechanics and Microengineering*, 22(11):115036, 2012. ISSN 0960-1317. doi: 10.1088/0960-1317/22/11/115036. URL [↗](#).
- [324] S. Pal, S. R. Samuelson, X. Zhang, and H. Xie. Large in-plane displacement microactuators based on electro-thermal bimorphs with folded multiple segments. *2013 Transducers and Eurosensors XXVII: The 17th International Conference on Solid-State Sensors, Actuators and Microsystems, TRANSDUCERS and EUROSENSORS 2013*, (June):1587–1590, 2013. doi: 10.1109/Transducers.2013.6627086.

- [325] L Liu, S Pal, and Huikai Xie. MEMS mirrors based on curved concentric electrothermal actuators with very small lateral shift and tilt. *Solid-State Sensors, Actuators and Microsystems, 2011 16th International Conference on*, pages 2522–2525, 2011. ISSN 2159-547X. doi: 10.1109/TRANSDUCERS.2011.5969759.
- [326] Sean R. Samuelson and Huikai Xie. Electrothermally actuated large displacement waveguides. *International Conference on Optical MEMS and Nanophotonics*, (August):109–110, 2013. ISSN 21605033. doi: 10.1109/OMN.2013.6659083.
- [327] Quentin A. A. Tanguy, Can Duan, Wei Wang, Huikai Xie, Sylwester Bargiel, Przemyslaw Struk, Philippe Lutz, and Christophe Gorecki. A 2-axis electrothermal MEMS micro-scanner with torsional beam. In *International Conference on Optical MEMS and Nanophotonics*, volume 2016-Sept, 2016. ISBN 9781509010356. doi: 10.1109/OMN.2016.7565919.
- [328] Quentin A A Tanguy, Sylwester Bargiel, Can Duan, Wei Wang, Huikai Xie, Philippe Lutz, and Christophe Gorecki. A 2-axis MEMS scanning micromirror with a 45 degree auto-positioning mechanism for endoscopic probe. *IEEE Transducers' 17*, 2:1947–1950, 2017.
- [329] David Capel. Image Mosaicing. In *Image Mosaicing and Super-resolution*, chapter Image Mosa, pages 47–49. London, springer edition, 2004. URL [↗](#).
- [330] Oscar Pizarro and Hanumant Singh. Toward large-area mosaicing for underwater scientific applications. *IEEE Journal of Oceanic Engineering*, 28(4):651–672, 2003. ISSN 03649059. doi: 10.1109/JOE.2003.819154.
- [331] Authors Lingfeng Zhou, Zhiming Chen, Jin Cheng, Yingtao Ding, and Huikai Xie. Investigation of dynamic thermal behaviors of an electrothermal micromirror Abstract. *Sensors and Actuators: A. Physical*, 263:269–275, 2017. ISSN 09244247. doi: 10.1016/j.sna.2017.06.002. URL [↗](#).
- [332] X X Feng, A Jain, S Pal, L Xiao, T Nishida, and H Xie. LVD micromirror for rapid reference scanning in optical coherence tomography. *MEMS/MOEMS Components and Their Applications IV*, 6464:M4640–M4640, 2007. ISSN 0277786X. doi: Artn64640m\rDoi10.1117/12.703221.
- [333] Ryan Hickey, Marek Kujath, and Ted Hubbard. Heat transfer analysis and optimization of two-beam microelectromechanical thermal actuators. *Journal of Vacuum Science and Technology A: Vacuum, Surfaces, and Films*, 20(3):971, 2002. ISSN 07342101. doi: 10.1116/1.1468654.
- [334] J. Barnothy. Bosworth (thermal inductance).pdf. *Nature*, 158:309, 1946. doi: 10.1038/158309a0. URL [↗](#).
- [335] Lei Wu. *Low-voltage, large-range MEMS optical scanners and their applications*. PhD thesis, University of Florida, 2009. URL [↗](#).
- [336] F. Kreith and M. S. Bohn. Principles of heat transfer. *West Publ.*, 1993.

- [337] Z. L. Wang and D. W. Tang. Investigation of heat transfer around microwire in air environment using 3 omega method. *International Journal of Thermal Sciences*, 64:145–151, 2013. ISSN 12900729. doi: 10.1016/j.ijthermalsci.2012.08.002. URL [↗](#).
- [338] Kyle A. Brucker and Joseph Majdalani. Effective thermal conductivity of common geometric shapes. *International Journal of Heat and Mass Transfer*, 48(23-24):4779–4796, 2005. ISSN 00179310. doi: 10.1016/j.ijheatmasstransfer.2005.05.007.
- [339] Stephen Timoshenko. Analysis of Bi-Metal Thermostats. (1):233–255, 1925. doi: <http://dx.doi.org/10.1364/JOSA.11.000233>.
- [340] Milton Ohring. *Materials science of thin films*. Academic p edition, 2001.
- [341] Yvon Villarceau. *Recherches sur le mouvement et la compensation des chronomètres*. Mallet-bac edition, 1862.
- [342] Wuyong Peng, Zhixiong Xiao, and K. R. Farmer. Optimization of thermally actuated bimorph cantilevers for maximum deflection. *Nanotech*, 1, 2003.
- [343] R. C. Hibbeler. *Mechanics of materials*. 1997.
- [344] Prasanna Srinivasan and S. Mark Spearing. Effect of heat transfer on materials selection for bimaterial electrothermal actuators. *Journal of Microelectromechanical Systems*, 17(3):653–667, 2008. ISSN 10577157. doi: 10.1109/JMEMS.2008.918617.
- [345] Huikai Xie, Yingtian Pan, and G.K. Fedder. A SCS CMOS micromirror for optical coherence tomographic imaging. *Technical Digest. MEMS 2002 IEEE International Conference. Fifteenth IEEE International Conference on Micro Electro Mechanical Systems (Cat. No.02CH37266)*, pages 495–498, 2002. ISSN 1084-6999. doi: 10.1109/MEMSYS.2002.984317.
- [346] David T. Read and James W. Dally. Mechanical behavior of Aluminum and copper thin films. In M. Schen, H Abe, and E. Suhir, editors, *Mechanics and materials for electronic packaging*, page 187. American s edition, 1994.
- [347] Toshiyuki Tsuchiya, Masakazu Hirata, and Norio Chiba. Young’s modulus, fracture strain, and tensile strength of sputtered titanium thin films. *Thin Solid Films*, 484(1-2):245–250, 2005. ISSN 00406090. doi: 10.1016/j.tsf.2005.02.024.
- [348] Hakan Urey. Torsional MEMS scanner design for high-resolution scanning display systems. page 27. International Society for Optics and Photonics, jun 2002. ISBN 0277-786x. doi: 10.1117/12.469198. URL [↗](#).
- [349] R. J. Roark, Warren C Young, and R. Plunkett. Formulas for Stress and Strain. *Journal of Applied Mechanics*, 43(3):522, 1976. ISSN 00218936. doi: 10.1115/1.3423917. URL [↗](#).
- [350] R. A. Buser and N. F. De Rooij. Very high Q-factor resonators in monocrystalline silicon. *Sensors and Actuators: A. Physical*, 21(1-3):323–327, 1990. ISSN 09244247. doi: 10.1016/0924-4247(90)85064-B.



- [351] Zsolt Kadar, Wilko Kindt, Andre Bossche, and Jeff Mollinger. Quality factor of torsional resonators in the low-pressure region. *Sensors and Actuators A: Physical*, 53(1-3):299–303, 1996. ISSN 0924-4247. doi: [http://dx.doi.org/10.1016/0924-4247\(96\)80153-1](http://dx.doi.org/10.1016/0924-4247(96)80153-1). URL [↗](#).
- [352] R. G. Christian. The theory of oscillating-vane vacuum gauges. *Vacuum*, 16(4):175–178, 1966. ISSN 0042207X. doi: 10.1016/0042-207X(66)91162-6.
- [353] H. Teimoori, R. T. Faal, and R. Das. Saint-Venant torsion analysis of bars with rectangular cross-section and effective coating layers. *Applied Mathematics and Mechanics (English Edition)*, 37(2):237–252, 2016. ISSN 15732754. doi: 10.1007/s10483-016-2028-8.
- [354] H. E. Bennett, Jean M. Bennett, and E. J. Ashley. Infrared Reflectance of Evaporated Aluminum Films. *Journal of the Optical Society of America*, 52(11):1245, 1962. ISSN 0030-3941. doi: 10.1364/JOSA.52.001245.
- [355] P J Brosens. Dynamic mirror distortions in optical scanning. *Applied optics*, 11(12):2987–2989, 1972. ISSN 0003-6935. doi: 10.1364/AO.11.002987.
- [356] Kemiao Jia. Development and Applications of High Fill-Factor, Small Footprint Mems Micromirrors and Micromirror Arrays. page 182, 2009.
- [357] Kieth Fedder. Simulation of Microelectromechanical Systems. *Univeristy of California at Berkley Doctoral Theis*, 1994. doi: oclc/33136497.
- [358] Stephen Timoshenko and J N Goodier. Theory of Elasticity, 1951. ISSN 0374-3535. URL [↗](#).
- [359] Quentin A. A. Tanguy, Sylwester Bargiel, Can Duan, Wei Wang, Przemyslaw Struk, Huikai Xie, Philippe Lutz, and Christophe Gorecki. A 2-axis electrothermal MEMS scanning micromirror with a 45deg auto-positioning mechanism for endoscopic probe. In *2017 19th International Conference on Solid-State Sensors, Actuators and Microsystems (TRANSDUCERS 17')*, pages 1947–1950, 2017. ISBN 978-1-5386-2732-7. doi: 10.1109/TRANSDUCERS.2017.7994450. URL [↗](#).
- [360] Riccardo D’Agostino and Daniel L. Flamm. Plasma etching of Si and SiO<sub>2</sub> in SF<sub>6</sub>-O<sub>2</sub> mixtures. *Journal of Applied Physics*, 52(1):162–167, 1981. ISSN 00218979. doi: 10.1063/1.328468.
- [361] Qiao Chen, Hao Zhang, Xiaoyang Zhang, Dacheng Xu, and Huikai Xie. Repeatability study of 2D MEMS mirrors based on S-shaped Al/SiO<sub>2</sub> bimorphs. *8th Annual IEEE International Conference on Nano/Micro Engineered and Molecular Systems, IEEE NEMS 2013*, 1:817–820, 2013. doi: 10.1109/NEMS.2013.6559850.
- [362] Tsung-Han Tsai, Benjamin Potsaid, Yuankai K. Tao, Vijaysekhar Jayaraman, James Jiang, Peter J. S. Heim, Martin F. Kraus, Chao Zhou, Joachim Hornegger, Hiroshi Mashimo, Alex E. Cable, and James G. Fujimoto. Ultrahigh speed endoscopic optical coherence tomography using micromotor imaging catheter and VCSEL technology. *Biomedical Optics Express*, 4(7):1119, 2013. ISSN 2156-7085. doi: 10.1364/BOE.4.001119. URL [↗](#).

- [363] Xiang Cheng, Hangquan Lu, Zhuoge Lou, Huikai Xie, Wei Wang, and Ming Zheng. An Integrated Optoelectronic Position Sensor for MEMS Scanning Mirrors. In *IEEE Transducers'17*, pages 3–6, 2017.
- [364] Victor Farm Guoo Tseng and Huikai Xie. Resonant Inductive Coupling-Based Piston Position Sensing Mechanism for Large Vertical Displacement Micromirrors. *Journal of Microelectromechanical Systems*, 25(1):207–216, 2016. ISSN 10577157. doi: 10.1109/JMEMS.2015.2499301.
- [365] Olivier Thomas. Dynamique linéaire et non linéaire de structures élastiques et piezoélectriques. Instruments de musique, micro/nano systèmes électromécaniques, contrôle de vibration. page 168, 2011. URL [↗](#).

## Publications in peer-reviewed journals

- **Q. A. A. Tanguy**, S. Bargiel, H. Xie, N. Passilly, M. Barthès, O. Gaiffe, J. Rutkowski, P. Lutz & C. Gorecki. Design and fabrication of a 2-axis electrothermal MEMS micro-scanner for optical coherence tomography. *MDPI Micromachines*, **8**(5), pp. 146, 2017. doi: 10.3390/mi8050146
- W. Wang, J. Chen, A. S. Zivkovic, **Q. A. A. Tanguy** & H. Xie. A Compact Fourier Transform Spectrometer on a Silicon Optical Bench with an Electrothermal MEMS Mirror. *Journal of Microelectromechanical Systems*, **25**(2), pp. 347–355, 2016. doi: 10.1109/JMEMS.2016.2522767
- C. Duan, **Q. A. A. Tanguy**, A. Pozzi, & H. Xie. Optical coherence tomography endoscopic probe based on a tilted MEMS mirror. *Biomedical Optics Express*, **7**(9), pp. 3345–3354, 2016. doi: 10.1364/BOE.7.003345

## Presentations in international symposiums

- X. Dai, H. Yang, J. Tang, C. Duan, **Q. A. A. Tanguy**, H. Xie & H. Jiang. Miniature multimodal endoscopic probe based on double-clad fiber. In *Proceedings of SPIE*, **10040**, 2017. doi: 10.1117/12.2251510
- **Q. A. A. Tanguy**, S. Bargiel, C. Duan, W. Wang, P. Struk, H. Xie, P. Lutz & C. Gorecki. A 2-axis MEMS scanning micromirror with a 45° auto-positioning mechanism for endoscopic probe. In *19th International Conference on Solid-State Sensors, Actuators and Microsystems, TRANSDUCERS 17'*, pp. 1947–1950, 2017. doi: 10.1109/TRANSDUCERS.2017.7994450
- **Q. A. A. Tanguy**, C. Duan, W. Wang, H. Xie, S. Bargiel, P. Struk & C. Gorecki. A 2-axis electrothermal MEMS micro-scanner with torsional beam. In *IEEE International Conference on Optical MEMS and Nanophotonics*, Vol. 2016–September. doi: 10.1109/OMN.2016.7565919
- X. Zhang, L. Zhou, C. Duan, D. Zheng, S. Koppal, **Q. A. A. Tanguy** & Xie, H. A Wide-angle Immersed MEMS Mirror and Its Application in Optical Coherence Tomography. *IEEE International Conference on Optical MEMS and Nanophotonics (OMN)*, pp. 8–9, 2016. doi: 10.1109/OMN.2016.7565908
- W. Wang, J. Chen, **Q. A. A. Tanguy** & H. Xie. A Monolithic Michelson Interferometer with a Large Piston MEMS Micromirror. *International Conference on Optical MEMS and Nanophotonics (OMN)*, **3**(c), pp. 2–3, 2016. doi: 10.1109/OMN.2016.7565818
- M. T. Chikhaoui, M. Ourak, **Q. A. A. Tanguy**, P. Struk, K. Rabenorosoa, S. Bargiel, B. Tamadazte, N. Passilly, O. Gaiffe, L. Froehly, N. Andreff. Endomicroscope for gastrointestinal cancer detection: concept and preliminary results. In *Proceedings of Surgetica*, pp. 9–11.

This document was generated with L<sup>A</sup>T<sub>E</sub>X.

It includes vector graphics from the TikZ package for L<sup>A</sup>T<sub>E</sub>X and figures generated with Python.

## Abstract:

The work presented in this manuscript consists in the conception of an electro-thermo-mechanical optical micro-scanner. In a first time, a design and a model are proposed and the micro-device was fabricated, characterized and a draft of integration onto a Mirau micro-interferometer was carried out in order to build an endoscopic probe for the detection of early stage gastrointestinal cancers using an imaging technique called Optical Coherence Tomography (OCT). The very contribution of the thesis is the development and the fabrication of micro actuators driven electrothermally to control the angular position a micro mirror plate conceived in this purpose. Different architectures of micro-scanners are proposed to best comply with the specifications determined by both the optical expectations and the medical standards requirements of the final apparatus *in vivo*. This work, part of a project called "DEMO4" was financed by the French LabEx Action funding source in cooperation between the departments AS2M and MN2S of the French research institute Femto-ST as well as the university of Florida in the USA to deliver a first demonstrator of endoscopic OCT probe. Several batches of fabrication were realized by means of techniques of complementary metal oxide semi-conductor (CMOS)-based microfabrication in exchange between Femto-ST and the university of Florida before being assembled (for lack of monolithic integration capability) onto a micro-interferometer using automated processes specifically developed in this purpose. Finally, an experimental setup is proposed to characterize in order to evaluate the performances achieved and initiate the first tests of optical imaging using the micro-system.

**Keywords:** Micro Optical ElectroMechanical System (MOEMS), optical microscanner, microfabrication, electrothermal actuation, Optical Coherence Tomography (OCT), endoscopy.

## Résumé :

Les travaux présentés dans cette thèse reposent d'une part sur le design et la modélisation electro-thermo-mécanique d'un micro scanner optique et d'autre part sur sa fabrication, et sa caractérisation ainsi qu'un début d'intégration à un micro interféromètre de Mirau pour le développement d'une sonde endoscopique conçue pour la détection des cancers gastrointestinaux dans leur phase initiale par une technique d'imagerie appelée Tomography de Cohérence Optique (OCT). Le cœur de la contribution de cette thèse porte sur le développement et la fabrication de micro actionneurs commandés thermiquement pour l'orientation contrôlée d'un micromiroir conçu à cet effet. Différentes architectures de micro scanners sont proposées afin de répondre au mieux aux problématiques imposées par les exigences en matière de qualité d'imagerie optique et de compatibilité avec les normes dans le cadre de l'utilisation médical *in vivo* du dispositif final. Ces travaux s'inscrivent dans le projet DEMO4 financé par le LabEx Action en coopération entre les départements MN2S et AS2M de l'institut de recherche Français Femto-ST ainsi que de l'université de Floride aux États-Unis afin de délivrer un premier démonstrateur de sonde endoscopique OCT. Plusieurs séries de fabrication ont été mises en œuvre grâce à des techniques de microfabrication de semiconducteurs développées en échange entre l'université de Floride et Femto-ST avant d'être assemblées (à défaut d'intégration monolithique) par procédés robotisés à un micro-interféromètre développé à Femto-ST. Finalement, un montage expérimental pour la caractérisation du micromiroir est également proposé pour permettre l'évaluation des performances atteintes et afin d'amorcer les premiers tests d'imagerie optiques du micro système.

**Mots-clés :** MOEMS, micro scanner optique, micro fabrication, actionnement électro-thermique, Tomography de Cohérence Optique (OCT), endoscopie.

The logo for SPIM (École doctorale SPIM) features the letters 'S', 'P', 'I', and 'M' in a large, white, sans-serif font. The 'S' is stylized with a thick, light green horizontal bar behind it.

■ École doctorale SPIM 1 rue Claude Goudimel F - 25030 Besançon cedex

■ tél. +33 (0)3 81 66 66 02 ■ [ed-spim@univ-fcomte.fr](mailto:ed-spim@univ-fcomte.fr) ■ [www.ed-spim.univ-fcomte.fr](http://www.ed-spim.univ-fcomte.fr)

The logo for the University of Franche-Comté (UFC) features the letters 'U' and 'FC' in a large, bold, black font. Below them, the text 'UNIVERSITÉ DE FRANCHE-COMTÉ' is written in a smaller, black, sans-serif font. A small yellow vertical bar is positioned to the left of the 'U'.